TECHNISCHE UNIVERSITÄT MÜNCHEN

TUM School of Engineering and Design

Numerical simulation of asymmetrically heated high aspect ratio duct flows under secondary flow influence

Thomas Kaller

Vollständiger Abdruck der von der TUM School of Engineering and Design der Technischen Universität München zur Erlangung des akademischen Grades eines

Doktors der Ingenieurwissenschaften

genehmigten Dissertation.

Vorsitzender:	Prof. Dr.-Ing. Manfred Hajek
Prüfer der Dissertation:	1. Prof. Dr.-Ing. Nikolaus A. Adams
	2. Prof. Dr.-Ing. Stefan Hickel

Die Dissertation wurde am 25.08.2021 bei der Technischen Universität München eingereicht und durch die TUM School of Engineering and Design am 17.05.2022 angenommen.

ThomasKaller1987@gmail.com

Released November 17, 2022
Typesetting LaTeX

Abstract

In this thesis, well-resolved large-eddy simulations (LES) of the turbulent flow through straight and curved asymmetrically heated high aspect ratio cooling ducts (HARCDs) are presented. Two principal configurations are investigated: (I) a long straight HARCD set-up using liquid water at a bulk Reynolds number of $Re_b = 110 \cdot 10^3$, an average Nusselt number of $Nu_{xz} = 371$ and wall to bulk temperature difference of $T_w - T_b = 40\,\mathrm{K}$, and (II) a curved HARCD set-up with varying curvature radius and a short straight inlet section using ideal gas air at $Re_b = 40 \cdot 10^3$, Nu_{xz} up to 68 and $T_w - T_b = 105\,\mathrm{K}$. Geometry and boundary conditions of the former set-up follow a companion experiment defined in cooperation with project partners. The experimental-numerical comparison shows good agreement. Differences are further improved by employing an updated experimental set-up, which has been enhanced partly based on findings of the LES.

Based on the straight water HARCD set-up, we study the influence of asymmetric heating on the duct flow with a specific focus on the interaction of turbulence-induced secondary flow and turbulent heat transfer as well as the related spatial thermal boundary layer development and associated viscosity variation. We find that the viscosity drop towards the heated wall leads to a decrease in turbulent mixing, turbulent length scales and turbulence anisotropy as well as to a weakening of turbulent ejections. The overall secondary flow strength continuously reduces along the heated duct compared to the adiabatic duct section. Furthermore, the assumption of a constant turbulent Prandtl number is assessed and shown to be invalid for turbulent heat transfer in an asymmetrically heated HARCD.

The curved air HARCD set-ups are derived from the water HARCD and have an identical cross-sectional geometry. The curved end sections of varying curvature are attached after a shortened straight section. The analysis comprises analogously the effects of asymmetric heating on the flow field of the straight section for the different temperature dependence of the viscosity of air, and additionally the effects of the developing curvature-induced secondary flow. The viscosity of air rises in a heated boundary layer flow and consequently the inverse behaviour as for the water HARCD is observable for turbulence profiles, and the turbulence-induced secondary flow weakens. The interaction of turbulence-induced and curvature-induced secondary flow is analysed and the effects of the combined cross-flow field on the increasing turbulent heat transfer studied. The curvature radii of three configurations are defined such that the Dean vortex strengths vary from comparably strong to 10 times stronger than the turbulence-induced secondary flow. For the latter set-up, Dean vortices are dominating the cross-flow field, whereas for the former an interaction and gradual coalescence takes place.

Moreover, the well-resolved LES databases for both HARCD configurations are utilised to assess the prediction capabilities of various Reynolds-averaged Navier-Stokes (RANS) turbulence models and turbulent heat flux closure approaches. The analysis separately points out deviations for the different models in predicting (I) the turbulence-induced secondary flow field, (II) the

complex interaction of turbulence- and curvature-induced secondary flow field and (III) the associated turbulent heat transfer and temperature distributions in the straight and curved sections.

Zusammenfassung

Im Rahmen dieser Dissertation werden fein aufgelöste Grobstruktursimulationen (large-eddy simulation, LES) turbulenter Strömungen durch gerade und gekrümmte asymmetrisch beheizte Kühlkanäle mit hoher Streckung (high aspect ratio cooling duct, HARCD) vorgestellt. Zwei Hauptkonfigurationen werden untersucht: (I) eine lange gerade HARCD Konfiguration, welche flüssiges Wasser bei einer Reynolds-Zahl von $Re_b = 110 \cdot 10^3$ bezogen auf die Kernströmung, einer mittleren Nusselt-Zahl von $Nu_{xz} = 371$ und einer Temperaturdifferenz von Wand zu Kernströmung von $T_w - T_b = 40\,\mathrm{K}$ verwendet, und (II) eine gekrümmte HARCD Konfiguration mit variablem Krümmungsradius und verkürtem geraden Einlaufstück, welche Luft als ideales Gas bei $Re_b = 40 \cdot 10^3$, Nu_{xz} bis zu 68 und $T_w - T_b = 105\,\mathrm{K}$ aufweist. Für die erstgenannte Konfiguration basieren Geometrie und Randbedingungen auf einem begleitenden Experiment, welches in Kooperation mit Projektpartnern definiert wurde. Die Übereinstimmung der Ergebnisse von Simulation und Experiment ist sehr gut und wird durch ein Update des experimentellen Aufbaus, welches teilweise auf Erkenntnissen der LES basiert, weiter verbessert.

Die Untersuchung des geraden Wasser-HARCDs zeigt den Einfluss asymmetrischer Beheizung auf das Strömungsfeld des Kanals mit einem besonderen Fokus auf der Interaktion von turbulenzinduzierter Sekundärströmung und turbulenter Wärmeübertragung, ebenso wie die damit verbundene räumliche Entwicklung der Temperaturgrenzschicht und einhergehende Veränderung der Viskosität. Der Viskositätsabfall in der beheizten Grenzschicht bewirkt eine Reduktion der turbulenten Durchmischung, der turbulenten Längenskalen und der Turbulenzanisotropie genauso wie eine Abschwächung der turbulenten Ejektionen von der Wand. Im Vergleich zum adiabaten Kanalabschnitt reduziert sich entlang des beheizten Kanals die Gesamtstärke der Sekundärströmung kontinuierlich. Außerdem wird die Annahme einer konstanten turbulenten Prandtl-Zahl beurteilt und gezeigt, dass diese für den Fall turbulenter Wärmeübertragung in einem asymmetrisch beheizten Kanal ungültig ist.

Der Aufbau der gekrümmten Luft-HARCDs ist von der vorherigen Wasser-HARCD Konfiguration abgeleitet. Die Konfigurationen weisen einen identischen Querschnitt auf, wobei an einen verkürzten geraden Kanalabschnitt ein gekrümmtes Endstück mit variablem Krümmungsradius angehängt ist. Analog zu vorher umfasst die Auswertung zunächst die Auswirkungen asymmetrischer Beheizung auf das Strömungsfeld des geraden Kanalsegments, nun bei mit der Temperatur ansteigender Viskosität, und zusätzlich die Effekte der sich entwickelnden krümmungsinduzierten Sekundärströmung. Entlang des geraden Segments nimmt zur beheizten Wand hin die Viskosität zu, weshalb für die Turbulenzprofile ein zum Wasser-HARCD inverses Verhalten beobachtet wird. Damit einher geht eine Abschwächung der turbulenzinduzierten Sekundärströmung. Entlang des gekrümmten Segments wird dann die Interaktion von turbulenz- und krümmungsinduzierter Sekundärströmung analysiert und die Auswirkungen des kombinierten Querströmungsfelds auf die resultierende turbulente Wärmeübertragung diskutiert. Die Krümmungsradien der drei

untersuchten Konfigurationen sind so gewählt, dass die Stärke der Dean-Wirbel im Vergleich zur turbulenzinduzierten Sekundärströmung zwischen ähnlich stark und bis zu 10 mal stärker variiert. Im letztgenannten Fall dominieren die Dean-Wirbel das Querströmungsfeld, wohingegen es im erstgenannten von einer Interaktion und allmählichem Zusammenwachsen der Sekundärströmungsstrukturen geprägt wird.

Des Weiteren werden die fein aufgelösten LES Referenzlösungen beider Konfigurationen dazu verwendet das Vorhersagepotential verschiedener Turbulenzmodelle und Ansätze zur Schließung des turbulenten Wärmeflusses im Rahmen von Reynolds-gemittelten Navier-Stokes (Reynolds-averaged Navier-Stokes, RANS) Simulationen zu beurteilen. Die Untersuchung geht gesondert auf Abweichungen der verschiedenen Modelle ein für die Prognose (I) des turbulenzinduzierten Sekundärströmungsfelds, (II) der komplexen Interaktion von turbulenz- und krümmungsinduziertem Sekundärströmungsfeld und (III) der damit verbundenen turbulenten Wärmeübertragung und Temperaturverteilungen in den geraden und gekrümmten Kanalsegmenten.

Danksagung

Zuallererst möchte ich mich bei Herrn Professor Adams für die Ermöglichung der Promotion sowie die Betreuung und Unterstützung über die letzten Jahre bedanken. Trotz Ihrer Doppelbelastung als Lehrstuhlleiter und Dekan haben Sie sich immer kurzfristig für Fragen Zeit genommen. Sie haben mir vertrauensvoll große wissenschaftliche Freiheiten gelassen und es mir ermöglicht mehrere internationale Konferenzen zu besuchen. Vielen Dank dafür!

Ein besonderer Dank gebührt Professor Stefan Hickel. Du hast als Leiter der LES-Gruppe einen großen Beitrag daran gehabt mir nach meinem wissenschaftlichen Ausflug nach Köln meine Promotion am Lehrstuhl im Rahmen des SFB-TRR40 zu ermöglichen. Durch deine motivierende intensive Betreuung habe ich sehr viel im Bereich der Methodenentwicklung, Turbulenzmodellierung und numerischen Strömungssimulation insgesamt gelernt. Dafür vielen Dank, ebenso für deine Zusage als Prüfer dieser Arbeit!

Nicht unerwähnt bleiben darf auch Dr. Steffen Schmidt als Leiter der Gasdynamik-Gruppe. Dir möchte ich für die zahlreichen hilfreichen Diskussionen danken, sowohl für die fachlichen tief numerischen als auch für die fachverwandten "hinter-den-Kulissen" Gespräche. Ebenfalls Danke an Vito und Alex für die Unterstützung und erfolgreiche Zusammenarbeit, sowohl in der Code-Entwicklung als auch Ergebnisdarstellung bei den SFB-Treffen. Das spätnächtliche/frühmorgendliche Erstellen von Foliensätzen, am besten mit Alex' stilvollen Metal-Balladen im Hintergrund, wird mir immer bestens in Erinnerung bleiben. Alex gebührt zusätzlich noch ganz besonderer Dank für die Korrektur der ersten Version dieser Dissertation. Alex, Theresa, Antonio, Xiuxiu, Julie und Michael: danke an euch den Lehrstuhl nicht zu einem reinen Arbeitsplatz gemacht zu haben, sondern zu einem Ort, an welchem man auch Spaß haben und Freundschaften schließen kann. Die Kurztrips nach Madrid, Israel, Vancouver und Balkonien waren eine wunderbare Zeit! Extrem wichtig waren auch die Freunde im realen nicht-TUM Leben, die mich immer wieder erfolgreich geerdet und mir aufgezeigt haben, dass das Leben noch etwas anderes beinhaltet als numerische Strömungssimulationen. Danke hierfür an Almut, Birte, Christoph, Fay, Felix, Jasmin, Marc, Thomas und Verena!

Zu guter Letzt geht ein herzliches Dankeschön an meine Familie, an meine Mutter Lieselotte, meinen Bruder Jürgen und meinen Patenonkel Rainer. Eine besonders wichtige Rolle nahm auch mein Vater Hans ein, der es schaffte mich von klein auf in der heimischen Schreinerwerkstatt für Technik zu begeistern und mich entsprechend förderte, dem es aber leider nicht vergönnt war mitzuerleben welchen Karriereweg ich nach der Schulzeit einschlagen würde.

List of Publications

Several journal publications, book chapter and conference contributions have been produced during this PhD. This thesis is partly based upon these publications. Reproduced text sections are marked and the necessary authorisation from the corresponding publisher has been obtained.

Peer–Reviewed Journal Papers

1. **T. Kaller**, V. Pasquariello, S. Hickel and N. A. Adams (2019) Turbulent flow through a high aspect ratio cooling duct with asymmetric wall heating. *Journal of Fluid Mechanics*, **860**, 258-299. doi:10.1017/jfm.2018.836.

2. **A. Doehring**, T. Kaller, S. J. Schmidt and N. A. Adams (2021) Large-eddy simulation of turbulent channel flow at transcritical states. *International Journal of Heat and Fluid Flow*, **89**, 108781. doi:10.1016/j.ijheatfluidflow.2021.108781.

Peer–Reviewed Book Chapter Contributions

1. **T. Kaller**, A. Doehring, S. Hickel, S. J. Schmidt and N. A. Adams (2021) Assessment of RANS turbulence models for straight cooling ducts: secondary flow and strong property variation effects. In N. A. Adams, W. Schröder, R. Radespiel, O. Haidn, T. Sattelmayer, C. Stemmer, B. Weigand (eds) *Future Space-Transport-System Components under High Thermal and Mechanical Loads: Results from the DFG Collaborative Research Center TRR40*, Notes on Numerical Fluid Mechanics and Multidisciplinary Design, vol 146, Springer, Cham. doi:10.1007/978-3-030-53847-7_20.

Conference Proceedings

1. **T. Kaller**, V. Pasquariello, S. Hickel and N. A. Adams (2017) Large-eddy simulation of the high-Reynolds-number flow through a high-aspect-ratio cooling duct. In *Proceedings of the 10th International Symposium on Turbulence and Shear Flow Phenomena (TSFP-10)*, Chicago, USA.

2. **T. Kaller**, V. Pasquariello, S. Hickel and N. A. Adams (2017) Numerical investigation of the flow in a high-aspect-ratio cooling duct. In *66. Deutscher Luft- und Raumfahrtkongress 2017*, München, Germany.

3. **T. Kaller**, S. Hickel and N. A. Adams (2018) LES of an asymmetrically heated high aspect ratio duct at high Reynolds number at different wall temperatures. In *12th*

AIAA/ASME Joint Thermophysics and Heat Transfer Conference, Atlanta, USA. doi:10.2514/6.2018-4287.

4. **T. Kaller**, S. Hickel and N. A. Adams (2020) Prediction capability of RANS turbulence models for asymmetrically heated high-aspect-ratio duct flows. In *AIAA Scitech 2020 Forum*, Orlando, USA. doi:10.2514/6.2020-0354.

Peer–Reviewed Technical Reports

1. **T. Kaller**, V. Pasquariello, S. Hickel and N. A. Adams (2016) Numerical investigation of the flow in a high aspect ratio water cooling duct. In *Annual Report 2016 of the Sonderforschungsbereich/Transregio 40.*

2. **T. Kaller**, V. Pasquariello, S. Hickel and N. A. Adams (2017) Large-eddy simulation of the high-Reynolds-number flow through a high-aspect-ratio cooling duct. In *Annual Report 2017 of the Sonderforschungsbereich/Transregio 40.*

3. **T. Kaller**, A. Doehring and N. A. Adams (2019) Numerical investigation of a high-aspect-ratio cooling duct flow with different RANS turbulence models. In *Annual Report 2019 of the Sonderforschungsbereich/Transregio 40.*

Contents

List of Figures

List of Tables

1 Introduction

This thesis summarises the major part of my work over the past six years at the Chair of Aerodynamics and Fluid Mechanics of the Department of Mechanical Engineering at the Technical University of Munich. During this time my work has been a part of the collaborative research centre SFB-TRR40[1] funded by the German Research Foundation DFG. The comprehensive goal of the SFB-TRR40 has been the investigation of the *'technological foundations for the design of thermally and mechanically highly loaded components of future space transport systems'*, with the focus being on liquid-propellant rocket engine (LRE) propulsion. An example is the Vulcain LRE family used in the European Ariane 5 and Ariane 6 launcher systems. The specific topic of my sub-project within the SFB-TRR40 has been *'heat transfer in nozzle cooling channels'*, which is investigated using computational fluid dynamics (CFD). In LRE temperatures up to 3600 K and heat fluxes up to $160\,\mathrm{MW/m^2}$ are present, demanding for an efficient structural cooling. For this purpose an array of high aspect ratio cooling ducts (HARCDs) is arranged around the LRE combustion chamber and nozzle. To gain a deeper understanding of the interaction of flow turbulence, secondary flows and turbulent heat transfer high-fidelity simulations of generic HARCD configurations have been performed and cross-validated with experimental results of project partners. The findings are of fundamental nature, i.e. they are applicable to a wide range of technical cooling applications from electric vehicle battery to gas turbine cooling.

1.1 Duct Flow and Secondary Flow Physics

Turbulent flow and heat transfer in a high aspect ratio cooling duct (HARCD) with rectangular cross-section is of great importance for many technical applications. The examples range from building ventilation systems over cooling ducts for the thermal management of batteries in electrical vehicles to the cooling systems of rocket engines. In order to predict the cooling efficiency and the lifetime of the respective system, the detailed understanding of cooling duct flows is a prerequisite.

Turbulent flows through heated ducts are strongly influenced by secondary flow features. These include e.g. the generation of vortex arrays in wake regions (Kelvin-Helmholtz instability), buoyancy-driven flow (Rayleigh-Bénard convection) as well as turbulence- and curvature-driven secondary flow. The latter two are in the focus of the present work and are also known as Prandtl's flow of the first kind (curvature-induced) and Prandtl's flow of the second kind (turbulence-induced). Figures 1.1 and 1.2 depict the typical flow field obtained for a square and rectangular cross-section.

Prandtl's flow of the second kind develops due to the anisotropy of the Reynolds stress tensor (Demuren and Rodi, 1984) and is relatively weak with a strength of $1-3\%$ of the bulk flow

[1] http://www.sfbtr40.de/

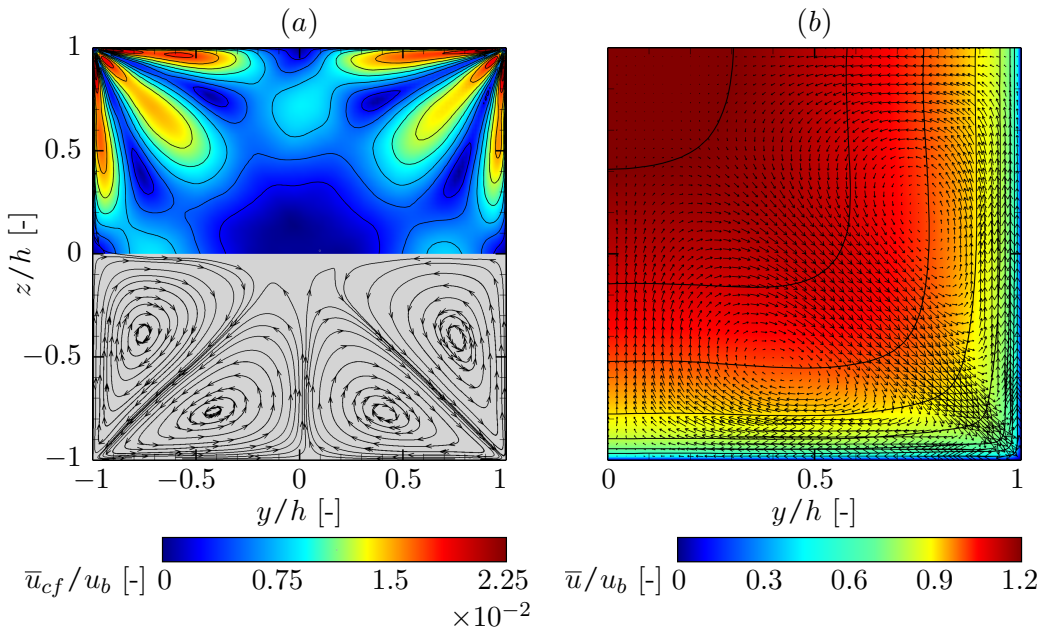

Figure 1.1: Secondary flow field in the straight square duct cross-section at $Re_b = 40 \cdot 10^3$: (a) cross-flow field $\overline{u}_{cf} = \sqrt{\overline{v}^2 + \overline{w}^2}$ and (b) influence on streamwise velocity field in the lower right quadrant. Isolines for $\overline{u}_{cf}$ are drawn from $0.25 \cdot 10^{-2}$ to $2.25 \cdot 10^{-2}$ in steps of $0.25 \cdot 10^{-2}$ and for $\overline{u}$ from 0.6 to 1.2 in steps of 0.1.

velocity u_b (Salinas-Vásquez and Métais, 2002). Consequently, it forms for all turbulent flows through geometries of angular cross-sectional shape, yet it does not appear in laminar flows or flows through smoothly curved profiles, for example circular pipes. The dominant turbulent mechanism for generating turbulence-driven secondary flow are the ejections from the wall (Huser and Biringen, 1993; Salinas-Vásquez and Métais, 2002). The wall boundary layer flow structure is made up of narrow alternating low- and high-momentum streaks elongated in streamwise direction with a spanwise distance between the streaks of ≈ 100 viscous length scales. Kline et al. (1967) attribute low-momentum streaks to intermittent eruptions away from the wall, a chaotic process described as bursting and the resulting fluid movement as turbulent ejections. These structures have been found to be responsible for the predominant majority of vertical momentum transport away from the wall and consequently Reynolds stress generation and turbulent kinetic energy production (Kline et al., 1967; Kim et al., 1971). The turbulent ejection strength as well as their frequency vary noticeably between each of the duct sidewall centres and the corners. Due to the high shear present in each wall centre turbulent ejections are intensified, whereas the weakening shear towards the corner region causes them to rapidly drop to zero. The ejection variation along the sidewalls causes a compensating secondary flow oriented from the duct core towards its corners and in consequence generates the anisotropic Reynolds stress distribution. An equipotent approach to analyse the generation of Prandtl's flow of the second kind is by employing the streamwise vorticity equation, in which gradients of the anisotropic Reynolds stresses act as source term for vorticity production. Specifically the difference of the terms containing the cross-sectional Reynolds shear stress and those comprising the cross-sectional

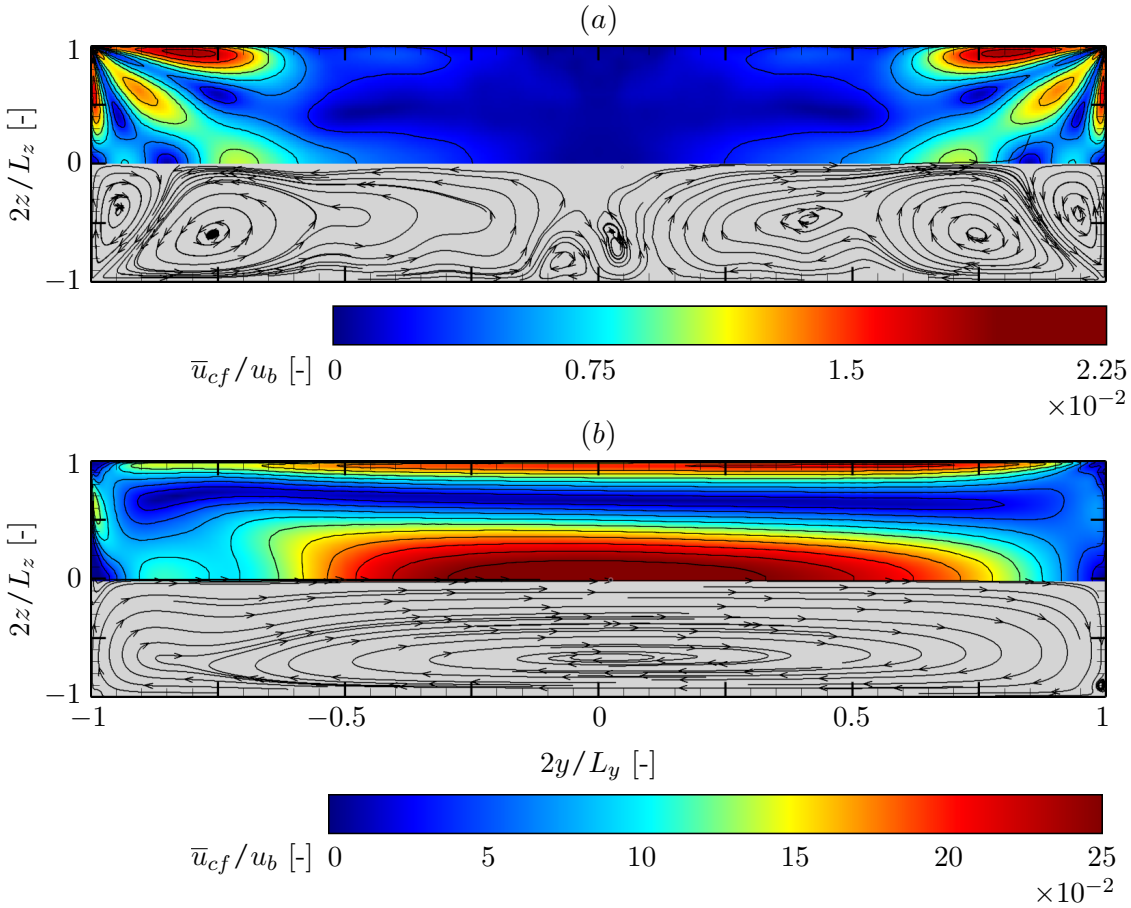

Figure 1.2: Secondary flow field $\overline{u}_{cf} = \sqrt{\overline{v}^2 + \overline{w}^2}$ in the HARCD cross-section: (a) straight adiabatic section at $Re_b = 110 \cdot 10^3$ and (b) curved section end plane after a 90° bend at $Re_b = 40 \cdot 10^3$. The inner radius wall is at $y = y_{min}$ and the outer radius wall at $y = y_{max}$. Isolines in (a) are drawn from $0.25 \cdot 10^{-2}$ to $2.25 \cdot 10^{-2}$ in steps of $0.25 \cdot 10^{-2}$ and in (b) from $2.5 \cdot 10^{-2}$ to $25 \cdot 10^{-2}$ in steps of $2.5 \cdot 10^{-2}$.

Reynolds normal stresses are driving the secondary flow (Demuren and Rodi, 1984).

The resulting secondary flow field is depicted in figure 1.1 for a square duct configuration. Due to the symmetric set-up the developing corner vortex system is symmetric with an equally strong counter-rotating vortex pair forming in each of the duct quadrants, transporting fluid from the duct core towards the respective corner region and upwards into the duct core along the midplanes. Even though the secondary flow strength is relatively weak, the impact on the streamwise momentum distribution is clearly visible by the bulging of the $\overline{u}$-isolines towards the duct corners along the bisecting line and the bulging towards the duct core along the midplane-axes $y = 0$ and $z = 0$, respectively. The turbulence-induced secondary flow field in a HARCD geometry, as considered within this thesis, is shown in figure 1.2 (a). Here, the different sidewall lengths lead to an asymmetric secondary flow field with the smaller vortex of each quadrant vortex pair being oriented towards the short sidewall and the larger vortex towards the extended

sidewall. The additional vortical structures in the duct core vanish with increasing sampling time.

In figure 1.2 (b), the flow field of the curvature-induced Prandtl's flow of the first kind is exemplarily shown, also known as skew-induced or pressure-driven secondary flow. Depending on the curvature radius and associated centrifugal forces and pressure gradient, this type of secondary flow is significantly stronger than the turbulence-induced one with values reaching up to $20-30\%$ of u_b (Demuren and Rodi, 1984). It may form in laminar as well as turbulent flows through geometries of arbitrary cross-section, but is absent in straight ducts. When a critical Dean number De_{crit} is surpassed, the so-called Dean instability occurs and a base pair of counter-rotating Dean vortices forms. The flow physics are as follows: fluid entering the curved section changes its principal flow direction by centripetal forces acting on it. An adverse pressure gradient forms between inner and outer radius walls with a reduced pressure at the convex and an increased pressure at the concave wall. The pressure rise causes a deceleration, whereas the pressure drop causes an acceleration of streamwise velocity. This variation causes the pair of counter-rotating base Dean vortices to form. Within the scope of this thesis only configurations with $De > De_{crit}$ for the base instability are considered, even though the exact values of De_{crit} for our complex configurations are unclear as they depend on a multitude of influence factors, e.g. aspect ratio and wall heating (Fellouah et al., 2006; Chandratilleke and Nursubyakto, 2003). The base secondary flow may also become unstable and further Dean vortices develop, such that the resulting array of Dean vortices depends heavily on geometrical and boundary conditions of the configuration and varies significantly along a curved duct (Li et al., 2017). In the exemplary depicted end section after a 90° bend of figure 1.2 (b), the secondary flow field consists of the principal counter-rotating Dean vortices, each extending over one half of the cross-section, accompanied by four weak turbulence-induced vortices close to the duct corners. The mixing is increased significantly with the highest secondary flow strength present along the midplane, transporting fluid upwards from the inner to the outer radius wall, and along the lateral sidewalls conveying fluid downwards.

HARCD flows affected by secondary flow structures have been investigated both experimentally and numerically. For the numerical representation of HARCD configurations, three principal simulation classes exist: direct numerical simulation (DNS), large-eddy simulation (LES) and Reynolds-averaged Navier-Stokes (RANS) simulation. In DNS all temporal and spatial scales of the turbulent energy cascade are resolved, and consequently no turbulence modelling is required. The disadvantage is the high numerical effort as the smallest scale size correlates with the Reynolds number rendering DNS unfeasible for the simulation of many relevant flows in the field of engineering. On the contrary, in RANS the complete turbulent spectrum is modelled alleviating computational costs especially for simulating complex configurations. However, an accurate turbulence model is required particularly for HARCD configurations to correctly predict turbulence-induced secondary flow as well as turbulent heat fluxes, and consequently the overall flow field and heat transfer. If the selected RANS model is based on the Boussinesq turbulent viscosity hypothesis and an isotropic turbulence closure, such as the widely used k-ε model, it fails to represent the corner vortex system (Speziale, 1982; Mani et al., 2013). Employing Reynolds stress transport models for turbulence closure, the secondary flow development can be adequately represented. Nonetheless, the main shortcomings of RANS remain: the Navier-Stokes

equations are solved approximately for the ensemble-averaged flow state, where all scales of the turbulent energy cascade are modelled. A well-resolved LES creates an individual time sample like DNS and unlike RANS, and the large-scale turbulent structures of the energy cascade are resolved. Thus, it offers the best compromise between RANS and computationally expensive DNS. One of the main challenge for LES is to correctly predict the influence of the unresolved turbulent scales on the resolved flow field, which is known as subgrid-scale modelling and which will be further discussed in section 2.2.2.

1.2 Experimental and Numerical Studies

Several experimental and numerical studies investigated straight and curved duct flows with different cross-sections of various complexity affected by Prandtl's flow of the first and second kind. This literature review is structured as follows: initially an overview is given over experimental studies, separated into straight duct flows, i.e. turbulence-induced secondary flow is in the focus, and curved duct flows, where curvature-induced secondary flow is central. Afterwards the equally separated numerical studies are presented. For the straight duct investigations also studies focusing on complex cross-sectional shapes as well as heat transfer enhancement by secondary flow modulation are included. The author's own contributions will be discussed in the subsequent chapters and are therefore excluded from this literature review.

First experimental studies of straight ducts with non-circular cross-sections have been conducted by Prandtl (1926), republished in Prandtl (1927), and Nikuradse (1930), who first described the existence of secondary flow structures perpendicular to the main flow as source for the mean streamwise isoline-bending towards the duct corner. A first secondary flow quantification has been reported by Hoagland (1960) employing hot-wire anemometry for a square duct set-up. The methodology was adopted and with improved accuracy used by Baines and Brundrett (1964), Gessner and Jones (1965) and Launder and Ying (1972). Baines and Brundrett (1964) thoroughly examined the Reynolds stress tensor and vorticity production, concluding that the basic secondary flow appearance is Reynolds number independent yet for increasing Reynolds number the flow penetrates deeper into the duct corners, and that vorticity production is highest in the duct corner region dominated by the cross-sectional gradient of Reynolds normal stress difference. However, Gessner and Jones (1965) showed that for vorticity production the cross-sectional Reynolds shear stress gradient is of the same order of magnitude by employing a higher accuracy X-array hot-wire probe for a square and rectangular duct configuration at Reynolds numbers from $50 \cdot 10^3$ to $300 \cdot 10^3$. Launder and Ying (1972) investigated the effect of wall roughness stating that the secondary flow intensity increases when normalised with bulk velocity yet profiles collapse with smooth duct results when normalised with friction velocity. Note, the results of the previous experiments are hampered by the measurement technique and not fully developed flow conditions (Demuren and Rodi, 1984). Melling and Whitelaw (1976) performed experiments using a non-intrusive laser Doppler anemometry technique for measuring the flow and turbulence field in developing and nearly full developed adiabatic square duct set-ups. They were able to qualitatively confirm the previous results, although at a higher resolution, accuracy and more precise quantification of the measurement error. The effects of wall heating on turbulence statistics has been analysed by Wardana et al. (1992) and Wardana et al. (1994) for a turbulent

channel flow configuration, reporting an increase in viscous dissipation close to the heated wall and an intensification of turbulent ejections due to volumetric expansion. Heated square duct experiments have been conducted by Brundrett and Burroughs (1967), Hirota et al. (1994) and Hirota et al. (1997) investigating the effects of secondary flow for smooth and rough walls on turbulent heat flux and temperature as well as turbulent Prandtl number distributions. The latter have shown the invalidity of the assumption $Pr_t = const.$ Adiabatic rectangular duct flows have been studied by Gessner and Jones (1965) with a low aspect ratio of $AR = 2$, by Tracy (1963) with a high aspect ratio of $AR = 6.4$ and Monty (2005) with $AR = 11.7$. They mainly focused on the asymmetric secondary flow structure differing from a square duct. Monty (2005) especially investigated the applicability of HARCD set-ups to perform channel flow experiments, concluding that in the HARCD centre the required two-dimensionality is achieved for $AR > 7.0$ and that there the law of the wall profile is met despite the three-dimensionality of the flow field. Recently, an equilaterally heated vertical low Reynolds number duct at $AR = 6$ has been investigated by Kim et al. (2021) to analyse the onset of heat transfer deterioration for nuclear reactor cavity cooling systems affected by strong buoyancy forces. They reported a correlation between duct aspect ratio, its hydraulic diameter, the resulting secondary flow field and heat transfer deterioration. Particle image velocimetry (PIV), volumetric particle tracking velocimetry (PTV) and laser-induced fluorescence (LIF) results for flow and temperature field of the companion experiment of an asymmetrically heated HARCD at $AR = 4.3$ have been presented in Rochlitz et al. (2015), Rochlitz and Scholz (2018) and Hötte et al. (2021).

Pioneering studies of curved duct flows have been conducted by Dean (1927) and Dean (1928) developing the Dean instability theory. Detailed experimental studies of Prandtl's flow of the first kind have been performed by Humphrey et al. (1981) using laser Doppler anemometry for a 90° bend with a square duct profile. He reported the secondary flow field to be mainly dominated by centrifugal effects and the strength to reach values up to 28% of the bulk velocity. Li et al. (2016) and Li et al. (2017) combined experimental and numerical studies in their works employing PIV and RANS simulations, respectively, to analyse the development of the secondary flow structure along unheated 120° curved ducts with continuously varying curvature. A wide range of Reynolds numbers from $Re_b = 2.4 \cdot 10^4$ to $Re_b = 1.4 \cdot 10^5$ and aspect ratios of $AR = 0.4$, $AR = 1$ and $AR = 2.3$ have been included in their work. Depending on the interaction of the three varied parameters a rich array of different Dean vortices could be observed forming along the duct length from the primary Dean vortices to those emerging due to secondary instabilities. Meyer (1997) investigated turbulent heat transfer in uniformly heated straight and curved duct flows and compared the HARCD result of $AR = 10$ to a square duct result, showing that the aspect ratio is of little importance for the curvature-induced heat transfer enhancement.

The first numerical simulation for a periodic square duct flow has been performed by Launder and Ying (1973) employing RANS with an algebraic approach to model the Reynolds stress production terms of turbulence-induced secondary flow, i.e. the difference of cross-sectional Reynolds normal stresses as well as the turbulent shear stresses. Demuren and Rodi (1984) optimised this approach by employing a wall proximity correction and retaining previously neglected secondary velocity gradient terms. However, deviations with respect to experimental square duct flow results persisted and depending on the respective model an underestimation or overestimation of secondary flow intensity has been reported, which requires case-specific

parameter fine-tuning. With increasing computational power, LES and DNS of periodic turbulent duct flows at low friction Re_τ and bulk Reynolds numbers Re_b became feasible in the nineties. Madabhushi and Vanka (1991) carried out a first LES of an adiabatic square duct at $Re_\tau = 360/Re_b = 5810$, and Gavrilakis (1992) and Huser and Biringen (1993) first DNS at $Re_\tau = 300/Re_b = 4410$ and at $Re_\tau = 600/Re_b = 10620$, respectively. All three publications reported good agreement of secondary flow and its turbulent production terms with previous experimental observations. Furthermore, analysing the streamwise vorticity equation terms and performing a Reynolds quadrant analysis, Huser and Biringen (1993) concluded that the turbulent ejections from the wall are the dominant turbulent mechanism for the generation of turbulence-driven secondary flow. Joung et al. (2007) used Gavrilakis' square duct set-up of $Re_b = 4410$ to characterise in detail the secondary flow pattern employing a conditional quadrant analysis. Pinelli et al. (2010) conducted a series of DNS to study the physical mechanisms responsible for Prandtl's flow of the second kind with Reynolds numbers ranging from $Re_b = 2154$ to $Re_b = 7000$. They concluded that the mean flow field is determined by the preferred locations of coherent structures in the buffer layer, and first reported a contrasting scaling behaviour of mean streamwise vorticity and cross-flow streamfunction by presenting evidence for a scaling in viscous as well as in outer units. Matin et al. (2018) performed square duct DNS at $Re_b = 3800$ with a Lattice-Boltzmann method and utilised the dataset for a proper orthogonal decomposition, which revealed the secondary flow to be composed of instantaneous organised contributions of various length scales. The previous numerical studies have been conducted at relatively low Reynolds numbers. In contrast, Zhang et al. (2015) and Pirozzoli et al. (2018) presented DNS of adiabatic square duct flows up to $Re_\tau = 1055/Re_b = 40 \cdot 10^3$ with a focus on Reynolds number dependence of mean and secondary flow field. Evaluating the streamwise vorticity balance equation terms for a wide range of Re_b, Pirozzoli et al. (2018) found the vorticity in the duct corner region to scale in viscous units and that in the duct core to scale in outer units causing a growing separation of corner and core vorticity for increasing Reynolds number. In Modesti et al. (2019) compressible square duct simulations were performed for a Mach number range from $Ma = 0.2$ to $Ma = 3$ and Re_b up to $14.6 \cdot 10^3$ focusing on compressibility effects on secondary flow and applicability of compressibility transformations. Recently, the DNS database of Pirozzoli et al. (2018) has been utilised for a cross-sectional friction drag analysis by Fan et al. (2020) highlighting the secondary flow contribution to friction drag redistribution along the duct perimeter.

The varying flow and turbulence field for flows through high aspect ratio adiabatic periodic rectangular ducts has been analysed by Vinuesa et al. (2014) employing DNS for various aspect ratios ranging from $AR = 1$ to $AR = 7$. They first reported the existence of an array of secondary vortices forming along the long sidewalls for high enough aspect ratio. This work has been extended by Vidal et al. (2017b) and Vidal et al. (2017a) investigating the influence of rounding off the duct corners on the secondary flow structure for square and rectangular ducts. Contrary to first assumptions, an intensification of Prandtl's flow of the second kind has been observed. Further studies of turbulence-induced secondary flow variation for complex cross-sectional geometries include Lammers et al. (2012) employing micropatterned surface morphology, Marin et al. (2016) for a hexagonal duct and Orlandi et al. (2018) for a rich array of different shapes, which are generated taking the peripheral profile of a circular pipe and superimposing it with sinusoidal perturbations. All three highlighted the complex turbulence-induced secondary

flow field and by comparing his configuration to previous $k-\varepsilon$ based RANS studies, Marin et al. (2016) pointed out significant discrepancies in the mean velocity field attributed to the misrepresentation of Reynolds stress anisotropy.

Salinas-Vásquez and Métais (2002) performed LES of turbulent heat transfer in an asymmetrically heated periodic square duct using air as working fluid at $Re_\tau = 393/Re_b = 6000$ and reported a significant heating-induced enhancement of turbulence statistics and intensification of the secondary flow. Hébrard et al. (2005) continued this work with a focus on the spatial development of the temperature boundary layer along a spatially resolved extended straight duct. Sekimoto et al. (2011) performed DNS at low $Re_b = 3000$ and $Re_b = 4400$ for various Richardson numbers with the main focus on the interaction of turbulence- and buoyancy-driven secondary flow and the resulting cross-flow field in an asymmetrically heated square duct. Yang et al. (2009) and Zhu et al. (2010) presented coarse DNS and LES of a straight heated duct for high Reynolds numbers ranging from $Re_b = 10^4$ to $Re_b = 10^6$, however, at relatively low spatial resolution. Recently, Schindler et al. (2019) presented results for a periodic heated duct flow including a discussion of grid resolution and domain length effects, of heated wall boundary conditions, and of the invalidity of the constant turbulent Prandtl number assumption. In contrast to the previous publications, Choi and Park (2013) analysed the turbulent heat transfer for rectangular ducts with moderate aspect ratios ranging from $AR = 0.25$ to $AR = 1.5$, showing that with rising AR the changes in the corner vortex system dynamics locally effect a thinning of temperature boundary layers and increasing heat transfer.

Surface roughening of the heated wall is able to improve the heat transfer. Its augmentation by secondary flow enhancement has been studied by Salinas-Vásquez et al. (2005) introducing small ridges at the heated wall. Similarly, Turnow et al. (2012) investigated the effect of dimples on flow structure and resulting heat transfer. Ahn et al. (2005), Fang et al. (2017) and Zheng et al. (2019) employed ribs of various arrangements for surface roughening, analysing the effects on secondary flow and assessing the heat transfer enhancement capabilities. Pallares and Davidson (2002) and Qin and Pletcher (2006) analysed the heat transfer enhancement in rotating ducts compared to stationary ones. An extensive overview of heat transfer augmentation methods for internal cooling is given by Ligrani (2013).

Prandtl's flow of the first kind and the Dean instability have been intensively studied for both laminar and turbulent flows. For heated laminar duct flows, Chandratilleke and Nursubyakto (2003) and Chandratilleke et al. (2012) conducted extensive parameter studies varying heat flux, Dean number and duct aspect ratio to analyse the effect on the Dean instability onset and the structure of the resulting secondary flow field. Bhunia and Chen (2009) likewise investigated laminar flow through curved ducts, although with variation in the duct aspect ratio along a 90° bend and studied the effects on Dean vortex generation. The latter three studies also highlighted the rich array of Dean vortices emerging due to secondary flow instability after the initial formation of the base Dean vortex. A similar study for turbulent duct flows has been done by Ko and Wu (2009). They studied turbulent flow through heated curved ducts using RANS with the $k-\varepsilon$ turbulence model at $Re_b = 20 \cdot 10^3$ and aspect ratios ranging from $AR = 0.25 - 4$ with a focus on entropy generation, and concluded that the latter is minimal for a square duct flow compared to rectangular profiles at identical flow conditions. Pizzarelli et al. (2011) performed extensive RANS studies employing the isotropic Spalart–Allmaras turbulence

model for asymmetrically heated single- and double-curvature HARCDs of various curvature radii using supercritical hydrogen as coolant to assess the effect of curvature on heat transfer and pressure loss in liquid rocket engine cooling ducts. First LES analysing Prandtl's flow of the first kind have been performed by Su and Friedrich (1994) and Breuer and Rodi (1994). The former presented laminar and turbulent fully developed flow for square and rectangular ducts of $AR = 2$, whereas the latter studied the flow development along a 180° bend using straight square duct results as inlet condition. In order to achieve the rather high $Re_b = 56690$, a wall-modelled LES based on standard wall functions has been utilised. A good agreement with DNS data has been reported for the lower $Re_b = 4410$ case and unsatisfactory results for the $Re_b = 56690$ case. The LES of Hébrard et al. (2004), based on Salinas-Vásquez and Métais (2002), analysed the heat transfer enhancement by the additionally forming Dean vortices along an S-shaped duct with square cross-section and the impact on the turbulent flow field. Münch and Métais (2007) modified the previous set-up to a single unheated bend studying the effects of curvature radius variation on the resulting turbulence statistics and mean flow. The influence of the stronger secondary flow on heat transfer has been addressed in Münch and Métais (2006).

1.3 Objectives and Accomplishments

One of the main challenges of simulating HARCDs is the sensitivity of turbulence-induced secondary flow to the correct representation of turbulence intensities and the Reynolds stress anisotropy. Hence, both a high grid resolution as well as correct behaviour of the LES model towards the wall is required, which leads to a high computational effort especially for realistic configurations at high Reynolds number. As the variation of turbulent ejections from the wall between sidewall centre and duct corner is the diving mechanism for the corner vortex system, a fine resolution is required throughout the entire HARCD cross-section only alleviating the resolution requirements towards the HARCD core. Additionally, the configuration has to be simulated spatially resolved due to the evolving temperature boundary layer, which further increases the computational costs. For these reasons, significant effort has been put on an optimised grid generation and load balancing on the one hand and on the other hand on solver optimisation for high-performance computing (HPC) systems. The main achievements in the course of this work are:

- Code adaptions and optimisation for large-scale parallel simulations as well as validation for adiabatic square duct flows at Reynolds numbers up to $Re_b = 40 \cdot 10^3$ for the incompressible LES flow solver INCA and the compressible LES flow solver CATUM. Additionally, an extensive postprocessing framework has been implemented.

- Well-resolved LES of a straight generic incompressible water HARCD configuration with asymmetrical wall heating at a considerably high Reynolds number of $Re_b = 110 \cdot 10^3$ have been performed with the flow solver INCA. The geometry and flow parameters of these simulations are identical to a companion experiment by project partners. In this study the focus is set on the interaction of turbulence-induced secondary flow and turbulent heat transfer. The simulation has been carried out on 254 nodes corresponding to 7088 CPUs on SuperMUC Phase 2 and two configurations at different wall temperature have

been considered. The results of the higher T_w set-up are not shown in this thesis but are included in Kaller et al. (2018).

- The results of the aforementioned LES have been used to support project partners to develop and enhance the companion experimental water HARCD set-up. This included sensitivity analyses of geometrical and PIV parameters based on the LES results and assessment of wall roughness effects employing RANS simulations. The latter results are not included in this thesis.
- Well-resolved LES of an asymmetrically heated compressible air HARCD consisting of a straight part with a curved section of varying curvature radius attached at $Re_b = 40 \cdot 10^3$ have been performed with the flow solver CATUM. This study is centred on the interaction of turbulence-induced and curvature-induced secondary flow of varying strength and the effects on turbulent heat transfer. The simulations have been carried out on 224 nodes corresponding to 10752 CPUs on SuperMUC-NG with six configurations running simultaneously (3 curvature radii for $Re_b = 40 \cdot 10^3$ and $Re_b = 17.8 \cdot 10^3$). The results of the simulations at $Re_b = 17.8 \cdot 10^3$ are not shown in this thesis.
- Well-resolved RANS simulations have been performed with the commercial solver ANSYS CFX for all analysed HARCD configurations employing various turbulence models and turbulent heat flux closures. The objective of this study is the assessment of RANS prediction capabilities for the generic HARCD flow configurations.

1.4 Outline

This thesis is subdivided into six chapters. Initially an introduction into cooling duct flows and generally flows through geometries of rectangular cross-section with a special focus on secondary flow structures relevant for this thesis has been given together with a selective overview of available literature. In chapter 2, the governing equations and numerical modelling is presented separately for the three solvers employed within this thesis, namely the in-house LES solvers INCA and CATUM, as well as the commercial solver ANSYS CFX. Subsequently, the three main chapters follow, distinguished based on the analysed configuration and solver employed. In chapter 3, the results of a long straight water HARCD configuration are discussed with the simulations based on the LES flow solver INCA, and compared to the companion experiment that was performed at the Technical University of Braunschweig. The main objective is the investigation of the interaction of turbulence-induced secondary flow and turbulent heat transfer. In chapter 4, this set-up is extended by a curved section of varying curvature radius and modified to be simulated efficiently with the solver CATUM using ideal gas air as fluid. The discussion focuses on the interaction of Prandtl's flow of the first and second kind as well as the resulting effect on turbulent heat transfer. In chapter 5, both HARCD configurations are recreated to be simulated with ANSYS CFX applying various RANS turbulence closure models. The analysis comprises the assessment of RANS prediction capabilities for the cooling HARCD configurations. The thesis is concluded in chapter 6, in which the main findings are summarised as well as an outlook for future work on the research topic is given.

2 Physical and Numerical Model

The following subsections present the physical and numerical modelling of the solvers utilised within this thesis. Initially an overview of the relevant dimensionless quantities characterising the flow through heated HARCDs with and without curvature is given. Then the in-house LES solver INCA is described in detail used for the incompressible water HARCD simulations followed by the in-house LES solver CATUM used for the compressible air HARCD simulations. Eventually the modelling within the commercial RANS solver ANSYS CFX is addressed.

2.1 Characteristic Quantities

This section summarises the relevant characteristic quantities required for the analysis of straight and curved high aspect ratio heated ducts, which are used throughout this thesis. Both the general definitions and those used within the present work are given.

The cross-sectional geometry of high aspect ratio ducts is characterised by the aspect ratio AR and the hydraulic diameter d_h. The former sets the duct height h_{cs} in relation to the duct width w_{cs} and the latter serves as a replacement quantity for non-circular cross-sections. Comparing the flow passage area to the wetted perimeter of the duct profile, d_h constitutes a characteristic integral length scale. The two quantities are defined as

$$AR = \frac{h_{cs}}{w_{cs}}, \tag{2.1}$$

$$d_h = \frac{2\,h_{cs}\,w_{cs}}{h_{cs} + w_{cs}}, \tag{2.2}$$

with the subscript $(\cdot)_{cs}$ indicating a cross-sectional value. The Reynolds number Re forms the ratio of inertial and viscous forces acting on the turbulent flow field and is written as

$$Re = \frac{u_{char}\,l_{char}}{\nu} = \frac{u_b\,d_h}{\nu}, \tag{2.3}$$

with the kinematic viscosity derived from the dynamic viscosity by division through the fluid density $\nu = \mu/\rho$. As characteristic velocity the bulk flow velocity u_b is used and d_h as characteristic length scale. The friction Reynolds number Re_τ is an important quantity for the description of wall-bounded flows and is defined as

$$Re_\tau = \frac{u_\tau\,l_{char}}{\nu_w} = \frac{u_\tau\,d_h}{\nu_w}, \tag{2.4}$$

with the friction velocity $u_\tau = \sqrt{\tau_w/\rho_w}$, where the wall shear stress τ_w is defined as $\tau_w = \mu_w\,(\partial u/\partial n)|_w$. The subscript $(\cdot)_w$ indicates an evaluation directly at the wall and n is the

coordinate measuring the distance from the wall. In contrast to the literature for boundary layer, pipe and square duct flows, the hydraulic diameter is used as characteristic length scale throughout this work, regardless of whether the long or short sidewall boundary layer of a HARCD configuration is investigated.

The Froude number Fr is defined as the ratio of inertial and gravity forces,

$$Fr = \frac{u_{char}}{\sqrt{g\, l_{char}}} = \frac{u_b}{\sqrt{g\, d_h}}, \tag{2.5}$$

with g being the gravitational acceleration.

To estimate the influence of compressibility effects for a given flow configuration, the Mach number Ma is utilised comparing the flow velocity to the speed of sound c

$$Ma = \frac{u_{char}}{c} = \frac{u_b}{c}, \tag{2.6}$$

where c is a function of the fluid properties and the thermodynamic state.

For the characterisation of configurations involving heat transfer the Nusselt and Grashof numbers are important. These are defined as

$$Nu = \left.\frac{h\, l_{char}}{k}\right|_w = \frac{-l_{char}}{\Delta T|_{char}} \left.\frac{\partial T}{\partial n}\right|_w = \frac{-d_h}{T_w - T_b} \left.\frac{\partial T}{\partial n}\right|_w, \tag{2.7}$$

$$Gr = \frac{g\,\beta\ (\Delta T|_{char})\, l_{char}^3}{\nu^2} = \frac{g\,\beta\ (T_w - T_b)\, d_h^3}{\nu^2}. \tag{2.8}$$

The evaluation of the local Nusselt number is based on equating the convective heat transfer with the thermal conduction for the wall-next cells at the heated wall, with h denoting the heat transfer coefficient and k the thermal conductivity. The Grashof number represents an integral value and forms the ratio of buoyancy to viscous forces. Throughout this work the characteristic temperature difference $\Delta T|_{char}$ is defined as $(T_w - T_b)$. As reference length the hydraulic diameter is used, $l_{char} = d_h$, even though the heating is applied asymmetrically at the short sidewall.

The molecular Prandtl number Pr is specified as the ratio of momentum and thermal diffusivity

$$Pr = \frac{\nu}{\alpha}, \tag{2.9}$$

and the turbulent Prandtl number Pr_t analogous as the ratio of turbulent eddy viscosity and turbulent eddy thermal diffusivity

$$Pr_t = \frac{\nu_t}{\alpha_t}. \tag{2.10}$$

The molecular Prandtl number is a thermodynamic quantity, whereas Pr_t is related to the modelling of turbulence.

For configurations, in which streamline curvature has a relevant impact on the flow field, the Dean number De becomes important describing the tendency for Prandtl's flow of the first kind to form, i.e. the onset of Dean instability. The Dean number sets inertial and centripetal forces in correlation with viscous forces and is defined as

$$De = \frac{u_{char}}{\nu} \cdot \sqrt{\frac{l_{char}^3}{2\, r_c}} = Re \cdot \sqrt{\frac{l_{char}}{2\, r_c}} = Re_b \cdot \sqrt{\frac{d_h}{2\, r_c}}, \tag{2.11}$$

where r_c is the curvature radius. To derive the integral Dean number, l_{char} is set to d_h and Re taken at bulk conditions.

2.2 Modelling within Solver INCA

In the following the governing equations and the numerical modelling within the in-house LES flow solver INCA are described. INCA is used for the straight HARCD simulations with incompressible water as fluid.

Several validation studies and flow applications, for which wall-bounded turbulence is crucial, have been published and can be found for example in Hickel and Adams (2007), Hickel and Adams (2008), Grilli et al. (2012), Quaatz et al. (2014) and Pasquariello et al. (2017).

2.2.1 Governing Equations

The system to be solved are the Boussinesq equations as utilised e.g. by Remmler and Hickel (2012) and Remmler et al. (2015) for the simulation of atmospheric flows. See Remmler (2016) for additional references and a complete set of validation results.

To derive the Boussinesq equations we start with the compressible Navier-Stokes equations in conservation form considering gravitational forces in the vertical y-direction

$$\partial_t \rho + \nabla \cdot (\rho \mathbf{u}) = 0, \tag{2.12a}$$

$$\partial_t (\rho \mathbf{u}) + \nabla \cdot (\rho \mathbf{u}\mathbf{u}) = -\nabla p + \nabla \cdot \mathbf{T} - \rho\, g\, \mathbf{e}_y, \tag{2.12b}$$

$$\partial_t (\rho e_{tot}) + \nabla \cdot (\, \mathbf{u}(\rho e_{tot} + p)\,) = \nabla \cdot (\mathbf{u} \cdot \mathbf{T} - q), \tag{2.12c}$$

with the velocity vector $\mathbf{u} = [u, v, w]$, pressure p, density ρ and total energy e_{tot}. The gravitational force is assumed to act in the y-direction on the flow, $\mathbf{e_y}$ defining the vertical unity vector. The viscous stress tensor $\mathbf{T}$ for a Newtonian fluid with application of Stokes' hypothesis is defined as

$$\mathbf{T} = \mu \cdot \left[\left(\nabla \mathbf{u} + (\nabla \mathbf{u})^T \right) - \frac{2}{3} \mathbf{I} \, (\nabla \cdot \mathbf{u}) \right], \tag{2.13}$$

with $\mathbf{I}$ being the unity matrix. The heat flux q is written as

$$q = -k \, \nabla T, \tag{2.14}$$

which is known as Fourier's law with k being the thermal conductivity. The total energy for water as working fluid is defined as

$$\rho \, e_{tot} = \rho \, c_{v,H_2O} \, T + \frac{\rho \, \mathbf{u}^2}{2} + \rho \, g \, \mathbf{x} \cdot \mathbf{e}_y, \tag{2.15}$$

with the spatial coordinate vector $\mathbf{x} = [x, y, z]$ and the specific heat capacity c_{v,H_2O}.

The compressible system of equations 2.12 is able to reproduce the propagation of sound waves. For our application of a heated water HARCD this ability is not required, and additionally limits the possible time step size of the explicit time integration scheme and consequently increases the computational effort. Assuming small variations in pressure, temperature and density

around a constant background state denoted by subscript $(\cdot)_0$, the time- and location-dependent distributions exemplarily shown for the density can be split into

$$\rho(\mathbf{x},t) = \rho_0 + \rho'(\mathbf{x},t) = \rho_0 \left(1 + \frac{\rho'(\mathbf{x},t)}{\rho_0}\right). \tag{2.16}$$

Moreover, the density distribution is linked to the temperature fluctuations by

$$\rho(\mathbf{x},t) = \rho_0 \left(1 + \beta\, T'(\mathbf{x},t)\right), \tag{2.17}$$

with β being the thermal expansion coefficient. Further assuming hydrostatic equilibrium for the background state, $\nabla p_0 = -\rho_0\, g\, \mathbf{e}_y$ and $\rho'/\rho_0 \ll 1$, as well as employing the incompressibility condition $\nabla \cdot \mathbf{u} = 0$, the Boussinesq approximation of the Navier-Stokes equations reads

$$\nabla \cdot \mathbf{u} = 0, \tag{2.18a}$$

$$\partial_t \mathbf{u} + \nabla \cdot (\mathbf{u}\mathbf{u}) = -\frac{\nabla p}{\rho_0} + \nabla \cdot \left(\mu \left(\nabla \mathbf{u} + \nabla \mathbf{u}^T\right)\right) - \frac{\rho'}{\rho_0}\, g\, \mathbf{e}_y, \tag{2.18b}$$

$$\partial_t \rho' + \nabla \cdot (\rho' \mathbf{u}) = \nabla \cdot (-q). \tag{2.18c}$$

Due to the weak heating in our HARCD investigations and utilising pure liquid water, the assumption of small density variations can be justified. Equation system 2.18 is now incompressible and the density variations, respectively the temperature variations using equation 2.17 for conversion, are transported as active scalars. The density fluctuations can be replaced by a buoyancy variable denoted as $\rho^* = -g\,(\rho'/\rho_0)$. Making the flow quantities dimensionless leads to the incompressible three-dimensional Boussinesq equations as used within the flow solver INCA, the tilde-symbol here indicating a non-dimensionalised quantity

$$\nabla \cdot \tilde{\mathbf{u}} = 0, \tag{2.19a}$$

$$\partial_t \tilde{\mathbf{u}} + \nabla \cdot (\tilde{\mathbf{u}}\tilde{\mathbf{u}}) = -\nabla \tilde{p} + \nabla \cdot \left(\frac{1}{Re}\left(\nabla \tilde{\mathbf{u}} + \nabla \tilde{\mathbf{u}}^T\right)\right) - \frac{\tilde{\rho}^*}{Fr^2}\mathbf{e}_y, \tag{2.19b}$$

$$\partial_t \tilde{\rho}^* + \nabla \cdot (\tilde{\rho}^* \tilde{\mathbf{u}}) = \nabla \cdot \left(\frac{1}{Pr\, Re} \nabla \tilde{\rho}^*\right). \tag{2.19c}$$

The velocity vector $\mathbf{u}$ is made dimensionless by the bulk velocity u_b, all coordinates by the hydraulic diameter d_h, time by d_h/u_b, pressure by $\rho_b\, u_b^2$ and buoyancy ρ^* by g. For the definition of the characteristic quantities the reader is referred to the previous section 2.1. Note, in equation 2.19 only Fr remains constant, Pr and Re change due to the heating-induced non-constant thermodynamic flow state.

The temperature- and density-dependent transport properties are updated using polynomial correlations defined by the International Association for the Properties of Water and Steam (IAPWS) with the critical enhancement neglected, see Wagner and Pruß (2002), IAPWS (2008) and IAPWS (2011). The instantaneous density and temperature are retrieved from the flow solution of ρ^* via

$$\rho = \rho_b\,(1 + \tilde{\rho}^*) \qquad \text{and} \qquad T = T_b - \frac{1}{\beta} \cdot \tilde{\rho}^*. \tag{2.20}$$

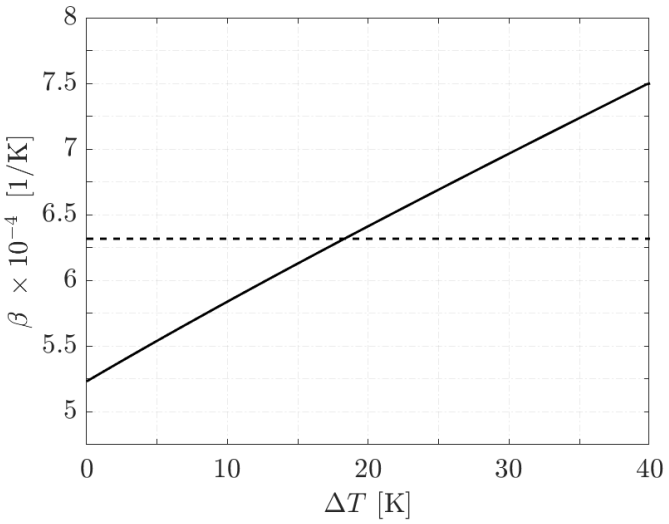

Figure 2.1: Thermal expansion coefficient β as function of temperature $\Delta T = T - T_b$ with (——) denoting $\beta(T)$ and (- - - -) the constant $\beta = 6.32 \cdot 10^{-4}\,\mathrm{K}^{-1}$.

Within the current work, for β a mean value is utilised averaged over the possible temperature range from $T_b = 333.15\,\mathrm{K}$ to $T_w = 373.15\,\mathrm{K}$ as shown in figure 2.1, yielding

$$\beta = -\frac{1}{\rho}\frac{\partial \rho}{\partial T} \approx -\frac{1}{\rho_b}\frac{\rho(T_w) - \rho_b}{T_w - T_b} = 6.32 \cdot 10^{-4}\,\mathrm{K}^{-1}. \tag{2.21}$$

Based on $\rho(\mathbf{x}, t)$ and $T(\mathbf{x}, t)$ the viscosity, thermal conductivity and specific heat capacity are evaluated with the IAPWS correlations and the local $Pr(\mathbf{x}, t)$ and $Re(\mathbf{x}, t)$ numbers in equation system 2.19 are updated accordingly. Note, for simplification and readability the tilde-symbol ($\tilde{\cdot}$) is dropped for the remainder of this thesis.

2.2.2 Numerical Modelling

INCA is a finite-volume based LES flow solver for compressible as well as incompressible flow problems. For the latter the numerical modelling is presented with a strong emphasis on the implicit LES model.

The Boussinesq equation system 2.19 is discretised by a fractional step method on a multiblock structured staggered Cartesian grid. For time advancement the explicit third-order accurate Runge-Kutta scheme of Gottlieb and Shu (1998) is utilised and the time step size is adjusted dynamically such that a Courant number of 1.0 is achieved. To satisfy the Courant–Friedrichs–Lewy condition the individual limits of advection, diffusion and buoyancy, respectively density variation, terms are taken into account. The pressure Poisson equation is solved in every Runge-Kutta substep employing a Krylov subspace solver with an algebraic-multigrid preconditioner. The viscous flux is discretised by a second-order central difference scheme.

The core of a LES solver is formed by the specific LES model. Turbulent flows are characterised by a three-dimensional, time-varying and chaotic flow field consisting of a wide range of spatial

and temporal scales. The largest integral scales within this field depend on the geometry and boundary conditions of the investigated configuration, whereas the smallest dissipative scales are more universal. The former are characterised by the problem-dependent integral length scale l_{int} and the latter by the Kolmogorov length scale l_η. As the scale ratio $l_{int}/l_\eta \sim Re^{3/4}$ for isotropic turbulence, see Pope (2000), the computational effort for a DNS resolving all turbulent scales becomes unfeasible for high Reynolds number configurations surpassing those of modest academic cases. In LES, a spatial scale separation is performed resolving only the large turbulent scales containing the most energy. For temporal scales it is assumed that all scales are resolved by choosing a small enough time step, cf. Adams et al. (2004). Due to the typically coarser grid, the so-called subgrid-scales (SGS) remain unresolved and a LES turbulence model has to be utilised to appropriately model the energy transfer between resolved and unresolved scales, i.e. correctly predict the influence of the SGS on the resolved flow field. Defining an universally applicable SGS model is supported by Kolmogorovs local isotropy hypothesis, stating that the small scales behave statistically isotropic for high enough Reynolds numbers and are therefore independent from the specific flow configuration. The computational effort reduction has been analysed by Choi and Moin (2012), who estimate the resolution requirement for a flat plate boundary layer configuration to drop from a proportionality of $\sim Re^{37/14}$ for a DNS to $\sim Re^{13/7}$ for a wall-resolved LES. Here the Reynolds number is calculated with the flat plate length as characteristic length.

Solving the Boussinesq equation system implicitly generates a scale separation on the one hand by the computational grid consisting of control volumina of finite size and on the other hand by the numerical discretisation of the continuous operators. The latter leads to a subdivision of the resolved scales into the larger *represented resolved scales* and the smallest *represented non-resolved scales*, which are larger than the grid cells yet manipulated by numerical errors (Garnier et al., 2009). Following Leonard (1975), the scale separation is mathematically identical to a convolution of the transport equations with a homogeneous filter kernel resulting in the filtered Boussinesq equations. This filter operation leads to additional unclosed terms stemming from the nonlinear terms in the governing equations. For modelling these so-called SGS stresses two major classes are distinguished, namely *explicit* and *implicit* SGS models. For explicit models the filtered governing equations are first extended by additionally derived terms modelling the SGS stress influence on the resolved part of the flow field and afterwards the extended equation system is discretised. The assumption behind explicit models is that the turbulence model and numerical dissipation due to truncations errors do not influence each other. However, for example Adams et al. (2004) and Hickel et al. (2014) have pointed out that for typically employed LES grid resolutions this assumption is not necessarily justified. Utilising higher-order schemes reduces the truncation errors at the cost of a higher computational effort, but can not guarantee, that the truncation errors have a smaller order of magnitude than the SGS model terms, see e.g. Vreman et al. (1995), Ghosal (1996) and Kravchenko and Moin (1997). In implicit LES (ILES) models the basic principle is to use the truncation errors to act implicitly as SGS model. The filtered transport equations are consequently discretised in unmodified form saving the computational effort to compute SGS model terms (Adams et al., 2004). Hence, for ILES the modelling problem is shifted to modifying the truncation errors in such a way, that the unresolved scales influence on the resolved flow field is represented physically correct.

INCA employs the *Adaptive Local Deconvolution Method* (ALDM). ALDM is a nonlinear finite volume method, that provides a physically consistent subgrid-scale ILES model for incompressible (Adams et al., 2004; Hickel et al., 2006) and compressible turbulence (Hickel et al., 2014). Hickel et al. (2007) extended ALDM to passive scalar mixing and Remmler and Hickel (2012) to active scalars for flows governed by the Boussinesq equations. ALDM acts only on the convective flux discretisation as for high Reynolds number flows the influence of the truncation errors of the remaining terms is assumed to be negligible. The method is composed of three elements:

1. Adaptive local deconvolution operator for the reconstruction of the approximate unfiltered flow quantities at the cell faces. The local reconstruction is performed by a convex combination of dynamically weighted Harten-type polynomials based on the filtered flow field smoothness. To reduce the computational effort, Hickel and Adams (2007) introduced a simplified ALDM model based on a reconstruction using one Gauss point per cell face. The latter model is used within the present work.

2. Numerical flux function operating on the reconstructed solution to obtain the regularisation. The chosen approach utilises a modified Lax-Friedrichs flux function consisting of the physical Navier-Stokes flux and a dissipative regularisation term operating on the error of the cell face reconstruction.

3. Numerical integration procedure to obtain averaged fluxes over the cell faces.

From both the reconstruction procedure and the tailored numerical flux function free ALDM parameters emerge, which are finetuned to calibrate the spatial truncation error. Hickel et al. (2006) determined the parameter set for incompressible homogeneous turbulence by employing an evolutionary optimisation procedure minimising the deviation between spectral numerical viscosity and eddy viscosity based on the *Eddy Damped Quasi Normal Markovian* (EDQNM) approach (Lesieur et al., 2005). The deconvolution parameters remain identical for incompressible and compressible turbulence, and have been already used in numerous publications investigating a wide range of various flow problems. The numerical flux parameters are updated in Hickel et al. (2014) for compressible turbulence.

For wall-bounded flow simulations the SGS dissipation tends to be overestimated towards the walls. To remedy this deficiency, Hickel and Adams (2007) introduced an additional van Driest-type wall-damping acting on the dissipative momentum flux weights of the numerical flux function. Throughout this work a damping function based on the coherent structures (CS) model by Kobayashi (2005) is applied. It possesses the form $f_{wd} = \pi \cdot |f_{CS}|^{3/2} \cdot f_\Omega$ with the coherent structure function f_{CS} and the energy-decay suppression function $f_\Omega = (1 - f_{CS}) \cdot 0.9$, see Kobayashi (2005) for further details and the derivation of f_{CS}. The eventual damping functional is obtained as running average over the last 100 time steps.

2.3 Modelling within Solver CATUM

In the following the governing equations and the numerical modelling within the in-house LES flow solver CATUM is described. CATUM is used for the curved HARCD simulations with compressible ideal gas air as fluid.

M [kJ/kmol]	σ_{LJ} [nm]	$(\varepsilon/k)_{LJ}$ [K]	T_{crit} [K]	$c_{\Omega,i} \times 10^{-2}$ [-]
28.9586	0.360	103.3	132.6312	$(43.100, -46.230, 8.406, 0.534, -0.331)$

Table 2.1: Matter constants for the air gas mixture used to calculate viscosity and thermal conductivity in equations 2.23 and 2.25. The values are taken from Lemmon and Jacobsen (2004).

2.3.1 Governing Equations

The system to be solved are the compressible Navier-Stokes equations as presented in equation 2.12, although the gravity term is now omitted and the total energy is defined as

$$\rho\, e_{tot} = \frac{p}{\gamma - 1} + \frac{\rho\, \mathbf{u}^2}{2} \qquad \text{and} \qquad p = \rho\, R_{air}\, T, \tag{2.22}$$

with the specific gas constant $R_{air} = 287.1155\ \mathrm{J/kg\,K}$. We treat air as a pseudo-pure fluid with a fixed composition gas mixture consisting of $x_{N2} = 78.084\%$ nitrogen, $x_{O2} = 20.946\%$ oxygen, $x_{AR} = 0.934\%$ argon and $x_{CO2} = 0.0407\%$ carbon dioxide (Haynes, 2016), where x_i here denotes the molar fraction of species i. For viscosity μ and thermal conductivity k polynomial correlations following Lemmon and Jacobsen (2004) are employed and the specific heat capacity is calculated based on the NASA polynomials allowing for a non-constant molecular Prandtl number distribution. To reduce the computational effort, the μ- and k-correlations have been simplified such that the maximum error in the whole solution field is $< 0.068\%$ for μ and $< 0.099\%$ for k with respect to using all correlation terms including the residual gas contribution. The interval to estimate this error ranges from $97000 - 103000\,\mathrm{Pa}$ for the pressure and from $333.15 - 438.15\,\mathrm{K}$ for the temperature. The simplified correlations read

$$\mu = 0.0266958 \cdot \frac{\sqrt{M \cdot T}}{\sigma_{LJ}^2 \cdot \Omega(T^*)}, \tag{2.23}$$

$$k = 1.308 \cdot \mu + 1.405 \cdot \left(\frac{T}{T_{crit}}\right)^{1.1} - 1.036 \cdot \left(\frac{T}{T_{crit}}\right)^{0.3}, \tag{2.24}$$

where M denotes the molar mass, σ_{LJ} the Lennard-Jones size parameter, T_{crit} the critical temperature and $\Omega(T^*)$ the collision integral, which is defined as

$$\Omega(T^*) = \exp\left(\sum_{i=0}^{4} c_{\Omega,i} \cdot \left(\ln(T^*)\right)^i\right), \tag{2.25}$$

with T^* the static temperature normed with the Lennard-Jones energy parameter $(\varepsilon/k)_{LJ}$. See table 2.1 for matter constants and coefficients $c_{\Omega,i}$. The parameters for the NASA polynomials are derived based on $c_p|_{mix} = \sum c_{p,i} \cdot y_i$ with the species mass fraction y_i. Hence, the NASA polynomial for the mixture heat capacity of the air gas mixture reads

$$c_p|_{air} = 943.816 + 0.4053 \cdot T - 0.93 \cdot 10^{-3} \cdot T^2 + 1.28 \cdot 10^{-6} \cdot T^3 - 0.55 \cdot 10^{-9} \cdot T^4. \tag{2.26}$$

2.3.2 Numerical Modelling

CATUM is a finite-volume based LES flow solver for compressible flow with a strong focus on cavitating flow problems. The in-house LES solvers INCA and CATUM share many similarities with respect to numerical modelling and implementation. Both similarities as well as differences of relevance are addressed within this section.

The compressible Navier-Stokes equation system is discretised on a multiblock structured collocated contour-adaptive grid. For time advancement the explicit second-order accurate, four-stage Runge-Kutta scheme of Schmidt (2015) with enhanced stability region is utilised and the time step size is adjusted dynamically to satisfy a Courant number of 1.4. Comparative simulations with the third-order Runge-Kutta scheme by Gottlieb and Shu (1998) and $CFL = 1.0$ (as used in INCA) show no significant change in flow statistics.

The viscous stresses and heat conduction are discretised by a linear second-order central difference scheme. The original CATUM implementation relies on Gauss' divergence theorem to operate on arbitrary mesh geometries, which results eventually in a larger stencil for the face gradient calculation. To calculate the viscous fluxes for a quantity u at face $i + \frac{1}{2}$, in the original CATUM version the values of all four finite volumes u_{i-1}, u_i, u_{i+1} and u_{i+2} are employed, see figure 2.3. First, the u gradients are calculated for the left-sided volume i based on the difference between u_{i-1} and u_{i+1} and for the right-sided volume $i + 1$ based on the difference between u_{i+2} and u_i. The face gradient is then obtained as arithmetic mean of the left- and right-sided cell value and the viscous flux by multiplication with the left- and right-sided viscosity and subsequent averaging, respectively. For our case of well-resolved duct flows, two disadvantages have been observed for the near-wall velocity field:

- The diffusive fluxes between the first and second cell in wall-normal direction and the required gradients, respectively, are approximated by an averaged gradient between the second and third cell value and the wall due to velocity mirroring at the wall boundary condition. This definition reduces the accuracy close to the walls, if not specifically taken into account by the grid generation.

- Oscillations, especially for the wall-normal velocity, are developing close to the wall and are not damped by the viscous flux as the specific gradient calculation results in a zero-gradient, see figure 2.2 for illustration. This impaired velocity field is then used to determine the local wall-damping for the ILES flux function amplifying the error in the near-wall flow field. Consequently, errors in the Reynolds stress distributions, turbulent ejections and secondary flow generation are to be expected.

To avoid oscillations towards the wall and undesirable interference with the coherent structures based wall-damping function of the SGS model, the discretisation is modified to operate on a smaller stencil of only the two neighbouring cells of face $i + \frac{1}{2}$ to calculate the face gradients of the flow quantities in between, i.e. the gradient is calculated as the difference between u_{i+1} and u_i. Additionally, the size difference of the two neighbouring cells is now implicitly taken into account. This approach follows the viscous flux calculation of the flow solver INCA and is illustrated in figure 2.2. Thus, oscillations vanish and the near-wall flow field accuracy is improved significantly.

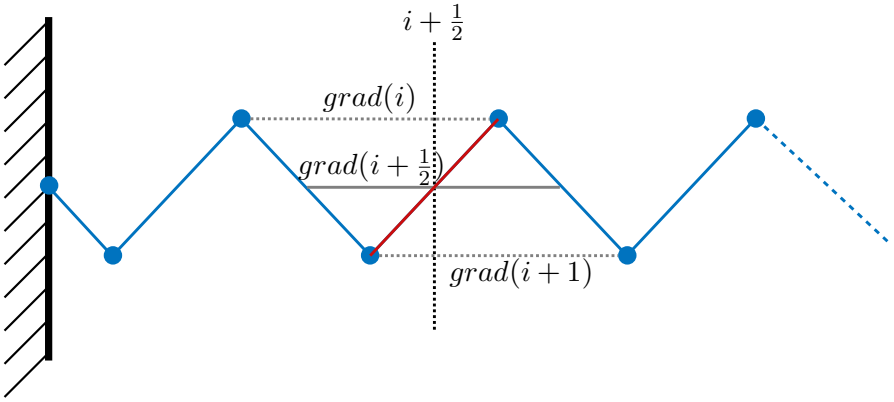

Figure 2.2: Exemplary sketch of near-wall oscillations in the wall-normal velocity field in wall-normal direction and cell face gradient definition for the diffusive flux calculation at face $i + \frac{1}{2}$. The original CATUM implementation is depicted as (——) and the left- and right-sided gradients as (·····), respectively, and the new implementation as (——). See also figure 2.3 for CATUMs stencil definition.

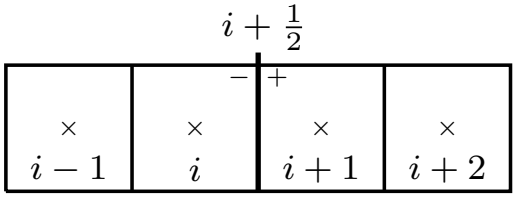

Figure 2.3: Sketch of CATUMs four-cell stencil.

The CATUM LES model follows that of INCA. Hence, for an introduction of ILES and ALDM the reader is referred to section 2.2.2. For the convective flux calculation a compact four-cell stencil is utilised and a hybrid scheme for reconstruction employed, see figure 2.3. To reconstruct the cell face quantities a higher-order central scheme by Egerer et al. (2016) is implemented consisting of a linear fourth-order central scheme for velocities and pressure. For thermodynamic quantities an arithmetic averaging is performed over the values reconstructed by an upwind-biased scheme approaching the considered cell face from the left and from the right. Based on a sensor functional the reconstruction can be locally dynamically adjusted to a more dissipative upwind-biased scheme presented in Budich (2018). For the sensor functional the vorticity-dilation sensor by Ducros et al. (1999) is employed. As implicit SGS model an ALDM-type regularisation term is added to account for the effects of the unresolved subgrid scales. In contrast to the original INCA ALDM implementation, CATUM employs a more robust version adjusted for cavitating flows, see Egerer (2016). The main differences are the usage of a four-cell stencil instead of the original six-cell stencil as well as a different reconstruction procedure for cell-face gradients using only two first- and third-order Lagrange polynomials with a fixed weighting parameter. Consequently, the CATUM ALDM implementation is lacking the solution-adaptiveness. The free ALDM parameters are again calibrated by minimising the

difference of spectral numerical viscosity and eddy viscosity for homogeneous turbulence based on the EDQNM method (Lesieur et al., 2005).

As in INCA, towards the walls a wall-damping function is applied to dampen the dissipative momentum flux weights of the numerical flux function following the coherent structures model of Kobayashi (2005). Its form has been slightly modified for the compressible solver CATUM to $f_{wd} = \pi \cdot |f_{CS}|^2 \cdot f_\Omega$ with $f_\Omega = (1 - f_{CS}) \cdot 1.33$. In contrast to section 2.2.2, the proportionality for compressible turbulence has changed from $f_{wd} \sim |f_{CS}|^{3/2}$ to $f_{wd} \sim |f_{CS}|^2$ following Kobayashi (2005). The f_Ω-parameter has been adjusted from 0.9 to 1.33 based on a square duct LES simulation at $Re = 40 \cdot 10^3$, such that at $y^+ \approx 200$ the undamped ALDM formulation is retrieved. To smoothen the f_{wd}-distribution, the eventual damping functional is obtained as running average over the last $100 \cdot 10^3$ time steps, where only every 100^{th} iteration is utilised for speed-up.

As the solver INCA, likewise CATUM is a proven LES solver. Several studies using the flow solver CATUM have been published, examples are Egerer et al. (2016), Budich et al. (2018), Trummler et al. (2020) for cavitation applications and recently Doehring et al. (2021) for wall-bounded turbulence under transcritical conditions.

2.4 Modelling within Solver ANSYS CFX

Within the current section the governing equations and the numerical model within the commercial flow solver ANSYS CFX used for the Reynolds-averaged Navier-Stokes (RANS) simulations are described. For detailed information the reader is referred to ANSYS Inc. (2020b) and ANSYS Inc. (2020a).

The basis of RANS forms the idea to solve the Navier-Stokes equations approximately for the ensemble-averaged flow state. Hence, in contrast to LES all turbulence scales of the energy cascade are modelled and no individual time sample is produced. The RANS equations are obtained by first decomposing the instantaneous flow quantities in a mean and a fluctuating component $\varphi(\mathbf{x}, t) = \overline{\varphi}(\mathbf{x}) + \varphi'(\mathbf{x}, t)$, then substituting $\varphi(\mathbf{x}, t)$ in the governing equation system and subsequently averaging of the equation system. The averaging of $\varphi(\mathbf{x}, t)$ is considered to be performed over a time span, which is large compared to turbulent time scales and small compared to time scales relevant for the global flow problem (unsteady RANS approach). Due to the Reynolds averaging additional unclosed terms emerge. In our case the unknown Reynolds stress tensor and the turbulent heat flux are relevant. This constitutes the so-called closure problem in RANS. Generally, statistical turbulence models are employed to close the equation system and to solve the flow problem.

Throughout this thesis we use the compressible RANS equation system with the total enthalpy equation, here written in Einstein notation for Cartesian coordinates:

$$\frac{\partial \overline{\rho}}{\partial t} + \frac{\partial}{\partial x_j}\left(\overline{\rho}\,\overline{u}_j\right) = 0, \tag{2.27a}$$

$$\frac{\partial \overline{\rho}\,\overline{u}_i}{\partial t} + \frac{\partial}{\partial x_j}\left(\overline{\rho}\,\overline{u}_i\,\overline{u}_j\right) = -\frac{\partial \overline{p}}{\partial x_i} + \frac{\partial}{\partial x_j} \cdot \left(\overline{\mathbf{T}}_{ij} - \overline{\rho}\,\overline{u_i' u_j'}\right), \tag{2.27b}$$

$$\frac{\partial \overline{\rho}\,\overline{h}_{tot}}{\partial t} - \frac{\partial \overline{p}}{\partial t} + \frac{\partial}{\partial x_j}\left(\overline{\rho}\,\overline{u}_j\,\overline{h}_{tot}\right) = \frac{\partial}{\partial x_j}\left(\lambda \frac{\partial T}{\partial x_j} - \overline{\rho}\,\overline{u_j' h'}\right) + \frac{\partial}{\partial x_j}\left[\overline{u}_i \cdot \left(\overline{\mathbf{T}}_{ij} - \overline{\rho}\,\overline{u_i' u_j'}\right)\right], \tag{2.27c}$$

with the total enthalpy defined as

$$h_{tot} = h + \frac{\overline{u}_i^2}{2} + \frac{\overline{u_i'}^2}{2}. \tag{2.28}$$

The last term corresponds to the turbulent kinetic energy $TKE = 0.5 \cdot \overline{u_i'}^2$. Compared to the original compressible Navier-Stokes equation system 2.12, the influence of gravity is neglected and a transport equation for the total enthalpy h_{tot} is used instead of the related internal energy e with $h = e + p/\rho$. For forced convection problems the gravity can be neglected if $Gr/Re \ll 1$, which will be discussed in sections 3.2 and 4.1 for our configurations. The viscous stress tensor is again defined by equation 2.13. The fluid properties are evaluated based on the IAPWS IF97 formulation when liquid water is utilised as working fluid and on Sutherland's law and NASA polynomials for ideal gas air.

Equations 2.27 have a similar structure as the instantaneous Navier-Stokes equations with the additional unknown terms of the Reynolds stress tensor $\overline{u_i'u_j'}$ in the momentum and enthalpy equations, and the turbulent heat flux $\overline{u_j'h'}$ in the enthalpy equation. To find an approximate correlation for the Reynolds stresses two main turbulence model classes exist and are considered in the present work: The eddy viscosity models (EVM) and Reynolds stress models (RSM). The EVM rely on the Boussinesq turbulent viscosity hypothesis and an isotropic turbulence closure. The unknown $\overline{u_i'u_j'}$-tensor is treated similar as the viscous stress tensor $\mathbf{T}_{ij}$ introducing a turbulent viscosity ν_t, for which additional transport equations are solved. One of the most popular two-equation models is the SST $k-\omega$ turbulence model. Differential RSMs require a higher computational effort as an additional transport equation is solved for each of the six $\overline{u_i'u_j'}$-components considering the tensor symmetry. A benefit, especially relevant for the investigation of turbulence-induced secondary flow, is the fact that RSMs are able to account for turbulence anisotropy. Explicit algebraic Reynolds stress models (EARSM) are an extension of two-equation models and derived from RSMs with the specific target to improve the prediction capabilities for flow configurations affected by secondary flow, streamline curvature and system rotation. These flow features are taken into account without adding transport equations, but instead using nonlinear algebraic correlations for the Reynolds stress tensor components based on mean strain rate and vorticity (ANSYS Inc., 2020a). An extensive overview over RANS turbulence modelling is given in Wilcox (2006) and Pope (2000).

To approximate the unknown turbulent heat flux $\overline{u_j'h'}$ a widely used method is to utilise a gradient transport approach assuming a constant turbulent Prandtl number. Thus, the turbulent diffusivity is calculated based on the turbulent viscosity as $\alpha_t = \nu_t/Pr_t$. However, several studies, e.g. Kays (1994), Hirota et al. (1997), Remmler and Hickel (2014), Schindler et al. (2019) and Kaller et al. (2019), have proved this assumption to be invalid. Possible solutions for non-constant Pr_t flows are to introduce additional transport equations for the single components of $\overline{u_j'h'}$ analogous to RSMs or to utilise an algebraic closure model relating the turbulent heat flux to the Reynolds stresses and available mean flow quantities similar to EARSMs. For a detailed discussion of the interaction of different modelling approaches for the Reynolds stresses and turbulent heat fluxes, here for application in turbomachinery flows, the reader is referred to Rochhausen (2017).

Within this thesis the following turbulence models have been employed as implemented in

ANSYS CFX, i.e. the standard unmodified set of parameters is used, to approximate $\overline{u_i' u_j'}$. The model names follow the CFX nomenclature:

- SST: The *Shear Stress Transport* (SST) model is an isotropic turbulence two-equation EVM switching between a low-Reynolds $k-\omega$ formulation in near-wall regions and a $k-\varepsilon$ formulation in the free stream. The extra computational effort remains relatively small as only two additional partial differential equations (PDEs) are introduced to calculate the distribution of turbulent viscosity ν_t.

- BSL RSM: The *Baseline Reynolds Stress* (BSL RSM) model is a RSM based on the ω-equation to determine turbulent scales. The computational effort is increased noticeably as for every component of $\overline{u_i' u_j'}$ and the specific dissipation ω an additional PDE is solved. Hence, in total 7 additional PDEs are introduced. The benefits are the low-Reynolds capability for wall-bounded flows and the inherent representation of turbulence anisotropy.

- SSG RSM: The SSG RSM by Speziale, Sarkar and Gatski is a Reynolds stress model based on the ε-equation to determine turbulent scales. The computational effort is increased noticeably as for every component of $\overline{u_i' u_j'}$ and the dissipation ε an additional PDE is solved. In total 7 additional PDEs are introduced. Benefits include the inherent representation of turbulence anisotropy and disadvantages the lacking low-Reynolds capability.

- BSL EARSM: The *Baseline Explicit Algebraic Reynolds Stress* (BSL EARSM) model is an EARSM based on the ω-equation to determine turbulent scales. The computational effort is kept relatively small as nonlinear algebraic relations using mean strain rate and vorticity are employed to model Reynolds stress tensor anisotropy instead of adding PDEs. The benefits are the low-Reynolds capability for wall-bounded flows and the representation of turbulence anisotropy.

For modelling the turbulent heat flux $\overline{u_i' h'}$ the following methods are applied within this work:

- Gradient approach with a constant Pr_t: this method is the standard model within ANSYS CFX. The turbulent heat fluxes are linked to the mean enthalpy gradients via the isotropic turbulent diffusivity α_t with $\alpha_t = \nu_t / Pr_t$.

- Second moment closure model: Additional PDEs are solved for each component of $\overline{u_i' h'}$ analogous to RSMs. This method is yet a beta feature within ANSYS CFX (CADFEM GmbH, personal communication, 3rd December 2018).

- Algebraic Daly-Harlow model (Daly and Harlow, 1970): An anisotropic turbulent diffusivity tensor is derived as a function of the Reynolds stress tensor and enthalpy gradient components:

$$-\overline{u_i' h'} = c_{DH} \frac{TKE}{\varepsilon} \overline{u_i' u_j'} \frac{\partial \overline{h}}{\partial x_j}, \tag{2.29}$$

  with $c_{DH} = 0.3$.

- Algebraic Younis model (Younis et al., 2005): An extended more accurate anisotropic turbulent diffusivity tensor is derived as

$$\begin{aligned} -\overline{u_i' h'} =& c_{Y1} \frac{TKE^2}{\varepsilon} \frac{\partial \overline{h}}{\partial x_i} + c_{Y2} \frac{TKE}{\varepsilon} \overline{u_i' u_j'} \frac{\partial \overline{h}}{\partial x_j} + \\ & c_{Y3} \frac{TKE^3}{\varepsilon^2} \frac{\partial \overline{u}_i}{\partial x_j} \frac{\partial \overline{h}}{\partial x_j} + c_{Y4} \frac{TKE^2}{\varepsilon^2} \left(\overline{u_i' u_k'} \frac{\partial \overline{u}_j}{\partial x_k} + \overline{u_j' u_k'} \frac{\partial \overline{u}_i}{\partial x_k} \right) \frac{\partial \overline{h}}{\partial x_j}, \end{aligned} \tag{2.30}$$

  with $c_{Y1} = -4.55 \cdot 10^{-2}$, $c_{Y2} = 3.73 \cdot 10^{-1}$, $c_{Y3} = -3.73 \cdot 10^{-3}$ and $c_{Y4} = -2.35 \cdot 10^{-2}$.

To simulate the flow in near-wall regions all ω-based models in ANSYS CFX are combined with the so-called *automatic wall treatment* functionality switching gradually from using wall functions to a low-Reynolds number formulation based on the local grid resolution (ANSYS Inc., 2020a). Note, the Reynolds number here denotes the turbulent Reynolds number $Re_t = \sqrt{TKE}/(\nu\,\varepsilon)$. The low-Reynolds number approach resolves the complete turbulent boundary layer (TBL) profile including the viscous sublayer, provided that the wall-normal grid spacing is fine enough. ANSYS Inc. (2020a) recommends $y^+_{min} < 2$ directly at the wall and resolving the boundary layer with at least 10 nodes to reduce the error associated with the automatic switch. The scalable wall function approach is used for all ε-based turbulence models and for too coarse meshes in the near-wall region. The approach provides empirical formulas for the near-wall velocity profiles based on the logarithmic law of the wall. A TBL resolving method is not available due to the inherent inability of the $k-\varepsilon$ model class to simulate low Re_t flow promoting numerical instabilities (ANSYS Inc., 2020a).

3 Straight Heated HARCD Simulations (INCA)

In this chapter the results for the asymmetrically heated straight HARCD configuration using liquid water as cooling fluid are presented. The simulations have been performed using the flow solver INCA and the configuration is defined in cooperation with project partners from the Technical University of Braunschweig, who conducted a corresponding experiment. First the experimental and numerical set-ups are introduced. Then the numerical accuracy is assessed achievable with the resolution determined based on an extensive grid sensitivity study by comparison with square duct DNS data and the experimental HARCD results. The latter includes a discussion of modifications of the experimental measurement set-up motivated partly by the numerical results. Based on the LES results, we thoroughly investigate the influence of the asymmetric wall heating on the duct flow. The main objectives are (I) to analyse the effect of asymmetric wall heating and the accompanying local viscosity reduction on the mean flow, especially the influence on the secondary and the turbulent flow field, (II) to characterise the impact of the secondary flow on turbulent heat transfer and on the development of the thermal boundary layer along the spatially resolved heated duct including the thermal entrance region and (III) to investigate the validity of a constant turbulent Prandtl number assumption.

Note, the original article of Kaller et al. (2019) is complemented by an extended experimental-numerical comparison including PIV results of an updated measurement campaign as well as an investigation of the heating-induced secondary flow modulation evaluating the streamwise vorticity and the terms of its balance equation. For the remaining sections only minor cosmetic alterations have been made.

3.1 Reference Experiment Configuration

In cooperation with the colleagues from the Technical University of Braunschweig conducting the companion reference experiment a generic cooling duct set-up has been defined. The goal of the configuration has been to allow for high-accuracy experimental PIV, PTV and LIF measurements

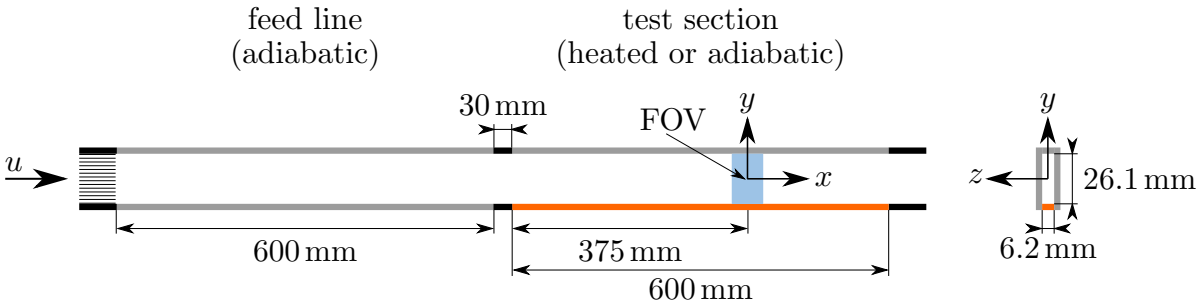

Figure 3.1: Experimental HARCD set-up, reproduced from Rochlitz et al. (2015).

with well-determined boundary conditions as well as for well-resolved LES simulations. At the same time the set-up has to be able to represent the characteristic flow features present in a realistic rocket engine cooling duct. The HARCD design represents a trade-off between these three goals.

Figure 3.1 shows the initial experimental HARCD set-up as used in the second funding period of the SFB-TRR40 and upon which the publications Rochlitz and Scholz (2015), Rochlitz et al. (2015), and Rochlitz and Scholz (2018) are based. As cooling fluid liquid water has been chosen. The duct has a rectangular cross-section with a nominal width and height of 6.00 mm × 25.80 mm. The resulting aspect ratio is $AR = 4.3$ and the hydraulic diameter $d_h = 9.74\,\text{mm}$. Due to fabrication tolerances (P. Scholz and H. Rochlitz, personal communications, 2015–2018) slight deviations are present in the experiment. The mean duct width and height evaluated at several streamwise locations are 6.23 mm and 26.10 mm, reducing the aspect ratio to 4.19 and increasing d_h to 10.06 mm. The length of both straight duct sections, the unheated feed line and the heated test section, is equally 600 mm corresponding to $\approx 60\,d_h$. The bottom wall in the feed line is made of aluminium and in the test section of copper, and the side and upper walls made of polymethyl methacrylate (PMMA) for optical accessibility. All walls are hydraulically smooth with an average roughness of $R_a < 0.1\,\mu\text{m}$. The heatable copper wall forms the tip of a so-called heat nozzle, which is a large cone-shaped block of copper facilitating a spatially uniform temperature distribution for the heated wall. In order to ensure an isothermal wall boundary condition, i.e. a constant wall temperature, the copper block is equipped with several cartridge heaters and temperature sensors to regulate the heating in a closed loop control system.

The experiment is conducted as follows: water is pumped from a reservoir, where it can be preheated or cooled down, through a curved pipe, the rectangular feed line and the heatable test section, see figure 3.1. After the test section the water flows back into the reservoir. The flow rate is regulated using an electromagnetic flowmeter, which is installed upstream of the pump. Between the curved pipe and the rectangular feed line a smooth transition connector piece is installed as well as a flow straightener to homogenise the flow field and to break up larger secondary flow structures having formed along the pipe. Over the 600 mm long unheated feed line a fully developed turbulent duct flow profile forms. To ensure, that the chosen length is sufficient, a further test run with an additional 2000 mm long feed line has been executed. To obtain homogeneous inflow conditions for the heated test section of equally 600 mm, a further flow straightener is installed between feed line and test section. The test section can be extended

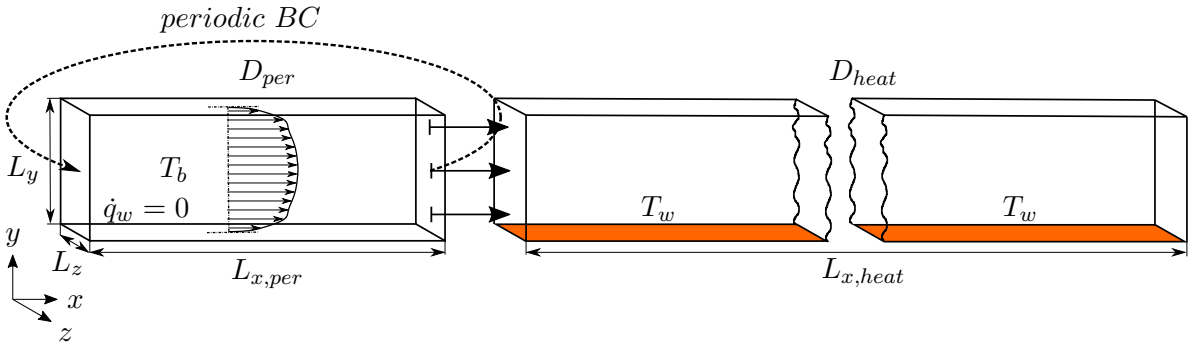

Figure 3.2: Computational straight HARCD set-up, reproduced from Kaller et al. (2017).

by a 90° curved heated section (not shown in figure 3.1). After the test section the coolant flows back into the reservoir. To investigate the details of the flow field particle image velocimetry (2C2D-PIV), stereo PIV (3C2D-PIV) and volumetric particle tracking velocimetry (3C3D-PTV) measurements have been carried out. The first two methods give two (2C), respectively three velocity components (3C) in a plane (2D), whereas PTV gives three components in a volume (3D). As tracer particles hollow glass spheres with a diameter of 10 µm are used. The laser light-sheet used for illumination is spanned from above the test section and forms a plane at the centre of the duct ranging from the bottom to the upper wall. The field of view (FOV) extends from $350 - 400$ mm with respect to the test section inlet. The laser sheet thickness is 1 mm for PIV and for PTV the laser sheet extends over the entire duct width. For the temperature field measurements the laser-induced fluorescence (LIF) method is employed using the organic fluorescent dyes Rhodamine B and Rhodamine 110. Further details on the PIV measurements can be found in Rochlitz et al. (2015) and on the LIF measurements in Rochlitz and Scholz (2018). Experiments including the 90° curved heated section have been carried out, but have not been published yet.

3.2 Computational Set-up

In this section the computational set-up modelling the experimental set-up of the previous section 3.1 is presented comprising the configuration and its boundary conditions, the numerical discretisation, simulation procedure and the dimensionless characteristic numbers.

The computational set-up is shown in figure 3.2. The configuration consists of two sub-domains: the non-heated periodic section D_{per} and the heated section D_{heat}. D_{per} serves as a model for the isothermal feed line of the experiment. The periodic box length of the precursor domain $L_{x,per}$ is a priori unknown and can not be determined straightforward. On the one hand, the domain should be as short as possible to not unnecessarily increase the computational costs and on the other hand it has to be long enough to resolve all relevant turbulent structures. Otherwise the length constraint might lead to unphysical inflow conditions for D_{heat}. In wall-bounded flows the so-called large-scale motions in the outer region of the TBL can reach lengths of up to $12.5 \cdot d_h$, as has been reported by Guala et al. (2006) and Monty et al. (2007) for pipe and channel flows.

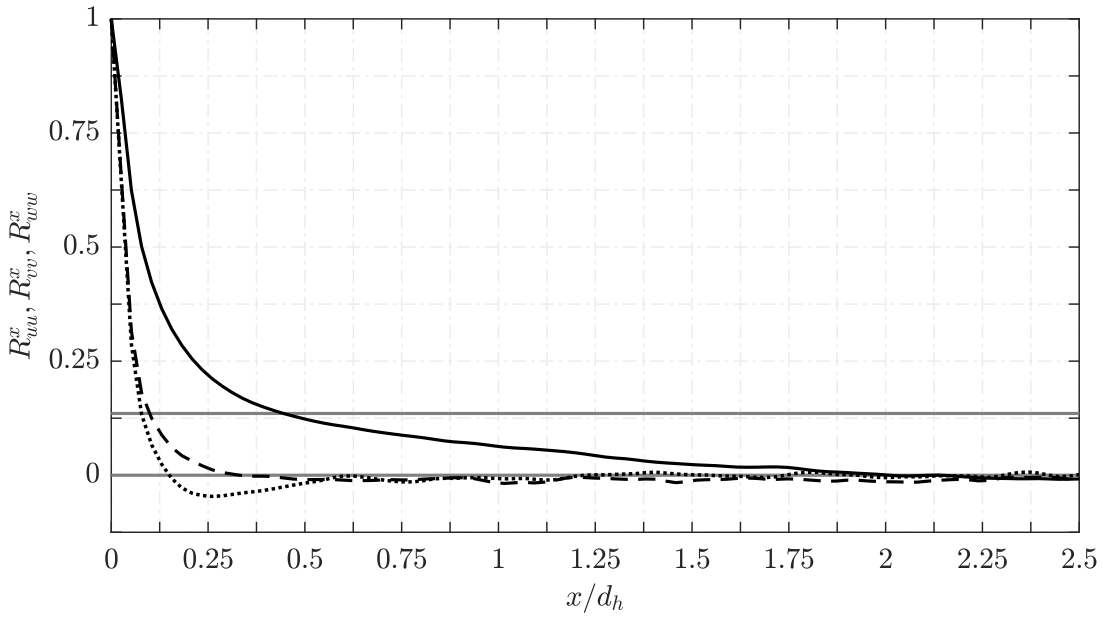

Figure 3.3: Two-point correlations for the adiabatic domain D_{per} in streamwise direction at $(y, z) = (0, 0)$ with R^x_{uu} (——), R^x_{vv} (- - - - -) and R^x_{ww} (·····). The zero- and $1/e^2$-lines are indicated by (——).

Domain	$L_x \times L_y \times L_z$ [mm^3]	u_b [m/s]	T_b [K]	T_w [K]
D_{per}	$73.0 \times 25.8 \times 6.0$	5.3833	333.15	333.15
D_{heat}	$600.0 \times 25.8 \times 6.0$	5.3833	333.15	373.15

Table 3.1: Geometry and flow parameters for the straight HARCD set-up.

Lozano-Durán and Jiménez (2014) have investigated in detail the influence of the periodic domain size on turbulent channel flow results, concluding that box sizes smaller than the large-scale structures can indeed give suitable results. In this case the large-scale motions are represented as indefinitely long, but the interaction between the large-scale structures and well-resolved turbulent scales can be correctly represented. Pirozzoli et al. (2018) briefly investigates the box length influence on square duct flow results and reported only marginal differences between using $2\pi \cdot d_h$ and $4\pi \cdot d_h$. To the author's knowledge no such study is yet available for HARCD flows. For the present case the periodic box length is set to $L_{x,per} = 7.5 \cdot d_h$ following low Re_b DNS data by Vinuesa et al. (2014) for an $AR = 5$ case and experimental channel flow data by Monty et al. (2007). The two-point correlations in figure 3.3 show, that the chosen box length is indeed long enough to capture the large-scale turbulent structures in the duct centre at $(y, z) = (0, 0)$. The intersections of the correlations with the zero- and $1/e^2$-lines indicate the turbulent length scales, e being Euler's number. For a detailed discussion of turbulent length scales present within the HARCD the reader is referred to section 3.5.6.

The heated section is spatially resolved, i.e. the experimental duct length of $L_{x,heat} = 600\,\text{mm}$ is fully simulated, which is required due to the thermal boundary layer development in streamwise

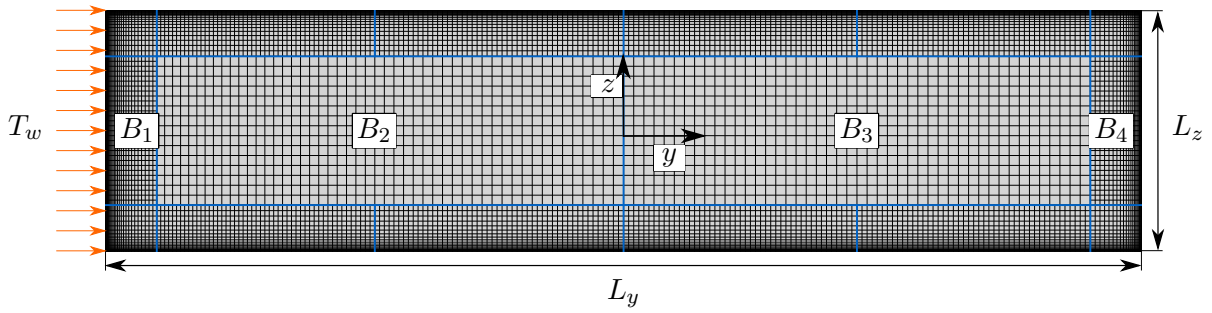

Figure 3.4: Cross-sectional computational grid and blocking highlighted in blue (every second grid line shown). Relevant block names B_i are included for identification.

direction. Both duct sections are simulated simultaneously, D_{per} serving as a time-resolved turbulent inflow generator for the heated section. At the outflow of D_{heat} a second-order order Neumann boundary condition is applied for velocity and density fluctuations. All sidewalls are treated as smooth adiabatic walls except for the lower wall of D_{heat}. The heated sidewall is defined as a smooth isothermal wall with a fixed temperature of $T_w = 373.15\,\mathrm{K}$, respectively with the corresponding value of ρ^* evaluated using equation 2.20. Table 3.1 contains the geometrical dimensions and the main flow parameters for the straight heated HARCD set-up.

For discretisation a block-structured Cartesian grid is used with $\approx 280 \cdot 10^6$ cells for the complete straight HARCD set-up of D_{per} and D_{heat}. Both domains possess the same meshing to avoid the necessity of an interpolation function and the associated errors at the interface. The cross-sectional grid and its blocking structure is shown in figure 3.4. To reduce the number of cells and the associated computational effort as well as to gain a higher flexibility in mesh generation to optimise numerical accuracy, the grid is separated into boundary layer and core blocks. Between a core and a boundary layer block, for example between B_2 and B_1, a 2:1 coarsening is applied. Towards the sidewalls a hyperbolic grid stretching is utilised, exemplarily for the y-direction following

$$y_j = l_y \cdot \tanh\left(\frac{\gamma_y(j-1)}{N_y - 1}\right) \Big/ \tanh(\gamma_y). \tag{3.1}$$

Here j is the respective grid point index, N_y the number of points, γ_y the stretching factor and l_y the edge length of the block in y-direction. This meshing law is used for all sidewalls. Likewise a slight hyperbolic stretching is used for block B_2 due to being affected by the asymmetric heating, whereas B_3 has a uniform cell distribution in the yz-plane, see figure 3.4. In streamwise direction all blocks possess an uniform discretisation. The grid parameters are determined with the help of a thorough grid sensitivity analysis (presented in the subsequent section 3.3.1) and are summarised in table 3.4 for the mesh of the complete configuration.

The simulation procedure is divided into several sub-steps:

1. Simulation of the periodic adiabatic HARCD flow for a coarse grid version of D_{per} until a fully developed turbulent flow state is reached. As initial state the velocity profile for a

Domain	Re_b	$Re_\tau\|_{y_{min}}$	$Re_\tau\|_z$	Pr_b	$Pr\|_{y_{min}}$	$Nu_{xz}\|_{y_{min}}$	Gr_b
D_{per}	$110 \cdot 10^3$	$4.82 \cdot 10^3$	$5.47 \cdot 10^3$	3.00	3.00	–	–
D_{heat}	$110 \cdot 10^3$	$7.25 \cdot 10^3$	$5.44 \cdot 10^3$	3.00	1.75	370.7	$8.4 \cdot 10^5$

Table 3.2: Characteristic quantities for the straight HARCD set-up.

fully developed laminar duct flow taken from Shah and London (1978) is set, superimposed with white noise of amplitude $A \approx 5\%$ of u_b.

2. Interpolation of the previous result onto the fine grid version of D_{per} and continuation of the simulation for several flow-through times (FTT) until flow convergence for the statistical quantities is reached.

3. Initialisation of the heated section D_{heat} based on the D_{per} flow field, where D_{heat} is built as a sequence of several D_{per} sections.

4. Start simulation of the complete set-up with heating applied and continuation for 1.33 FTT with respect to $L_{x,heat}$ and u_b, corresponding to 11 FTT with respect to $L_{x,per}$, to dispose of initial disturbances in the domain.

5. Start statistical sampling at a constant temporal sampling rate of $\Delta t_{sample} = 0.025 \cdot d_h / u_b$ and continuation of the simulation for over 20 FTT with respect to $L_{x,heat}$.

The simulations run in parallel on 7088 cores (254 compute nodes) on SuperMUC Phase 2.

In table 3.2 the non-dimensional characteristic quantities for the set-up are listed. For Re_b and Re_τ the hydraulic diameter d_h is used as characteristic reference length. To determine Re_b bulk flow quantities for liquid water at $T = T_b$ are used, and Re_τ is evaluated in the centre of the respective sidewall. Hence, Re_b is an integral value, whereas Re_τ is a local value. For the heated section Re_τ is given as a streamwise averaged value over the last $7.5\, d_h$. Due to the heating the molecular Prandtl number varies from $Pr_b = 3.00$ for the unheated flow state to $Pr|_{y_{min}} = 1.75$ directly at the heated wall. For a detailed discussion on the turbulent Prandtl number Pr_t the reader is referred to section 3.5.4. Equation 2.7 gives a two-dimensional $Nu(x, z)$ distribution at the heated wall. Averaging in both span- and streamwise directions results in the listed average value $Nu_{xz}|_{y_{min}}$ for D_{heat}. Note, for the Nusselt number the hydraulic diameter is again used as reference length and not the width of the heated wall. Following Wardana et al. (1994) buoyancy effects can be neglected when $Gr / Re^2 \ll 1$. For the present set-up this ratio at bulk conditions is $Gr_b / Re_b^2 = 6.9 \cdot 10^{-5}$. Hence, buoyancy effects are expected to be negligible.

3.3 Assessment of Numerical Accuracy

In the following the numerical accuracy of the well-resolved straight heated duct simulation is evaluated. First an extensive grid sensitivity analysis for the given HARCD configuration is presented and the eventually used grid resolution derived. Based on this spatial discretisation a moderately high Reynolds number square duct LES is performed and compared to available DNS data by Pirozzoli et al. (2018).

Grid	$N_x \times N_y \times N_z$	$\Delta x^+ \times \Delta y^+_{min} \times \Delta z^+_{min}$	$\frac{\Delta y_{max}}{\Delta y_{min}} \times \frac{\Delta z_{max}}{\Delta z_{min}}$	$\gamma_y \times \gamma_z$	$\tau_w\|_y \times \tau_w\|_z$
G_{base}	$380 \times 469 \times 153$	$98.6 \times 1.28 \times 1.45$	25.3×23.6	2.30×2.30	58.4×72.2
$G^a_{w_\parallel}$	$380 \times 325 \times 106$	$92.3 \times 1.20 \times 1.35$	36.9×36.5	2.52×2.53	51.2×63.0
$G^b_{w_\parallel}$	$380 \times 245 \times 83$	$87.0 \times 1.13 \times 1.26$	50.6×47.4	2.65×2.69	45.5×54.7
$G^a_{w_\perp}$	$380 \times 485 \times 181$	$98.2 \times 1.01 \times 1.00$	26.9×27.4	2.35×2.36	57.9×72.9
$G^b_{w_\perp}$	$380 \times 427 \times 115$	$96.6 \times 2.16 \times 2.44$	24.4×24.0	2.32×2.32	56.1×69.3
$G^a_{\Delta x}$	$580 \times 469 \times 153$	$63.2 \times 1.25 \times 1.43$	25.3×23.6	2.30×2.30	55.8×70.6
$G^b_{\Delta x}$	$760 \times 469 \times 153$	$47.1 \times 1.23 \times 1.40$	25.3×23.6	2.30×2.30	53.4×67.6

Table 3.3: Grid sensitivity study parameters and resulting wall shear stresses in [Pa].

3.3.1 Grid Sensitivity Analysis

The goal of this grid sensitivity analysis is to determine the required spatial discretisation to assure a well-resolved cooling duct LES at affordable numerical costs. The study focuses on the adiabatic periodic section D_{per}, see figure 3.2. The results are eventually used to derive the heated set-up mesh. The grids cross-sectional block splitting is identical to that shown in figure 3.4 for the full configuration, with the difference being a y- and z-symmetric meshing as no heating is applied. Starting from an initial already well-resolved grid G_{base}, three parameters are chosen to be varied and their influence on the periodic duct flow field evaluated:

1. maximal wall-tangential cell size using the grids G_{base}, $G^a_{w_\parallel}$ and $G^b_{w_\parallel}$
2. minimal wall-normal cell size using the grids G_{base}, $G^a_{w_\perp}$ and $G^b_{w_\perp}$
3. streamwise cell size using the grids G_{base}, $G^a_{\Delta x}$ and $G^b_{\Delta x}$

The main parameters for the considered grids within this study are summarised in table 3.3. The chosen grid requirements valid for all four sidewalls are:

- $\Delta y^+_{min} \approx \Delta z^+_{min} \approx 1$, Δy^+_{min} and Δz^+_{min} denoting the dimensionless wall distance of the wall-adjacent cell based on the complete respective cell height
- dimensionless velocity profile follows the analytical law of the wall
- sufficient near-wall grid resolution to correctly capture turbulence production within the TBL, the main focus being on the streamwise Reynolds stress distribution

These requirements are evaluated in the respective centre of each sidewall. Temporal averaging of the periodic duct simulations is performed over a minimum of 33 FTT with a sampling rate of $\Delta t_{sample} = 0.025 \cdot d_h / u_b$. Subsequently a spatial averaging is conducted over the homogeneous streamwise direction, and the flow field symmetry with respect to the y- and z-axis utilised to perform a spatial averaging over the four quadrants. For the assessment of the grid sensitivity the main focus is put on the velocity and Reynolds stress profiles for the $y = y_{min}$ wall boundary layer, where the heating is applied in the resolved domain D_{heat}, see figure 3.4. The velocity profile is made dimensionless with the viscous length scale $l^+_\nu = \nu_w / u_\tau$ and friction velocity u_τ.

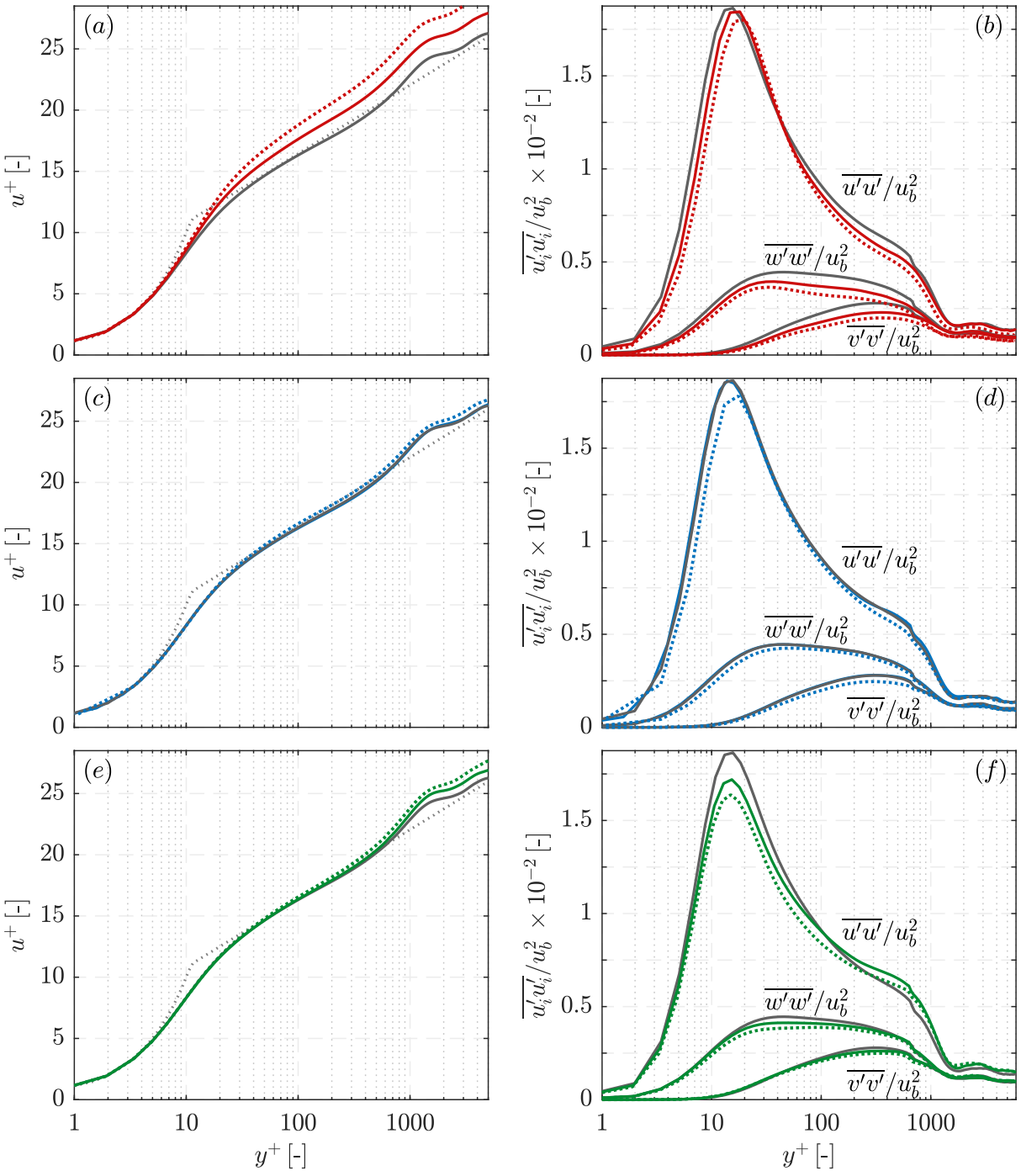

Figure 3.5: Grid sensitivity study based on D_{per}: (a, c, e) show temporally and spatially averaged dimensionless velocity profiles and (b, d, f) averaged Reynolds stress profiles along the midplane $z = 0$ for the lower wall TBL. In (a, b) the influence of the maximum wall-tangential cell size (G_{base} (——) versus $G^a_{w_\parallel}$ (——) and $G^b_{w_\parallel}$ (·····)), in (c, d) that of the minimal wall-normal cell size (G_{base} versus $G^a_{w_\perp}$ (——) and $G^b_{w_\perp}$ (·····)), and in (e, f) that of the streamwise cell size is investigated (G_{base} versus $G^a_{\Delta x}$ (——) and $G^b_{\Delta x}$ (·····)). (·····) represents the analytical law of the wall ($u^+ = 1/0.41 \cdot \ln y^+ + 5.2$). See also table 3.3.

Non-dimensionalisation for the Reynolds stresses is deliberately performed using u_b^2, and not u_τ^2 as often seen in the literature, to point out differences more clearly .

The results of the grid sensitivity study with respect to the three varied parameters shown in figure 3.5 are:

1. Figures 3.5 (a, b) depict the influence of varying the maximal wall-tangential cell size while keeping the streamwise discretisation Δx and the wall-adjacent cell heights Δy_{min} and Δz_{min} constant. Hence, the stretching factors of the hyperbolic meshing law γ_y and γ_z, and with it the cross-sectional discretisation is modified. Focusing on the short sidewalls $y = y_{min}/y_{max}$, the ratio of largest to smallest cell size $\frac{\Delta z_{max}}{\Delta z_{min}}$ is varied from 23.6 over 36.5 to 47.4, see table 3.3 for further details on the grids G_{base}, $G^a_{w_\parallel}$ and $G^b_{w_\parallel}$. For the finest resolution G_{base} the velocity profile follows closely the analytical law of the wall, whereas for $G^a_{w_\parallel}$ and $G^b_{w_\parallel}$ the profile in the log-law and wake region is shifted increasingly upwards with decreasing grid resolution. This shift is accompanied by a significant wall shear stress drop from $\tau_w|_{y,G_{base}} = 58.4\,\text{Pa}$ over $\tau_w|_{y,G^a_{w_\parallel}} = 51.2\,\text{Pa}$ to $\tau_w|_{y,G^b_{w_\parallel}} = 45.5\,\text{Pa}$ and likewise for the sidewalls. All Reynolds stress profiles show a decreasing magnitude with decreasing grid resolution and a shift of the $\overline{u'u'}$-maximum to higher y^+-values is observed from G_{base} over $G^a_{w_\parallel}$ to $G^b_{w_\parallel}$. The wall-normal resolution of all three grids within the current comparison is such, that they possess 9 cells until the streamwise Reynolds stress maximum, respectively 8 cells for the large sidewall TBLs. As conclusion for $\frac{\Delta y_{max}}{\Delta y_{min}}$ and $\frac{\Delta z_{max}}{\Delta z_{min}}$, respectively, a value of ≈ 25 is required.

2. Figures 3.5 (c, d) show the influence of the minimum wall-normal cell height while keeping the streamwise discretisation Δx and the stretching factors γ_y and γ_z, i.e. the maximal wall-tangential cell size ratios $\frac{\Delta y_{max}}{\Delta y_{min}}$ and $\frac{\Delta z_{max}}{\Delta z_{min}}$ constant. Hence, as before the cross-sectional discretisation is modified. The dimensionless wall-next cell height Δy^+_{min} is varied from $\Delta y^+_{min}|_{G^a_{w_\perp}} = 1.01$ over $\Delta y^+_{min}|_{G_{base}} = 1.28$ to $\Delta y^+_{min}|_{G^b_{w_\perp}} = 2.16$ and for the large sidewalls accordingly, see table 3.3 for further details on the grids G_{base}, $G^a_{w_\perp}$ and $G^b_{w_\perp}$. The velocity and turbulent stress profiles show coinciding results for the finest resolved $G^a_{w_\perp}$ and the slightly coarser G_{base}. For the even coarser $G^b_{w_\perp}$ an upwards shift of the velocity profile and a lower wall shear stress is observable as well as a decrease of all Reynolds stress magnitudes. The wall-normal resolution of the three grids is such, that for the finest $G^a_{w_\perp}$ 10 cells reside within the TBL until the Reynolds stress maximum, for G_{base} 9 and for $G^b_{w_\perp}$ 6. The conclusion is, that the wall-normal resolution of G_{base} is sufficient, whereas for $G^b_{w_\perp}$ it is too coarse to resolve the TBL profiles correctly.

3. In figures 3.5 (e, f) the influence of the streamwise cell size is depicted while the cross-sectional discretisation remains unchanged. See table 3.3 for details on the grids G_{base}, $G^a_{\Delta x}$ and $G^b_{\Delta x}$. The constant cell size Δx is modified by increasing the streamwise grid points from $N_x = 380$ in G_{base} by $\approx 50\%$ for $G^a_{\Delta x}$ and by 100% for $G^b_{\Delta x}$. This leads eventually to a Δx^+-range from $\Delta x^+|_{G_{base}} = 98.6$ over $\Delta x^+|_{G^a_{\Delta x}} = 63.2$ to $\Delta x^+|_{G^b_{\Delta x}} = 47.1$. With increasing resolution the wall shear stress drops slightly. Also an upwards shift of the velocity profiles is observable in the log-law region and stronger in the outer layer of the TBL. The magnitudes of all Reynolds stress tensor components decrease with increasing

streamwise resolution in the inner layer region of the TBL. For the $\overline{u'u'}$-profile this decrease is strongest. Additionally an $\overline{u'u'}$-increase in the outer layer from $y^+ \approx 100 - 1000$ is visible. The position of the $\overline{u'u'}$-maximum however remains constant and is therefore determined by the cross-sectional discretisation. To conclude, even though the streamwise turbulence intensity is slightly overpredicted, grid $G^a_{\Delta x}$ with $\Delta x^+ / \Delta y^+_{min} \approx 50$ offers a good compromise between numerical accuracy and simulation costs.

Based on the results of the grid sensitivity analysis performed for the periodic adiabatic section, the discretisation for the full heated configuration is derived. An overall good compromise between the previously mentioned requirements for a well-resolved LES and numerical costs is achieved by grid $G^a_{\Delta x}$. Hence, it serves as symmetric source grid for generating the asymmetric heated set-up mesh. For a heated flow with $Pr > 1$ thermal length scales are smaller than momentum length scales, and the thermal boundary layer is completely contained inside the momentum boundary layer. To resolve the temperature gradients at the lower heated wall $y = y_{min}$, the wall-normal resolution is increased. The discretisation in the upper half of the duct and the blocking structure remains unchanged leading to an asymmetric grid with respect to the z-axis. Based on Monin et al. (2007), the height of the first cell at the heated wall $\Delta y_{min}|_{heated}$ is reduced by the ratio of the smallest temperature scales and the Kolmogorov scales as

$$\frac{\Delta y_{min}|_{heated}}{\Delta y_{min}|_{adiabatic}} = \frac{\eta_\theta}{\eta_k} = \left(\frac{1}{Pr}\right)^{1/2}. \tag{3.2}$$

We adopt this originally DNS approach for LES by assuming an equivalent ratio for the viscous length scales l^+_ν to thermal scales as for Kolmogorov to thermal scales. The Prandtl number is set to $Pr = 3.0$, the value for water at T_b, and therefore the largest possible value for the investigated configuration as the Prandtl number drops with rising temperature to a minimum directly at the heated wall of $Pr_w = 1.75$. Hence, the wall-normal discretisation of the thermal boundary layer is finer than required. A further change with respect to the source grid $G^a_{\Delta x}$ is, that for block B_2 a slight stretching in y-direction is applied, whereas B_3 keeps a uniform distribution. The final production mesh is shown in figure 3.4 and its numerical parameters listed in table 3.4. Both the parameters for the adiabatic periodic section D_{per} and the heated section D_{heat} are included, for which the results at the finer resolved lower wall $y = y_{min}$ and the coarser resolved upper wall $y = y_{max}$ are listed due to the grid asymmetry. The temporally and spatially averaged results for τ_w and l^+_ν are based on streamwise averaging over the whole periodic domain for D_{per} and the last $7.5 \cdot d_h$ of D_{heat}, respectively.

In figure 3.6 the velocity and Reynolds stress profiles for the production mesh and the symmetric source grid $G^a_{\Delta x}$ are shown for the adiabatic domain D_{per}. Due to the asymmetry both upper and the finer resolved lower wall profiles are included. The velocity profiles coincide over a wide range except for the outer layer of the TBL, and the wall shear stresses show only a minor difference. In the Reynolds stress profiles, specifically in $\overline{u'u'}$ and less pronounced in $\overline{w'w'}$, a downwards shift for the lower wall profiles is visible due to the better grid resolution. Also the $\overline{u'u'}$-maximum shifts to a smaller y^+-value. The wall-normal resolutions of the production mesh are such, that it possesses 13 cells until the streamwise Reynolds stress maximum at the lower $y = y_{min}$ wall centre, which reduces to 11 with heating applied. At the upper $y = y_{max}$ wall centre it has 9 cells and at the large sidewall centres it has 8 cells until the $\overline{u'u'}$-maximum. The dimensionless

	$N_x \times N_y \times N_z$	$\Delta x^+ \times \Delta y^+_{min} \times \Delta z^+_{min}$	$\frac{\Delta y_{max}}{\Delta y_{min}} \times \frac{\Delta z_{max}}{\Delta z_{min}}$	$\gamma_y \times \gamma_z$	$\tau_w\|_y$
$D_{per}\|_{y_{min}}$	$576 \times 501 \times 141$	$62.7 \times 0.73 \times 1.42$	33.2×27.3	2.46×2.37	54.3
$D_{per}\|_{y_{max}}$	$576 \times 501 \times 141$	$62.9 \times 1.24 \times 1.42$	24.2×27.3	2.30×2.37	54.7
$D_{heat}\|_{y_{min}}$	$4740 \times 501 \times 141$	$94.5 \times 1.09 \times 1.42$	33.2×27.3	2.46×2.37	46.8
$D_{heat}\|_{y_{max}}$	$4740 \times 501 \times 141$	$62.8 \times 1.24 \times 1.42$	24.2×27.3	2.30×2.37	54.1

Table 3.4: Production mesh parameters and resulting wall shear stresses $\tau_w|_y$ in [Pa]. Additionally $\tau_w|_z = 69.9\,\text{Pa}$ for D_{per} and $\tau_w|_z = 68.9\,\text{Pa}$ for D_{heat}.

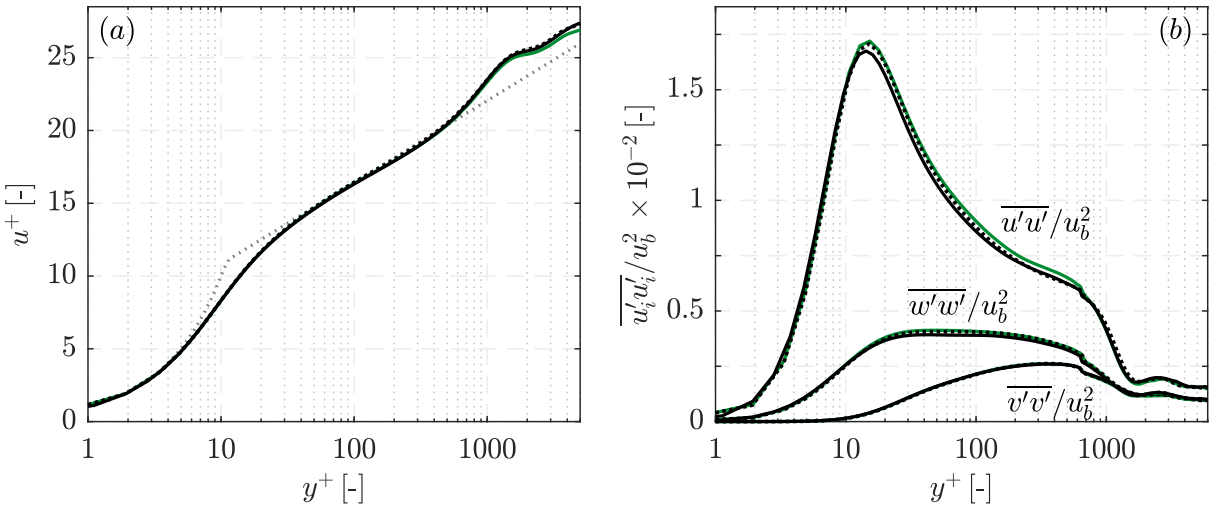

Figure 3.6: Production mesh results based on D_{per}: (a) shows the temporally and spatially averaged dimensionless velocity profile and (b) the likewise averaged Reynolds stress profiles along the duct midplane $z = 0$ for the lower wall TBL (——) and the upper wall TBL (·····). (——) denotes the symmetric $G^a_{\Delta x}$ from the sensitivity study. The analytical law of the wall ($u^+ = 1/0.41 \cdot \ln y^+ + 5.2$) is represented by (·····). See table 3.4 for further reference.

wall distance values of table 3.4 show, that the production mesh result can be considered as a well-resolved LES. Especially the heatable lower wall is well resolved with $\Delta y^+_{min} = 0.73$ in D_{per} and $\Delta y^+_{min} = 1.09$ in the heated section. It has to be noted, that the Δy^+_{min}- and Δz^+_{min}-values are based on the entire cell height of the respective first cell, whereas the flow variables are located and evaluated at the cell centre. i.e. at half cell height. Hence, the dimensionless cell heights at the variable storage location are $\Delta z^+_{min} = 0.71$ and $\Delta y^+_{min} = 0.37$, respectively $\Delta y^+_{min} = 0.55$, in a finite difference sense.

3.3.2 Comparison against Square Duct DNS

In order to assess the numerical accuracy of the well-resolved LES performed with the flow solver INCA, a comparison with DNS data by Pirozzoli et al. (2018) for an adiabatic square duct configuration at a Reynolds number of $Re_b = 40 \cdot 10^3$ and $Re_\tau = 1055$ is conducted. To the author's knowledge the so-called case D is currently the duct flow DNS with the highest

	$N_x \times N_y \times N_z$	$\Delta x^+ \times \Delta y^+_{min} \times \Delta z^+_{min}$	$\frac{\Delta y_{max}}{\Delta y_{min}} \times \frac{\Delta z_{max}}{\Delta z_{min}}$	$\frac{1}{2} Re_{\tau,c}$	$l^+_{\nu,c}$ [µm]
LES	$250 \times 136 \times 136$	$65.33 \times 1.06 \times 1.06$	23.41×23.41	1089	9.2
DNS	$2048 \times 512 \times 512$	$9.76 \times 0.61 \times 0.62$	10.67×10.67	1073	9.3

Table 3.5: Main grid and flow parameters for the square duct LES-DNS comparison (incompressible flow solver INCA) at $Re_b = 40 \cdot 10^3$. The streamwise box length for the DNS is larger with $6\pi h$ compared to the LES with $L_{x,per} = 15h$. $Re_{\tau,c}$ is halved following the square duct definition by Pirozzoli et al. (2018).

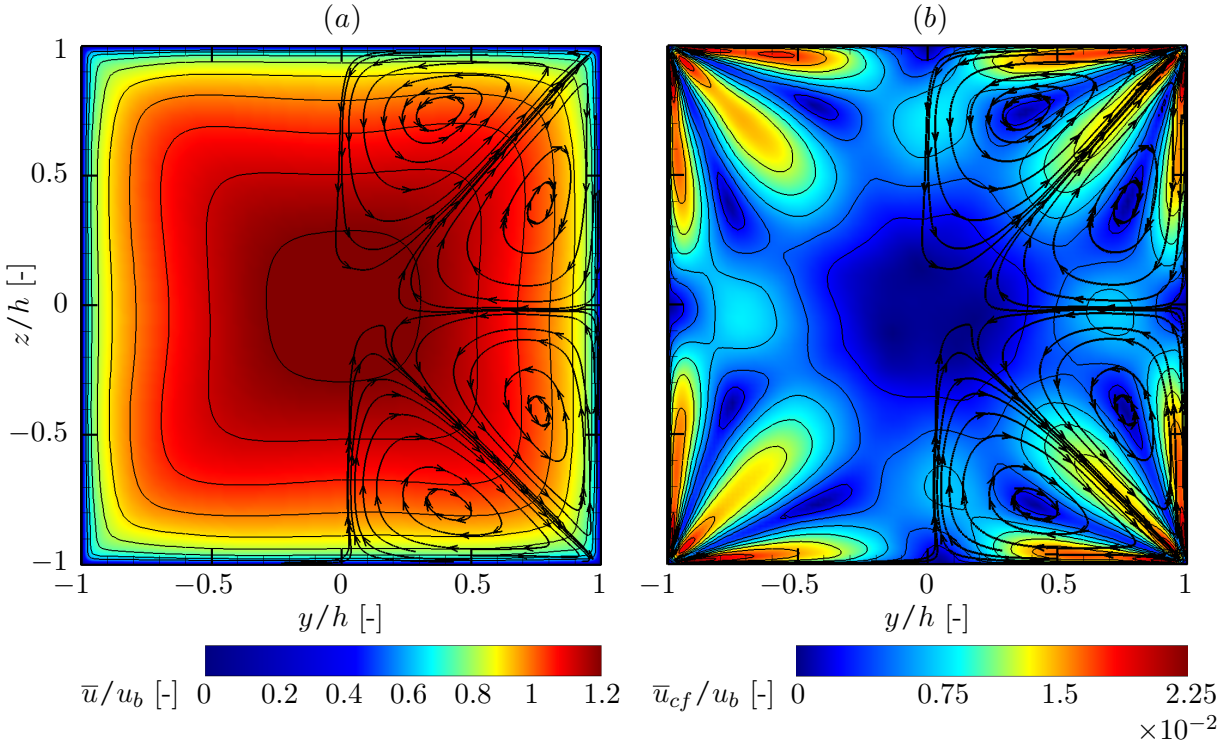

Figure 3.7: Adiabatic square duct flow field for the incompressible LES using INCA: (a) mean streamwise velocity distribution and (b) mean cross-sectional velocity distribution. The contour lines for $\overline{u}/u_b$ are drawn from 0.6 to 1.2 in steps of 0.075 and for $\overline{u}_{cf}/u_b$ from $0.25 \cdot 10^{-2}$ to $2.25 \cdot 10^{-2}$ in steps of $0.25 \cdot 10^{-2}$.

Reynolds number and accuracy available in the literature. For HARCD configurations only data at significantly lower Reynolds numbers is available.

The grid resolution for the square duct LES is chosen similar to that of the HARCD mesh as defined in section 3.3.1, i.e. comparable Δx^+, Δy^+ and Δz^+ are employed, see table 3.5 for further details. The length of the periodic simulation domain is set to the HARCD simulation value of $L_{x,per} = 7.5\, d_h$. The initialisation and simulation procedure follows that of the adiabatic precursor simulation domain as presented in section 3.2. Likewise liquid water at $T_b = 333.15$ K is used as fluid. For the flow statistics a temporal averaging over 200 FTT is performed followed by a spatial averaging in the homogeneous streamwise direction.

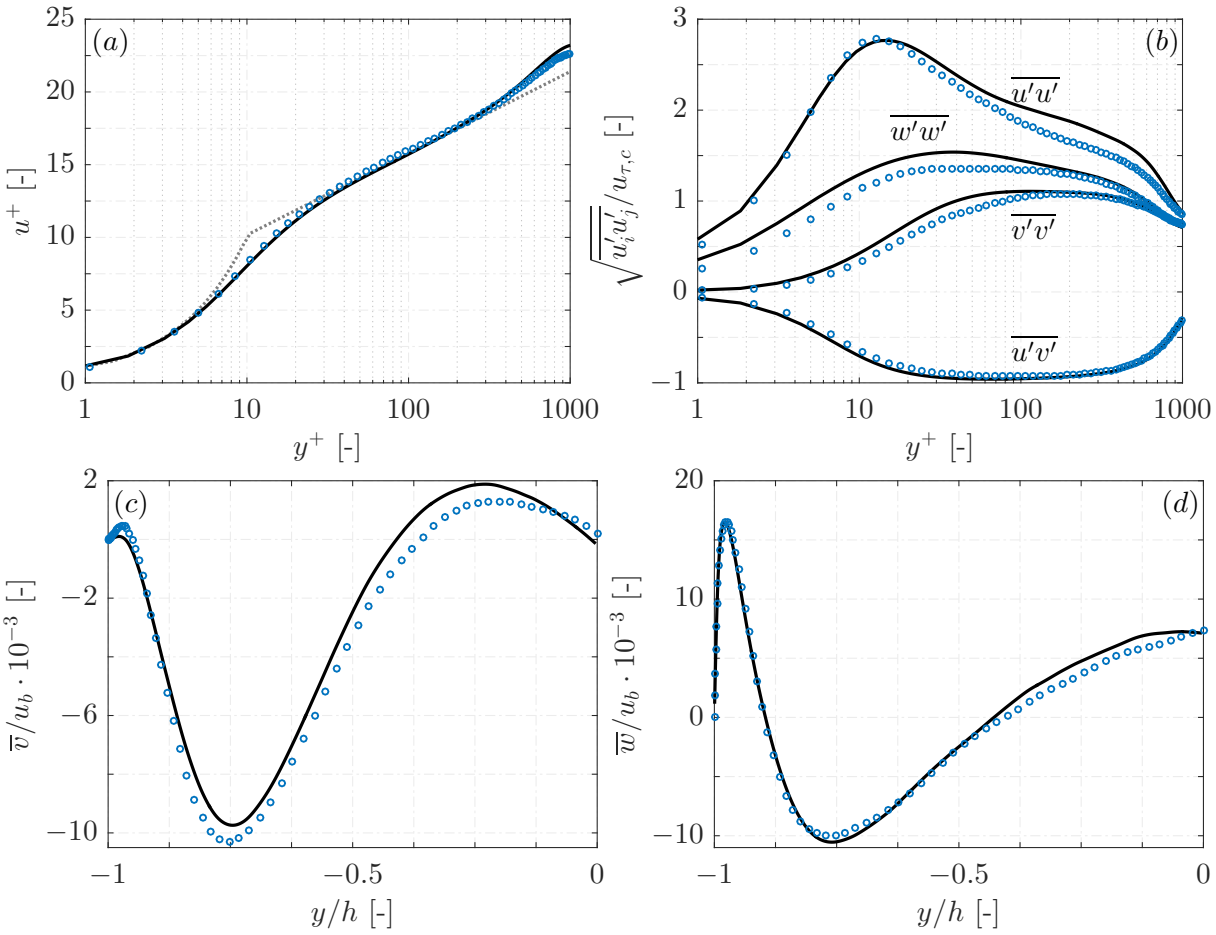

Figure 3.8: Comparison of the periodic adiabatic square duct incompressible LES using INCA (○) with DNS (——) results by Pirozzoli et al. (2018): (a) mean streamwise velocity and (b) Reynolds stress profiles along the duct midplane $z = 0$, and (c, d) cross-sectional velocity components of the secondary flow along $z/h = 0.75$. The analytical law of the wall (·····) in (a) is defined as $u^+ = 1/0.41 \cdot \ln y^+ + 4.55$.

The integral results for $Re_{\tau,c}$ and $l^+_{\nu,c}$ are in good agreement with the DNS data by Pirozzoli et al. (2018), see table 3.5. The index c denotes the wall centre value at $z = 0$. Figure 3.7 shows the mean streamwise and cross-flow velocity $\overline{u}_{cf} = \sqrt{\overline{v}^2 + \overline{w}^2}$ as well as the two pairs of counter-rotating corner vortices in the right duct half. The symmetry of the flow field and turbulence-induced vortices indicates the statistical convergence of the LES. Also the secondary flow strength is in good agreement ranging from $0 - 2.25 \cdot 10^{-2} \cdot u_b$ in the LES and from $0 - 2.11 \cdot 10^{-2} \cdot u_b$ in the DNS. Figure 3.8 compares the LES with the DNS flow field exemplarily along specific line cuts. The streamwise velocity and Reynolds stresses are normed by the wall centre friction velocity $u_{\tau,c}$, and the cross-sectional velocity components by the bulk flow velocity u_b. For the midplane profiles in figure 3.8 (a, b) an overall good agreement is observable, especially for the streamwise velocity. The LES $\overline{u'u'}$-profiles follow the DNS results closely in the near-wall region, whereas streamwise turbulence intensity is underestimated in the

logarithmic and wake region of the TBL. In contrast to that, the Reynolds stress components $\overline{u'v'}$, $\overline{v'v'}$ and $\overline{w'w'}$ show a slight underestimation up to $y^+ \approx 100$ and follow the DNS profiles well in the remaining outer part of the TBL. Overall, the turbulence levels in the logarithmic region of the TBL are slightly underpredicted compared to the DNS, which can be expected due to the coarser LES resolution. The cross-sectional velocity components in figure 3.8 (c, d) follow the DNS profiles closely indicating a sufficient grid resolution for the investigation of turbulence-induced secondary flow.

3.4 Experimental-numerical Data Comparison and Enhancement of the Experiment

Within this section the LES HARCD velocity field is compared against the experimental PTV and PIV results. Initially, this comparison is performed with the published experimental results of the first production measurement campaign (Rochlitz and Scholz, 2015; Rochlitz et al., 2015; Rochlitz and Scholz, 2018). Based on the deviations in the numerical-experimental comparison and a sensitivity analysis for experimental inaccuracies also using the LES results, recommendations have been derived for an enhancement of the experimental set-up in cooperation with the experimental investigators from the Technical University of Braunschweig. Finally, an updated comparison of LES and PIV data is presented with yet unpublished results of the second production measurement campaign (state at the end of june 2021). A set-up description of the latter is given in Hötte et al. (2021).

Figure 3.9 depicts the comparison of the cross-sectional velocity fields for LES and PTV results of the first measurement campaign. The LES data is based on a temporal averaging over 20 FTT and a subsequent streamwise averaging over the FOV. An overall good qualitative agreement is observable with minor deviations. Regarding the $\overline{u}$-distribution, the duct core region experiences a higher velocity in the LES. In the centre the maximum streamwise velocity $(\overline{u}/u_b)_{max}$ is 1.83% higher. This overestimation originates from deviations in the experimental duct geometry caused by fabrication tolerances leading to a slightly wider duct. Furthermore, the PTV results show a higher flow field asymmetry as can be expected solely due to the heating applied at $y = y_{min}$. Following Rochlitz et al. (2015) this asymmetry is probably caused by a slight laser sheet misalignment and is analogously observable for the unheated measurements. The PTV quality for the secondary flow components is worse than for the streamwise velocity containing a substantial amount of noise, and thus only allows for a rough comparison. Figures 3.9 (b, c) illustrate, that the secondary flow vortices are represented at comparable size and strength, although the PTV $\overline{w}$-component is overestimated.

In the following, the LES results are compared with the PIV results from the first measurement campaign in the heated duct centre plane averaged over the FOV, denoted by the lines (·····) and (·····), see figure 3.10. This comparison has been previously presented in Kaller et al. (2019). The LES profiles are generated by a weighted averaging across the duct centre plane (here the y-axis) using the reported finite laser sheet thickness of $\Delta_{LS} \approx 1$mm to approximate the filter effect of the PIV technique. The weighting is performed by assuming a Gaussian laser intensity distribution. Additionally, an aspect ratio compensation is introduced due to slight deviations

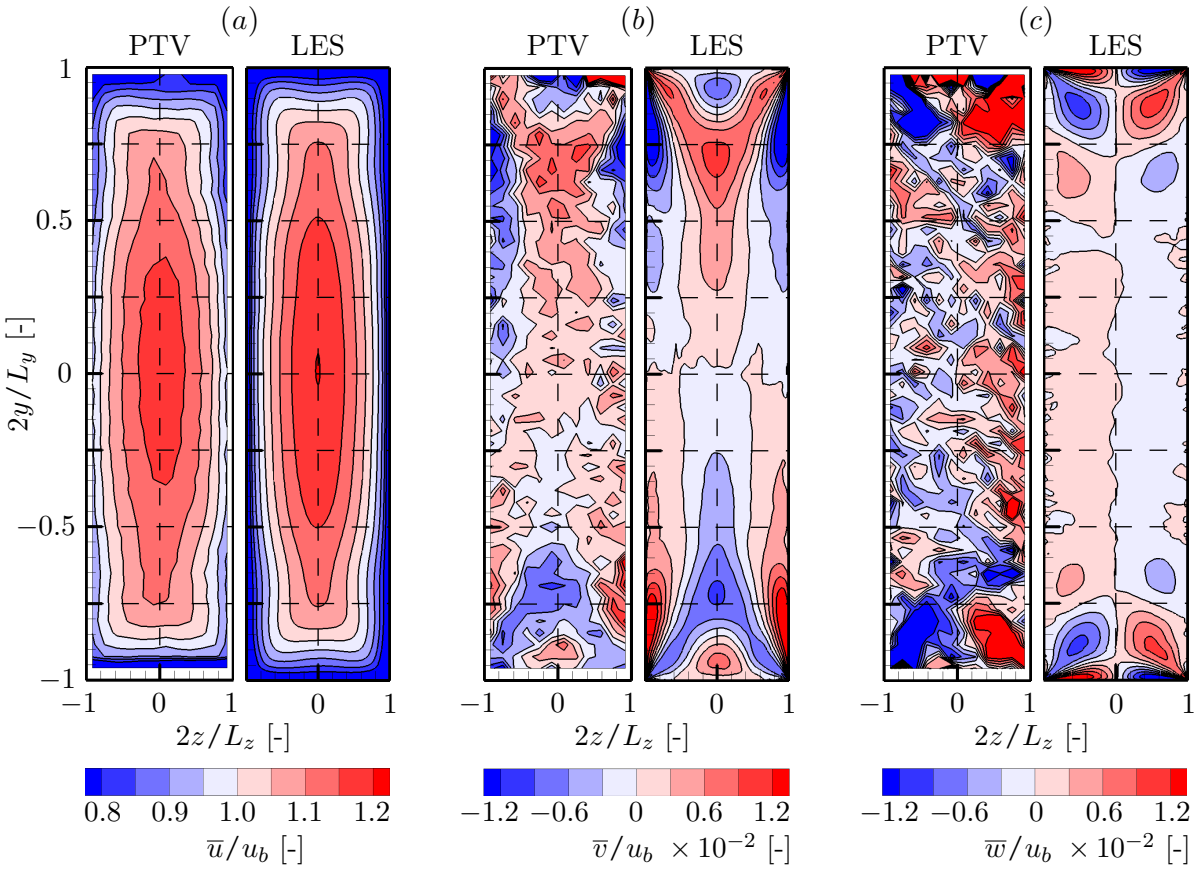

Figure 3.9: Comparison of (a) streamwise and (b, c) secondary flow velocity distribution in the heated duct cross-section averaged over the FOV, see figure 3.1 for reference. The heated wall is at $y = y_{min}$. Experimental PTV data in the vicinity of the walls is cut off due to reflections.

in the duct geometries caused by production tolerances. Thus, the LES data is rescaled by $y = y_{LES} \cdot (AR_{exp}/AR_{LES})$. Both postprocessing techniques are discussed in more detail in a subsequent paragraph.

Figure 3.10 (a) shows a very good agreement of the streamwise velocity in the vicinity of the walls until $2y/L_y \approx \pm 0.75$. The bottom wall shoulder section from -0.75 to -0.6 is in good agreement with the experimental data, whereas at the upper wall larger deviations are present due to the PIV asymmetry. In the duct centre the PIV $\overline{u}$-level is underestimated as already observed in the comparison of PTV and LES due to the wider cross-section of the experimental HARCD. Compared to the PIV results, for the LES $(\overline{u}/u_b)_{max}$ is 1.71% higher. The secondary flow velocity profiles in figure 3.10 (b) agree well, especially with respect to the AR-compensated vortex locations indicated by the $\overline{v}$-minima and -maxima. The secondary flow strength, however, is overestimated in the LES. The Reynolds stress component $\overline{u'u'}$ depicted in figure 3.10 (c) shows consistently lower values for the LES profile compared to the PIV. This deviation is probably due to measurement noise. A similar offset is observable for the $\overline{v'v'}$-term in figure 3.10 (e). Towards the bottom wall the LES and PIV profiles coincide, whereas at the upper wall an

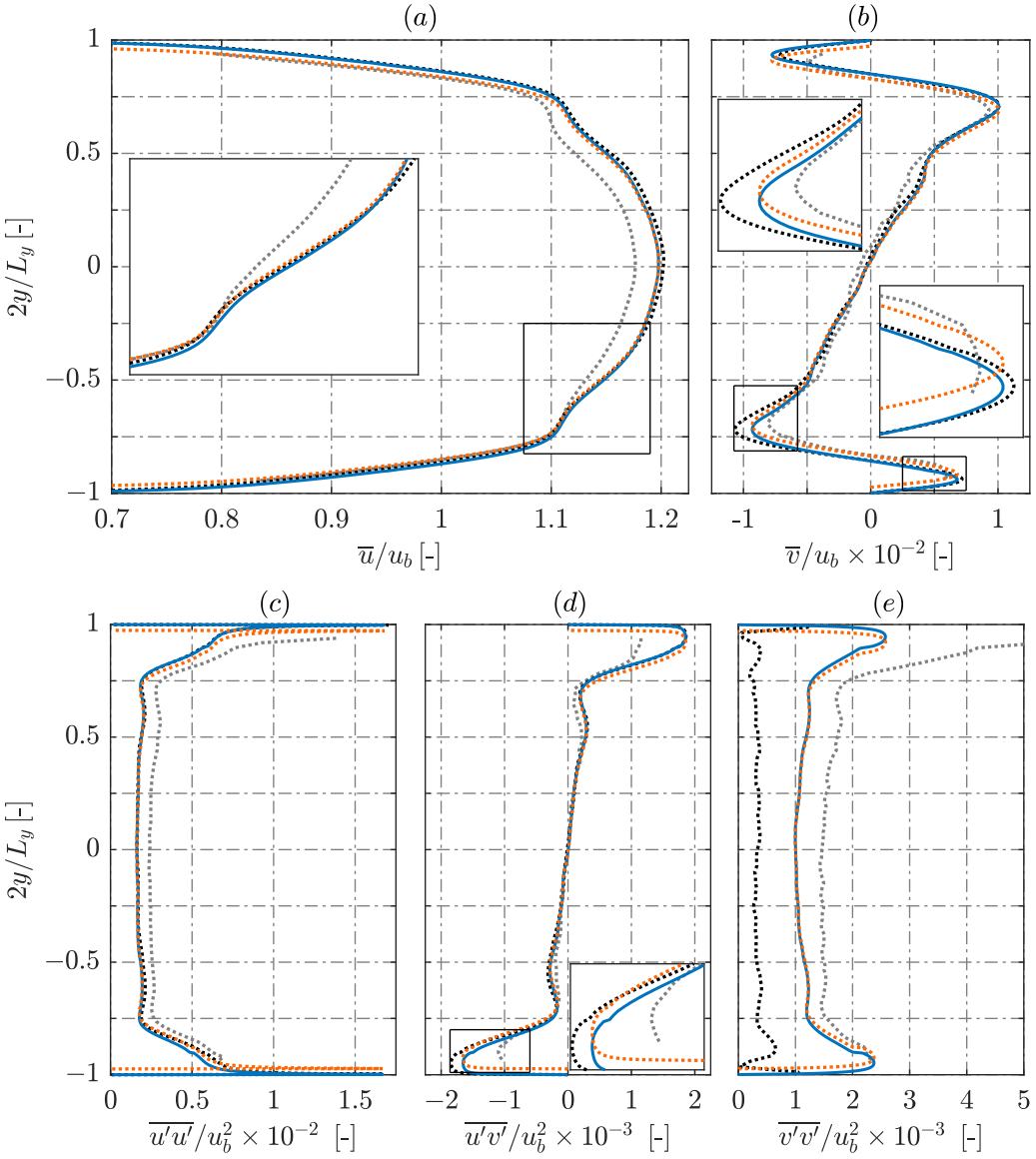

Figure 3.10: Comparison of experimental PIV and LES results for the heated HARCD averaged in streamwise direction over the FOV: (a) streamwise and (b) heated wall-normal velocity, and (c, d, e) Reynolds stress distributions along the duct centre plane. PIV data from the published first measurement campaign is shown as (·····) and from the second measurement campaign as (·····) with data taken from Günther et al. (2020). LES data modified by laser sheet averaging with $\Delta_{LS} = 1\,\text{mm}$ is marked by (——) and additionally modified by the aspect ratio compensation by (·····). All results are made dimensionless using their respective u_b and duct height L_y.

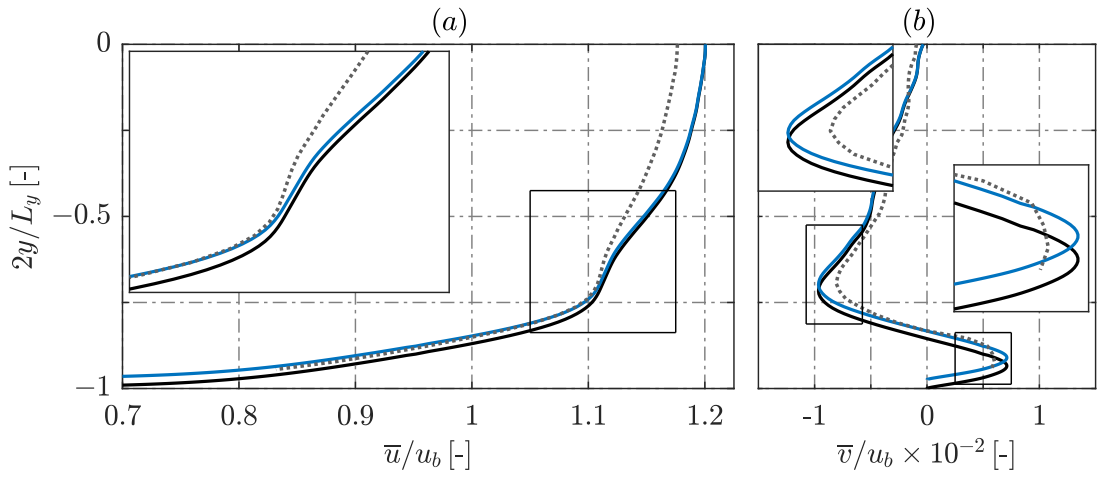

Figure 3.11: Influence of the aspect ratio normalisation on the (a) streamwise and (b) heatable wall-normal velocity in the heated duct centre plane averaged over the FOV. The finite laser sheet thickness is not taken into account. The experimental results of the first measurement campaign are denoted by (·····), the unmodified LES results by (——) and the normalised LES results by (——).

overshoot in the experimental data leads to large deviations. The $\overline{u'v'}$ profiles in figure 3.10 (d) match very well except in the vicinity of the walls, where the PIV underestimates the minimum at the lower wall and the maximum at the upper wall, respectively. As the duct core $\overline{u'u'}$- and $\overline{v'v'}$-profiles of the PIV are increased and no effect is visible for the cross-correlation $\overline{u'v'}$, the assumption can be made, that the random component of the measurement error is essentially uncorrelated Gaussian noise. Additionally, deviations in the vicinity of walls can be attributed to the typical PIV problem of spurious reflections and low seeding density in these regions.

Rochlitz et al. (2015) reported, that the experimental results exhibit uncertainties with respect to laser sheet misalignment and effective laser sheet thickness. The latter might be larger than the stated $\Delta_{LS} = 1\,\text{mm}$. Furthermore, geometrical deviations are present. Using the LES results, we investigate the influence and sensitivity of these uncertainties on the flow field:

- Duct geometry: the experimental duct cross-section has a slightly different geometry than the numerical one due to fabrication tolerances leading to a reduction of the aspect ratio from $AR_{LES} = 4.30$ to $AR_{exp} = 4.19$. The HARCD aspect ratio strongly influences the characteristic formation of the corner vortices and hence impacts the secondary and consequently also the main flow field, see for example Vinuesa et al. (2014). Especially the locations of the $\overline{v}$-velocity peaks and the resulting shoulders in the $\overline{u}$-profile are hereby defined. To account for small variations in the aspect ratio, an AR-compensation can be introduced in the form $y_{LES,AR} = y_{LES} \cdot (AR_{exp}/AR_{LES})$. The effect of this normalisation is shown in figure 3.11. The compression of the LES y-axis leads to an improved agreement of the $\overline{v}$-velocity peak locations and the $\overline{u}$-profile towards the walls. The duct centre profiles as well as the velocity levels remain unaffected.

- Laser sheet thickness Δ_{LS}: the influence of Δ_{LS} on the flow field results is presented in

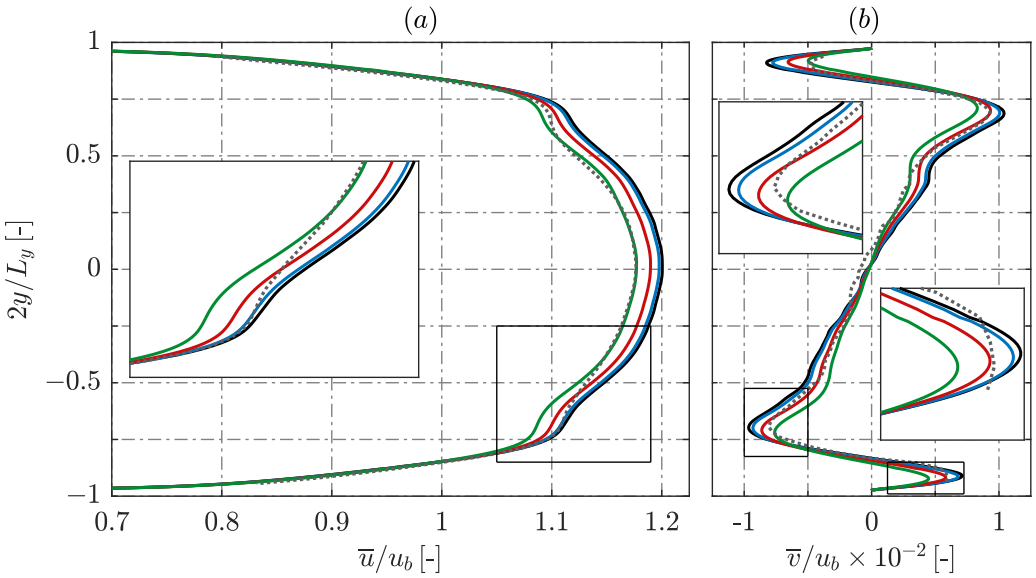

Figure 3.12: Influence of the finite laser sheet thickness on the (a) streamwise and (b) heatable wall-normal velocity in the heated duct centre plane averaged over the FOV. The experimental results are denoted by (·····), and the LES results by (——) for $\Delta_{LS} = 0\,\text{mm}$, (——) for $\Delta_{LS} = 1\,\text{mm}$, (——) for $\Delta_{LS} = 2\,\text{mm}$ and (——) for $\Delta_{LS} = 3\,\text{mm}$.

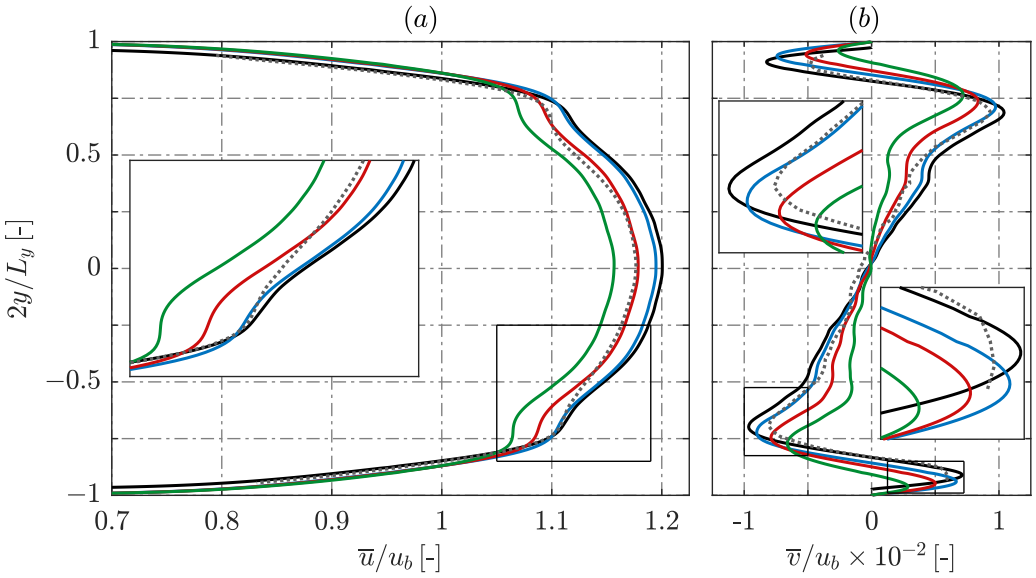

Figure 3.13: Influence of laser sheet misalignment on the (a) streamwise and (b) heatable wall-normal velocity in the heated duct centre plane averaged over the FOV. The experimental results are denoted by (·····), and the LES results by (——) for $MA_{LS} = 0\,\text{mm}$, (——) for $MA_{LS} = 0.25\,\text{mm}$, (——) for $MA_{LS} = 0.667\,\text{mm}$ and (——) for $MA_{LS} = 1\,\text{mm}$. The laser sheet thickness is set to $\Delta_{LS} = 1\,\text{mm}$ for all cases.

figure 3.12. Based on the LES cross-sectional flow field a weighted averaging across the centre line $z = 0$ is performed assuming a Gaussian laser intensity distribution. As already mentioned, this method is used to approximate the filter effect of the PIV technique. Increasing Δ_{LS} leads to a reduction of $\overline{u}$- and $\overline{v}$-velocity levels as well as a shift of the $\overline{v}$-peak locations towards the walls.

- Laser sheet misalignment MA_{LS}: the influence of MA_{LS} on the flow field results is presented in figure 3.13. Any misalignment along the FOV is treated as an average offset of the laser sheet z-position with respect to the duct centre $z = 0$. Hence, the previously mentioned Gaussian weighting function utilised on the LES cross-sectional flow field is shifted from the centre by MA_{LS} to the off-centre position. The MA_{LS}-effects are analogous to the ones observed varying Δ_{LS}, i.e. velocity levels are reduced and the $\overline{v}$-peak locations shifted towards the walls.

This sensitivity analysis shows that the agreement of PIV and LES data can be improved by taking a slight misalignment and an effective laser sheet thickness larger than 1mm into account.

During the third funding period of the SFB-TRR40, the experimental setup has been modified to additionally study the effects of wall roughness on the flow field and turbulent heat transfer. Modifications with respect to the first measurement campaign, partly supported by the findings of the LES and additional RANS simulations, include:

- Heat nozzle tip: the tip of the heat nozzle, i.e. the heatable HARCD wall is now exchangeable with each tip exhibiting a different wall roughness.

- Wall heating: the comparison of the LES temperature field and experimental data has shown significant deviations leading to the conclusion, that the wall-temperature is not uniform as assumed and lower than $T_W = 100°\mathrm{C}$. Hence, the installation of the temperature sensors as well as the regulation of the copper block heating has been improved to ensure a more uniform and constant wall temperature of $T_W = 100°\mathrm{C}$, respectively $T_W = 373.15\,\mathrm{K}$.

- Production accuracy: as the secondary flow vortices in HARCDs are highly sensitive to the duct geometry, the manufacturing accuracy is increased to reduce deviations in the cross-sectional geometry and geometrical variations in streamwise direction.

- Calibration accuracy: as figure 3.13 shows the high sensitivity of the flow profile to a measurement plane off-centre shift, the calibration procedure accuracy has been improved.

- Laser light source: the laser light sheet is not spanned any more from above, but from the downstream end of the test section to reduce reflections from the wall and obtain a higher quality flow profile towards the heated wall. The experimental set-up has been modified accordingly. With this configuration no curved duct piece can be added after the straight test section as in the first measurement campaign.

- Modified effective laser sheet thickness: as figure 3.12 shows, Δ_{LS} has a significant impact on the resulting flow field. The measurement accuracy of $\Delta_{LS}|_{nominal}$ for the dry state, i.e. no water flows through the set-up, is improved to ensure $\Delta_{LS}|_{nominal} = 1\,\mathrm{mm}$. Furthermore,

based on the PIV-LES-comparison it has been found, that an artificial broadening of the laser light sheet under operating conditions occurs. Light illuminating a particle within the boundaries of $\Delta_{LS}|_{nominal}$ leads to randomly directed reflections. This reflected light can illuminate particles outside of $\Delta_{LS}|_{nominal}$ leading to an increased $\Delta_{LS}|_{effective}$. The signal intensity is strongest in the centre of $\Delta_{LS}|_{effective}$ and becomes weaker towards the lateral sidewalls. During the postprocessing of the PIV raw data an intensity threshold can be defined determining which signal intensity is sufficient to be used in the correlation process to obtain the velocity field. This threshold value implicitly defines $\Delta_{LS}|_{effective}$. To determine the intensity threshold the LES $\overline{u}$-profile is utilised such, that the intensity threshold is defined as the value leading to an optimal match between PIV and LES $\overline{u}$-profile. To check the validity of the thus implicitly determined $\Delta_{LS}|_{effective}$, the comparison of PIV and LES for the secondary flow and Reynolds stresses can be used.

Figure 3.10 also includes a comparison of the LES with the yet unpublished PIV results from the second measurement campaign. As the HARCD geometry is identical for this comparison, no *AR*-compensation is applied to the LES data. For the following discussion the distributions of LES (——) and PIV (·····) are compared. The streamwise velocity profile in (a) shows the expected significant improvement of the PIV data, which is now slightly overestimated by $(\overline{u}/u_b)_{max} = 0.33\%$ in the duct centre with respect to the LES. Towards the upper wall a perfect match is observable and towards the lower wall a minor deviation is present. This deviation coincides with a slight overestimation of the $\overline{v}$-profile extrema, i.e. the secondary flow strength. At the unheated upper wall the secondary flow minimum and maximum match perfectly in strength and location. For the Reynolds stresses a similar trend is observable with the previously present deviations between LES and the PIV of the first measurement campaign being significantly reduced. The PIV $\overline{u'u'}$-distribution almost coincides with the LES and only a small deviation is visible towards the lower heated wall. The same applies to the $\overline{u'v'}$-profile. In contrast, the PIV $\overline{v'v'}$-profile is noticeably underestimated, the reasons being under investigation. Overall a significant improvement of the PIV results from the first to the second measurement campaign with respect to the LES data is visible.

3.5 Discussion of the Flow Field

In the following, we analyse the turbulent heat transfer in the asymmetrically heated water HARCD based on the LES results generated with the flow solver INCA. The section is separated into six subsections: in 3.5.1 the adiabatic and heated HARCD flow fields are discussed also comprising the influence of the wall heating on secondary flow and TBL profiles, and in subsection 3.5.2 streamwise vorticity and the terms of its balance equation are analysed to highlight heating-induced changes in the turbulence-induced secondary flow. The behaviour of turbulent sweeping and ejections motions, the latter as dominant turbulent mechanism for the generation of Prandtl's flow of the second kind, are investigated in 3.5.3. In subsection 3.5.4 the turbulent heat transfer is discussed with a special focus on Nusselt and turbulent Prandtl number distributions along the duct length as well as the applicability of the unity Pr_t assumption often employed in RANS turbulence modelling. The result section closes by analysing the heating-induced modulation of

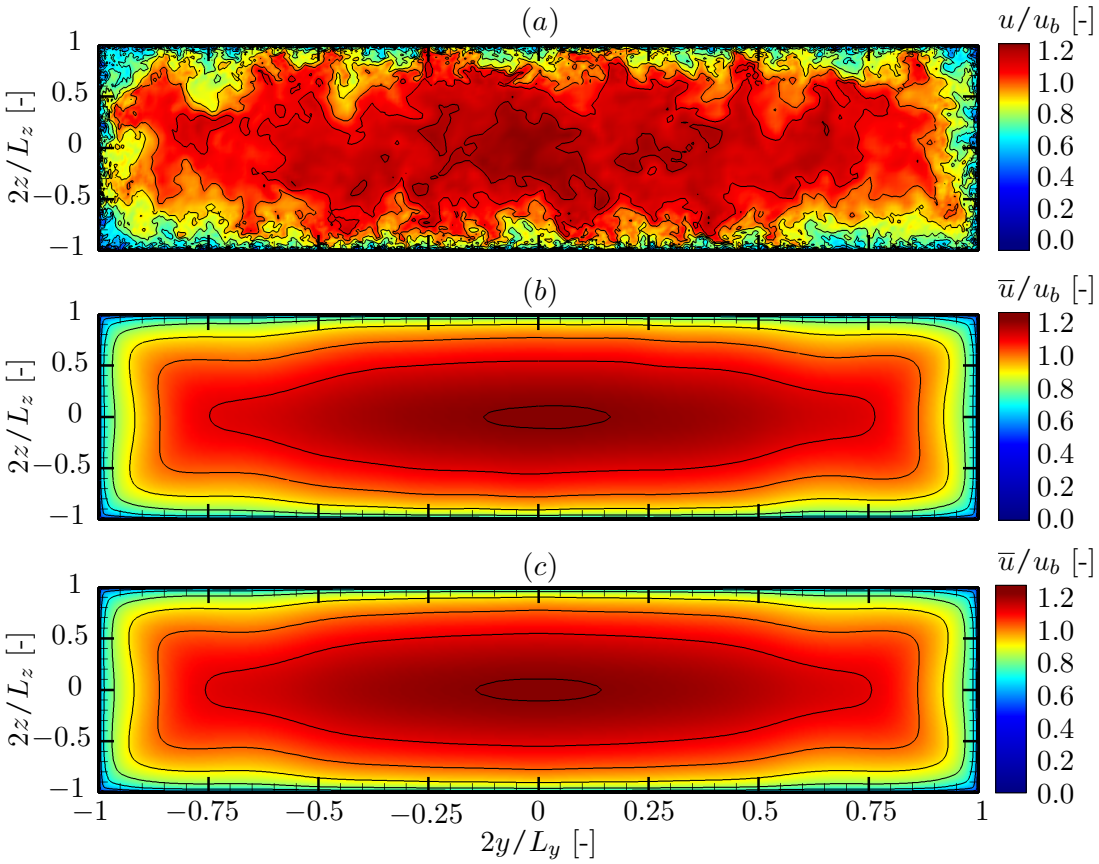

Figure 3.14: Cross-sectional streamwise flow field of the adiabatic duct with (a) distribution of instantaneous streamwise velocity, (b) mean streamwise velocity and (c) mean streamwise velocity with additional averaging of the four quadrants. Contour lines are drawn in steps of 0.1.

turbulence anisotropy in the HARCD cross-section in subsection 3.5.5 and studying the variation of turbulent length scales in 3.5.6.

3.5.1 Mean Flow Field of the Adiabatic and Heated Duct

The main focus of this section lies on investigating the differences of the adiabatic and the heated straight duct flow field, i.e. on the influence of the wall heating along the duct. Due to the heating, the temperature in the vicinity of the lower wall increases with streamwise distance, reducing the local viscosity, which may drop up to $\nu(T = T_w) = 0.62 \cdot \nu(T = T_b)$.

Figure 3.14 displays the cross-sectional streamwise flow field for the adiabatic duct with an instantaneous snapshot in (a), the temporally mean solution in (b) and a quadrant-averaged mean solution in (c). The instantaneous velocity field shows the highly turbulent flow with the highest velocities in the duct core and smaller low-velocity structures along the sidewalls and in the duct corner regions. To obtain the mean solution a temporal averaging over 164 FTT with respect to the periodic section length at a constant sampling rate of $\Delta t_{sample} = 0.025 \cdot d_h/u_b$ is performed resulting in $\approx 50 \cdot 10^3$ snapshots. Additionally, a subsequent spatial averaging is

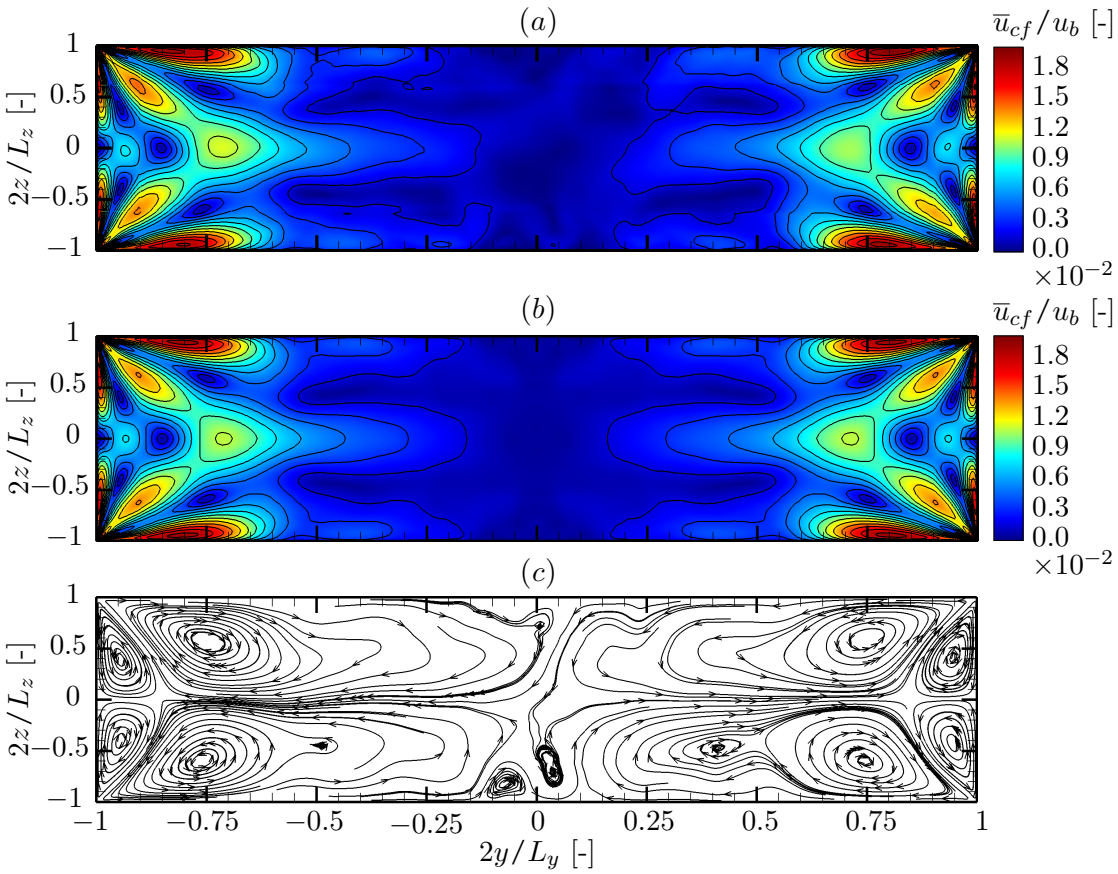

Figure 3.15: Cross-sectional secondary flow field of the adiabatic duct with (a) distribution of mean cross-flow velocity magnitude $\overline{u}_{cf} = \sqrt{\overline{v}^2 + \overline{w}^2}$, (b) mean cross-flow velocity magnitude $\overline{u}_{cf}$ with an additional averaging of the four quadrants and (c) counter-rotating corner vortex system represented by streamlines. Contour lines are drawn in steps of $0.15 \cdot 10^{-2}$.

applied in streamwise direction. In order to reduce the sample number required for a statistically convergent result the duct symmetry is exploited by a further averaging over the four quadrants. As Vinuesa et al. (2014) pointed out, the number of required samples is not reduced by a factor of four as the flow in the quadrants is not independent. In particular, the corner vortices in the vicinity of the short sidewalls are strongly correlated. To assess the convergence we utilise the symmetry of the flow field as a measure. Comparing figures 3.14 (b) and (c) shows qualitatively, that the streamwise velocity field is sufficiently converged as hardly any difference is visible. This is supported by the quantitative measure of the L2 norm of the streamwise velocity deviation between the not quadrant-averaged and the quadrant-averaged result, which reaches 0.5% in the yz-plane.

Figure 3.15 depicts the secondary flow field represented by the cross-flow velocity magnitude $\overline{u}_{cf} = \sqrt{\overline{v}^2 + \overline{w}^2}$ and streamlines for visualisation of the vortex structures. Generally, the convergence rate of the turbulence-induced secondary flow is slower than that of the streamwise velocity. The comparison with the quadrant-averaged solution, figures 3.15 (a) and (b), shows

that the result is not yet perfectly converged as the secondary flow field is slightly asymmetric. The deviation from the symmetric state is higher than for the streamwise velocity, although sufficiently small. One reason for the larger deviation is the presence of very weak vortices in the duct centre visible in figure 3.15 (c), which persist over very long averaging times. Such a formation of an array of secondary vortices along the long sidewalls of HARCDs has also been reported previously by Vinuesa et al. (2014).

The temperature boundary layer developing along the lower heated wall of the HARCD is strongly affected by secondary flow structures. Figure 3.15 (c) shows the counter-rotating vortex pairs forming in each of the duct corners. In the upper left quadrant ($y < 0$, $z > 0$), a small counter-clockwise (CCW) rotating vortex forms along the short sidewall and a large clockwise (CW) rotating vortex along the long sidewall (mirror-inverted for the opposite half of the duct). Each vortex extends to the respective symmetry plane, where it encounters the neighbouring vortex from the opposite side. The vortex strength is relatively weak. The maximum cross-flow velocity for the adiabatic duct is $\overline{u}_{cf}/u_b = 1.93\%$, which lies within the $1-3\%$ range reported in the literature, see e.g. Salinas-Vásquez and Métais (2002). Figures 3.16 $(a-f)$ depict the streamwise development of the temperature boundary layer at different positions along the heated straight HARCD for the lower duct quarter. The thermal boundary layer thickness increases in streamwise direction due to conduction, turbulent mixing and through transport by the mean secondary flow. The latter is responsible for the characteristic bent shape of the temperature profile as indicated by the cross-sectional flow vectors. In the left half of the duct the CW vortex transports hot fluid away from the heated wall along the long sidewall into the duct core and cold fluid downwards along the centre line. The CCW vortex conveys hot fluid from the corner along the heated wall to its centre at $z = 0$ and then upwards along the symmetry line until it mixes with the cold fluid transported downwards. Both vortices push cold fluid into the left corner, whereby the flow vectors follow a slightly flatter path than the corners bisecting line.

Even though the temperature increase and the accompanying viscosity decrease are overall moderate, a significant weakening of the secondary flow strength in figures 3.16 $(g-l)$ is noticeable. This is especially highlighted in the right halves of each picture, where the difference of the $\overline{v}$-field with respect to the adiabatic case, $\Delta\overline{v} = \overline{v} - \overline{v}_{per}$, is depicted. We observe a significant reduction of the vortex strength. The upwards transport of hot fluid in the vicinity of the lateral wall is slowed down increasingly along the duct length. In the end cross-section the maximum $\Delta\overline{v}/u_b$ is $\approx -4 \cdot 10^{-3}$ with a velocity of $\overline{v}/u_b \approx 1.5 \cdot 10^{-2}$, which corresponds to a reduction of more than 25%. The corner vortex positions only change marginally and are consequently mainly defined by the duct geometry. The small CCW vortex centre moves from $(2y/L_y,\, 2z/L_z) = (-0.947,\, 0.414)$ for the adiabatic duct to $(-0.948,\, 0.394)$ for the heated duct end plane at position 600 mm, and the large CW vortex centre from $(-0.752,\, 0.569)$ to $(-0.763,\, 0.601)$. Hence, we observe for the large vortex a slight shift towards both sidewalls and for the small one a slight shift towards the midplane.

As the corner vortices are turbulence-induced secondary flow structures, we further analyse the influence of the reduced wall viscosity on the mean turbulence and velocity profiles in the vicinity of the heated wall. In figure 3.17, the influence of wall heating on the duct centre turbulent boundary layer is shown by comparing the spatially averaged solutions over the adiabatic domain D_{per} with the last $7.5\,d_h$ of the heated duct. Both sections show a good agreement with the

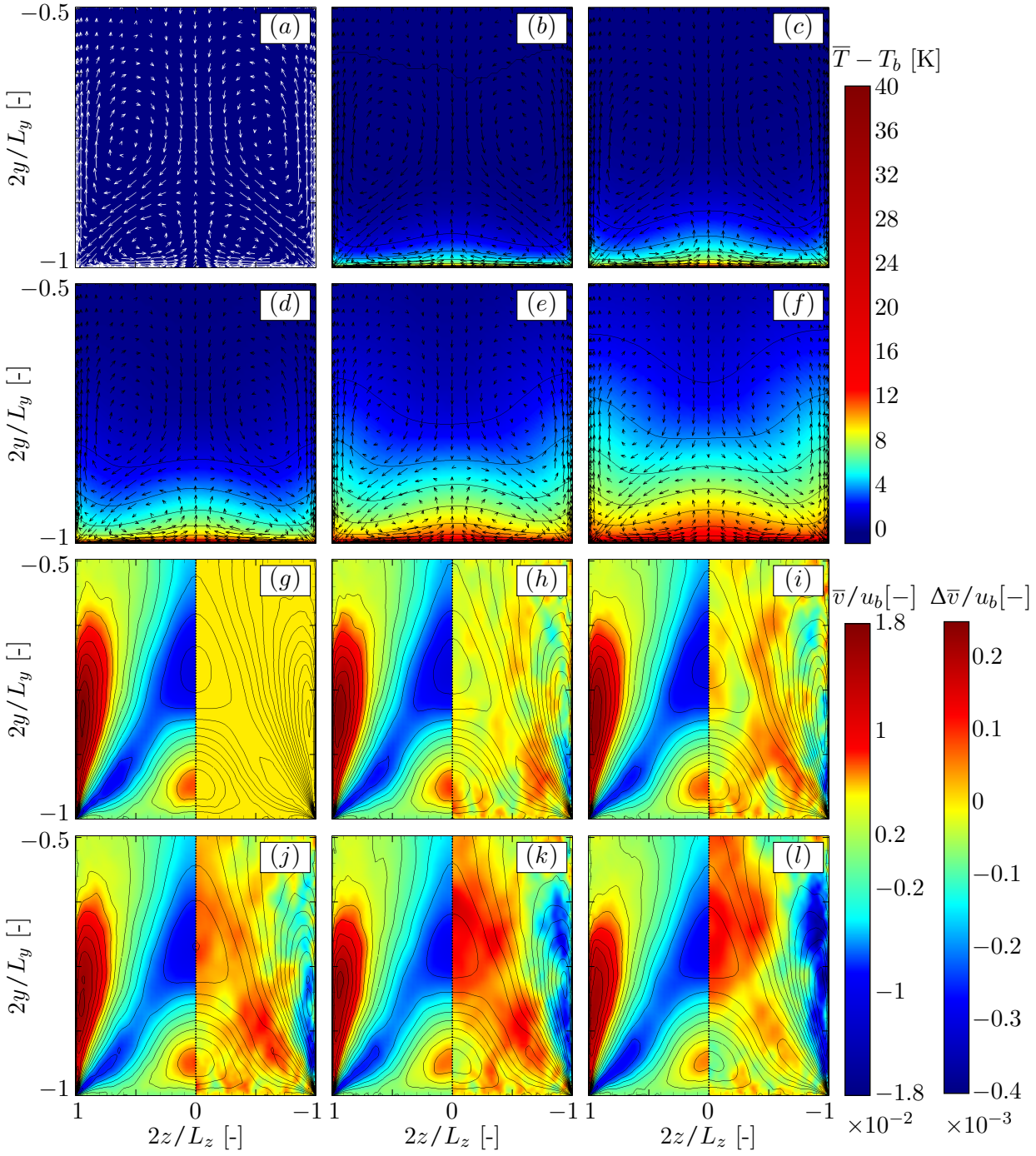

Figure 3.16: Development of cross-sectional $(a-f)$ temperature distribution and $(g-l)$ secondary flow velocity, exemplarily for the heated wall-normal component, in the lower duct quarter. The subfigures are taken for the (a, g) adiabatic duct and the heated duct at (b, h) 50 mm, (c, i) 100 mm, (d, j) 200 mm, (e, k) 400 mm and (f, l) 600 mm. In $(a-f)$ vectors are included to indicate the influence of the secondary flow and the $\overline{T}$ contour lines are drawn in steps of 2 K. In $(g-l)$ $\overline{v}$ is depicted on the left of the duct centre and on the right the change in $\overline{v}$ with respect to the unheated periodic duct is shown with $\Delta\overline{v} = \overline{v} - \overline{v}_{per}$. The contour lines are drawn in steps of $\overline{v}/u_b = 2 \cdot 10^{-3}$.

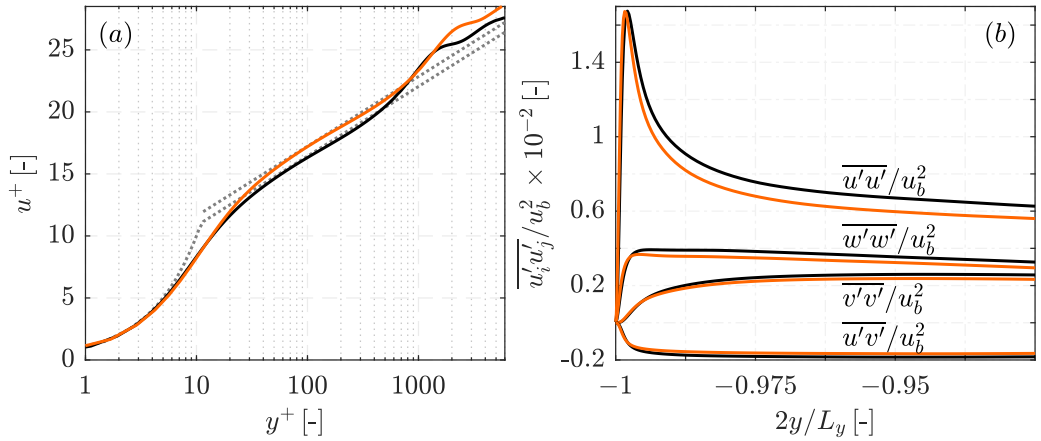

Figure 3.17: Distribution of (a) mean streamwise velocity and (b) Reynolds stresses along the duct midplane at $z = 0$ for the adiabatic (——) and the heated duct end section (——). The law of the wall ($u^+ = (1/0.41)\ln y^+ + 5.2$) is represented by (·····).

classical law of the wall velocity profile, i.e. for $y^+ \lessapprox 5$ in the viscous sublayer $u^+ = y^+$ and for $y^+ \gtrapprox 30$ in the log-law region $u^+ = 1/\kappa \cdot \ln y^+ + B$. Similarly as Lee et al. (2013), we observe in figure 3.17 (a) that the heating leads to an upward shift of the velocity profile in the log-law region changing the integration constant from $B = 5.2$ to $B = 6.0$ for the heated HARCD. The slope, i.e. the von Kármán constant remains unchanged at $\kappa = 0.41$. Figure 3.17 (b) depicts the change in the Reynolds stress profiles. The peak in $\overline{u'u'}$ shifts slightly towards the heated wall, whereas the maximum value remains unaltered. Similarly to Zonta et al. (2012), we observe that the turbulence intensities in all directions are reduced when heating is applied. Although counterintuitive, as one would expect an increase in turbulent fluctuations with lower viscosity, this observation is in agreement with previous studies showing that the heating of the fluid accompanied by a drop in viscosity has a stabilising effect on the boundary layer, see Lee et al. (2013) and Zonta et al. (2012).

In figures 3.18, 3.19 and 3.20 mean velocity, temperature and Reynolds stress distributions for three different spanwise z-locations are presented for the duct centre at $2z/L_z = 0$, at $2z/L_z = 0.5$ and at $2z/L_z = 0.9$. All figures compare the results for the adiabatic duct with those for the heated duct at 100 mm and 595 mm after the beginning of the heated section. For the adiabatic duct an additional streamwise averaging over the complete length $L_{x,per}$ and for the heated duct over an interval of 10 mm from −5 mm to +5 mm of the respective location is performed.

Comparing the first column of figure 3.18 from (a) to (c), representing the movement outwards from the duct centre towards the lateral wall, we observe for the adiabatic as well as the heated cases a broadening of the $\overline{u}$-profiles shoulder section, which is formed as a consequence of the corner vortex pair. The asymmetric heating applied to the duct leads to a mass flux redistribution. The flow in the lower quarter of the duct below $2y/L_y \approx -0.5$ is accelerated effecting a thickening of the near-wall profile. This behaviour is qualitatively consistent with previous channel flow and TBL studies by Sameen and Govindarajan (2007) and Lee et al. (2013). Moreover, the heated

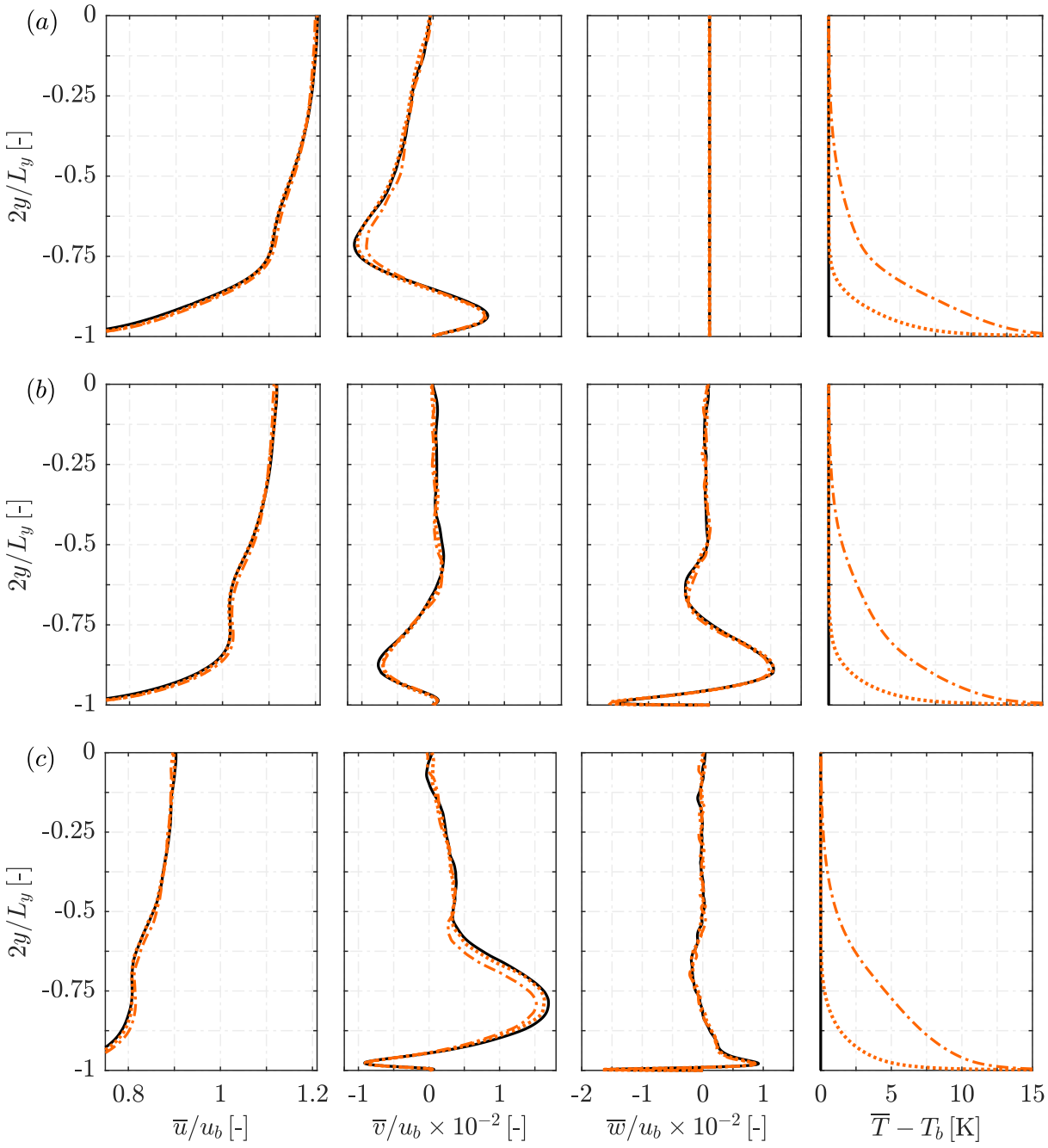

Figure 3.18: Distributions of mean velocity components and mean temperature increase along the heated wall-normal direction at spanwise positions of (a) $2z/L_z = 0$, (b) $2z/L_z = 0.5$ and (c) $2z/L_z = 0.9$ for the adiabatic duct (——), and the heated duct at streamwise positions of 100 mm (·····) and 595 mm (-·-·-) after the beginning of the heated section. Streamwise averaging is performed over 10 mm for the heated duct, respectively over $L_{x,per}$ for the periodic duct, and the y-symmetry is utilised.

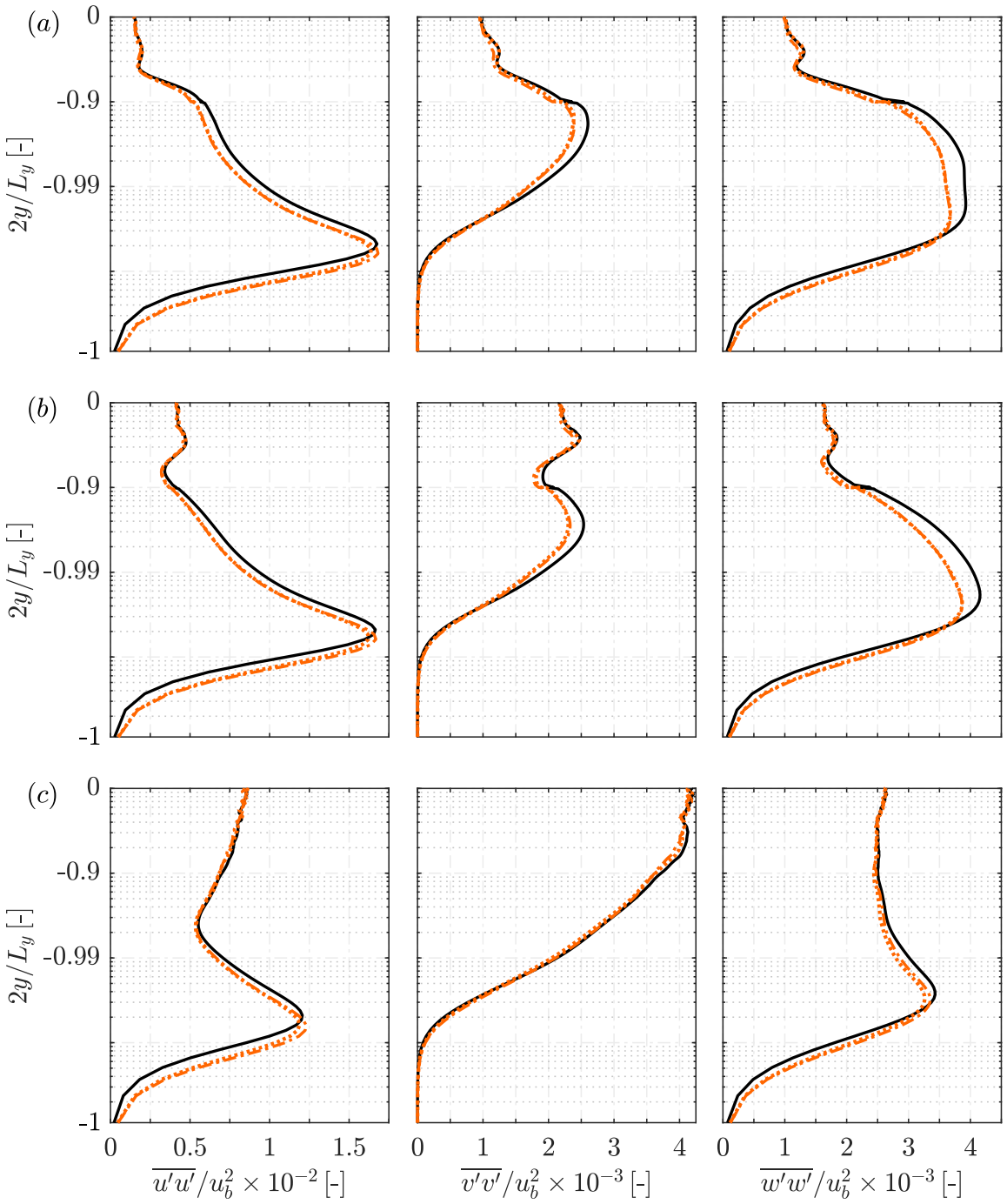

Figure 3.19: Distributions of diagonal components of the Reynolds stress tensor along the heated wall-normal direction at spanwise positions of (a) $2z/L_z = 0$, (b) $2z/L_z = 0.5$ and (c) $2z/L_z = 0.9$ for the adiabatic duct (——), and the heated duct at streamwise positions of 100 mm (·····) and 595 mm (-·-·-) after the beginning of the heated section. Streamwise averaging is performed over 10 mm for the heated duct, respectively over $L_{x,per}$ for the periodic duct, and the y-symmetry is utilised.

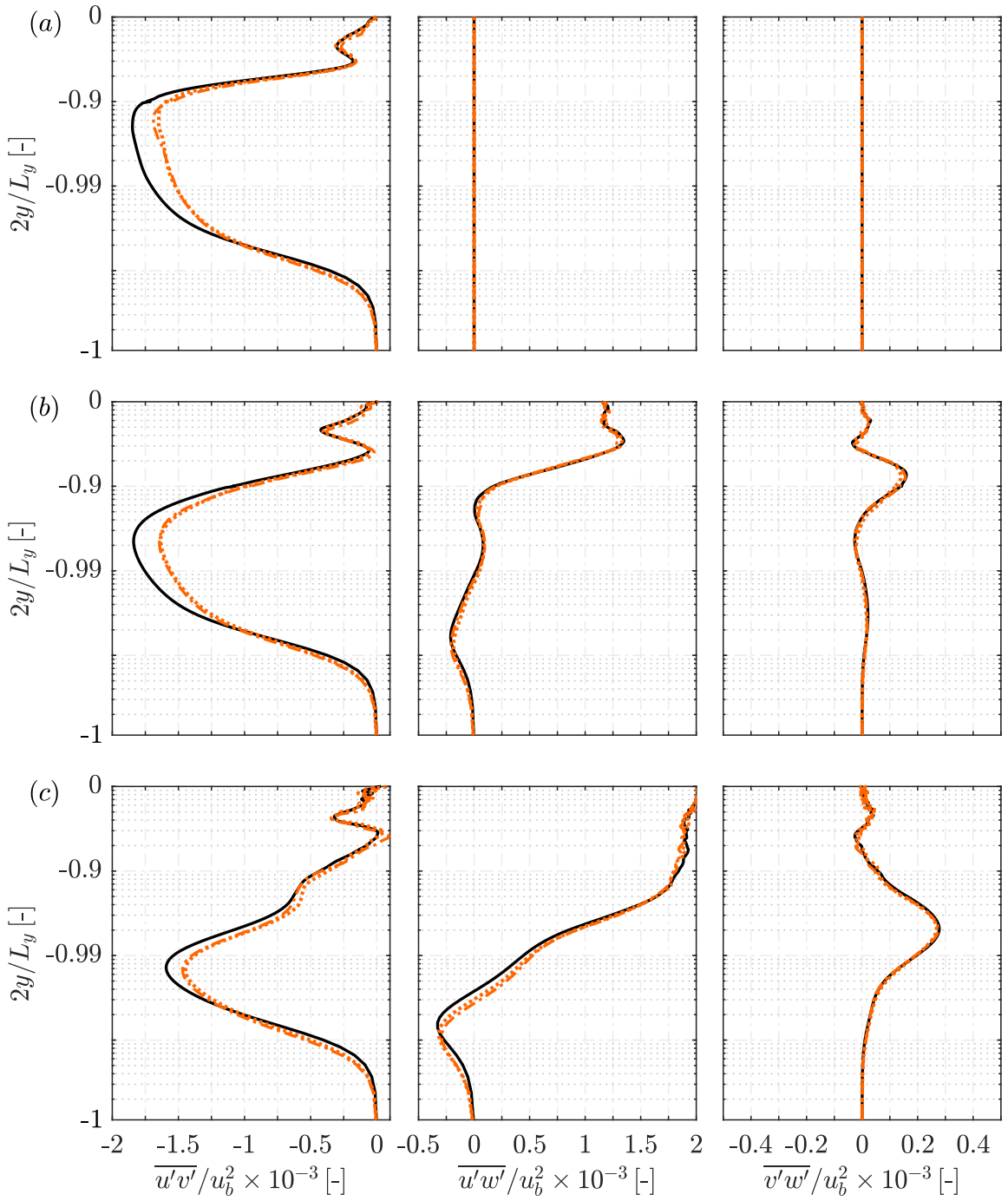

Figure 3.20: Distributions of off-diagonal components of the Reynolds stress tensor along the heated wall-normal direction at spanwise positions of (a) $2z/L_z = 0$, (b) $2z/L_z = 0.5$ and (c) $2z/L_z = 0.9$ for the adiabatic duct (——), and the heated duct at streamwise positions of 100 mm (·····) and 595 mm (-·-·-) after the beginning of the heated section. Streamwise averaging is performed over 10 mm for the heated duct, respectively over $L_{x,per}$ for the periodic duct, and the y-symmetry is utilised.

duct $\overline{u}$-profile exhibits a more pronounced shoulder section due to the weaker secondary flow and the accompanying reduced vertical momentum transport. In the duct core the streamwise velocity changes only marginally compared to the adiabatic case, for example at position $2z/L_z = 0$ and $x = 595\,\text{mm}$ $\overline{u}$ drops by 0.5%. Due to the symmetry with respect to the y- and z-axis, the duct centre secondary flow has only a $\overline{v}$-component with $\overline{w}$ vanishing. The $\overline{v}$-velocity maximum close to the lower wall is the signature of the two smaller corner vortices pushing fluid upwards, and the following $\overline{v}$-minimum is the signature of the two larger corner vortices pushing fluid downwards. The $\overline{w}$-profile close to the wall at $2z/L_z = 0.5$, see the third column of figure 3.18 (b), shows the effect of the small corner vortex transporting fluid from the duct corner to the midplane. The coincidence of the $\overline{v}$-minimum and the $\overline{w}$-maximum at $2y/L_y \approx -0.875$ marks the area, where both the small CW vortex and the large CCW vortex push fluid into the duct corner. The region close to the lateral wall at $2z/L_z = 0.9$ is then dominated by the large corner vortex transporting fluid upwards into the duct core. As discussed before with the help of figure 3.16, the viscosity modulation leads to a weakened secondary flow. This effect is especially visible in the $\overline{v}$-profiles, for which both the small and large vortex strengths represented by the $\overline{v}$-minimum and $\overline{v}$-maximum are getting weaker, particularly at $2z/L_z = 0.9$. In contrast, the $\overline{w}$-profiles remain nearly unaltered and only a slight reduction at the off-centre positions is observable. The extrema locations remain approximately constant signifying an only slight shift of the vortex positions as discussed before. The last column of figure 3.18 depicts the temperature distribution. The secondary flow influence on heat transport and $\overline{T}$-profiles is clearly visible, especially at position 595 mm. On the one hand we observe in spanwise direction a non-uniform distribution and on the other hand kinks in the wall-normal $\overline{T}$-profile, which coincide with the secondary flow extrema. A more detailed discussion of turbulent heat transfer and secondary flow influence follows in section 3.5.4.

The diagonal elements of the Reynolds stress tensor are depicted in figure 3.19 for the same positions as before. The results in the midplane resemble those presented in figure 3.17 (b), the main differences are the larger streamwise averaging interval and the logarithmic scaling for the y-axis. When heating is applied, the $\overline{u'u'}$-profiles show a slight shift of the turbulent production peak towards the wall. These results are in qualitative agreement with Salinas-Vásquez and Métais (2002) observing the inverse trend of shifting the peak further away from the heated wall for air as working fluid since the viscosity increases with heating. At position $x = 100\,\text{mm}$ the $\overline{u'u'}$-maximum is reduced compared to the adiabatic case, whereas at $x = 595\,\text{mm}$ it increases marginally. Due to the shift towards the heatable sidewall, the streamwise Reynolds stress component is lowered over a large area in the heated case until the adiabatic and heated duct results coincide in the unaffected bulk flow. Moving in spanwise direction from the centre towards the lateral wall, i.e. from the first column of figure 3.19 (a) to (c), this coinciding point moves closer to the heated wall from $2y/L_y \approx -0.75$ over $2y/L_y \approx -0.84$ to $2y/L_y \approx -0.97$. In contrast to $\overline{u'u'}$, no peak position shift occurs for the $\overline{v'v'}$-Reynolds stress profile, but likewise it experiences a drop of the maximum value in the duct midplane and at $2z/L_z = 0.5$. However, at $2z/L_z = 0.9$, for the position strongly influenced by the large vortex, the profile shape is changed entirely and no strong heating influence is visible. The $\overline{w'w'}$-profile shows a similar profile shift towards the lower wall as $\overline{u'u'}$. Likewise the peak values are reduced, regardless of the shape of the respective $\overline{w'w'}$-profile, which changes from a plateau-like maximum in the midplane to a

smaller sized maximum closer to the lateral wall.

In figure 3.20 the distributions for the off-diagonal components of the Reynolds stress tensor are depicted. Due to the symmetry with respect to the y-axis, the correlations including the spanwise w-fluctuation $\overline{u'w'}$ and $\overline{v'w'}$ vanish in the duct midplane, see the second and third column of figure 3.20. The off-centre $\overline{u'w'}$- and $\overline{v'w'}$-profiles are only marginally affected by the heating. As for the $\overline{u'u'}$- and $\overline{w'w'}$-profiles in figure 3.19, a shift of the $\overline{u'w'}$-minimum towards the heated wall is visible at both $2z/L_z = 0.5$ and $2z/L_z = 0.9$. The viscosity modulation has a significant impact on the $\overline{u'v'}$-component. For all three z-positions with their varying profile shapes, from a plateau-like maximum in the centre to a smaller sized peak close to the lateral wall, we observe a significant reduction of the respective $\overline{u'v'}$-peak. Again, a slight shift of the peak location towards the heated wall is noticeable, although less clear as for the $\overline{u'u'}$-profiles. The $\overline{u'v'}$-component comprises turbulent ejection and sweeping motions. As Huser and Biringen (1993) have stated, the dominant turbulent mechanism generating the turbulence-induced secondary flow is the ejections from the wall. We therefore will discuss the $\overline{u'v'}$-component in more detail in section 3.5.3 using the Reynolds stress quadrant analysis technique.

3.5.2 Streamwise Vorticity Field

Within the following subsection the influence of wall heating on turbulence-induced secondary flow is discussed by analysing the modulation of the single terms in the streamwise vorticity equation in the HARCD cross-section. The focus is set on the duct corner region with the highest values present.

In the $y-z$ cross-section the mean streamwise vorticity is defined as $\overline{\omega}_x = \partial\,\overline{w}/\partial y - \partial\,\overline{v}/\partial z$. Its transport equation can be derived by taking the curl of the momentum equations, leading for the temporally averaged x-component to

$$
\begin{aligned}
&\overbrace{\overline{u}\,\frac{\partial\,\overline{\omega}_x}{\partial x} + \overline{v}\,\frac{\partial\,\overline{\omega}_x}{\partial y} + \overline{w}\,\frac{\partial\,\overline{\omega}_x}{\partial z}}^{T_{\overline{\omega}_x,conv}} = \\
&\qquad \overbrace{\overline{\nu}\left(\frac{\partial^2\,\overline{\omega}_x}{\partial x^2} + \frac{\partial^2\,\overline{\omega}_x}{\partial y^2} + \frac{\partial^2\,\overline{\omega}_x}{\partial z^2}\right)}^{T_{\overline{\omega}_x,visc,1}} + \overbrace{\frac{\partial\,\overline{\nu}}{\partial z}\left(\frac{\partial\,\overline{\omega}_x}{\partial z} - \frac{\partial\,\overline{\omega}_z}{\partial x}\right) - \frac{\partial\,\overline{\nu}}{\partial y}\left(\frac{\partial\,\overline{\omega}_y}{\partial x} - \frac{\partial\,\overline{\omega}_x}{\partial y}\right)}^{T_{\overline{\omega}_x,visc,2}} \\
&+ \overbrace{\frac{\partial}{\partial y}\left[\frac{\partial\,\overline{\nu}}{\partial y}\left(\frac{\partial\,\overline{w}}{\partial y} + \frac{\partial\,\overline{v}}{\partial z}\right) + \frac{\partial\,\overline{\nu}}{\partial z}\left(2\cdot\frac{\partial\,\overline{w}}{\partial z}\right)\right] - \frac{\partial}{\partial z}\left[\frac{\partial\,\overline{\nu}}{\partial y}\left(2\cdot\frac{\partial\,\overline{v}}{\partial y}\right) + \frac{\partial\,\overline{\nu}}{\partial z}\left(\frac{\partial\,\overline{v}}{\partial z} + \frac{\partial\,\overline{w}}{\partial y}\right)\right]}^{T_{\overline{\omega}_x,visc,3}} \\
&\qquad + \overbrace{\overline{\omega}_x\,\frac{\partial\,\overline{u}}{\partial x} + \overline{\omega}_y\,\frac{\partial\,\overline{u}}{\partial y} + \overline{\omega}_z\,\frac{\partial\,\overline{u}}{\partial z}}^{T_{\overline{\omega}_x,stretch/tilt}} + \overbrace{\left(\frac{\partial^2}{\partial z^2} - \frac{\partial^2}{\partial y^2}\right)\left(\overline{v'w'}\right)}^{T_{\overline{\omega}_x,turb,1}} + \overbrace{\frac{\partial^2}{\partial y\,\partial z}\left(\overline{v'v'} - \overline{w'w'}\right)}^{T_{\overline{\omega}_x,turb,2}}.
\end{aligned}
\tag{3.3}
$$

The left-hand side term $T_{\overline{\omega}_x,conv}$ describes the convective transport of mean streamwise vorticity. The first three terms on the right-hand side denote the viscous diffusion terms, where the second and third term vanish for constant viscosity configurations and only $T_{\overline{\omega}_x,visc,1}$ remains. For the straight HARCD configuration approximatively local homogeneity is assumed corresponding

to a fully developed turbulent flow field and consequently gradients in streamwise direction are neglected. Note, in order to shorten the representation of term $T_{\overline{\omega}_x,visc,3}$, the streamwise derivatives have already been left out, whereas for all other terms they are still included in equation system 3.3. $T_{\overline{\omega}_x,stretch/tilt}$ denotes the vortex stretching and tilting by the mean velocity gradient being the source of Prandtl's flow of the first kind. In the present straight HARCD case this term vanishes entirely with the approximation of streamwise gradients to be zero and becomes important for curved configurations as presented in section 4.3.3 of the subsequent chapter. The last two expressions are the source terms for Prandtl's flow of the second kind. $T_{\overline{\omega}_x,turb,1}$ comprises the difference of second-order derivatives of the cross-sectional Reynolds shear stress $\overline{v'w'}$, and $T_{\overline{\omega}_x,turb,2}$ is the second-order mixed partial derivative of the cross-sectional Reynolds normal stress difference, i.e. that of $\overline{v'v'}$ and $\overline{w'w'}$. A detailed analysis of equation 3.3 with a special focus on turbulence-induced secondary flow can be found e.g. in Demuren and Rodi (1984), Gavrilakis (1992) and Pirozzoli et al. (2018).

Pirozzoli et al. (2018) distinguishes for the $\overline{\omega}_x$-investigation of the turbulence-induced corner vortices in a square duct between the vorticity field in the duct corner region up until $y^+/y^* = 150$ and $z^+/z^* = 150$, and that in the duct core region. They argued, that the relatively weak vorticity in the duct core scales well in outer units (u_b/d_h), whereas the stronger vorticity in the duct corners scales in mixed inner and outer units (u_b/l_ν^*). The superscript $(\cdot)^*$ here denotes a perimeter-averaged quantity. We focus the current study on the HARCD corner region, as there the wall heating exhibits the strongest impact and the terms of equation system 3.3 reach levels markedly deviating from zero. Consequently, normalisation of the streamwise vorticity and the single terms of equation system 3.3 is conducted with $\overline{\omega}_x^* = \overline{\omega}_x/(u_b/l_\nu^*)$ and $T^*_{\overline{\omega}_x,(\cdot)} = 10^6 \cdot T_{\overline{\omega}_x,(\cdot)}/(u_b/l_\nu^*)^2$. Analogous to Pirozzoli et al. (2018) the length scale l_ν^* is determined via averaging the viscous length scale over the whole HARCD perimeter. Note, that using this averaging procedure leads presumably to an artificial weakening of the observable changes between adiabatic and heated duct as the local viscous length scale differs more strongly than the perimeter-averaged one in an asymmetrically heated HARCD configuration. Nevertheless, the trends are clearly describable.

The mean streamwise vorticity distribution in the lower duct corner is depicted in figure 3.21. Left and right of the corner bisecting line a pair of primary vorticity regions of opposite sign is located accompanied by a layer of positive vorticity along the heatable wall, and negative vorticity along the lateral sidewall, respectively. The latter regions form as a result of the no-slip condition, see Orlandi (1990). The areas of strongest vorticity are located in the duct corners around the corner bisector and along the sidewalls, whereas the vorticity levels in the duct core remain relatively low. Pirozzoli et al. (2018) state based on scaling considerations, that for increasing Re flows the contribution of the stronger corner vorticity to secondary motions becomes less and less important compared to the weaker core vorticity, as the former scales with inner viscous units (u_b/l_ν^*) and the latter in outer units (u_b/d_h). Due to the present case being a high aspect ratio configuration, the core vorticity in each quadrant experiences a strong asymmetry between the vorticity region associated with the small vortex and that associated with the large vortex. For the corner vorticity, however, an approximately symmetrical behaviour is observed with the corner bisector vorticity patch close to the lateral wall being marginally more stretched than that adjacent to the lower short sidewall. When heating is applied, the

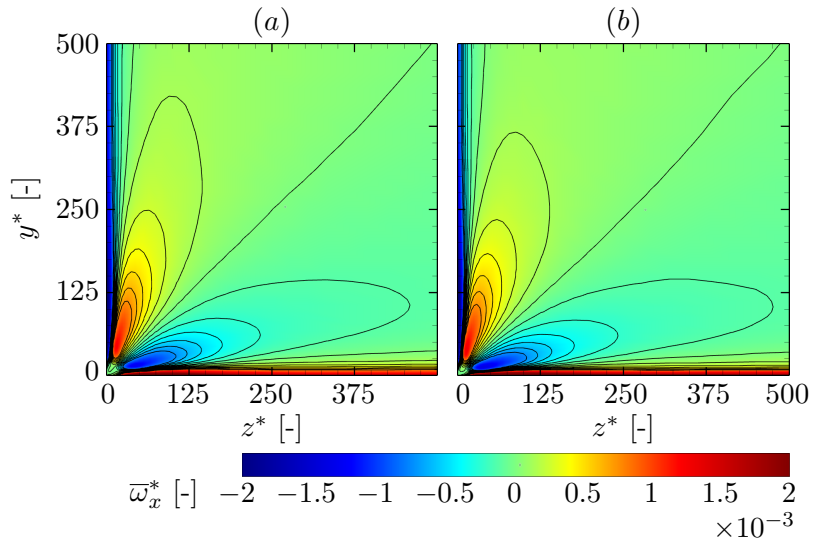

Figure 3.21: Normalised mean streamwise vorticity distribution $\overline{\omega}_x^* = \overline{\omega}_x/(u_b/l_\nu^*)$ in the lower left duct corner for the (a) adiabatic and the (b) end section of the heated duct. Isolines are drawn from $-0.75 \cdot 10^{-3}$ to $0.75 \cdot 10^{-3}$ in steps of $0.125 \cdot 10^{-3}$.

local Re_τ increases significantly causing the primary high vorticity patches to move further into the duct corner and increase in strength, see also the profiles of figure 3.24 (a). Likewise, the vorticity layers along the sidewalls flatten and intensify. This behaviour is in accordance with Pirozzoli et al. (2018), who reported the same effect for increasing Re_τ. For the core vorticity an asymmetric behaviour is present: a noticeable $\overline{\omega}_x^*$ decrease is observed in the area adjacent to the lateral wall, whereas the vorticity levels adjacent to the lower wall are only affected marginally, compare the modulation of the lowest magnitude $\overline{\omega}_x^*$-isolines bordering the primary vorticity patches. The asymmetric heating-induced vorticity modulation is in accordance with the asymmetric secondary flow change presented in figure 3.16 of the previous section 3.5.1, where also a significantly stronger weakening of the large lateral wall vortex compared to the smaller lower wall vortex has been observed. This result is attributed to the asymmetric wall heating and has not been observed for the unheated and thus symmetric square duct cases by Pirozzoli et al. (2018).

Figures 3.22 and 3.23 show the normalised distributions of the individual terms of the mean streamwise vorticity equation 3.3 in the lower left duct corner. The qualitative shape of all distributions as well as the quantitative order of magnitude are in good accordance with the distributions presented in Pirozzoli et al. (2018). For the viscous terms in figure 3.22 the dominant term is $T^*_{\overline{\omega}_x,visc,1}$, the remaining $T^*_{\overline{\omega}_x,visc,2}$ and $T^*_{\overline{\omega}_x,visc,3}$ only existing with a viscosity gradient present. Above the lower wall $T^*_{\overline{\omega}_x,visc,1}$ forms a tadpole-shaped positive-value region with a maximum value reached at $z^* \approx 40$ and with a small extension attached reaching into the duct corner. This region is accompanied by a slightly weaker negative-value region mirrored across the corner bisecting line. Note, that compared to Pirozzoli et al. (2018) deviations are visible: between the primary tadpole-shaped zone and the lower wall a flat secondary layer of negative $T^*_{\overline{\omega}_x,visc,1}$ forms, and inverted for the lateral sidewall, respectively. In the LES this wall-adjacent

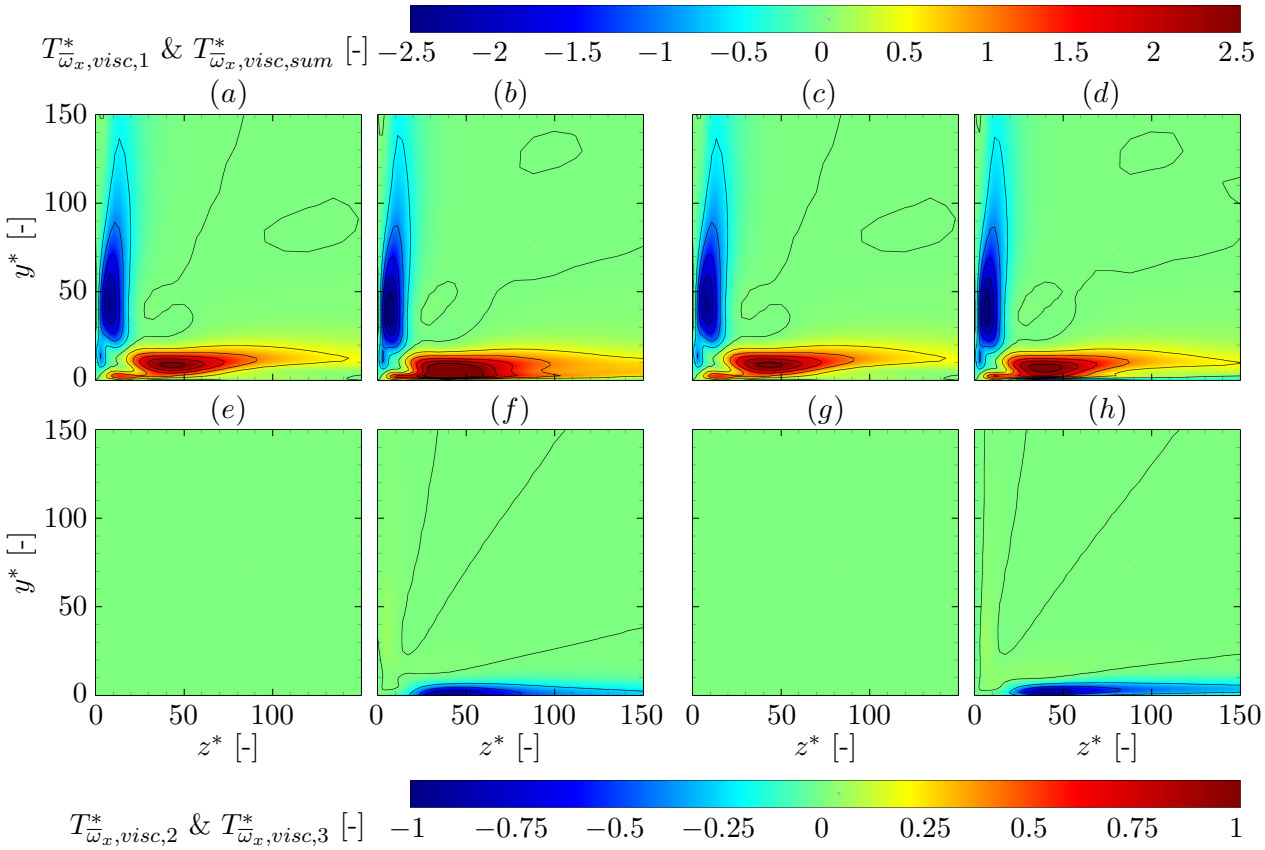

Figure 3.22: Viscous terms distributions of the $\overline{\omega}_x$-equation 3.3 in the lower left corner with $T^*_{\overline{\omega}_x,(\cdot)} = 10^6 \cdot T_{\overline{\omega}_x,(\cdot)}/(u_b/l^*_\nu)^2$: (a,b) $T^*_{\overline{\omega}_x,visc,1}$, (c,d) sum of all viscous terms $T^*_{\overline{\omega}_x,visc,sum}$, (e,f) $T^*_{\overline{\omega}_x,visc,2}$ and (g,h) $T^*_{\overline{\omega}_x,visc,3}$. On the respective left side of each figure pair the adiabatic duct result is shown and on the right that of the heated duct end section. Isolines in the upper row are drawn from −2.5 to 2.5 in steps of 0.5 and in the lower row from −1 to 1 in steps of 0.25.

layer is predicted to be weaker and less pronounced as well as to penetrate less deep into the duct corner as in the square duct DNS. Furthermore, this leads to the small extension running in parallel to the sidewalls and not in parallel to the corner bisecting line as in the DNS. We assume the coarser LES resolution in the corner region to be the reason for this marginal deficiency. The terms $T^*_{\overline{\omega}_x,visc,2}$ and $T^*_{\overline{\omega}_x,visc,3}$ form a negative-value layer above the lower wall with peak values also reached at $z^* \approx 40$. Due to the asymmetrical heating they are absent along the lateral sidewall. Individually both terms are noticeable smaller than $T^*_{\overline{\omega}_x,visc,1}$, yet their sum is able to significantly impact the viscous terms distribution $T^*_{\overline{\omega}_x,visc,sum}$ in the vicinity of the heated wall.

The individual turbulence terms composed of the Reynolds shear stress term $T^*_{\overline{\omega}_x,turb,1}$ and Reynolds normal stress difference term $T^*_{\overline{\omega}_x,turb,2}$ reach comparably high levels in the duct corner region, see figure 3.23 (e,g). At the lower heated wall the shear stress term distribution consists of a primary lens-shaped region adjacent to the wall with a maximum reached at $z^* \approx 25$ accompanied by a smaller and weaker secondary lens-shaped region of opposite sign above it, and mirror-inverted for the lateral sidewall, respectively. The normal stress term distribution in

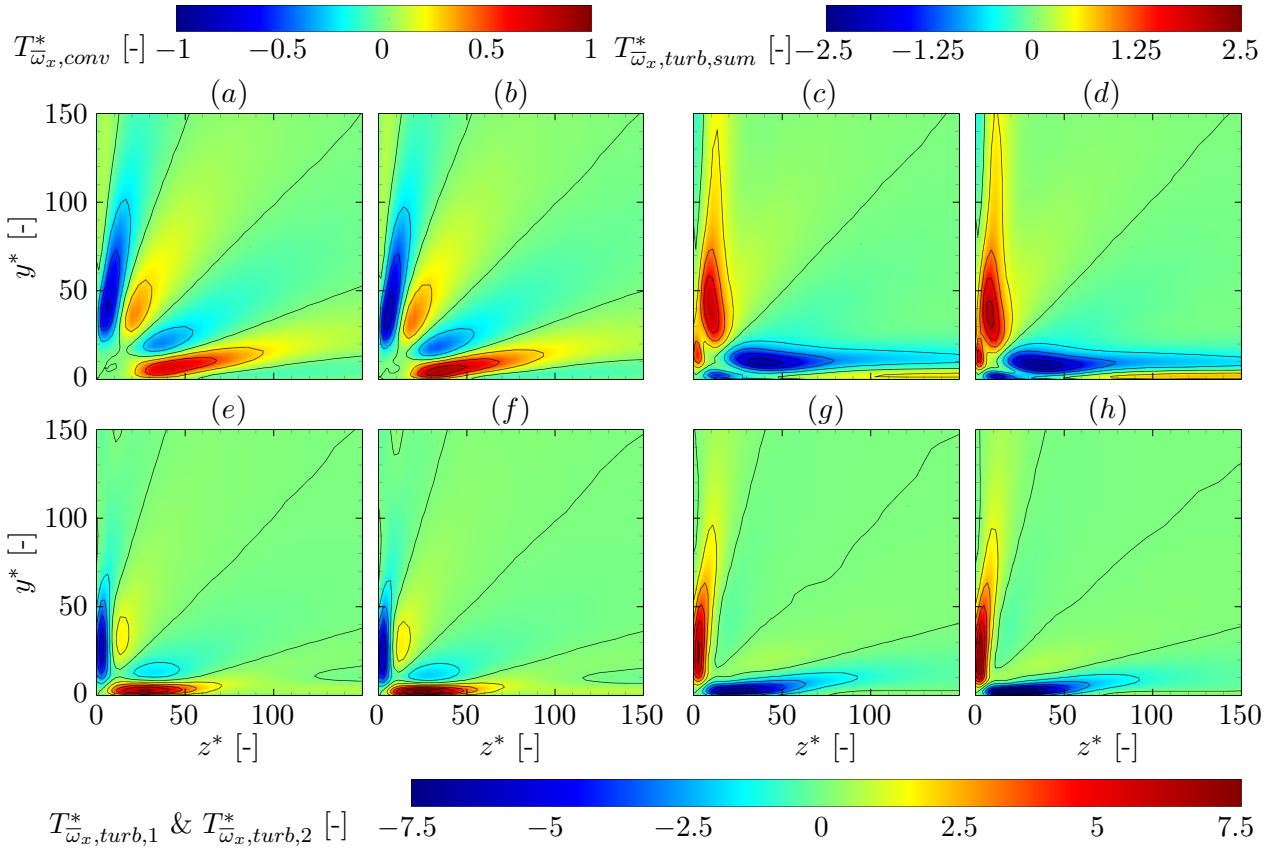

Figure 3.23: Normalised distributions of convective and turbulence terms of the $\overline{\omega}_x$-equation 3.3 in the lower left corner with $T^*_{\overline{\omega}_x,(\cdot)} = 10^6 \cdot T_{\overline{\omega}_x,(\cdot)}/(u_b/l^*)^2$: (a,b) convective term $T^*_{\overline{\omega}_x,conv}$, (c,d) sum of turbulence terms $T^*_{\overline{\omega}_x,turb,sum}$, (e,f) Reynolds shear stress term $T^*_{\overline{\omega}_x,turb,1}$ and (g,h) Reynolds normal stress difference term $T^*_{\overline{\omega}_x,turb,2}$. On the respective left side of each figure pair the adiabatic duct result is shown and on the right that of the heated duct end section. Isolines in the upper row for $T^*_{\overline{\omega}_x,conv}$ are drawn from -1 to 1 in steps of 0.25 and for $T^*_{\overline{\omega}_x,turb,sum}$ from -2.5 to 2.5 in steps of 0.5, and in the lower row from -7.5 to 7.5 in steps of 1.25.

the vicinity of the lower wall has likewise a lens-shaped primary region, but no secondary region is present. Furthermore, the region is stretched towards the duct core, slightly tilted against the wall and of opposite sign than the shear stress term. Adding up the individual turbulence terms with their opposite signs and comparable strengths lead to $T^*_{\overline{\omega}_x,turb,sum}$ being of similar strength and shape as the sum of viscous terms $T^*_{\overline{\omega}_x,visc,sum}$, although with opposite sign, see figures 3.23 (c) and 3.22 (c). The distribution of $T^*_{\overline{\omega}_x,turb,sum}$ consists likewise of a tadpole-shaped region with an extension below. Also, the same deviations with respect to the square duct DNS results of Pirozzoli et al. (2018) are noticed, i.e. a less pronounced region of opposite sign between the tadpole-shaped region and the wall and the extension being in parallel to the wall instead of running in parallel to the corner bisecting line. Comparing the three terms $T^*_{\overline{\omega}_x,conv}$, $T^*_{\overline{\omega}_x,visc,sum}$ and $T^*_{\overline{\omega}_x,turb,sum}$ for the adiabatic duct, we notice the turbulence and viscous terms to be larger than the convective term. Consequently, the vorticity equation is mainly dominated by a balance

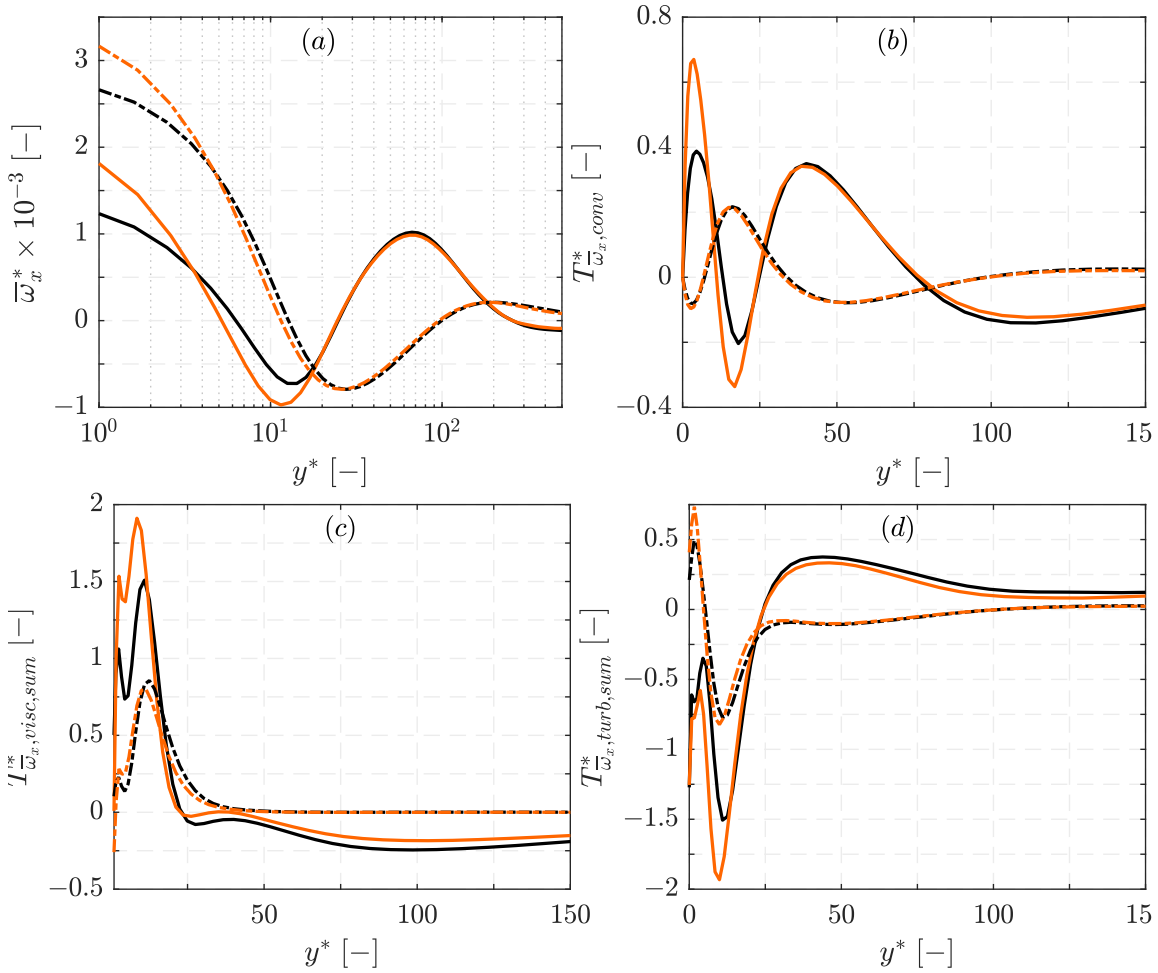

Figure 3.24: Normalised distributions along the heatable wall-normal y^*-axis of (a) streamwise vorticity, (b) convective term, (c) sum of viscous terms and (d) sum of turbulence terms of the $\overline{\omega}_x$-equation 3.3 in the lower left corner for $z^* = 25$ (solid lines) and $z^* = 100$ (dash-dotted lines). Adiabatic duct results are coloured black (——) and heated duct results orange (——).

between turbulence terms acting as source term and viscous terms acting as sink term. However, in contrast to Pirozzoli et al. (2018) $T^*_{\overline{\omega}_x,conv}$ yields a non-negligible contribution in our case.

When heating is applied, similar observations can be made as for the corner streamwise vorticity distribution: all terms of equation system 3.3 penetrate deeper into the duct core and increase in strength, compare the respective adiabatic duct results on the left hand-side with the heated duct results on the right for each image pair of figures 3.22 and 3.23. Furthermore, two additional viscous terms emerge due to variations in the viscosity field and reach non-zero values only in a narrow layer above the heated wall. For a quantitative evaluation see the distributions in the line plots of figure 3.24 $(b-d)$. As discussed with figure 3.22, the one-sided heating leads to an asymmetric modulation of the streamwise vorticity field, the vorticity associated with the large lateral wall vortex being reduced stronger than the small lower wall vortex. Comparing the

wall/domain	$T^*_{\overline{\omega}_x,turb,sum}$ [−]	$T^o_{\overline{\omega}_x,turb,sum}$ [−]	$T^*_{\overline{\omega}_x,visc,sum}$ [−]	$T^o_{\overline{\omega}_x,visc,sum}$ [−]
lower/adiabatic	−2.231	−58.254	2.642	68.967
lower/heated	−2.438	−70.163	2.847	81.953
lateral/adiabatic	1.968	51.381	−2.476	−64.636
lateral/heated	2.148	61.833	−2.726	−78.470

Table 3.6: Peak values of $T_{\overline{\omega}_x,turb,sum}$ and $T_{\overline{\omega}_x,visc,sum}$ of the $\overline{\omega}_x$-equation in the lower left corner for adiabatic and heated domain, $(\cdot)^*$ denotes normalisation by $(u_b/l^*_\nu)^2$ and $(\cdot)^o$ by $(u_b/d_h)^2$.

wall	$\Delta T^*_{\overline{\omega}_x,turb,sum}$[%]	$\Delta T^o_{\overline{\omega}_x,turb,sum}$[%]	$\Delta T^*_{\overline{\omega}_x,visc,sum}$[%]	$\Delta T^o_{\overline{\omega}_x,visc,sum}$[%]
lower	−9.252	−20.443	7.789	18.829
lateral	9.162	20.342	−10.124	−21.403

Table 3.7: Heating-induced change of the peak values of $T_{\overline{\omega}_x,turb,sum}$ and $T_{\overline{\omega}_x,visc,sum}$ in the lower left corner, $(\cdot)^*$ denotes normalisation by $(u_b/l^*_\nu)^2$ and $(\cdot)^o$ by $(u_b/d_h)^2$, see also table 3.6.

individual heating-induced changes of the $\overline{\omega}_x$-source and -destruction terms, i.e. $T^*_{\overline{\omega}_x,turb,sum}$ and $T^*_{\overline{\omega}_x,visc,sum}$, separately for the vicinity of the lower and the lateral wall, indicates an imbalance of the two terms to give a probable explanation for the previously observed behaviour. Tables 3.6 and 3.7 list the peak values reached for $\overline{\omega}_x$-production and -destruction terms normalised with mixed and outer units as well as the relative change between adiabatic and heated duct. As discussed before, the specific choice of determining l^*_ν leads to an underestimation of heating effects. It is noticed, that the heating-induced modulation of $T^*_{\overline{\omega}_x,turb,sum}$ is of comparable size for the lower and the lateral walls with the lower wall minimum becoming 9.25% stronger and the lateral wall maximum 9.16% stronger. In contrast, the viscous terms $T^*_{\overline{\omega}_x,visc,sum}$ show an asymmetric behaviour with the lower wall maximum only increasing by 7.80%, whereas the lateral wall minimum drops by 10.12%. The reduced drop of $T^*_{\overline{\omega}_x,visc,sum}$ at the lower wall is mainly caused by the additional presence of the terms $T^*_{\overline{\omega}_x,visc,2}$ and $T^*_{\overline{\omega}_x,visc,3}$ being of opposite sign than $T^*_{\overline{\omega}_x,visc,1}$. Consequently, the turbulent production terms become relatively stronger compared to the viscous terms in the vicinity of the lower wall, whereas at the lateral the opposite is the case. In effect this gives a possible explanation for the asymmetric behaviour of the $\overline{\omega}^*_x$-evolution in the duct core, with a noticeable drop present in the lateral wall region and almost no change noticeable in the lower wall region. Note, however, that the peak locations of $T^*_{\overline{\omega}_x,turb,sum}$ and $T^*_{\overline{\omega}_x,visc,sum}$ do not perfectly coincide.

3.5.3 Turbulent Sweeping and Ejection Motions

Introduced by Wallace et al. (1972), the quadrant analysis of the Reynolds stress tensor allows to identify the main contributions to turbulence (Wallace, 2016). The Reynolds shear stress $\overline{u'v'}$ is split into four quadrants depending on the sign of the streamwise u' and the heatable wall-normal velocity fluctuation v'. The first quadrant $Q_1\,(u' > 0/v' > 0)$ comprises outward motion of high-velocity fluid, the second quadrant $Q_2\,(u' < 0/v' > 0)$ outward motion of low-velocity fluid, the third quadrant $Q_3\,(u' < 0/v' < 0)$ inward motion of low-velocity fluid and the fourth

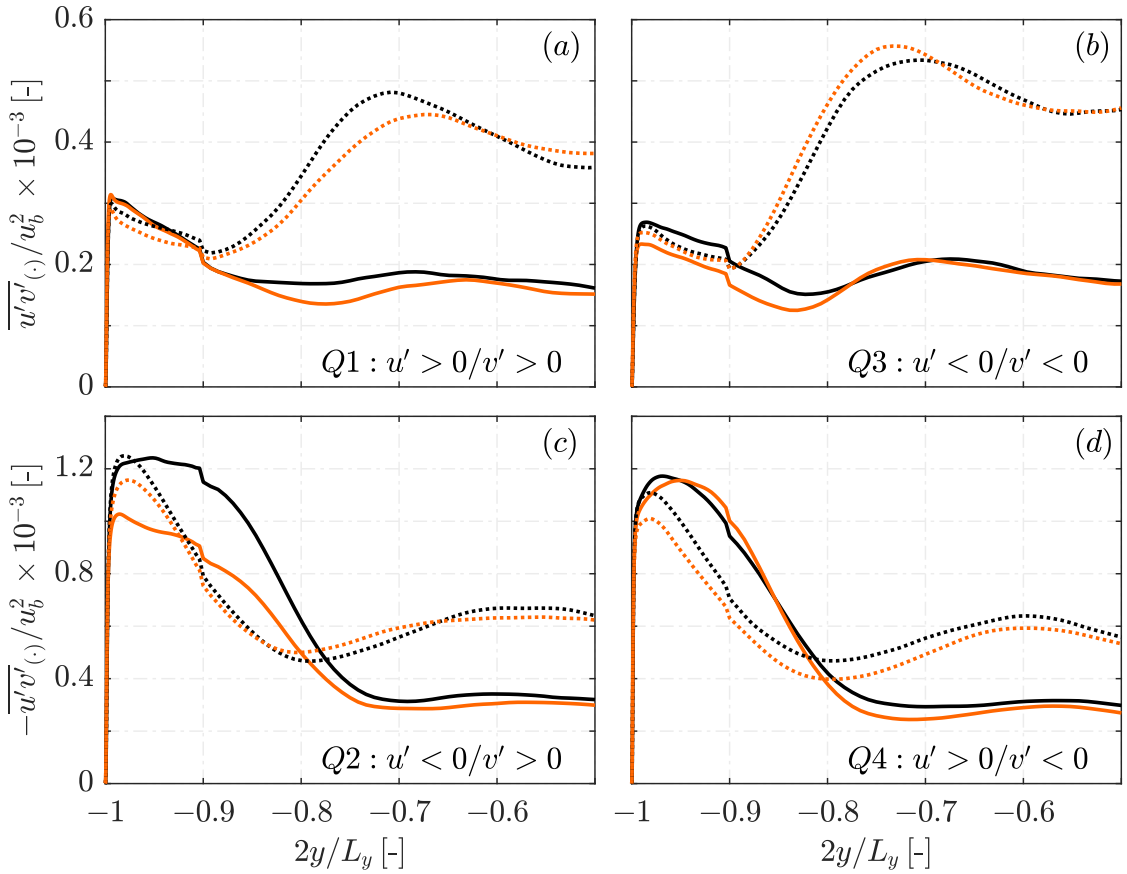

Figure 3.25: Quadrant analysis term distribution of the Reynolds shear stress component $\overline{u'v'}$ for the adiabatic (——) and the heated duct (——) along the midplane $z = 0$, and along $2z/L_z = 0.5$ marked by (·····) and (·····), respectively.

quadrant Q_4 $(u' > 0/v' < 0)$ inward motion of high-velocity fluid. Willmarth and Lu (1972) have shown for a TBL set-up that Q_2 is connected to turbulent ejection events and Q_4 to turbulent sweeping motions. For an octant analysis including additionally temperature fluctuations the reader is referred to section 4.3.4.

Figure 3.25 depicts the quadrant analysis for the Reynolds stress component $\overline{u'v'}$ for the adiabatic duct and the end section of the heated duct at $2z/L_z = 0$ and $2z/L_z = 0.5$, respectively. For the latter the symmetry is exploited by additional averaging of the left and right duct halves. The conditional sampling to obtain the results within this section has been performed over a shorter period of 8.5 FTT with respect to $L_{x,heat}$ with the same sampling rate as for the rest of the water HARCD investigation, the results are therefore somewhat noisier. The discussion concentrates on the Q_2- and Q_4-distributions and for completeness the ones for Q_1 and Q_3 are also included. First, the focus is set on the adiabatic case. In the midplane all four quadrant profiles experience a maximum in the vicinity of the heatable wall and fall off to an approximately constant value in the duct centre. In contrast to a TBL, this constant value is non-zero as the boundary layers originating from all sidewalls influence the duct core flow field. Similarly to

Salinas-Vásquez and Métais (2002) the size of the ejections is slightly larger than that of the sweeping motions indicated by the location of the respective maximum. The ejection size is $l_{ejec} = 0.115 \cdot L_y/2$ compared to $l_{sweep} = 0.085 \cdot L_y/2$ for the sweeping motions. We define this size as the distance from the wall to the location, where the intensity has dropped to 90% of the respective maximum. At $2z/L_z = 0.5$, the peak intensity of the ejections is slightly larger and that of the sweeps smaller than in the centre plane and the sizes of both the ejection and the sweeping motions are reduced significantly. Moreover, the constant duct centre value is larger due to the stronger lateral wall influence than in the midplane.

For the heated section, the maximum values of all four quadrants are reduced at both considered spanwise positions. In the duct centre the Q_2- and Q_3-extrema drop significantly stronger than the ones for Q_1 and Q_4. At $2z/L_z = 0.5$ we observe an even reduction of Q_2 and Q_4. Overall the intensity reduction of the ejections is more sensible to the viscosity modulation than the one of the sweeping motions. This result is in accordance with the heated TBL investigation by Lee et al. (2013), who also observed an intensity reduction of all four quadrants due to the stabilising effect of the viscosity modulation. The differences between their and our results are attributed to the influence of the lateral walls on the duct centre plane profiles. Moving from the midplane towards the lateral wall, we observe that the viscosity effect on the intensity drop weakens for the ejections and intensifies for the sweeping motions. The Q_2-maximum in the midplane drops by -17.3%, at $2z/L_z = 0.5$ by -7.4% and at $2z/L_z = 0.75$ by -7.4% (plot not shown). In the centre the drop of the sweeping motion intensity is significantly lower than the one of the ejections, but increasing towards the lateral wall, whereas the ejection intensity drop decreases. The Q_4-maximum intensity drop increases from -1.4% in the midplane over -8.9% at $2z/L_z = 0.5$ to -10.6% at $2z/L_z = 0.75$. Moreover, a heating-induced change in the size of these turbulent structures is observable. The effect is strongest in the centre plane, where the ejection size is reduced by -23.0% from $l_{ejec} = 0.115 \cdot L_y/2$ to $l_{ejec} = 0.089 \cdot L_y/2$. The sweep size increases by 11.7% from $l_{sweep} = 0.085 \cdot L_y/2$ to $l_{sweep} = 0.096 \cdot L_y/2$. At $2z/L_z = 0.5$ the effect is significantly weaker, so that the ejection as well as the sweeping motion sizes are reduced only marginally.

In contrast to Salinas-Vásquez and Métais (2002), we use liquid water as working fluid, which leads to a viscosity reduction at the heated wall, whereas the viscosity of air increases when heated. By observing the opposite effect on size and intensity of turbulent ejections as Salinas-Vásquez and Métais (2002), we can therefore confirm that the secondary flow modulation is a viscosity effect. In our case, the viscous length scale at the centre plane decreases from $l_\nu^+ = 2.02 \cdot 10^{-6}\,\mathrm{m}$ for the adiabatic case to $l_\nu^+ = 1.34 \cdot 10^{-6}\,\mathrm{m}$ corresponding to a drop of -39.1%. As streaky structures scale with the viscous thickness, the l_ν^+ drop leads to a reduction of their size. This is indicated in figure 3.19 with the $\overline{u'u'}$-maximum moving closer to the heated wall. Likewise the size and the intensity of the ejections is reduced significantly, which in turn leads to the observed weakening of the secondary flow along the duct length. For a further analysis of the correlation of turbulent ejections from the wall and turbulence-induced secondary flow modulation when asymmetrical heating is applied the reader is referred to section 4.3.4.

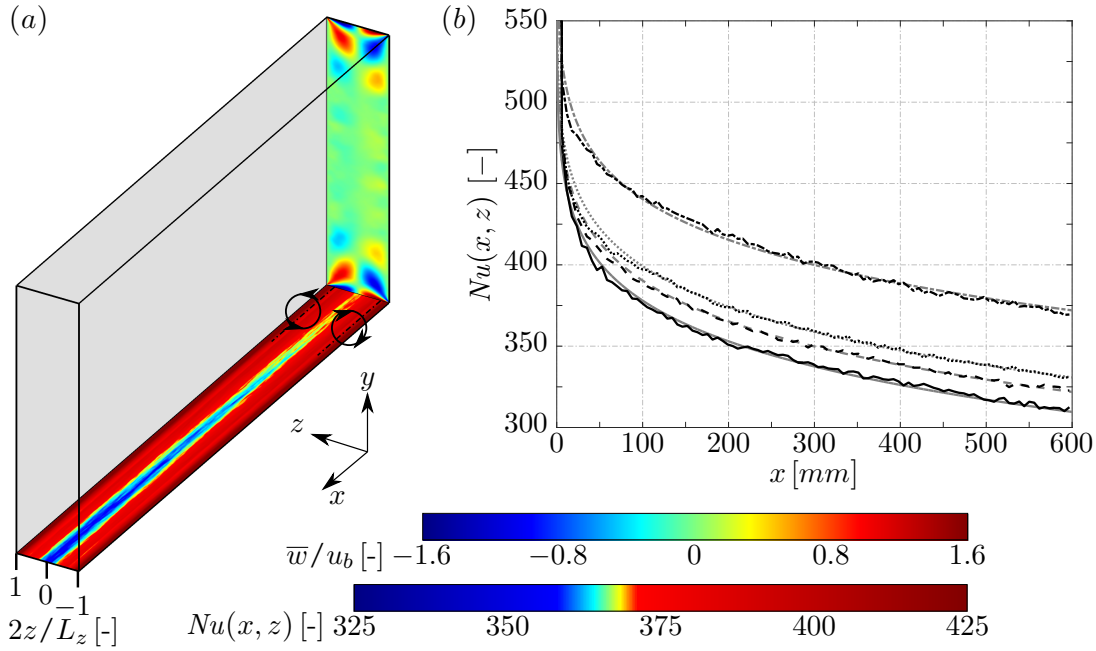

Figure 3.26: Nusselt number and spanwise velocity distribution in the interval from $200-250\,\mathrm{mm}$ in (a) and Nusselt number development along the heated wall of the straight HARCD configuration at different spanwise locations in (b). The location $2z/L_z = 0$ is marked by (——), $2z/L_z = 0.33$ by (- - - -), $2z/L_z = 0.75$ by (·····) and $2z/L_z = 0.9$ by (-·-·-). The fitting functions $Nu(x,z) = -220 \cdot x^{0.1} + c(z)$ are represented by the respective grey-coloured lines and the term $c(z)$ varies from 727 in the centre over 739 and 748 to 789 close to the lateral wall.

3.5.4 Turbulent Heat Transfer

Within this section we discuss the influence of turbulence-induced secondary flow vortices on the turbulent heat transfer by analysing the Nusselt number development and the turbulent Prandtl number distribution along the heated duct length.

Secondary flow structures enhance the mixing of hot and cold fluid and increase the heat transport away from the lower heated wall into the duct core. Figure 3.26 depicts the Nusselt distribution characterising the heat transfer, see equation 2.7 for its definition. Note, that for all Nusselt numbers throughout this work the hydraulic diameter is used as reference length. Due to the effect of the corner vortex pairs Nu varies significantly in streamwise and spanwise direction. A considerable spanwise heat transfer gradient is produced predominantly by the two smaller vortices adjacent to the heated bottom wall, which are indicated in figure 3.26 (a) with their respective sense of rotation. Transporting hot fluid into the bottom wall centre and in cooperation with the two larger vortices pushing cold fluid into the corner regions, the counter-rotating vortex pairs increase the temperature gradient in the corner area and reduce it in the centre. The heat transfer characterised by the local Nusselt number $Nu(x,z)$ varies for the considered section from ≈ 410 in the corner to ≈ 350 at the bottom wall centre. The streamwise development of the heat transfer follows a pattern, which is typical for thermal entrance problems, see figure 3.26 (b). The Nusselt number, respectively the heat flux into the cooling duct, reaches its highest values

at the inlet with the maximum temperature gradients present. After the temperature boundary layer has established the heat transfer decreases gradually. Due to the continuous secondary flow mixing of hot fluid at the heated wall with cold fluid in the duct core the heat flux remains relatively high compared to configurations without secondary flow presence, e.g. straight pipe or channel cooling flows. The local Nusselt number can be well approximated by a power law of the form $Nu(x,z) = a \cdot x^b + c(z)$ with a spanwise varying constant $c(z)$. For our case the functional constants are $a = -220$, $b = 0.1$ and $c(z)$ changes from 727 in the centre over 739 and 748 to 789 in the vicinity of the adiabatic lateral wall. Spatial averaging of the local Nusselt number distribution in spanwise and streamwise direction gives a mean value Nu_{xz} for the investigated configuration of $Nu_{xz} = 370.7$.

The turbulent Prandtl number Pr_t is defined as the ratio of turbulent eddy viscosity and turbulent eddy thermal diffusivity, $Pr_t = \nu_t/\alpha_t$. Especially in RANS modelling frequently a constant Pr_t is assumed based on the Reynolds analogy, which presumes an equal turbulent heat and momentum flux yielding a constant value of $Pr_t = 1$. As the turbulent Prandtl number depends on the molecular one this constant Pr_t value is often determined based on experimental data. This method has been used e.g. for the LES heated duct investigations by Salinas-Vásquez and Métais (2002) and Hébrard et al. (2005), in which Pr_t is set to 0.6. An extensive overview of available experimental data is given in Kays (1994).

For a classical TBL configuration with the x-axis orientated in flow direction and the y-axis perpendicular to it in wall-normal direction, the eddy viscosity can be determined as $\overline{u'v'} = -\nu_t \cdot (\partial\,\overline{u}/\partial y)$ and the eddy thermal diffusivity as $\overline{T'v'} = -\alpha_t \cdot (\partial\,\overline{T}/\partial y)$. This definition has also been applied for more complex configurations, e.g. for a mixed convection set-up of an asymmetrically heated channel and a heated cylinder closely above the heated wall (Kang and Iaccarino, 2010), and symmetrically heated square duct flows (Hirota et al., 1997; Schindler et al., 2019). However, for our case we want to analyse the cross-sectional Pr_t-distribution for the asymmetrically heated HARCD rendering the TBL definition unsuitable. Hence, a new turbulent Prandtl number formulation is introduced considering both the heated as well as the adiabatic lateral wall boundary layers. First, we define the following vectors of turbulent stresses and heat fluxes as well as mean velocity and temperature gradients in the cross-section

$$\mathbf{v}_{\nu_t,fluc} = \begin{bmatrix} \overline{u'v'} \\ \overline{u'w'} \end{bmatrix}, \quad \mathbf{v}_{\nu_t,grad} = -\begin{bmatrix} \partial\,\overline{u}/\partial y \\ \partial\,\overline{u}/\partial\,z \end{bmatrix}, \tag{3.4a}$$

$$\mathbf{v}_{\alpha_t,fluc} = \begin{bmatrix} \overline{T'v'} \\ \overline{T'w'} \end{bmatrix}, \quad \mathbf{v}_{\alpha_t,grad} = -\begin{bmatrix} \partial\,\overline{T}/\partial y \\ \partial\,\overline{T}/\partial z \end{bmatrix}. \tag{3.4b}$$

The angles between the turbulent flux and mean flow gradient vectors are

$$\varphi_M = \arccos\left(\frac{\mathbf{v}_{\nu_t,fluc} \cdot \mathbf{v}_{\nu_t,grad}}{|\mathbf{v}_{\nu_t,fluc}| \cdot |\mathbf{v}_{\nu_t,grad}|}\right), \tag{3.5a}$$

$$\varphi_H = \arccos\left(\frac{\mathbf{v}_{\alpha_t,fluc} \cdot \mathbf{v}_{\alpha_t,grad}}{|\mathbf{v}_{\alpha_t,fluc}| \cdot |\mathbf{v}_{\alpha_t,grad}|}\right). \tag{3.5b}$$

If the angles between the turbulent stresses and heat fluxes ($\mathbf{v}_{\nu_t,fluc}$ and $\mathbf{v}_{\alpha_t,fluc}$), and the mean flow gradient vectors ($\mathbf{v}_{\nu_t,grad}$ and $\mathbf{v}_{\alpha_t,grad}$) are zero, the Boussinesq turbulent viscosity hypothesis is valid and ν_t and α_t can be determined using the TBL formulation.

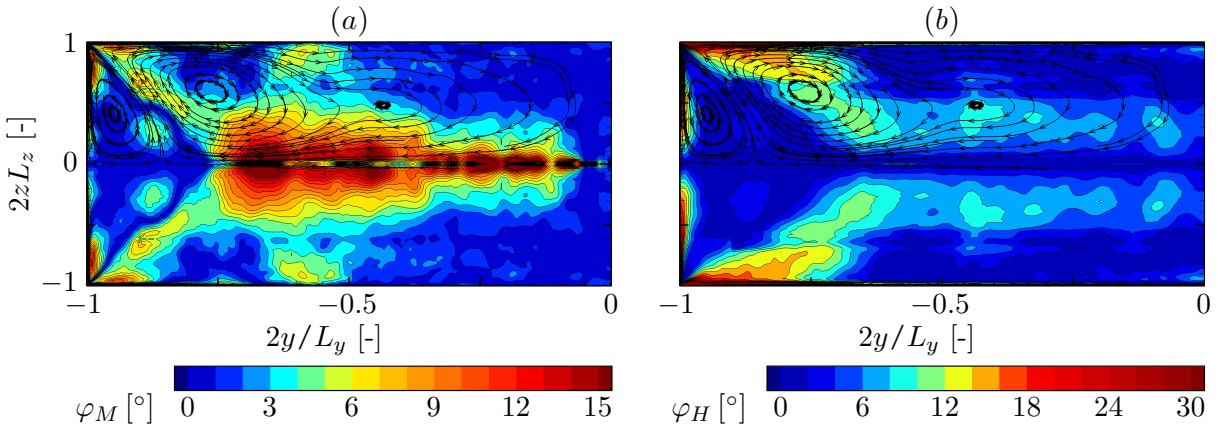

Figure 3.27: Distribution of the angles φ_M and φ_H in the lower half of the heated duct cross-section at a streamwise location of 595 mm, see equation 3.5 for the angle definition. Streamwise averaging is performed over 10 mm and the duct symmetry is utilised. The contour lines are drawn in steps of 1°.

The cross-sectional angle distributions defined by equation 3.5 are shown in figure 3.27. In regions influenced by the corner vortices both the values for φ_M as well as φ_H differ significantly from zero. Consequently, turbulence models based on an isotropic eddy viscosity and diffusivity fail in these areas. Nevertheless, for a specific location in the cross-section we are able to deduce an optimal eddy viscosity ν_t and eddy diffusivity α_t employing the least square method, leading to the definitions

$$\nu_t = \frac{\mathbf{v}_{\nu_t,fluc} \cdot \mathbf{v}_{\nu_t,grad}}{|\mathbf{v}_{\nu_t,grad}|^2}, \qquad \alpha_t = \frac{\mathbf{v}_{\alpha_t,fluc} \cdot \mathbf{v}_{\alpha_t,grad}}{|\mathbf{v}_{\alpha_t,grad}|^2}. \tag{3.6}$$

Figure 3.28 shows the streamwise development of the cross-sectional turbulent Prandtl number distribution along the heated duct. The evaluation is restricted to regions, where the local heating surpasses a threshold value of $\overline{T} - T_b = 0.05\,\mathrm{K}$. The Pr_t value range lies approximately between 0 and 1.3 in figure 3.28, which agrees well with data available in the literature, e.g. with Kang and Iaccarino (2010) using liquid water at a lower temperature, but a comparable temperature difference $T_w - T_b$.

For a detailed discussion of the Pr_t-distribution we focus on the duct end cross-section in figure 3.28 (d). In the immediate vicinity of the heated wall centre the turbulent Prandtl number reaches $Pr_t \approx 0.89$. Above the heated wall, we observe a dome-shaped region of enhanced turbulent Prandtl number coinciding with the influence region of the two smaller corner vortices. Hence, this increase is attributed to the mixing by the secondary flow. In the centre of this region, where the interaction of the small corner vortices leads to a strong upwards flow, a local maximum can be found with Pr_t reaching ≈ 1.06. This maximum is located slightly below the maximum $\overline{v}$-velocity. The dome-shaped area is limited by the interaction zone of the small and the related large corner vortex both transporting relatively cold fluid into the duct corner. In this border area Pr_t drops to values between ≈ 0.9 and ≈ 0.95. The mixing of the large corner vortices also leads to an area of enhanced turbulent Prandtl number. However, due to

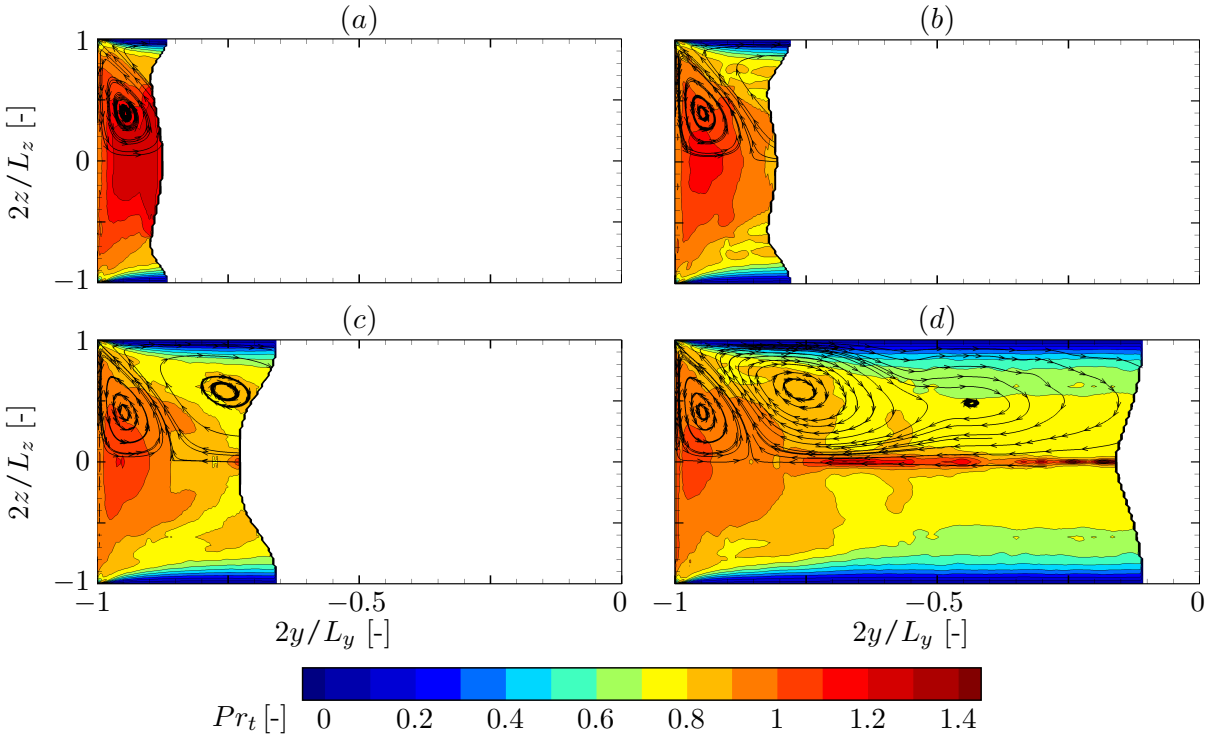

Figure 3.28: Turbulent Prandtl number distribution in the lower half of the heated duct cross-section at streamwise locations of (a) $x = 25\,\text{mm}$, (b) $x = 50\,\text{mm}$, (c) $x = 100\,\text{mm}$ and (d) $x = 595\,\text{mm}$. Streamwise averaging is performed over 10 mm and the duct symmetry is utilised. Pr_t is calculated where $\overline{T} - T_b > 0.05\,\text{K}$ and the contour lines are drawn in steps of 0.1.

the proximity of the adiabatic walls the Pr_t-levels are lower than in the small vortex influence zone. In the large vortex core Pr_t approaches ≈ 0.84 versus $Pr_t \approx 0.94$ in the small vortex core. Along the lateral sidewalls α_t is two orders of magnitude larger than ν_t leading to a turbulent Prandtl number of almost zero, which is a consequence of the adiabatic wall boundary condition and the chosen cross-sectional Pr_t definition. In spanwise direction Pr_t increases steadily from the sidewalls towards the $z = 0$ centre line. Depending on the considered y-location the local maximum lies either in the small or large vortex influence region, or for $2y/Ly > -0.7$ in a narrow maximum band stretching along the centre line. There, the global maximum is located with $Pr_t = 1.3$, situated slightly above the minimum $\overline{v}$-velocity in the interaction zone of the two large vortices.

From figures 3.28 (a) to (d) the turbulent Prandtl number levels in the vicinity of the heated wall drop continuously along the duct length. The local maximum values within the dome-shaped region drop from 1.28 at $x = 25\,\text{mm}$ over 1.16 at $x = 50\,\text{mm}$ and 1.11 at $x = 100\,\text{mm}$ to 1.06 at $x = 595\,\text{mm}$. Furthermore, the location of the local maximum moves slightly closer towards the heated wall. Close to the lateral sidewall, the variations in streamwise direction are smaller compared to those in the centre as this location is strongly influenced by the adiabatic wall boundary layer. Based on the Pr_t-distributions we conclude that the assumption of a constant value for the turbulent Prandtl number for asymmetrically heated duct flows is invalid. For a

comparison of our Pr_t-definition with LES and DNS literature data as well as an analysis of the Pr_t behaviour under the additional presence of curvature-induced secondary flow the reader is referred to section 4.3.5.

3.5.5 Turbulence Anisotropy

As the secondary flow field in straight ducts is a consequence of the Reynolds stress tensor anisotropy, we will subsequently analyse the influence of wall heating on turbulence anisotropy. For this investigation we apply the anisotropy-invariant map (AIM) and the barycentric anisotropy map (BAM), see Emory and Iaccarino (2014) for a detailed overview.

The Reynolds stress anisotropy tensor is defined as $a_{ij} = \overline{u_i' u_j'}/(2 \cdot TKE) - \delta_{ij}/3$ with the turbulent kinetic energy $TKE = \overline{u_n' u_n'}/2$ and the Kronecker delta δ_{ij}. Three limiting states are defined forming the vertices of the so-called Lumley triangle: The state of 1-component turbulence, for which turbulent fluctuations in one direction are dominant, the state of 2-component turbulence, for which turbulent fluctuations in two directions are much higher than in the third direction, and the state of 3-component isotropic turbulence, where fluctuations in all directions are equally high (Lumley, 1979; Choi and Lumley, 2001). Any anisotropy state a_{ij} can be described as a convex combination of these three limiting states, i.e. every realisable state has to reside within the borders of the Lumley triangle. The construction of the AIM is based on the anisotropy tensor eigenvalues λ_i. The two axes are the second and third invariant of the anisotropy tensor with $I_2 = a_{ij}a_{ji}/2 = \lambda_1^2 + \lambda_1\lambda_2 + \lambda_2^2$ and $I_3 = a_{ij}a_{jn}a_{ni}/3 = -\lambda_1\lambda_2\,(\lambda_1 + \lambda_2)$, respectively. The location of a certain turbulence state in the AIM then describes the shape of the Reynolds stress tensor, see Simonsen and Krogstad (2005).

Figure 3.29 presents the AIM for the heated and adiabatic case evaluated along the duct midplane at $z = 0$ and close to the lateral wall at $2z/L_z = 0.95$. The AIM describes the evolution of the turbulence anisotropy along the y-direction starting at the heatable wall and ending in the duct core at $y = 0$. For the duct midplane in figures 3.29 (a, b) the anisotropy development resembles that of a plane channel or boundary layer flow, cf. Banerjee et al. (2007) and Pasquariello et al. (2014). The trajectory starts at the 2-component limit edge and moves upwards in direction of the 1-component limit until the maximum anisotropy is reached in the buffer layer at $y^+ = 6.4$ for the adiabatic case. The trajectory then turns and follows a path parallel to the axisymmetric expansion limit until a kink in the log layer. Finally a state close to isotropic turbulence is reached at the duct symmetry line. For the second location at $2z/L_z = 0.95$, figures 3.29 (c, d) show an overall similar behaviour, but also the significant lateral wall influence. The trajectory starts closer to the 2-component axisymmetric limit and moves upwards to the 1-component limit. In contrast to the duct centre trajectory, the off-centre trajectory follows a steeper path than the axisymmetric expansion curve after the turning point, no kink exists in the log layer and in the duct centre the state of isotropic turbulence is not reached.

The wall heating effect on turbulence anisotropy is overall relatively small, restricted to the heated wall vicinity and more pronounced close to the lateral wall as compared to the duct midplane. The start points of both trajectories are situated at the 2-component limit and are shifted further towards the 1-component limit compared to the adiabatic case. Within the buffer

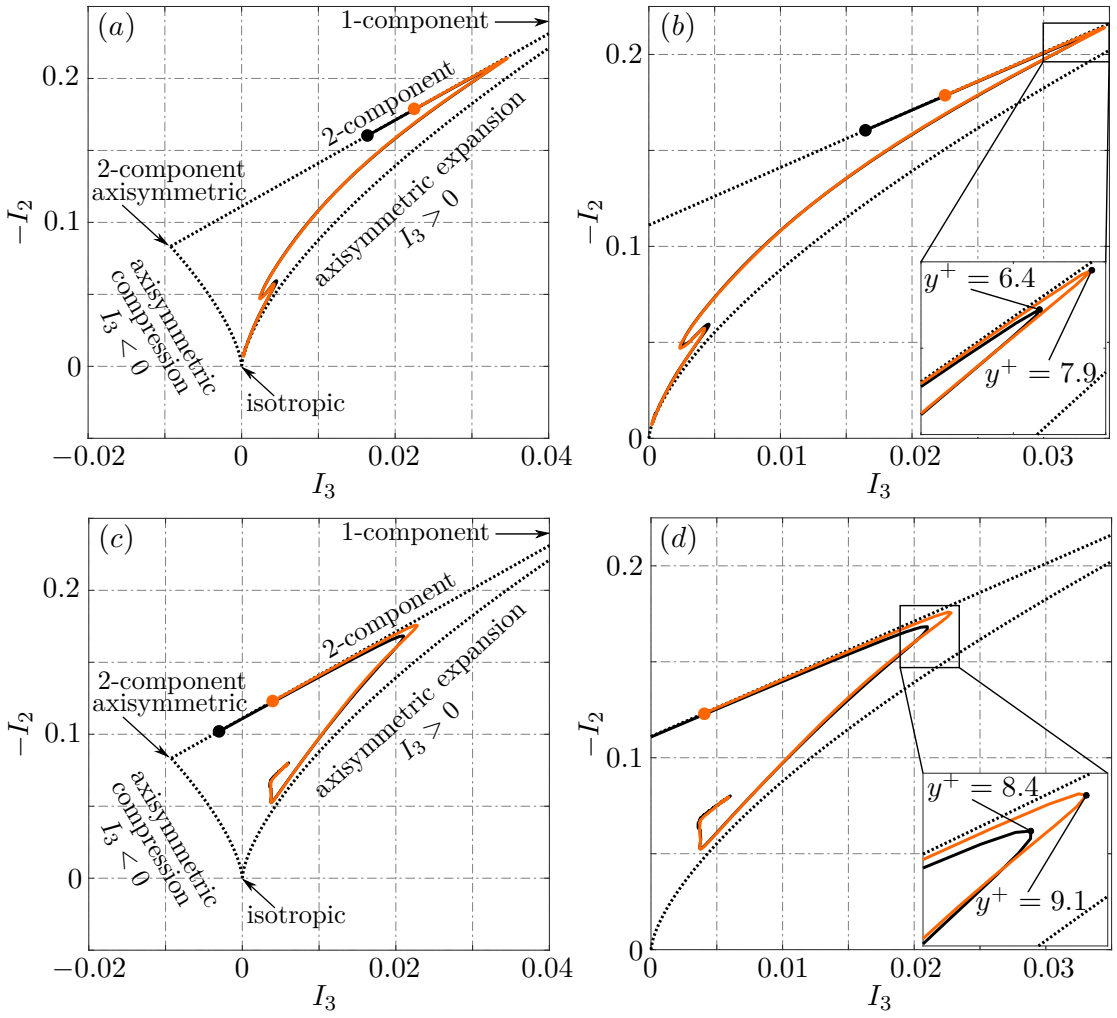

Figure 3.29: Reynolds stress AIM for the adiabatic (——) and the heated duct (——) evaluated along the y-lines (a, b) $2z/L_z = 0$ and (c, d) $2z/L_z = 0.95$ from the heatable wall to the duct core. The limiting states are defined by the Lumley triangle, and the wall values are represented by (•) and (•), respectively.

layer the heated duct trajectories follow a path slightly closer to the 2-component limit. The turning point of maximum anisotropy lies still within the buffer layer, however, it is located closer to the upper right corner of the Lumley triangle. Moreover, in figure 3.29 (a, b) a slight change of the kink in the log layer area is visible.

As the heating-induced changes are limited to the near-wall area, we investigate the anisotropy tensor components there in detail and compare our findings qualitatively with the results by Patel et al. (2016), who analysed the influence of viscosity gradients on the near-wall turbulence anisotropy of a channel flow configuration. In figure 3.30 we observe the same trends as Patel et al. (2016): the streamwise component of the Reynolds stress anisotropy tensor $\overline{a_{xx}}$ increases, and the spanwise component $\overline{a_{zz}}$ decreases with heating applied. Patel et al. (2016) reported

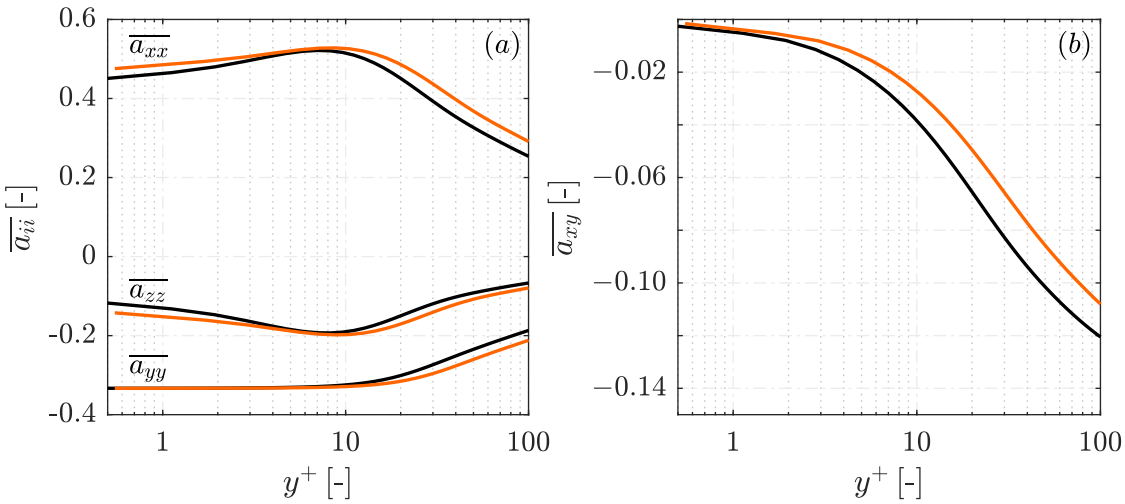

Figure 3.30: Midplane distribution of (a) diagonal components and (b) off-diagonal component $\overline{a_{xy}}$ of the Reynolds stress anisotropy tensor along the heated wall-normal direction for the adiabatic (——) and the heated duct (——).

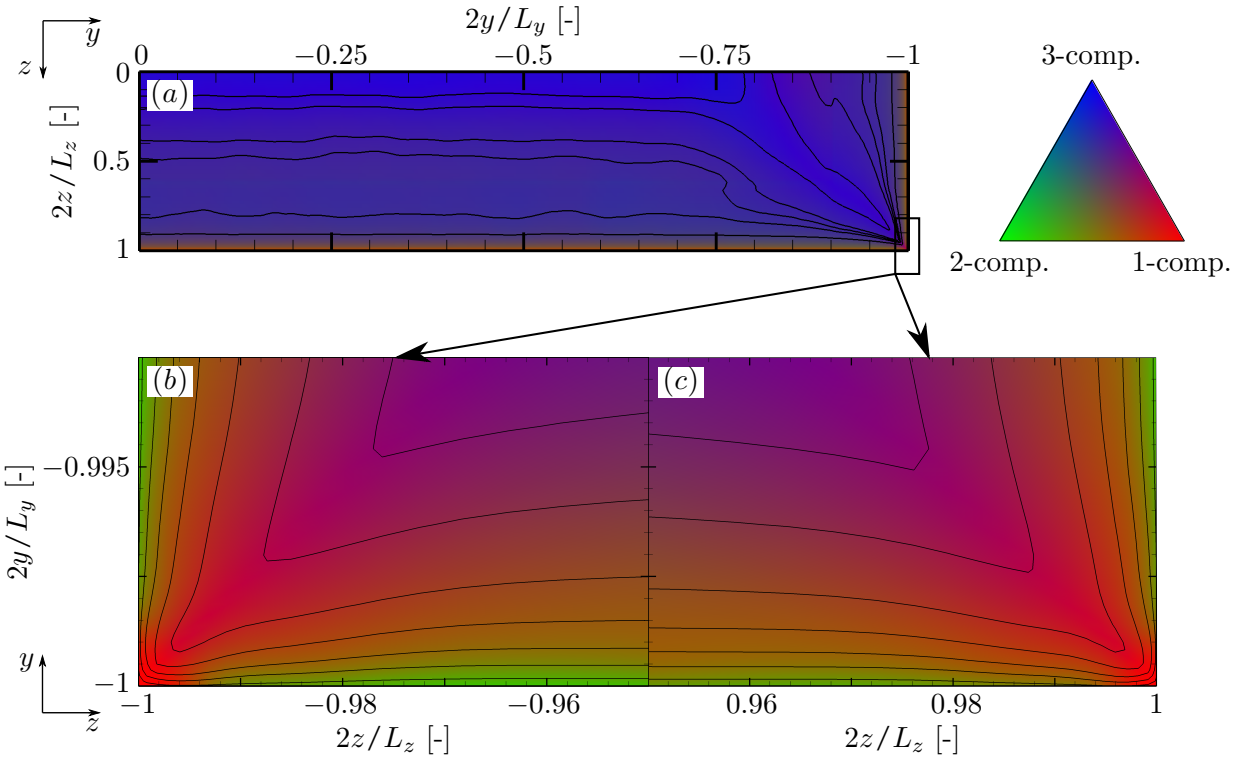

Figure 3.31: Barycentric anisotropy map illustrating regions of 1-, 2- and 3-component turbulence with (a) lower left quadrant of the adiabatic duct, (b) zoom into the lower left corner of the adiabatic duct and (c) the same detail for the heated duct (opposite corner shown). The isolines denote a constant 3-component turbulence fraction.

that the wall-normal component $\overline{a_{yy}}$ remains unaffected, however, in our case a decrease starting within the buffer layer is visible. The normalised turbulent shear stress $\overline{a_{xy}}$ in figure 3.30 (b) increases, indicating an augmented momentum transfer. The off-diagonal components $\overline{a_{yz}}$ and $\overline{a_{xz}}$ are negligible in the duct midplane.

In contrast to the classical AIM, the so-called barycentric map proposed by Banerjee et al. (2007) provides a more intuitive tool to analyse the turbulence anisotropy. The construction again is based on the eigenvalues λ_i of the Reynolds stress anisotropy tensor and relies on the fact, that any realisable turbulence state can be represented as a combination of the three limiting states of 1-, 2- and 3-component turbulence. The limiting states are now defined as the corners of an equilateral triangle with $\mathbf{x}_{1c} = (1, 0)$, $\mathbf{x}_{2c} = (0, 0)$ and $\mathbf{x}_{3c} = (1/2, \sqrt{3}/2)$. The coordinates of a certain turbulent state are then computed as $\mathbf{x} = C_{1c}\mathbf{x}_{1c} + C_{2c}\mathbf{x}_{2c} + C_{3c}\mathbf{x}_{3c}$. In contrast to the AIM, the BAM is a linear anisotropy invariant map, where the coordinates depend linearly on the eigenvalues with $C_{1c} = \lambda_1 - \lambda_2$, $C_{2c} = 2\,(\lambda_2 - \lambda_3)$ and $C_{3c} = 3\lambda_3 + 1$ ensuring $\sum C_{ic} = 1$. For visualisation the coefficient vector C_{ic} is mapped to the RGB triplet. Red corresponds to 1-component, green to 2-component and blue to 3-component turbulence.

Figure 3.31 (a) shows the application of the barycentric map combined with the RGB colouring for the lower left quadrant of the adiabatic duct. In the duct core the state of isotropic turbulence is almost reached, and in the vicinity of the walls a mixture of 2- and 1-component turbulence is found. As noted previously using the AIM, the 2-component turbulence transitions to 1-component turbulence in the buffer layer. In the duct corner 1-component turbulence is dominant as fluctuations perpendicular to the two walls are suppressed. The influence of the corner vortices on the turbulence anisotropy distribution is clearly visible in the C_{3c}-isolines with the mean secondary flow transporting fluid from the isotropic core region into the duct corner following approximately the corner bisecting line. Figures 3.31 (b, c) show the influence of the wall heating for the duct corner region. In the vicinity of the heatable wall, we observe for the heated case a reduction of 2-component turbulence in favour of 1- and 3-component turbulence. At the adiabatic upper wall (not shown) the turbulence anisotropy remains identical for both cases. The C_{3c}-isolines illustrate the anisotropy reduction in this region as an anisotropy measure can be defined as $C_{ani} = 1 - C_{3c}$ (Banerjee et al., 2007). As C_{3c} increases in the near-wall region, the flow becomes more isotropic leading in turn to the observed weakening of the secondary flow over the duct length.

3.5.6 Length Scales of Turbulent Structures

As previously discussed the increasing temperature and the associated viscosity reduction effectuate a reduction of size and strength of the ejections and streaky structures, see section 3.5.3. For air as working fluid Salinas-Vásquez and Métais (2002) have shown, that the ejections and streaks as well as turbulent length scales are growing with increasing viscosity. Consequently, we expect in the current case using water as working fluid a reduction of the turbulent length scales when heating is applied.

At first, we analyse the turbulent length scales qualitatively in a plane parallel to and directly above the heatable wall at $2y/L_y = 0.9975$. The chosen plane location corresponds to $y^+ = 16.1$ for the adiabatic duct and to $y^+ = 24.2$ for the heated duct end section with y^+ evaluated

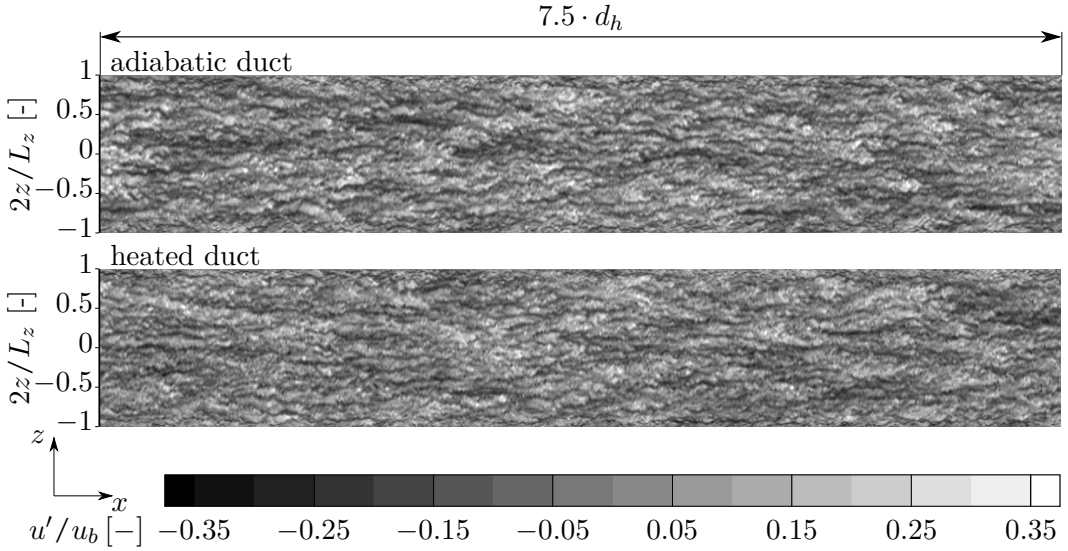

Figure 3.32: Streamwise velocity fluctuations in the heatable wall-parallel plane at $2y/L_y = 0.9975$ for the adiabatic and the heated duct.

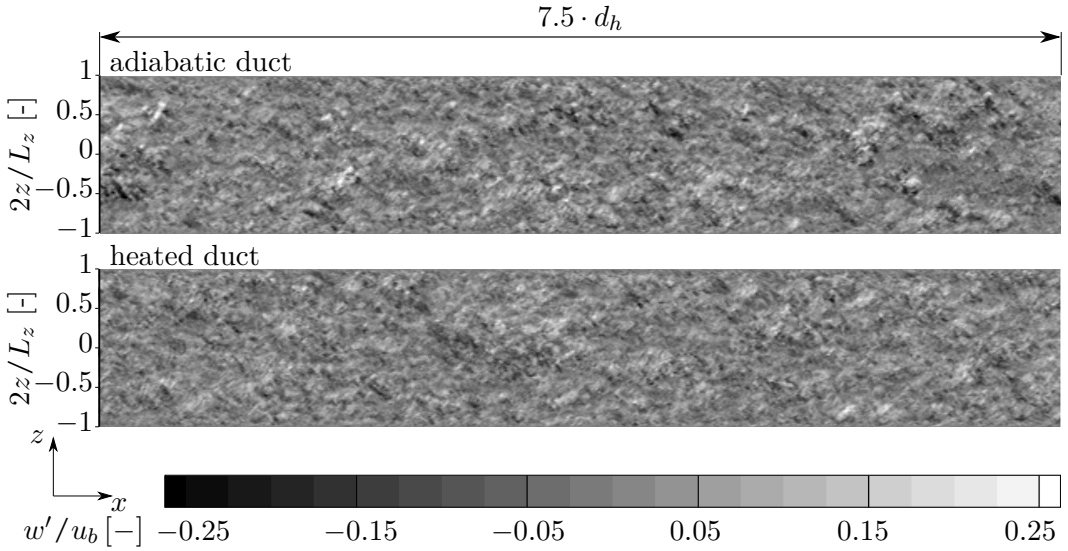

Figure 3.33: Spanwise velocity fluctuations in the heatable wall-parallel plane at $2y/L_y = 0.9975$ for the adiabatic and the heated duct.

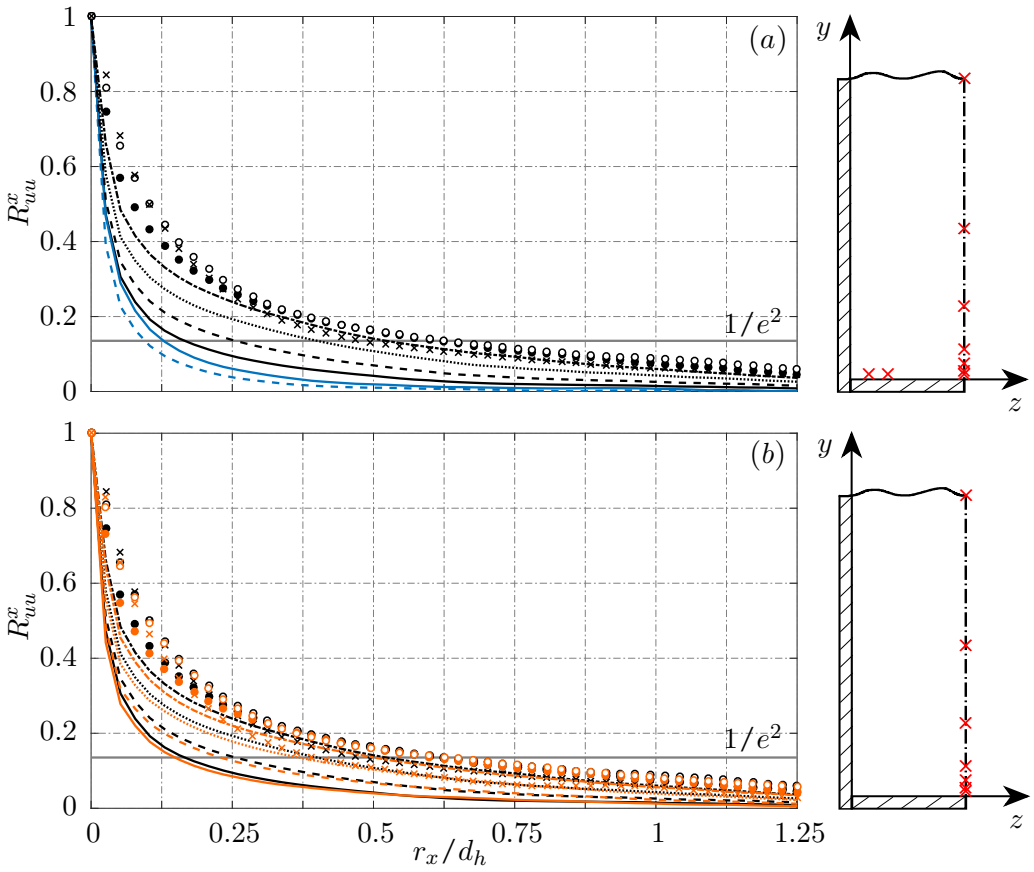

Figure 3.34: Longitudinal autocorrelations of streamwise velocity R^x_{uu} at different locations marked in the sketches on the respective right-hand side. In (a) the adiabatic duct results are shown and in (b) the deviation due to the viscosity modulation. Heated duct correlations are coloured orange and off-centre location correlations blue. The line (——) defines $R^x_{uu} = 1/e^2 = const.$ For figure legend and line parameters see table 3.8.

at the wall centre $2z/L_z = 0$. Figures 3.32 and 3.33 depict streamwise u'/u_b and spanwise velocity fluctuations w'/u_b within this plane. The typical streaky structures of the TBL with the darker regions of comparatively low-speed fluid surrounded by lighter regions of high-speed fluid are visible in figure 3.32. Due to the lateral wall boundary and its restricting influence the streaks towards the duct corners are thinner and shorter compared to those present in the centre. As the streak size scales with the viscous thickness and based on previous studies, a reduction of streak size as well as turbulent length scales in the heated duct is to be expected (Salinas-Vásquez and Métais, 2002; Zonta et al., 2012; Lee et al., 2013). However, the visual qualitative comparison of the two snapshots does not allow to draw a certain conclusion regarding differences in turbulent structures. For the spanwise fluctuations in figure 3.33 the same outcome is obtained. Consequently, we assume the heating in our case too weak to produce a distinct visual difference.

The use of autocorrelations allows for a quantitative investigation of turbulent length scales

and their respective change. In order to reduce the required sample number for a converged result, we assume local homogeneity in streamwise direction for the definition of the longitudinal autocorrelation function of the u-velocity R^x_{uu} (Pirozzoli et al., 2004). The sampling rate is every 25 time steps over a sampling period of 20 FTT with respect to $L_{x,heat}$, leading to a total of $\approx 56.7 \cdot 10^3$ samples utilised. The integral length scale is generally defined as $L^j_{ii} = \int_0^\infty R^j_{ii}(r_j)\, dr_j$. For the upper bound of integration, a finite value $r_{lim,j}$ has to be specified. O'Neill et al. (2004) proposed two methods: the integration up to the first zero-crossing of the correlation or up until the correlation function has fallen to a value of $1/e$. However, as the latter cuts off a large part of the correlation function, it tends to underestimate the turbulent length scale. Consequently we use a modified limit of $1/e^2$, so that $r_{lim,j}$ is defined as $r_{lim,j} = r_j(R^j_{ii} = 1/e^2)$.

Figure 3.34 shows the longitudinal autocorrelation functions R^x_{uu} at various (y/z)-positions for the heated and adiabatic duct section. All positions are located in the vicinity of the heatable wall, i.e. in the area influenced by the small corner vortices except for $R^x_{uu,7}$, which lies in the area influenced by the large corner vortices, see table 3.8 for line parameters and turbulent length scales. Figure 3.34 (a) allows for two observations: first the trivial result, that with increasing distance from the heatable wall the turbulent structures grow larger at a diminishing growth rate for each R^x_{uu}-curve, except for $R^x_{uu,7}$ at $2y/L_y \approx -0.8$, where a reduction in turbulent length scale is present. Second, the structures become significantly smaller towards the duct corner due to the increasing influence of the lateral wall. Comparing the turbulent length scales in the plane of figure 3.32 for the duct centre position $R^x_{uu,1}$ with the two off-centre positions $R^x_{uu,1a}$ and $R^x_{uu,1b}$, we measure a reduction of -15.0% and -34.7%, respectively. Further away from the wall the $2y/L_y = const$ correlation-triplets follow a similar trend. With help of figure 3.34 (b) we investigate the influence of the viscosity modulation on turbulent length scales L^x_{uu}. The expected heating induced shortening is noticeable for all considered locations with high values reached especially close to the heated wall, where the highest temperature and viscosity drop is present, e.g. at $y^+ = 16.1$ a maximum value of -10.2% is obtained. Upwards along the duct midplane, the reduction in the small corner vortex region becomes increasingly weaker, see table 3.8. However, the viscosity change does not only affect the immediate vicinity of the heated wall, but also the duct centre due to the modified secondary flow transport. This becomes apparent by comparing $R^x_{uu,6}$ at $2y/L_y \approx -0.9$ and $R^x_{uu,7}$ at $2y/L_y \approx -0.8$, the former being located in the influence region of the small corner vortices and the latter in that of the large corner vortices. The former experiences a viscosity drop approximately twice as large as the latter, but the length scale reduction increases noticeably from -1.6% for $R^x_{uu,6}$ to -14.8% for $R^x_{uu,7}$. Consequently, the turbulent length scale reduction is not a mere function of $\Delta\overline{T}$, but depends on the specific location as the viscosity modulation affects turbulent transport as well as the transport by secondary flows and both influence L^x_{uu}. This argument is supported by comparing the off-centre locations, exemplarily $R^x_{uu,1}$ with $R^x_{uu,1a}$ and $R^x_{uu,1b}$. The relative shortening in the centre is with -10.2% significantly higher than the -4.7% and -4.3%. Indeed the small vortices above the heatable wall produce a non-uniform viscosity and temperature distribution in spanwise direction, $\Delta\overline{T} = 19.6\,\mathrm{K}$ in the centre versus $\Delta\overline{T} = 17.9\,\mathrm{K}$ and $\Delta\overline{T} = 17.6\,\mathrm{K}$ towards the lateral wall. However, this $\Delta\overline{T}$-difference and the associated differing viscosity is too small as to explain the large deviation in length scale shortening and thus is concluded to be a secondary flow effect.

curve	style	$2y/L_y$	$y^+\|_a/y^+\|_h$	ΔT [K]	$\frac{\nu_h-\nu_a}{\nu_a}$	$L^x_{uu}\|_a/L^x_{uu}\|_h$	$\frac{L^x_{uu}\|_h-L^x_{uu}\|_a}{L^x_{uu}\|_a}$
$R^x_{uu,1}$	(——)	−0.9975	16/ 24	19.6	−22.8%	5.19/ 4.66	−10.15%
$R^x_{uu,1a}$	(——)	−0.9975	16/ 24	17.9	−21.2%	4.41/ 4.20	− 4.74%
$R^x_{uu,1b}$	(- - - - - -)	−0.9975	16/ 24	17.6	−20.9%	3.39/ 3.24	− 4.29%
$R^x_{uu,2}$	(- - - - - -)	−0.9953	30/ 45	17.0	−20.3%	7.27/ 6.54	−10.04%
$R^x_{uu,3}$	(·····)	−0.9905	61/ 91	14.9	−18.2%	11.11/10.08	− 9.30%
$R^x_{uu,4}$	(-·-·-)	−0.9811	121/ 182	13.2	−16.4%	15.04/13.92	− 7.45%
$R^x_{uu,5}$	(•)	−0.9528	302/ 455	10.8	−13.8%	18.27/17.65	− 3.37%
$R^x_{uu,6}$	(○)	−0.9019	627/ 945	8.1	−10.7%	19.90/19.59	− 1.55%
$R^x_{uu,7}$	(×)	−0.8029	1259/1898	4.0	− 5.5%	16.86/14.37	−14.75%

Table 3.8: Parameters for the longitudinal autocorrelations of streamwise velocity shown in figure 3.34. Listed are positions, dimensionless height above the heatable wall, temperature increase, viscosity drop, integral length scales and their relative change due to the viscosity modulation. All R^x_{uu} are evaluated in the duct centre $z = 0$ except for $R^x_{uu,1a}$ at $2z/L_z = 2/3$ and $R^x_{uu,1b}$ at $2z/L_z = 5/6$. The lengths L^x_{uu} are normalised by a factor of $(100 \cdot d_h)$.

figure	curve	style	$2y/L_y$	$2z/L_z$	ΔT[K]	$\frac{\nu_h-\nu_a}{\nu_a}$	$L^z_{ii}\|_a/L^z_{ii}\|_h$	$\frac{L^z_{ii}\|_h-L^z_{ii}\|_a}{L^z_{ii}\|_a}$
(*a*)	$R^z_{uu,1,lw}$	(——)	−0.9975	1.00	22.5	−25.3%	0.49/0.34	−31.09%
	$R^z_{uu,2,lw}$	(-·-·-)	−0.9811	1.00	13.0	−16.2%	0.48/0.42	−12.96%
	$R^z_{uu,3,lw}$	(·····)	−0.9528	1.00	10.0	−12.9%	0.60/0.49	−17.71%
(*b*)	$R^z_{uu,1}$	(——)	−0.9975	0.74	17.5	−20.8%	0.51/0.50	− 1.89%
	$R^z_{uu,2}$	(-·-·-)	−0.9811	0.74	11.0	−14.0%	1.61/1.59	− 1.11%
	$R^z_{uu,3}$	(·····)	−0.9528	0.74	8.7	−11.4%	2.43/2.36	− 3.12%
(*c*)	$R^z_{ww,1,lw}$	(——)	−0.9975	1.00	22.5	−25.3%	0.29/0.26	−10.45%
	$R^z_{ww,2,lw}$	(-·-·-)	−0.9811	1.00	13.0	−16.2%	0.30/0.27	−10.60%
	$R^z_{ww,3,lw}$	(·····)	−0.9528	1.00	10.0	−12.9%	0.32/0.29	− 8.45%
(*d*)	$R^z_{ww,1}$	(——)	−0.9975	0.74	17.5	−20.8%	0.78/0.82	5.19%
	$R^z_{ww,2}$	(-·-·-)	−0.9811	0.74	11.0	−14.0%	2.14/2.17	1.40%
	$R^z_{ww,3}$	(·····)	−0.9528	0.74	8.7	−11.4%	2.90/2.90	0.16%

Table 3.9: Autocorrelation parameters of stream- and spanwise velocity in z-direction, see figure 3.35. $R^z_{ii,k,lw}$ denote the curves evaluated at the lateral wall and $R^z_{ii,k}$ the ones at $2z/L_z = 0.74$. Listed are the position of the correlations, temperature increase, viscosity drop, integral length scales and their relative heating-induced change. All L^z_{ii} are normalised by a factor of $(100 \cdot d_h)$.

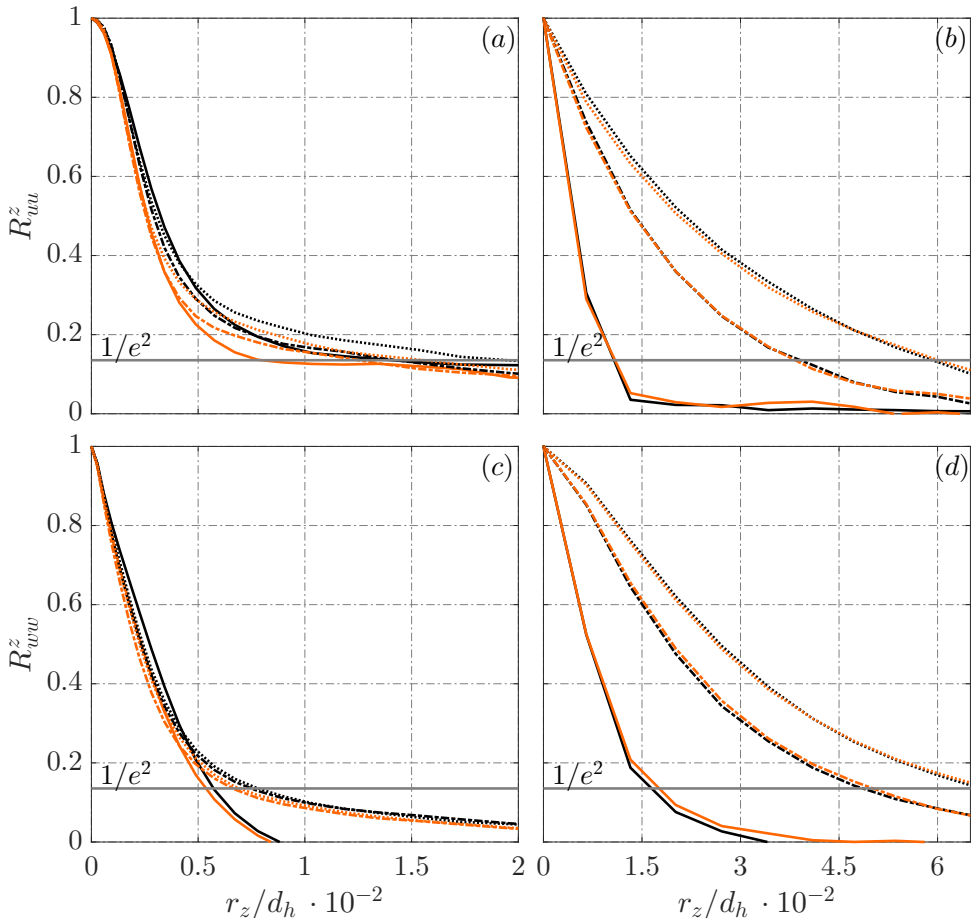

Figure 3.35: Transversal autocorrelations of streamwise velocity R^z_{uu} in (a, b) and longitudinal autocorrelations of spanwise velocity R^z_{ww} in (c, d) at different locations. In (a, c) the correlations at the lateral wall are shown and in (b, d) the ones at $2z/L_z = 0.74$. Results for the adiabatic duct are coloured black and for the heated duct orange. The line $R^z_{ii} = 1/e^2$ used to determine $r_{lim,z}$ is marked by (——). For figure legend and line parameters see table 3.9.

For the turbulent length scales in spanwise direction, specifically for the transverse autocorrelations R^z_{uu} and the longitudinal autocorrelations R^z_{ww}, data is gathered along a z-line with the same sampling parameters as before and evaluated following Pope (2000). Additionally, a quadrant-averaging is performed to utilise the symmetry with respect to the y-axis. The parameters for the correlations are listed in table 3.9. First, the results for the adiabatic case are discussed and subsequently the changes due to heat transfer are analysed at two specific spanwise locations.

In figure 3.35 (a, b) transversal correlations of streamwise velocity in spanwise direction R^z_{uu} are depicted. With increasing distance from the heatable wall the turbulent structures at both considered locations, i.e. adjacent to the lateral wall $L^z_{uu,k,lw}$ and at $2z/L_z = 0.74$ $L^z_{uu,k}$ grow in size. The $L^z_{uu,k,lw}$ growth is limited by the strong restricting influence of the lateral wall, see table 3.9, the length scales $L^z_{uu,k}$ are consequently larger. The longitudinal correlations R^z_{ww} are

shown in figure 3.35 (c, d). The $L^z_{ww,k}$ are consistently larger than the $L^z_{uu,k}$, whereas close to the lateral wall the scales $L^z_{ww,k,lw}$ are shorter than the $L^z_{uu,k,lw}$ as spanwise fluctuations are blocked by the wall boundary. The integral length scales support quantitatively the qualitative evaluation of turbulent structures in figures 3.32 and 3.33, for which the visual analysis results in the streaky structures to be noticeably more elongated than the structures in the w'-plot. This observation is supported quantitatively by the ratios of integral length scales being $L^x_{uu}/L^z_{uu} \approx 7.6$ and $L^x_{ww}/L^z_{ww} \approx 2.8$ at $2z/L_z = 0.74$ within the plane depicted in figures 3.32 and 3.33.

When heating is applied, we observe close to the lateral wall a significant reduction of $L^z_{uu,k,lw}$ by up to -31.1% and of $L^z_{ww,k,lw}$ by up to -10.6%. At $2z/L_z = 0.74$ however, no definite trend is visible. The $L^z_{uu,k}$ at all three considered positions are slightly shortened and the $L^z_{ww,k}$ increase slightly, showing again that the length scale change is not a mere function of the local viscosity drop. Additionally, the integral length scale ratios of the turbulent structures change. At $2y/L_y = -0.9975$ and $2z/L_z = 0.74$, the ratio of streamwise to spanwise length scale reduces from $L^x_{uu}/L^z_{uu} \approx 7.6$ to ≈ 7.4 and that for the spanwise velocity from $L^x_{ww}/L^z_{ww} \approx 2.8$ to ≈ 2.6.

4 Curved Heated HARCD Simulations (CATUM)

In the following the results for the asymmetrically heated curved HARCD configurations using air as working fluid are presented. The configurations are based on the previous straight water HARCD investigations and accordingly the experimental HARCD set-up. The simulations have been performed using the in-house LES flow solver CATUM at a reduced Reynolds number of $Re_b = 40 \cdot 10^3$ to lower computational costs, and thus allow for consideration of multiple configurations. The current chapter possesses a similar structure as the previous chapter 3 of the straight water HARCD: at first the computational set-up is introduced followed by an assessment of the achieved numerical accuracy compared to both DNS and previous INCA LES results for the square duct case of Pirozzoli et al. (2018). The subsequent discussion of the flow field results focuses again on the interaction of asymmetrical heat transfer and turbulence-induced secondary flow with increasing viscosity towards the heated wall contrary to the water HARCD. The analysis is then expanded by an investigation of the interaction of turbulence- and additionally evolving curvature-induced secondary flow, and the effects of the resulting secondary flow field on mean flow and turbulence statistics, turbulent heat transfer and validity of the constant turbulent Prandtl number assumption.

4.1 Computational Set-up

Based on the heated water HARCD set-up presented in section 3.2, three curved HARCD configurations are derived. Within the current section these set-ups are presented including their respective characteristic non-dimensional numbers and boundary conditions as well as the simulation procedure.

The main differences with respect to the previous set-up are motivated by the additional curved duct section and the usage of the compressible LES flow solver CATUM allowing for contour-adaptive grids. In order to investigate multiple configurations at different curvature radii at affordable numerical costs, the following additional changes with respect to the set-up of section 3.2 are adopted:

- reduction of the straight heated duct length $L_{x,heat,straight}$ to $\approx 1/3$ of the previous value leading to $L_{x,heat,straight} = 21.5 \cdot d_h = 209.32\,\mathrm{mm}$
- reduction of the Reynolds number from $Re_b = 110 \cdot 10^3$ to $Re_b = 40 \cdot 10^3$ and $Re_b = 17.8 \cdot 10^3$, respectively (results for the latter not shown in the present work)
- change of the cooling fluid from liquid water to ideal gas air in order to increase the possible explicit time step size of the compressible solver depending on the speed of sound

	$L_x \times L_y \times L_z$ [mm^3]	$u_{b,in}$ [m/s]	T_b [K]	T_w [K]	$\overline{p}_{out}$ [Pa]	$\overline{p}_{in}$ [Pa]
D_{per} /RC60	$72.2 \times 25.8 \times 6$	78.042	333.15	333.15	102054	102054
D_{heat}/RC60	$219.1 + 94.2 \times 25.8 \times 6$	78.195	333.15	438.15	98100	101054
D_{per} /RC180	$72.2 \times 25.8 \times 6$	78.042	333.15	333.15	102054	102054
D_{heat}/RC180	$219.1 + 94.2 \times 25.8 \times 6$	78.380	333.15	438.15	98100	100820
D_{per} /RC900	$72.2 \times 25.8 \times 6$	78.042	333.15	333.15	102054	102054
D_{heat}/RC900	$219.1 + 141.4 \times 25.8 \times 6$	78.175	333.15	438.15	98100	101080

Table 4.1: Geometry and flow parameters for the curved HARCD set-ups. The streamwise length L_x is the duct centre value and D_{heat} comprises the straight and the curved section. L_x denotes the streamwise, L_y the heated wall normal and L_z the spanwise dimensions.

- choosing the temperature range of T_b and T_w such that on the one hand the flow can still be considered as incompressible ($Ma_{max} = 0.272 < 0.3$) for a relatively high u_b to allow for faster flow through times, and that on the other hand the viscosity ratio of the curved HARCD simulation is the inverse of the previous water HARCD simulation $(\nu_w/\nu_b)_{air\ duct} \approx (\nu_b/\nu_w)_{water\ duct}$

The computational set-ups are shown in figure 4.1 and consist each of three domains, for geometrical and flow parameters see table 4.1. All three domains are computed simultaneously. As in the previous set-up a periodic precursor simulation is used as a time-resolved turbulent inflow generator for a spatially resolved straight heated section $D_{heat,straight}$. D_{per} has a similar length as for the water HARCD of $L_{x,per} \approx 7.4 \cdot d_h$ and the streamwise bulk velocity is again kept constant using a PI-controller. The length $L_{x,heat,straight}$ has been shortened to $21.5 \cdot d_h$, which equates to $\approx 3 \cdot L_{x,per}$. After the straight section a curved heated section follows with a varying curvature radius of 60 mm, 180 mm and 900 mm. The streamwise length measured in the duct centre $L_{x,heat,curved}$ is identical for configurations RC60 and RC180 and is based on the 90°-bend case with $r_c = 60$ mm. For RC900 the curved section has been elongated by 50% after initial simulation runs to allow for a further development of the secondary flow field. At the end of the curved parts two block rows of streamwise length $1 \cdot d_h$ and progressively coarser meshing are tangentially attached in order to increase the distance to the outlet, and thus diminish the influence of the boundary condition on the bend flow field. These additional block rows are not shown in figure 4.1.

At the inlet of $D_{heat,straight}$ a zero-gradient Neumann type BC is set for the pressure and likewise implicitly for the density ρ via the equation of state. For the temperature and the velocity vector $\mathbf{u}$ extracted from D_{per} a Dirichlet type BC is utilised. The cross-sectional temperature profile is reset to $T(y,z) = T_b = const.$ The velocity profile is modified to obtain the same Re_b for both domains with $\nu_b \approx f(T_b)$ in the considered pressure range, i.e. the momentum $(\rho\,\mathbf{u})$ is kept constant over the interface. Hence, the velocity field $\mathbf{u}$ itself is adjusted depending on the instantaneous inlet density and pressure, respectively. At the outlet of the spatially resolved part a zero-gradient Neumann type BC is set for velocity and temperature, and a Dirichlet type BC for pressure. The density again is evaluated based on the EOS as $f(p,T)$. As strong Dean vortices form along the bend leading to a non-uniform cross-sectional pressure profile, the outlet

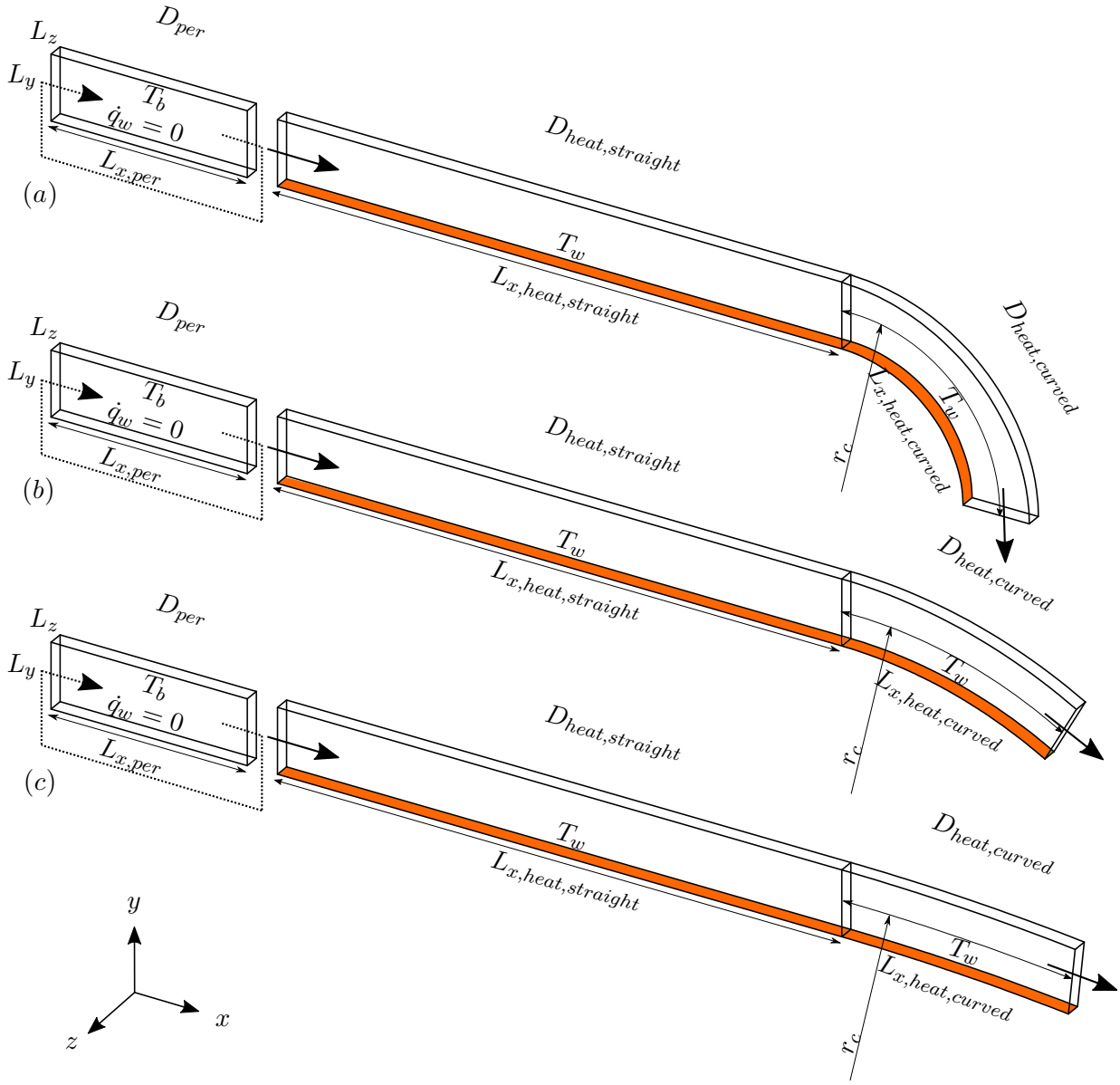

Figure 4.1: Computational curved HARCD set-ups for the cases (*a*) RC60 with r_c = 60 mm / $\alpha = 90°$, (*b*) RC180 with $r_c = 180$ mm / $\alpha = 30°$ and (*c*) RC900 with $r_c = 900$ mm / $\alpha = 6°$. The angle α denotes the angle between the beginning and end of the curved section and r_c the curvature radius. For RC900 an elongated version with $\alpha = 9°$ is mainly used within this work.

pressure BC is defined as an area-averaged pressure over the whole outlet plane. Furthermore, the outlet pressure is set to be reached asymptotically to avoid unphysical repercussions on the duct flow field. All sidewalls are treated as smooth walls. In the periodic section isothermal walls are utilised with $T_w = T_b$ to minimise the heating of the fluid. In the heated domains all sidewalls are defined as adiabatic walls except for the lower heated wall, which is treated as isothermal wall with a fixed wall temperature of $T_w = 438.15\,\mathrm{K}$. To avoid undesired interactions of the wall heating and the inlet BC, a temperature ramp is implemented. From the inlet until $\Delta x = 0.5 \cdot d_h$ the wall temperature is set to $T_w = T_{inlet} = T_b$, then until $\Delta x = 1 \cdot d_h$ the temperature increases linearly to $T_w = 438.15\,\mathrm{K}$ and remains at this value afterwards. For an overview of the case-specific flow parameters the reader is referred to table 4.1.

For the discretisation a contour-adaptive block-structured Cartesian grid is used with cell numbers ranging from $\approx 40.26 \cdot 10^6$ cells for the case $r_c = 60\,\mathrm{mm}$ to $\approx 45.29 \cdot 10^6$ cells for case $r_c = 900\,\mathrm{mm}$. The cross-sectional grid and its blocking structure is shown in figure 4.2 and discussed in detail in the following section 4.2.1.

The simulation procedure follows that of section 3.2 for the incompressible simulations and is extended to take the curvature and compressibility into account. The substeps are:

1. Simulation of D_{per} with initial conditions $T = T_b = 333.15\,\mathrm{K}$, $p = p_{b,init} = 101325\,\mathrm{Pa}$ and the velocity profile for a fully developed laminar duct superimposed with white noise of amplitude $A = 5\%$ following Shah and London (1978). The bulk velocity u_b is set to $u_b = 78.042\,\mathrm{m/s}$ to satisfy $Re_b = 40 \cdot 10^3$. The simulation is carried out until a fully developed turbulent flow state is reached.

2. Perform several RANS simulations for the set-up to determine the outlet pressure p_{out}, which leads to an inlet pressure of $p_{inlet} \approx 101325\,\mathrm{Pa}$. This produces $\rho_{inlet} \approx \rho_{per}$, and thus similar flow velocities across the interface between D_{per} and $D_{heat,straight}$. Consequently, a drop in the time step size of the explicit time integration scheme can be prevented.

3. Initialisation of the heated sections $D_{heat,straight}$ and $D_{heat,curved}$ based on the converged flow field of D_{per}. For the curved section the flow field is rotated accordingly and the temperature set to $T = T_b$ throughout.

4. Simulation of the full set-ups for ≈ 2.25 FTT and then start of the statistical sampling over ≈ 30 FTT with respect to the complete heated section length. A constant iteration-based sampling rate of 250 iterations is applied. The simulations run in parallel on 2688 cores (56 compute nodes) for case RC60, 2736 (57 compute nodes) for case RC180 and 3024 cores (63 compute nodes) for case RC900 on SuperMUC-NG.

In table 4.2 the dimensionless characteristic numbers for the three set-ups are given. The characteristic length scale l_{ref} is set to the hydraulic diameter d_h. The friction Reynolds numbers Re_τ as well as the Prandtl number $Pr|_{y_{min}}$ are defined as local values, whereas the rest of the listed quantities are integral values. The local quantities are evaluated in the middle of the straight section, i.e. at a streamwise distance of 110 mm from the inlet of the heated resolved section, in the centre of the respective sidewall. Additionally, a streamwise averaging over 5 mm is performed in the heated section and over the whole length of D_{per} for the periodic section. The

Domain/Case	Re_b	$Re_\tau\|_{y_{min}}$	$Re_\tau\|_z$	$Pr\|_{y_{min}}$	$Nu_{\overline{xz}}\|_{y_{min}}$	Gr_b	De	Ma_{in}
D_{per} /RC60	$40 \cdot 10^3$	1991	2188	0.7082	–	–	–	0.2125
D_{heat}/RC60	$40 \cdot 10^3$	1492	2161	0.7045	67.71	7961	$11.4 \cdot 10^3$	0.2125
D_{per} /RC180	$40 \cdot 10^3$	1991	2188	0.7082	–	–	–	0.2125
D_{heat}/RC180	$40 \cdot 10^3$	1432	2161	0.7045	61.66	7961	$6.6 \cdot 10^3$	0.2125
D_{per} /RC900	$40 \cdot 10^3$	1991	2188	0.7082	–	–	–	0.2125
D_{heat}/RC900	$40 \cdot 10^3$	1406	2161	0.7045	59.50	7961	$2.9 \cdot 10^3$	0.2125

Table 4.2: Characteristic numbers for the curved HARCD set-ups. D_{heat} comprises the straight and the curved section. The quantities are evaluated in the respective sidewall centre. The values for D_{heat} are measured close to the straight section end at $x = 200\,\text{mm}$ with a streamwise averaging of $\Delta x = 5\,\text{mm}$. Variations in $Re_\tau|_{y_{min}}$ are heating- and curvature-dependent.

Prandtl numbers are evaluated for outlet pressure conditions. In contrast to the water HARCD, the Pr values are not significantly influenced by the heating. The Nusselt number is an integral value for the whole configuration of $D_{heated,straight}$ and $D_{heated,curved}$. As $Gr_b/Re_b^2 = 5 \cdot 10^{-6} \ll 1$ buoyancy effects are negligible, see Wardana et al. (1994). The Dean numbers for the three cases are based on the duct curvature radius measured in its centre and have been chosen, such that $De_{r_c=180} \approx 0.5 \cdot De_{r_c=60}$ and $De_{r_c=900} \approx 0.25 \cdot De_{r_c=60}$.

4.2 Discretisation and Assessment of Numerical Accuracy

The following two sections summarise briefly the results of a further grid sensitivity study performed for the flow solver CATUM, present the numerical discretisation of the three curved HARCD set-ups and assess the numerical accuracy achievable with the chosen resolution. For the latter both the INCA LES results and the DNS data for the square duct case by Pirozzoli et al. (2018) serve as reference.

4.2.1 Grid Generation and Grid Sensitivity Analysis

As for INCA in section 3.3.1 also for the flow solver CATUM an extensive grid sensitivity analysis has been conducted. As reference the periodic unheated square duct case by Pirozzoli et al. (2018), precisely the cases A, C and D with $Re_b = 4410$, $Re_b = 17800$ and $Re_b = 40000$, respectively, have been utilised. For the sake of clarity, the single cases are not shown explicitly, but the main results are summarised briefly. Based on the results of the grid sensitivity analysis the differences of the two LES solvers are discussed and the meshes for the three curved HARCD configurations derived as a trade-off between numerical costs and accuracy.

The case definitions used as part of the sensitivity analysis follow the periodic square duct set-ups of sections 3.3.2 and 4.2.2, and the HARCD periodic duct set-up has been presented in the previous section 4.1. As for the water HARCD grid sensitivity study in section 3.3.1 the main focus of the analysis is set on the representation quality of the TBL profiles of u^+ and Reynolds stresses, specifically the streamwise $\overline{u'u'}$. For a given mesh resolution, in contrast to the INCA LES results both profiles show an upwards shift in the region of the streamwise

turbulence maximum at $y^+ \approx 15$. Overcoming this deficiency has been the main motivation of the additional grid sensitivity study for the flow solver CATUM. However, this goal has not been fully achieved and the deviations with respect to the INCA LES and DNS results are clearly visible in the subsequent section 4.2.2.

The main conclusions drawn for varying the grid parameters of the wall-tangential, wall-normal and streamwise resolution are:

1. The wall-tangential cell size exhibits a significant influence on the resulting flow field. With higher cross-sectional resolution, i.e. a decrease in the ratio $\Delta y_{max}/\Delta y_{min}$, Re_τ increases and the u^+-profile as well as the $\overline{u'u'}$-maximum experience a downwards shift.

2. The size of the first cell in wall-normal direction has no significant effect on the flow profiles when chosen sufficiently small. In the investigated cases no difference is visible for a resolution of $\Delta y^+_{min} \approx 1.5$ compared to smaller values of Δy^+_{min}.

3. With increasing resolution in the periodic streamwise direction, i.e. increasing Δx-resolution, Re_τ drops as well as the streamwise turbulence intensity $\overline{u'u'}$.

Comparing the CATUM grid sensitivity study with the one performed for INCA in section 3.3.1 an overall similar behaviour of the implicit LES solvers is visible as can be expected. It has been found, however, that for a comparable result quality a significantly higher grid resolution is required using CATUM. Differences between the solvers are attributed to INCA being well-optimised for the simulation of wall-bounded flows, whereas CATUM has been specifically developed for the simulation of cavitating flow. To examine the origin of the different solver behaviour and possibly improve CATUMs performance several test runs have been carried out. Neither changing the time integration scheme, nor the diffusive flux discretisation, nor the specific wall-damping implementation have a relevant positive impact on the resulting flow field in the vicinity of the walls. However, it has been found, that modifying the weighting coefficient ω^Δ for the first and third order gradient approximation in the reconstruction within the ILES flux function as defined by Egerer et al. (2016) does have a significant impact. The remaining free ALDM regularisation parameters are identical in CATUM and INCA. Hence, the cause for the deviations between the two implicit ALDM-based solvers is attributed to the specific implementation of ALDM and specifically the reconstruction procedure in the convective flux calculation. To recapitulate, in INCA the reconstruction of the local unfiltered flow field is performed based on a solution-adaptive combination of three Harten-type deconvolution polynomials taking the grid-stretching explicitly into account. However, in CATUM a more robust ALDM implementation is used based on two Langrangian-type polynomials for cell face gradient reconstruction with a non-solution adaptive fixed weighting. Thus, grid-stretching is not taken into account. The latter deficiency has been remedied, although for a fine enough discretisation towards the walls no major influence has been observed by including the grid-stretching. Hence, for further investigations of wall-bounded flows with CATUM it is highly recommended to switch to the solution-adaptive original ALDM implementation of INCA. For a detailed description of the numerical modelling of the two solvers the reader is referred to sections 2.2 and 2.3.

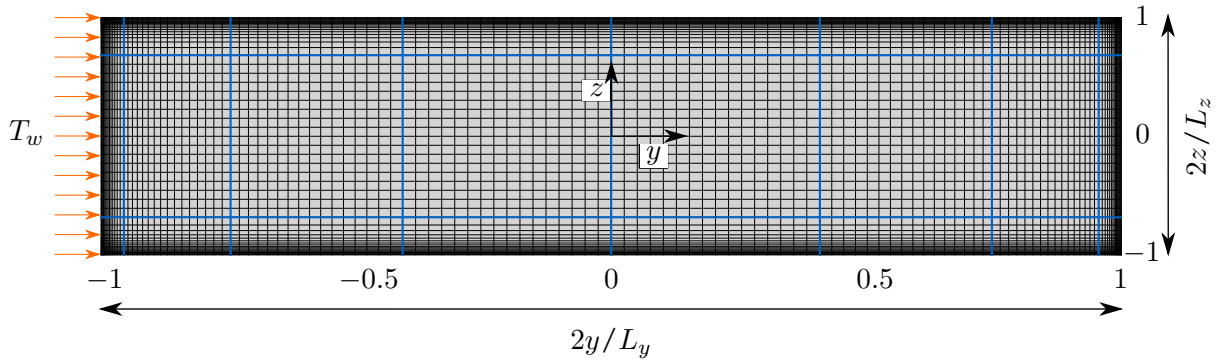

Figure 4.2: Cross-sectional computational grid and blocking highlighted in blue for the curved HARCD simulations (every second grid line shown).

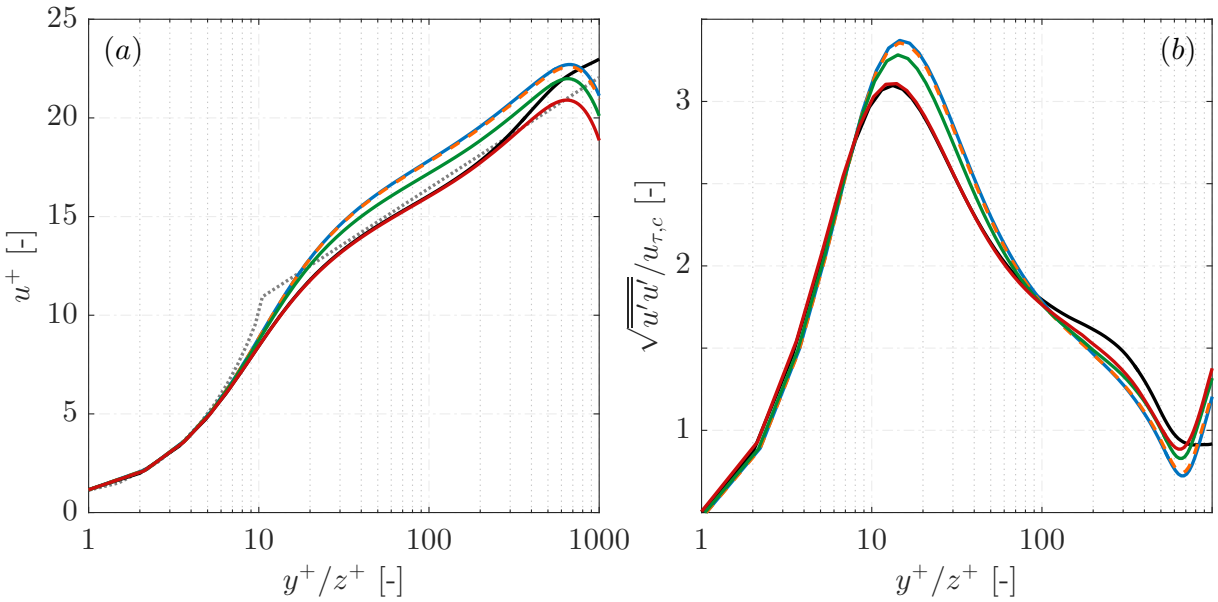

Figure 4.3: Dimensionless velocity profiles (a) and streamwise Reynolds stress distributions (b) for the unheated HARCD along different cut positions of $2z/L_z = 0$ (——), $2y/L_y = 0$ (——), $2y/L_y = -0.25$ (- - - -), $2y/L_y = -0.5$ (——) and $2y/L_y = -0.75$ (——). The analytical law of the wall (·····) is defined as $u^+ = 1/0.41 \cdot \ln y^+ + 5.2$.

The computational meshes for the three curved air HARCD set-ups are defined based on the experiences of the previous water HARCD simulations with INCA and the grid sensitivity analysis for CATUM. The cross-sectional computational grid and its blocking structure is shown in figure 4.2 and remains unchanged in streamwise direction along the whole configuration. As before a differentiation is made between boundary layer and core blocks with the boundary layer blocks utilising a hyperbolic grid-stretching towards the walls. To optimise the computational efficiency all blocks contain the same number of cells and the block splitting is such, that every two block rows in streamwise direction fill one complete node, i.e. the 48 blocks are simulated on the 48 CPUs of one computational node of SuperMUC-NG. As a higher grid resolution is required for CATUM to obtain the same result quality as INCA a trade-off has been made between numerical costs and the required resolution. Especially the lower and upper quarter of the HARCD require a high mesh resolution as these areas are highly influenced by the turbulence-induced secondary flow, and the lower quarter additionally by its interaction with heating. In the duct centre the resolution is coarsened to save computational costs. In contrast to the water HARCD set-up no 2:1 coarsening is used, but 1:1 block-connections. Thus, the numerical costs have to be lowered by a reduction in the wall-tangential resolution in both the core and the boundary layer blocks leading to an underestimation of Re_τ in the duct centre. The influence of the different resolutions used within the duct cross-section is indicated in figure 4.3 by means of TBL profiles, specifically dimensionless velocity and streamwise turbulence intensity profiles, along various y- and z-slices. Note, that an interaction of local grid resolution and flow conditions influenced by the secondary flow vortices both affect the shown profiles. The best resolution is achieved by the lower wall-normal slice at $2z/L_z = 0$, for which the agreement with the analytical law of the wall is very good. The same discretisation quality with respect to velocity and turbulence profiles is reached for the lateral wall-normal slice at $2y/L_y = -0.75$. The remaining lateral wall-normal slices experience increasing wall-tangential cell sizes from $(\Delta z_{max}/\Delta z_{min})_{2z/L_z=0} = 17.51$ and $(\Delta y_{max}/\Delta y_{min})_{2y/L_y=-0.75} = 16.29$ over $(\Delta y_{max}/\Delta y_{min})_{2y/L_y=-0.5} = 22.69$ to $(\Delta y_{max}/\Delta y_{min})_{2y/L_y=0} = 25.36$ in the duct core. The decreasing resolution leads to an upwards shift of both the velocity profile and the turbulence intensity as well as an underestimation of Re_τ. For a further discussion of the numerical accuracy see the following section 4.2.

In contrast to the water HARCD a symmetric grid with respect to both the z- and the y-axis is used despite of the asymmetrically applied heating as $Pr_{air} < 1$. For flows with a molecular Prandtl number smaller than one the thermal boundary layer is larger than the momentum boundary layer and thermal scales are larger than momentum scales. Thus, the latter determine the required grid resolution for a well-resolved LES. Furthermore, due to the heating-induced viscosity increase the resolution in the vicinity of the heated wall is enhanced compared to the unheated periodic section. The parameters for the production meshes are listed in table 4.3. The grids are identical for the three cases up to the beginning of the curved section. For the latter the number of cells in streamwise direction becomes higher with increasing curvature radius to avoid sudden strong changes in Δx at the interface of straight and curved heated section. Additionally, RC900 possesses an elongated curved section. The remaining $26 \times 256 \times 108$ cells of the outlet domain following the curved section up to the outlet BC are not included in the table. Note, that for the evaluation of Δy^+_{min} the full cell height is taken into account, although the storage

	$N_x \times N_y \times N_z$	$\Delta x^+ \times \Delta y^+_{min} \times \Delta z^+_{min}$	$\frac{\Delta y_{max}}{\Delta y_{min}} \times \frac{\Delta z_{max}}{\Delta z_{min}}$	$Re_{\tau,c}\vert_{y_{min}}$
D_{per} /RC60	$273 \times 256 \times 108$	$54.1 \times 1.33 \times 1.46$	25.36×17.51	1991
D_{heat}/RC60	$832 + 325 \times 256 \times 108$	$40.6 \times 1.00 \times 1.44$	25.36×17.51	1492
D_{per} /RC180	$273 \times 256 \times 108$	$54.1 \times 1.33 \times 1.46$	25.36×17.51	1991
D_{heat}/RC180	$832 + 351 \times 256 \times 108$	$38.9 \times 0.96 \times 1.44$	25.36×17.51	1432
D_{per} /RC900	$273 \times 256 \times 108$	$54.1 \times 1.33 \times 1.46$	25.36×17.51	1991
D_{heat}/RC900	$832 + 507 \times 256 \times 108$	$38.2 \times 0.94 \times 1.44$	25.36×17.51	1406

Table 4.3: Production mesh parameters and resulting lower wall $Re_{\tau,c}$. Additionally, $Re_{\tau,c}|_z = 2188$ for D_{per} and $Re_{\tau,c}|_z = 2161$ for D_{heat}. The derived quantities are evaluated in the respective sidewall centre. The values for D_{heat} are measured close to the straight section end at $x = 200\,\text{mm}$ with a streamwise averaging of $\Delta x = 5\,\text{mm}$.

	$N_x \times N_y \times N_z$	$\Delta x^+ \times \Delta y^+_{min} \times \Delta z^+_{min}$	$\frac{\Delta y_{max}}{\Delta y_{min}} \times \frac{\Delta z_{max}}{\Delta z_{min}}$	$\frac{1}{2} Re_{\tau,c}$
CATUM(coarse)	$180 \times 160 \times 160$	$56.80 \times 1.33 \times 1.35$	25.40×25.40	1022
CATUM(fine)	$198 \times 190 \times 190$	$54.16 \times 1.39 \times 1.39$	17.51×17.51	1072
INCA	$250 \times 136 \times 136$	$65.33 \times 1.06 \times 1.06$	23.41×23.41	1089
DNS	$2048 \times 512 \times 512$	$9.76 \times 0.61 \times 0.62$	10.67×10.67	1073

Table 4.4: Main grid and flow parameters for the square duct LES-DNS comparison (compressible flow solver CATUM) at $Re_b = 40 \cdot 10^3$. The streamwise box length for the DNS is larger with $6\pi\,h$ compared to the CATUM LES with $L_{x,per} = 10\,h$. The parameters for the INCA LES with $L_{x,per} = 15\,h$ from table 3.5 are included for comparison. $Re_{\tau,c}$ is halved following the square duct definition by Pirozzoli et al. (2018).

location of the cell-centred variables is at half cell height. Consequently, the wall-resolution is actually finer than indicated by the value of Δy^+_{min}.

4.2.2 Comparison against Square Duct DNS

Analogous to section 3.3.2 a comparison with adiabatic square duct DNS data by Pirozzoli et al. (2018) is conducted to assess the numerical accuracy of the well-resolved LES performed with the flow solver CATUM.

The grid resolution for the square duct LES is chosen similar to that of the HARCD mesh as defined in section 4.2.1, i.e. a fine and a coarse grid are defined with the fine one resembling the spatial discretisation in the lower/upper quarter of the HARCD and the coarse one that in the duct core, respectively. For the flow statistics a temporal averaging over ≈ 200 FTT is performed followed by a spatial averaging in the homogeneous streamwise direction. Note, for the CATUM simulations the periodic box length is reduced to $L_{x,per} = 5\,d_h$ instead of $L_{x,per} = 7.5\,d_h$ to save computational time as the differences in the flow statistics are only marginal. The relevant parameters are listed in table 4.4.

The velocity field symmetry of figure 4.4 demonstrates the sufficiently converged flow state. The secondary flow strength values are in the expected range of $0 - 2.29 \cdot 10^{-2} \cdot u_b$ (as reference

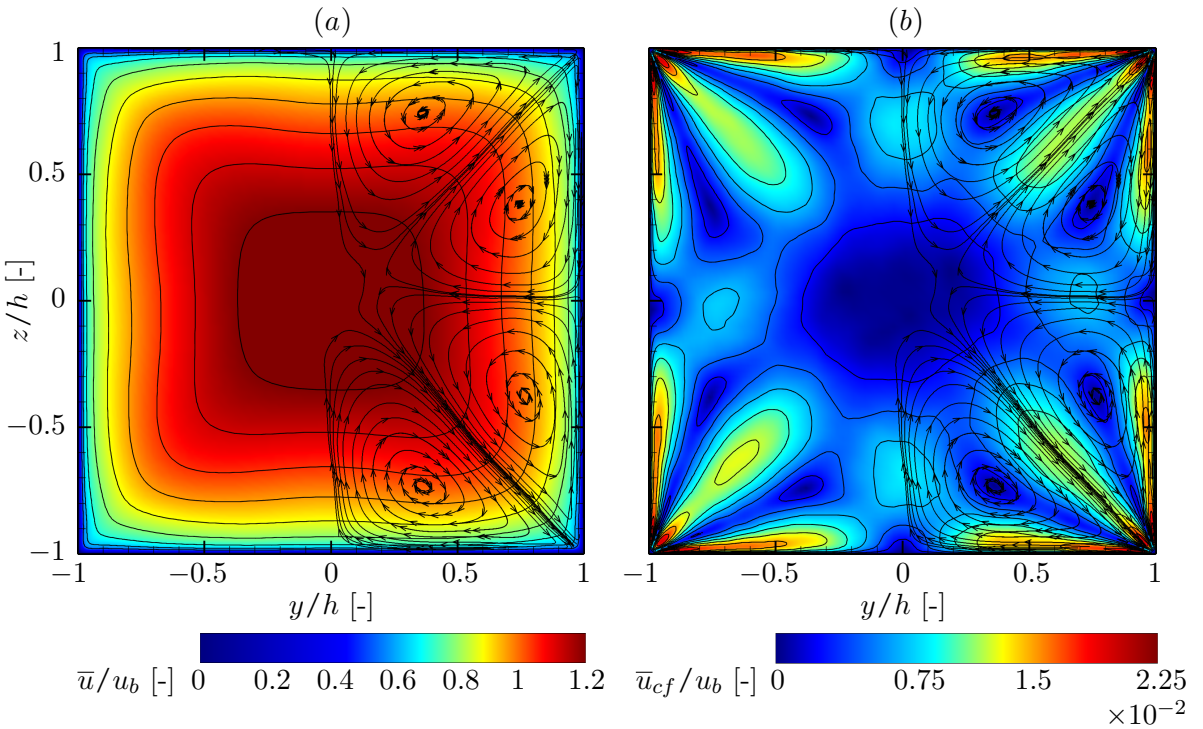

Figure 4.4: Adiabatic square duct flow field for the compressible LES using CATUM for the fine grid: (a) mean streamwise velocity distribution and (b) mean cross-sectional velocity distribution with $\overline{u}_{cf} = \sqrt{\overline{v}^2 + \overline{w}^2}$. The contour lines for $\overline{u}/u_b$ are drawn from 0.6 to 1.2 in steps of 0.075 and for $\overline{u}_{cf}/u_b$ from $0.25 \cdot 10^{-2}$ to $2.25 \cdot 10^{-2}$ in steps of $0.25 \cdot 10^{-2}$.

$0 - 2.11 \cdot 10^{-2} \cdot u_b$ for the DNS). This range is nearly identical to that obtained with INCA, although the overall secondary flow strength in the duct core is slightly weaker in the CATUM simulations. Figure 4.5 compares the LES with the DNS flow field exemplarily along specific line cuts. In subfigure (a) the CATUM coarse grid velocity profile experiences a constant upwards shift due to the underprediction of Re_τ, see table 4.4. The CATUM fine grid u^+-profile and Re_τ follow closely the DNS. However, in contrast to the INCA results a small bump-like upwards shift in the region $y^+ \approx 10 - 30$ is visible. This observed upwards shift coincides with an overestimation of the $\overline{u'u'}$-maximum visible in figure 4.5 (b), whereas the location of the maximum is in good agreement with the DNS data. For the CATUM coarse grid simulation this overestimation is increased and the maximum location is shifted away from the wall. This overestimation has not been observed with the incompressible flow solver INCA and is attributed to the differences in the implementation of the convective fluxes and the specific ALDM LES model. In the logarithmic and wake region the streamwise turbulence intensity is uniformly underpredicted for all LES simulations. The remaining Reynolds stress terms in subfigure (b) are in good agreement with DNS data, although slightly underestimated. The secondary flow distributions in figures 4.5 (c) and (d) show a good agreement with the DNS data for all LES simulations.

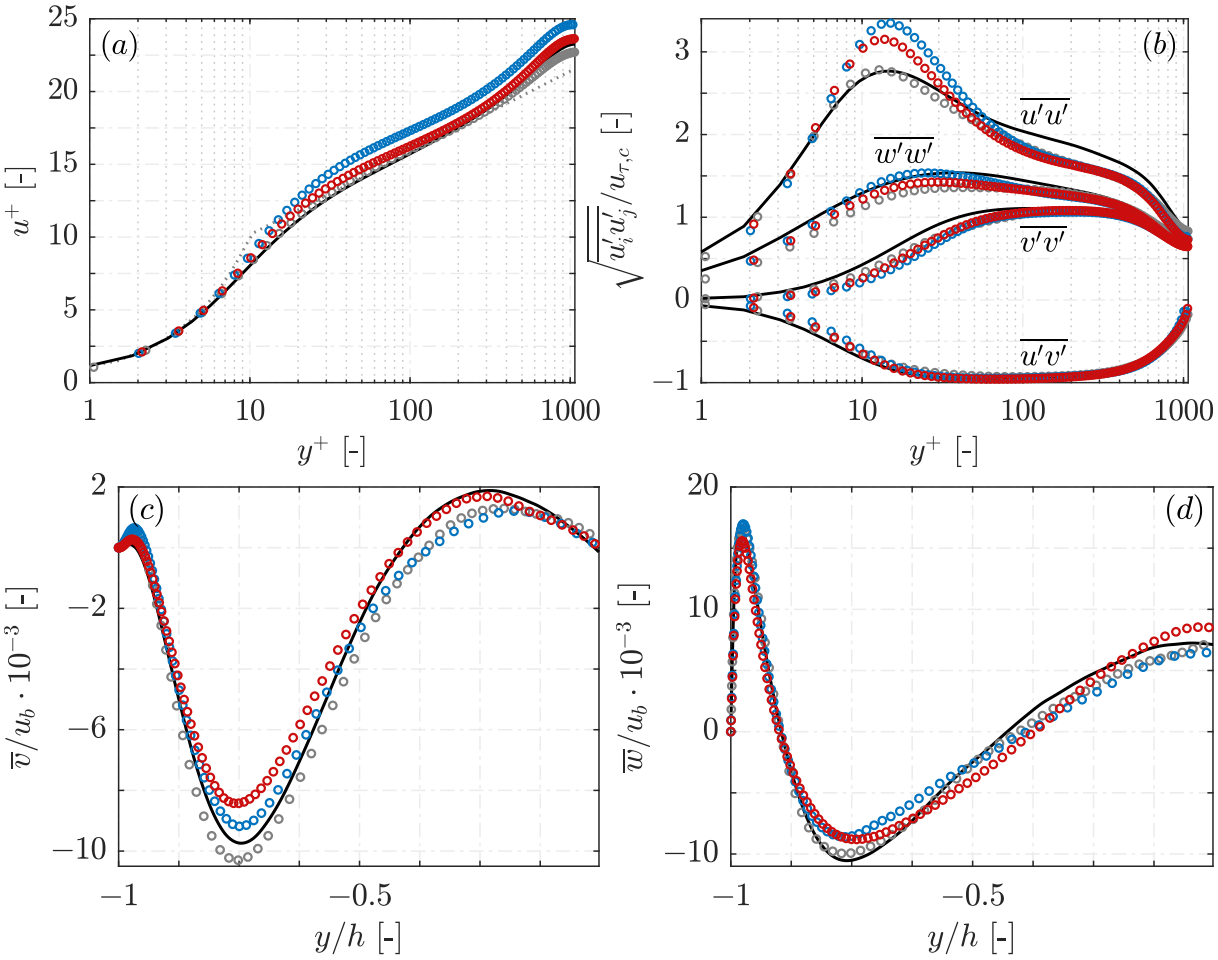

Figure 4.5: Comparison of the periodic adiabatic square duct compressible LES using CATUM for a coarse (○) and a fine grid resolution (○) with DNS (——) results by Pirozzoli et al. (2018): (a) mean streamwise velocity and (b) Reynolds stress profiles along the duct midplane $z = 0$, and (c, d) cross-sectional velocity components of the secondary flow along $z/h = 0.75$. The analytical law of the wall (·····) in (a) is defined as $u^+ = 1/0.41 \cdot \ln y^+ + 4.55$, and the incompressible INCA results included as (○) for comparison.

4.3 Discussion of the Flow Field

In the following we analyse the turbulent heat transfer in the asymmetrically heated curved air HARCDs based on the LES results. The current results section is separated into five parts: in subsection 4.3.1 the flow field is discussed with a special focus on the streamwise and secondary flow development along the curved sections and the influence of the different curvature radii; in 4.3.2 the effect of the secondary flow field on the TBL profiles is analysed including the application of appropriate scaling laws and their limits, followed by an investigation of the secondary flow evolution employing the streamwise vorticity equation. Subsequently, the modulation of turbulent sweeping and ejection motions by the influence of heating and Prandtl's flow of the first kind is presented in subsection 4.3.4. Eventually, in subsection 4.3.5 the turbulent heat transfer is discussed analogous to section 3.5.4 with a focus on the evolution of Nusselt and turbulent Prandtl number distributions along the HARCD sections. The latter also includes a discussion of the applicability of the unity Pr_t assumption and isotropic turbulence modelling when significant secondary flow currents are present in the duct cross-section.

The evaluation of the results is based on a temporal averaging over ≈ 30 FTT with respect to the resolved heated domain length for case RC60 and similarly for cases RC180 and RC900, see section 4.1 for details. For the curved section a coordinate transformation is applied, such that $\mathbf{x} = [x, y, z]$ denotes in both the straight and the curved section the contour-adaptive streamwise, vertical (from heatable bottom to top short sidewall) and spanwise (from one lateral large sidewall to the other) direction, and likewise for velocity components $\mathbf{u} = [u, v, w]$. The transformation matrix

$$\mathbf{R} = \begin{pmatrix} \cos\alpha & -\sin\alpha & 0 \\ \sin\alpha & \cos\alpha & 0 \\ 0 & 0 & 1 \end{pmatrix}, \tag{4.1}$$

is employed for conversion with α here denoting the local rotation angle. The z-components remain unchanged due to the two-dimensional rotation. Contour-adaptive (subscript $(\cdot)_{ca}$) coordinates for the curved section $\mathbf{x}_{ca}$ are obtained with the HARCD centre located at $(y, z) = (0, 0)$ as

$$\begin{pmatrix} x \\ y \\ z \end{pmatrix}_{ca} = \begin{pmatrix} x_{cc} + \frac{r_{c,l}\,\pi\,\alpha}{180} \\ y_{cc} + r_{c,l} \\ z \end{pmatrix} \quad \text{with} \quad r_{c,l} = \sqrt{(x - x_{cc})^2 + (y - y_{cc})^2}. \tag{4.2}$$

The latter is the local curvature radius $r_{c,l}$, and (x_{cc}, y_{cc}) the curvature radius centre coordinates. Velocities and turbulent heat fluxes are determined as

$$\begin{pmatrix} u \\ v \\ w \end{pmatrix}_{ca} = \mathbf{R} \cdot \begin{pmatrix} u \\ v \\ w \end{pmatrix}, \qquad \begin{pmatrix} u'T' \\ v'T' \\ w'T' \end{pmatrix}_{ca} = \mathbf{R} \cdot \begin{pmatrix} u'T' \\ v'T' \\ w'T' \end{pmatrix}, \tag{4.3}$$

and the components of the Reynolds stress tensor as

$$\begin{pmatrix} u'u' & u'v' & u'w' \\ u'v' & v'v' & v'w' \\ u'w' & v'w' & w'w' \end{pmatrix}_{ca} = \mathbf{R}^T \cdot \begin{pmatrix} u'u' & u'v' & u'w' \\ u'v' & v'v' & v'w' \\ u'w' & v'w' & w'w' \end{pmatrix} \cdot \mathbf{R}. \tag{4.4}$$

For readability, the subscript $(\cdot)_{ca}$ is dropped in the remainder of the discussion and an identical notation is used for coordinates, velocities and stresses in the periodic, straight and curved duct sections.

4.3.1 Mean Flow Field of the Curved Heated Duct

At first, the straight section results are discussed briefly and differences with respect to the water HARCD pointed out. The main focus then lies on the evolution and interaction of turbulence- and curvature-induced secondary flow of different strengths and the impact of the secondary flow field on the temperature distribution along the curved cooling duct configurations. Eventually, the secondary flow effect on the streamwise velocity distribution is analysed.

Figure 4.6 depicts the secondary flow and temperature development along the straight section in the lower duct quarter of case RC60. As expected, the turbulence-induced secondary flow field resembles in structure and strength that of the water HARCD presented in section 3.5.1. Note that the comparability of the set-ups is limited due to the different boundary conditions as well as the employed meshing and solver specific discretisation schemes, which may have a non-negligible impact on the rather sensitive turbulence-induced secondary flow. The cross-flow velocity field $\overline{u}_{cf} = \sqrt{\overline{v}^2 + \overline{w}^2}$ (not shown here) has an identical structure and reaches a similar strength as previously discussed with a maximum value of $\overline{u}_{cf}|_{max} = 2.2\%$ of u_b in the unheated periodic section (1.93% of u_b for the water HARCD). A pair of counter-rotating vortices is present in each duct corner, a smaller one adjacent to the heatable wall and a larger one adjacent to the lateral sidewall. The mixing by the vortex system leads to the typical bulging of the $\overline{T}$-profile, becoming apparent by an upwards bending in the centre and close to the sidewalls, and a downwards bending roughly along the corner bisecting lines. The duct centre bulging is slightly less pronounced compared to the previous water HARCD results. With the formation and growth of the temperature boundary layer along the straight section an increase of the near-wall viscosity is associated. In contrast to the water HARCD, for which a heating induced viscosity decrease is present, the viscosity increase here leads to an increase of the secondary flow strength. Especially the small vortex adjacent to the heatable wall becomes stronger, which can be observed by comparing the midplane of figures 4.6 (f, g) with (e). At a streamwise distance of 150 mm the midplane upwards velocity $\overline{v}$ is increased locally by up to $\Delta\overline{v}/u_b \approx 2 \cdot 10^{-3}$, which corresponds to a growth of $\approx 45\%$ with respect to the unheated section. This strength augmentation is also visible in the line plot of figure 4.13 (b) followed by a drop of the large vortex strength. Similar as for the water HARCD, the larger sidewall vortex also becomes weaker, although significantly less distinct for the air HARCD. At a streamwise position of 200 mm the influence of the curved section downstream already becomes apparent. Hence, figures 4.6 (d, h) are case-specific, whereas $(a - c)$ and $(e - f)$ are identical for all three configurations and curvature-independent. In figures 4.6 (d, h), the first development stages of the curvature-induced secondary flow is visible, the pressure minimum at the inner radius side of the bend and the pressure-maximum at the outer radius side causing a downwards oriented secondary flow upstream of the curved section. The strength of this secondary flow possesses the same order of magnitude, yet is stronger than the already present corner vortex system. Focusing on the left corner, the interaction with the existing turbulence-induced secondary flow leads to a significant weakening and constriction of

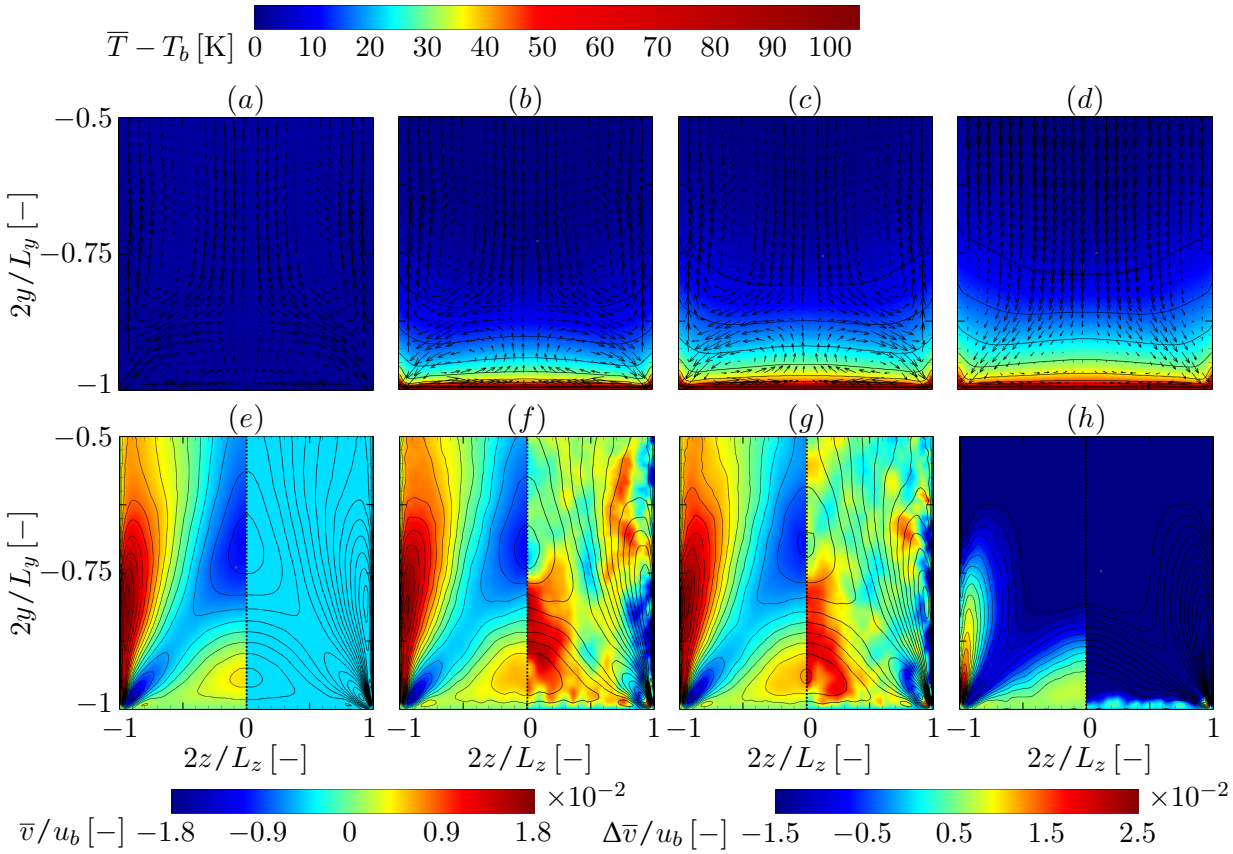

Figure 4.6: Cross-sectional temperature distribution $(a-d)$ and heated wall-normal secondary flow velocity development $(e-h)$ in the vicinity of the heated wall: (a, e) periodic section, and heated section at streamwise distances of (b, f) 100 mm, (c, g) 150 mm and (d, h) 200 mm after T_w remains constant. In $(a-d)$ cross-flow velocity vectors are added to indicate the secondary flow influence on the temperature distribution and the contour lines are drawn from $0-75$ K in steps of 7.5 K. In $(e-h)$ on the left the wall-normal velocity is depicted and on the right the change in $\overline{v}$ with respect to the unheated periodic duct, $\Delta\overline{v} = \overline{v} - \overline{v}_{per}$. The contour lines for $\overline{v}/u_b$ are drawn from $-1.8 \cdot 10^{-2}$ to $1.8 \cdot 10^{-2}$ in steps of $0.2 \cdot 10^{-2}$. In (h) the pressure-induced secondary flow leads to a strong reduction of $\overline{v}$ not entirely covered by the chosen colour range.

both the small CCW vortex and the large CW vortex. Consequently, the secondary flow field changes from being dominated by Prandtl's flow of the second kind to Prandtl's flow of the first kind. For cases RC180 and RC900 with reduced curvatures, the turbulence-induced vortex system is able to remain stable for a longer distance due to a weaker pressure-induced secondary flow.

Figures 4.8, 4.9 and 4.10 depict the development of the secondary flow field, which forms as a result of the interaction of Prandtl's flow of the first and the second kind, along the curved sections of the three investigated cases at varying curvature as well as the associated temperature distribution within the cooling duct. To study the $\overline{u}_{cf}$-evolution seven yz-planes are considered

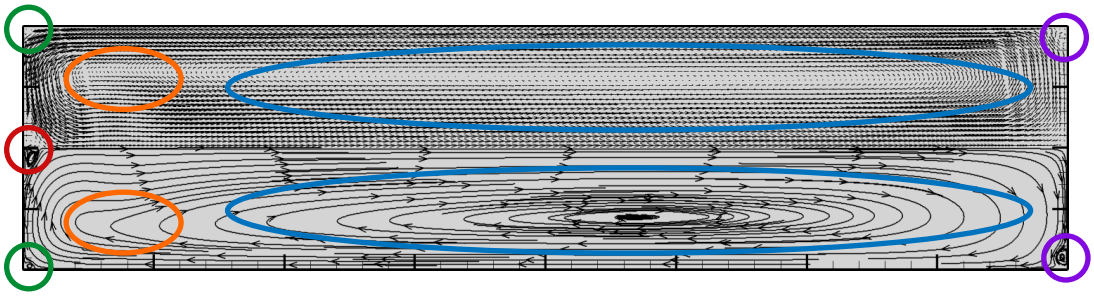

Figure 4.7: Cross-sectional vortex naming with (——) base Dean vortex, (——) corner region Dean vortex, (——) inner curvature wall (ICW) Dean vortex, (——) developing split base Dean vortex and (——) remaining turbulence-induced corner vortex. The naming convention follows Bhunia and Chen (2009), Li et al. (2016) and Li et al. (2017). The flow field is taken from RC60 at 60°, depicted in figure 4.8 (k). For a magnified view see figures 4.11 (a, b).

at similarly distributed streamwise positions. Each cross-sectional distribution is obtained by first performing a coordinate transformation applying the rotation matrix and subsequent spatial averaging over $\pm 2.5°$(RC60), $\pm 0.833°$(RC180) and $\pm 0.25°$(RC900) of the respective position, which corresponds to ≈ 20 yz-planes in streamwise direction. To support the analysis the naming convention for the Dean vortex system is added in figure 4.7.

For the strong curvature case RC60 the previously discussed pressure-induced downwards oriented flow already starting to form upstream of the curved section is visible in figure 4.8 (a). Until position 2.5° the secondary flow field structure remains nearly unchanged with the flow towards the heated inner radius wall intensifying especially along the lateral sidewalls, which is attributed to the lower streamwise impulse of the flow particles there compared to the duct core. The lower wall corner vortices have initially been displaced and have already vanished completely until 2.5°, whereas at the upper wall the smaller one of the corner vortex pair is increasingly constricted into the corner. At position 7.5° the imbalance of centrifugal forces and pressure gradient leads to the formation of a pair of counter-rotating base Dean vortices with their core close to the outer radius HARCD wall. The creation of this secondary flow is known as Dean instability and occurs when a certain critical Dean number is surpassed. To balance out the downwards mass transfer along the lateral sidewalls an initially weak upwards oriented secondary flow is emerging along the midplane region. Between figures 4.8 (e) 7.5° and (g) 30° the Dean vortex flow field increases noticeably in strength. The vortex core becomes flatter and is shifting slightly towards the duct centre, and the remaining outer radius corner vortex is shrinking further. The increase in secondary flow strength as well as the shift of the Dean vortex centre towards the inner radius wall continues until the end section. At position 45° in figure 4.8 (i), the described trend of growing secondary flow strength continues and two additional small pairs of Dean-type vortices are noticeable at the inner radius side, the corner region Dean vortices and the Dean vortices attached to the centre of the inner curvature wall (ICW Dean vortex). These extra vortex pairs are forming in the interval between 30° and 45° (ICW Dean vortex), and from 15° onwards (corner region Dean vortex). The latter interacts with the rest of the turbulence-induced vortices, which will be further discussed in section 4.3.3. The

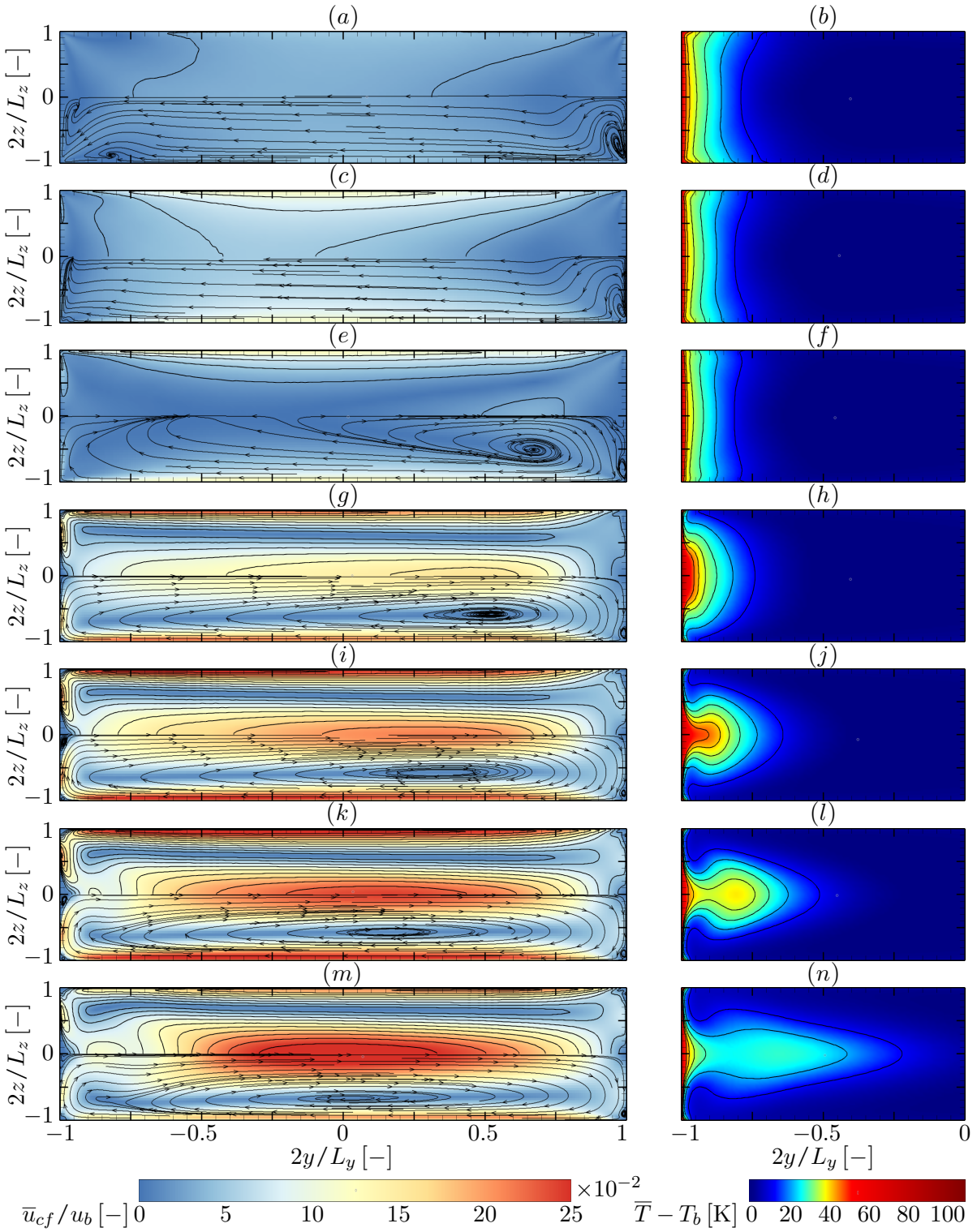

Figure 4.8: Secondary flow and temperature development along case RC60: (a, b) straight section at 200 mm after T_w remains constant, (c, d) curved section at 2.5°, (e, f) at 7.5°, (g, h) at 30°, (i, j) at 45°, (k, l) at 60° and (m, n) at 87.5°. The contour lines for $\overline{u}_{cf}/u_b$ are drawn from $0 - 0.25$ in steps of 0.025 and for $\Delta\overline{T}$ from $7.5 - 45$ K in steps of 7.5 K. The $\overline{u}_{cf}$ development is visualised with streamlines in the lower duct half.

case	all	all	RC60	RC180	RC900
domain	straight(unheated)	straight(heated)	curved	curved	curved
position	-	150 mm	end(87.5°)	end(29.17°)	end(8.75°)
$\overline{u}_{cf}/u_b\vert_{max}$	2.22%	2.35%	26.09%	11.85%	3.80%

Table 4.5: Maximum cross-sectional velocity $\overline{u}_{cf} = \sqrt{\overline{v}^2 + \overline{w}^2}$ reached for individual locations and cases.

naming convention for the Dean vortices has been adopted from Li et al. (2017) and Bhunia and Chen (2009). A detailed view of the vortex system at the inner and outer radius wall is given in figure 4.11 (a, b). In figure 4.8 (k) at 60° the lateral wall region maximum $\overline{u}_{cf}$ is reached and afterwards decreases. Furthermore, a noticeable constriction of the Dean vortex starts to form at $2y/L_y \approx -0.75$ and becomes stronger towards the end section. Based on the results by Li et al. (2017), we conclude that here a 4^{th} type of Dean vortex is developing, the so-called split base vortex, which is created by splitting the base vortex into two. However, due to our narrower HARCD and/or the short streamwise configuration length this vortex pair does not fully develop. In the end section, the overall maximum secondary flow velocity is obtained along the midplane with $\overline{u}_{cf}$ reaching 26.1% of the bulk velocity, see also table 4.5 for comparison with the other cases. The ICW Dean vortex vanishes, similarly observed by Li et al. (2016) and Li et al. (2017), whereas the corner region Dean vortices and the turbulence-induced vortex at the outer radius wall are still present. The cross-sectional temperature distributions in the right column of figure 4.8 are intimately linked to the secondary flow evolution. Initially the downwards oriented flow leads to a compression of the temperature boundary layer having formed along the straight HARCD section. At position 7.5° in figure 4.8 (f), a downward kink of the $\overline{T}$-profile at the lateral sidewalls is noticeable, which is caused by the relatively high $\overline{u}_{cf}$ along the sidewall TBL. In figure 4.8 (h), the increasing secondary flow strength leads to cold fluid reaching the inner radius heated wall corner regions. The previously present hot fluid has been transported along the heated wall into its centre by the respective Dean vortex accumulating there and creating a dome-shaped temperature profile. At position 45° in figure 4.8 (j), the hot fluid in the centre of the heated wall starts to be uplifted along the midplane by the interacting Dean vortices while mixing in cold fluid coming from the direction of the lateral sidewalls. A profile resembling the shape of a candle flame or spear head is evolving and by the increasing mixing process along the remainder of the section stretched out towards the duct core. Especially the end section shows the dominant effect of the Dean vortex system compared to the corner vortex system with respect to heat transfer into and heat distribution within the cooling duct. Eventually, a relatively evened out heat distribution is achieved within the complete lower half of the duct, whereas initially the hot fluid has been restricted to the immediate vicinity of the heated wall forming a sort of insulation and limiting the overall heat transfer. For a detailed discussion on the heat transfer the reader is referred to section 4.3.5.

For case RC180 the secondary flow development is overall similar to case RC60, although at a reduced strength of $\overline{u}_{cf}|_{RC180} \lessapprox 50\% \, \overline{u}_{cf}|_{RC60}$, see also table 4.5. Consequently, the turbulence-induced secondary flow remains stable over a longer distance. For instance, at the first position in figure 4.9 (c), the complete corner vortex system is still present, although noticeably influenced

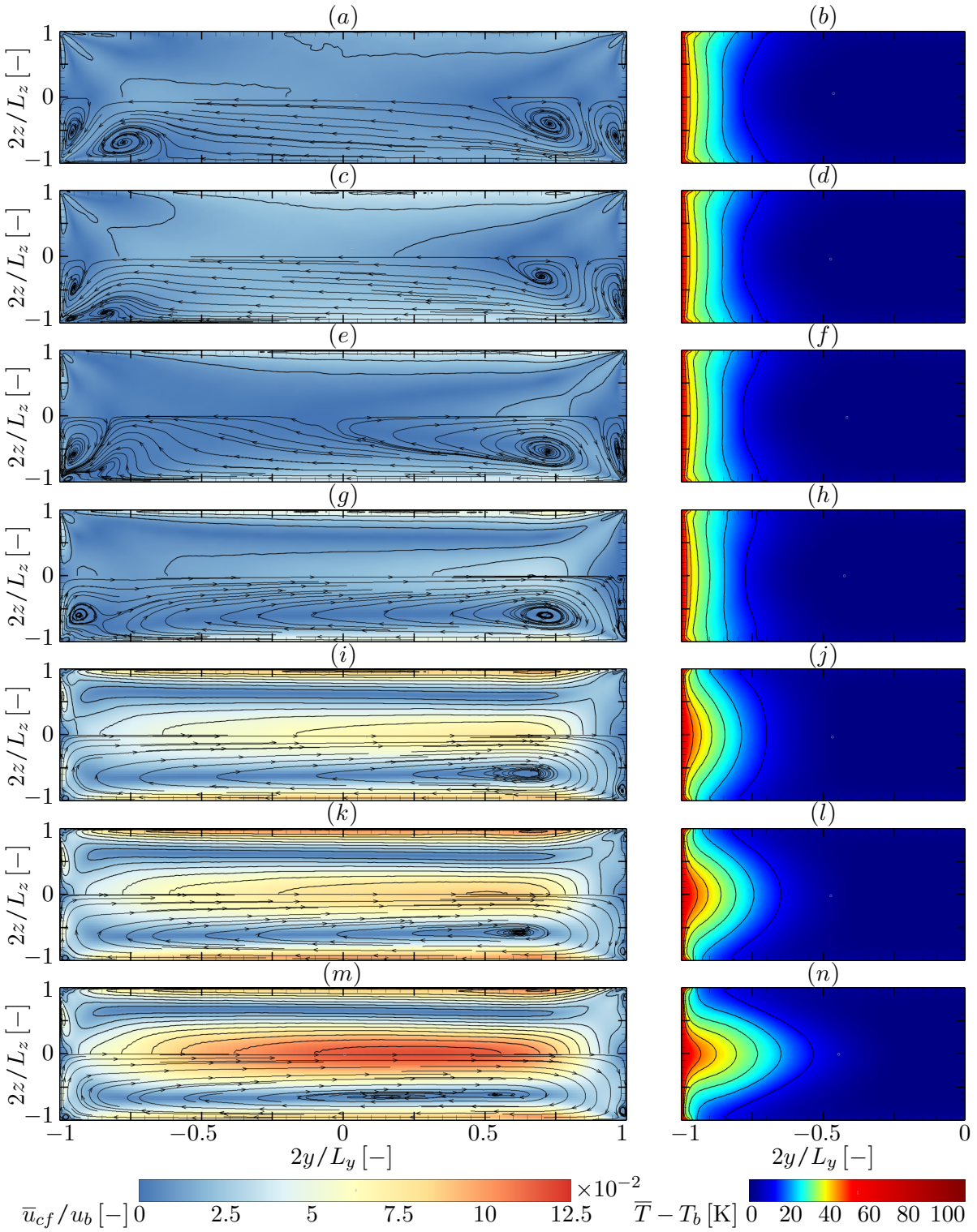

Figure 4.9: Secondary flow and temperature development along case RC180: (a, b) straight section at 200 mm after T_w remains constant, (c, d) curved section at 0.83°, (e, f) at 2.5°, (g, h) at 5°, (i, j) at 15°, (k, l) at 20° and (m, n) at 29.17°. The contour lines for $\overline{u}_{cf}/u_b$ are drawn from $0 - 0.125$ in steps of $1.25 \cdot 10^{-2}$ and for $\Delta\overline{T}$ from $7.5 - 45$ K in steps of 7.5 K. The $\overline{u}_{cf}$ development is visualised with streamlines in the lower duct half.

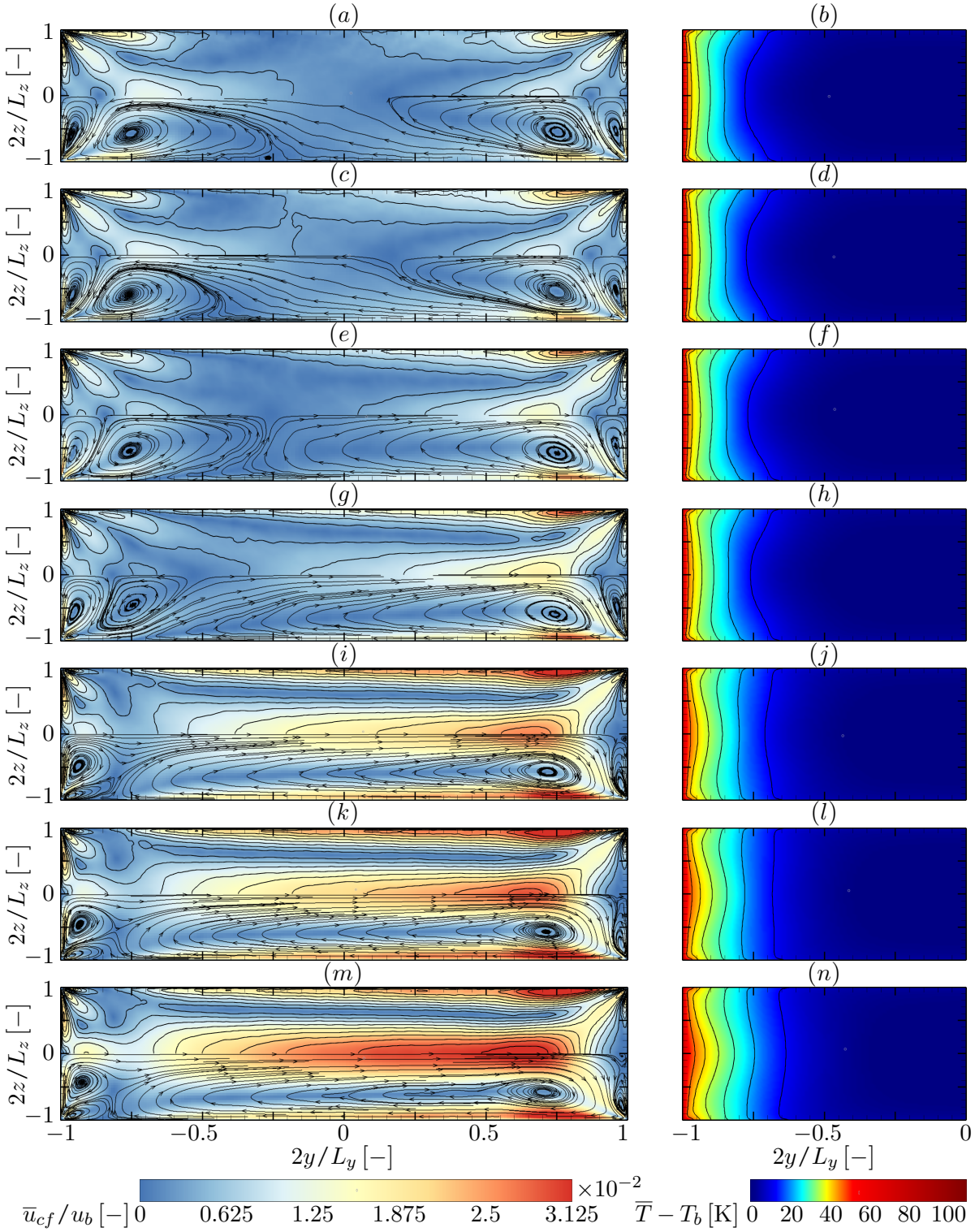

Figure 4.10: Secondary flow and temperature development along case RC900: (a, b) straight section at 200 mm, (c, d) curved section at 0.25°, (e, f) at 0.75°, (g, h) at 1.5°, (i, j) at 4.5°, (k, l) at 6° and (m, n) at 8.75°. The contour lines for $\overline{u}_{cf}/u_b$ are drawn from $0 - 3.125 \cdot 10^{-2}$ in steps of $3.125 \cdot 10^{-3}$ and for $\Delta\overline{T}$ from $7.5 - 45$ K in steps of 7.5 K. The $\overline{u}_{cf}$ development is visualised with streamlines in the lower duct half.

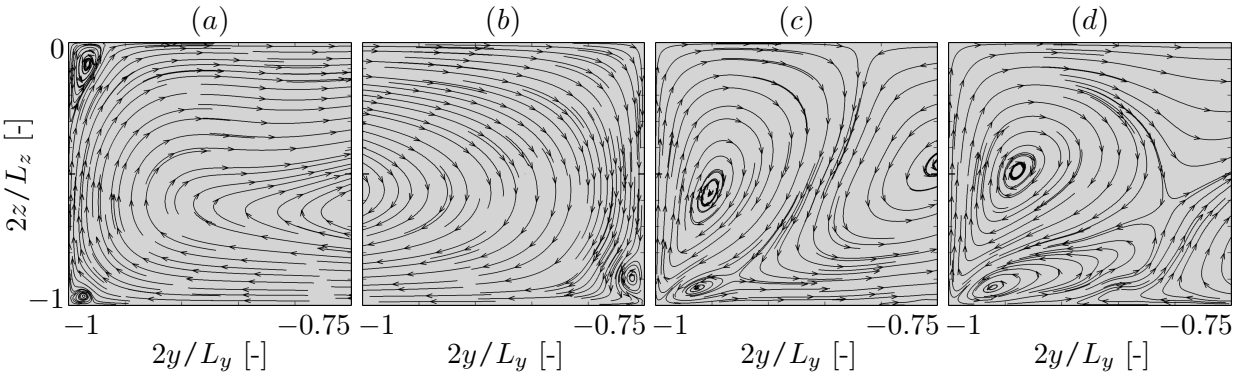

Figure 4.11: Close-up of cross-sectional vortex system for (a) inner radius wall of case RC60 at position 60°, (b) outer radius wall of case RC60 at position 60°, (c) inner radius wall of case RC900 at position 1.5° and (d) inner radius wall of case RC900 at position 4.5°.

by the downwards pressure-induced cross-flow. Similarly as described for case RC60, after the initial formation of the base Dean vortices the cross-flow velocity increases and the vortex cores are shifted gradually towards the inner radius wall along the curved section. Due to the weaker Prandtl's flow of the first kind, the turbulence-induced vortex in the outer radius corner remains larger. At the inner radius wall, the larger one of the corner vortex pair breaks down after 2.5° with an enlarged inner radius wall corner Dean vortex remaining, and the smaller one is absorbed into the Dean vortex between 5° and 15°, compare figures 4.9 (e, g, i). In contrast to case RC60, the ICW Dean vortex is not forming at all. However, a split base Dean vortex is evolving towards the end section in the upper duct half by segregation of the base Dean vortex, see the $\overline{u}_{cf}$-evolution from figure 4.9 (k) to (m). The $\overline{T}$-distribution follows again the secondary flow distribution with profile changes requiring a longer distance due to the weaker $\overline{u}_{cf}$. Initially, again a slight compression of the temperature boundary is noticeable caused by the pressure-induced secondary flow, which is followed by the evolution of a dome-shaped profile until position 15° corresponding to figure 4.9 (j). In contrast to case RC60, cold fluid does not reach the heated wall and the development of the candle flame shaped distribution is delayed, such that until the end section a noticeably lower mixing of hot and cold fluid is achieved. The heating influence remains confined to the lower portion of the duct quarter.

For the lowest curvature case RC900 Prandtl's flow of the first and second kind are of comparable strength. Therefore the evolving cross-flow velocity field is defined by their interaction. Along the HARCD the curvature-induced secondary flow becomes increasingly stronger, which leads to a gradual transformation from a corner vortex dominated flow field to one dominated by Dean vortices. The overall corner vortex structure persists from the curved section inlet until position 1.5°, i.e. from figure 4.10 $(a - g)$. The increasing superimposing curvature-induced secondary flow leads to a continuous strengthening of the outer radius side turbulence-induced large corner vortex, which steadily transforms into the base Dean vortex. This steady strengthening leads on the one hand to a displacement of the small turbulence-induced corner vortex at the outer radius side being pressed increasingly flatter against the upper wall, and on the other hand to a displacement of the opposite large turbulence-induced inner radius side corner vortex, restricting

its influence area to the vicinity of the lower wall. In figure 4.10 (i) showing position 4.5°, we observe a rearrangement of the corner vortex system at the inner radius wall, with the large corner vortex having vanished and the remains constricted to the duct corner displacing the smaller one slightly towards the midplane. Subsequently, the interacting large vortex remainder and corner region Dean vortex grow slightly towards the end section at the cost of the former small corner vortex. For a detailed view of the changing vortex system in the vicinity of the inner radius wall the reader is referred to figures 4.11 (c, d). The small vortex is getting steadily absorbed by the base Dean vortex, while simultaneously $\overline{u}_{cf}$ in its influence region intensifies. The continuous secondary flow strength augmentation in this area is especially well visible in the line plot of figure 4.13 (e). For the temperature distribution only minor changes are noticeable compared to a $\overline{T}$-profile only affected by turbulence-induced secondary flow. Until position 6° in figure 4.10 (l) a spanwise flattening of the $\overline{T}$-isolines in the outer layer of the temperature boundary layer takes place. However, in the vicinity of the heated wall an increasing upward bulging is observable in the midplane caused by the continuously strengthening small turbulence-induced vortex, in the end section also affecting the outer layer of the $\overline{T}$-profile.

The secondary flow influence on the mean streamwise profiles is assessed based on figure 4.12. For both the unheated periodic and the heated straight section a small influence is only noticeable in the duct corner regions due to the weak turbulence-induced secondary flow. The flow distribution is relatively symmetrical, which changes along the curved section. For the case with the strongest secondary flow RC60, we observe at the beginning of the curved section a considerable shift of the flow towards the heated wall, i.e. the inner radius side, leading to a significant increase of the $\overline{u}$-levels in the lower half of the duct and likewise a strong $\overline{u}$-decrease in the upper half, see figure 4.12 (c). In the end section of RC60, the intense upwards flow caused by the Dean vortices interaction leads to a strong bulging of the $\overline{u}$-profile in the lower duct half midplane, although in the rest of the cross-section an evened out flow distribution is present. For the medium curvature case RC180 altogether similar trends are observed, but the Dean vortex effect on the $\overline{u}$-distribution is significantly less pronounced. For case RC900 the influence on the streamwise velocity profile initially resembles that of the straight section, whereas in the end section a slight upwards shift of the flow profile towards the outer radius wall is noticeable.

The line plots of figures 4.13 and 4.14 are included to support the qualitative observations quantitatively for the straight as well as the curved sections of the three configurations. Note that for the cross-flow velocities different x-axes are employed for the straight section and RC900 as for RC60 and RC180 to account for the significant difference in secondary flow strengths. Furthermore, only the lower duct half is shown for the straight section due to negligible heating-induced effects on the upper half. For the streamwise $\overline{u}$-profile we observe for the straight duct a insignificant variation and for RC900 a slight shift of the $\overline{u}$-profile towards the outer radius wall only in the end section due to the low secondary flow strength. This shift is more pronounced with increasing curvature for cases RC180 and especially for RC60, where the straight section flow profile is completely disrupted by an initially strong shift towards the inner radius wall with an additional increase of $\overline{u}|_{max}$, followed by a shift towards the outer radius wall with a drop of $\overline{u}|_{max}$ in the end section. The comparison between figures 4.13 (b) and (e) shows the relatively small influence of the heating-induced viscosity reduction compared to the additionally superimposed curvature-induced secondary flow on the cross-flow velocity. Figure

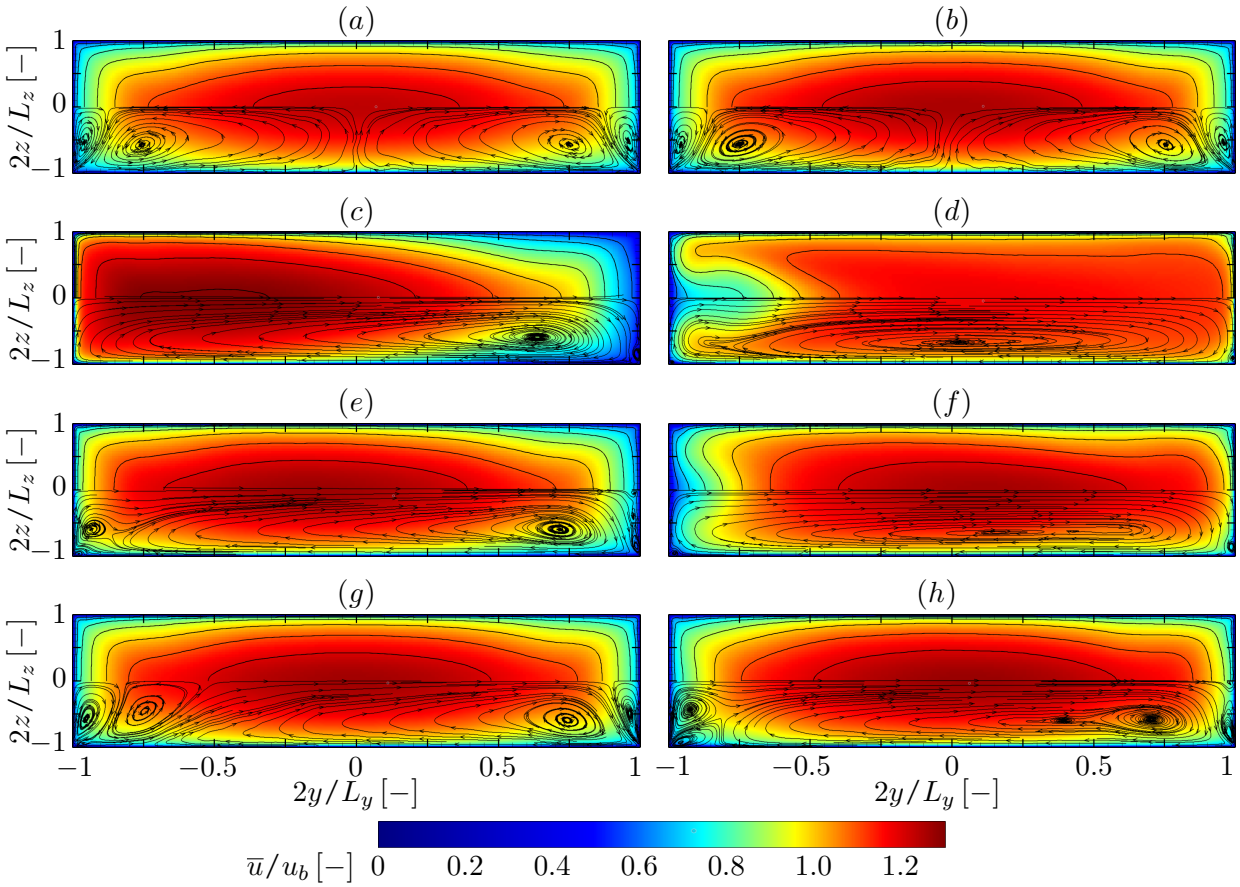

Figure 4.12: Cross-sectional streamwise velocity distribution and secondary flow structures: case RC60 in the (a) periodic duct section, (b) heated straight section at 150 mm after T_w remains constant, (c) curved section at 15° and (d) at 87.5° as well as case RC180 at (e) 5° and (f) 29.17° and case RC900 at (g) 1.5° and (h) 8.75°.

4.13 (e) supports the previous qualitative discussion of figure 4.10 for case RC900. At the inner radius side, the small turbulence-induced vortex indicated by the local $\overline{v}$-maximum becomes stronger along the curved section and is steadily incorporated into the base Dean vortex, which is indicated by the velocity difference with respect to the following local $\overline{v}$-minimum. In contrast, at the outer radius wall the turbulence-induced vortex midplane influence is only visible until position 1.5° and vanishing thereafter. Overall it can be observed that even a slight curvature is able to alter the secondary flow field significantly. For cases RC180 and RC60 the $\overline{v}$-profiles are entirely dominated by Prandtl's flow of the first kind evolving and strengthening along the HARCD section. In the end section of figure 4.13 (k) (case RC60) a distinct local $\overline{v}$-maximum followed by a $\overline{v}$-minimum has formed at $2y/L_y \approx -0.75$ with a visible impact on the $\overline{u}$- and $\overline{T}$-distributions. In this area a local constriction of the base Dean vortex is visible, see figure 4.8 (m), which we assume to be the initial stages of a splitting of the base Dean vortex. The right column of figure 4.13 depicts the heated wall-normal $\overline{w}$-distribution at the off-centre position $2z/L_z = 0.75$. Note that for the off-centre regions the statistical convergence is slower than along

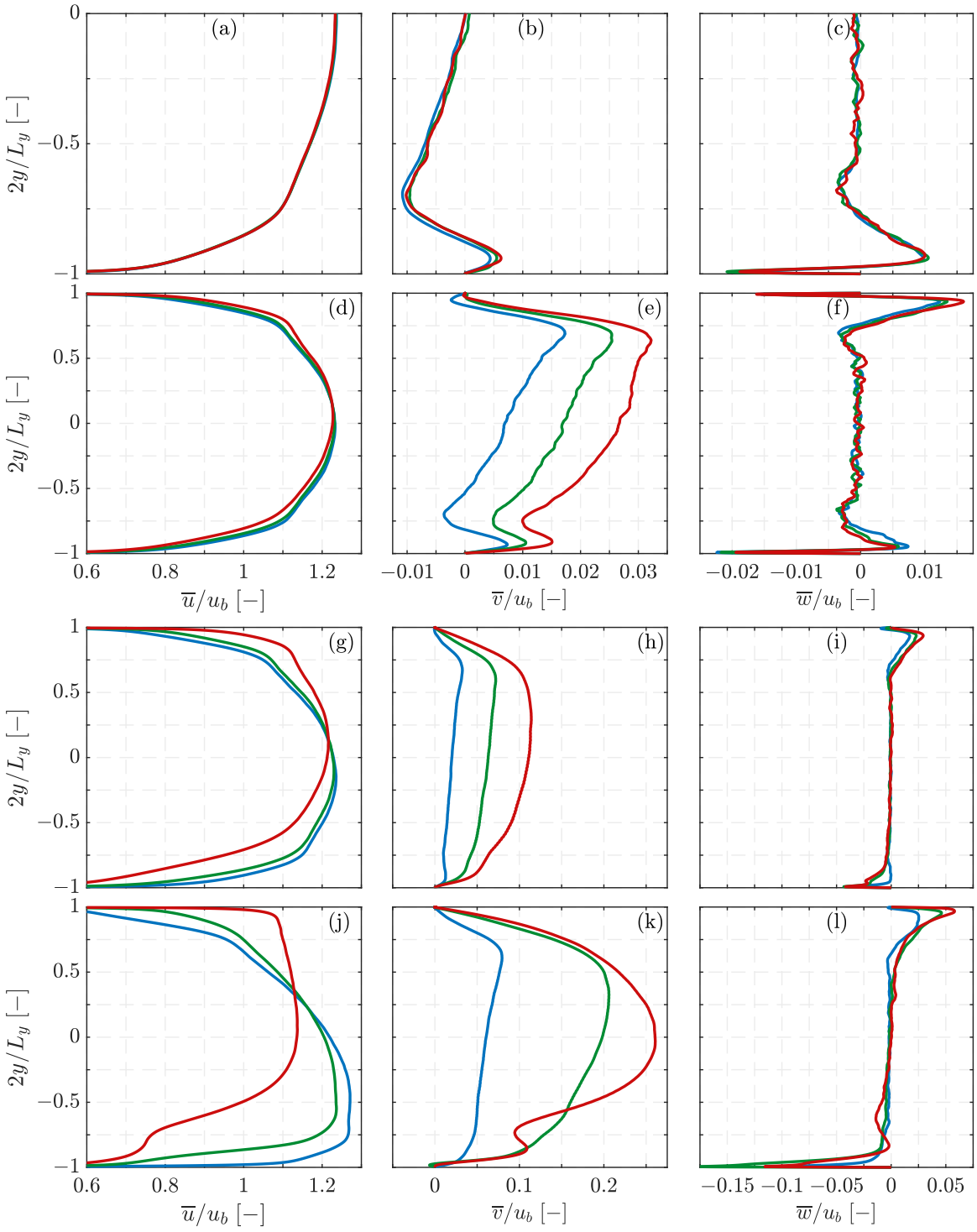

Figure 4.13: Midplane $\overline{u}$- and $\overline{v}$-, and $\overline{w}$-profiles at $2z/L_z = 0.75$ for the straight $(a-c)$ and the curved sections of case $(d-f)$ RC900, $(g-i)$ RC180 and $(j-l)$ RC60. For the straight section positions of (——) 0 mm, (——) 25 mm and (——) 150 mm, and for the curved sections (——) 15°/5°/1.5°, (——) 45°/15°/4.5° and (——) 87.5°/29.17°/8.75° are included.

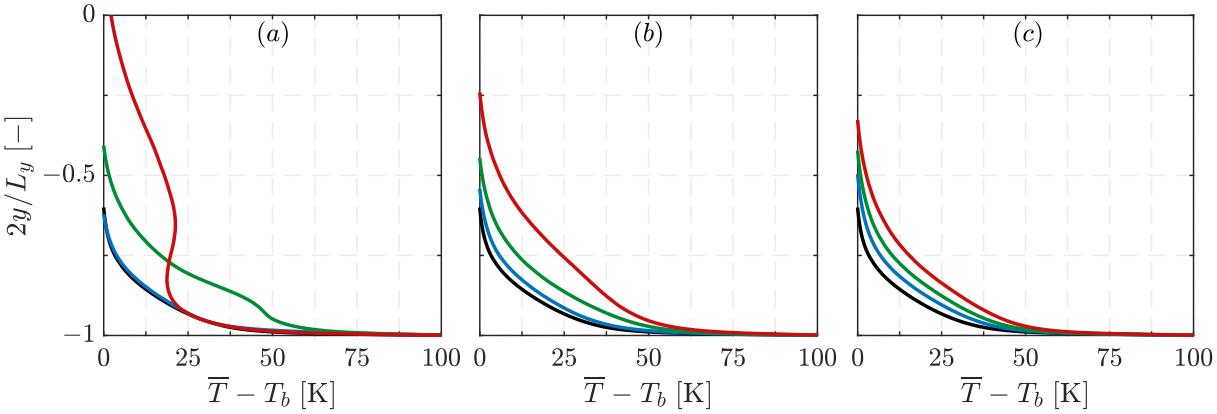

Figure 4.14: Midplane temperature profiles for the cases (*a*) RC60, (*b*) RC180 and (*c*) RC900 at streamwise positions of (——) 150 mm in the straight section and in the curved section at positions of (——) 15°/5°/1.5°, (——) 45°/15°/4.5° and (——) 87.5°/29.17°/8.75°.

the midplane, i.e. the interaction zone of the secondary flow vortices. Likewise, the secondary flow strength itself affects the convergence rate, such that in regions of low cross-flow velocity white noise fluctuations around the zero-line are noticeable, see especially figures 4.13 (c, f). Consequently, $\overline{u}$- and $\overline{v}$-profiles reach a higher statistical convergence than spanwise velocity, which vanishes along the midplane. For the straight section $\overline{w}$-profiles no relevant variation is noticeable, whereas for the curved part of case RC900 the increasing asymmetry of inner radius and outer radius vortex system becomes apparent. For the higher curvature cases we mainly notice an augmentation of the Dean vortex strength and the associated growth of spanwise fluid transport from the lateral walls towards the midplane. An exception forms the RC60 end section, where the imminent secession of a part of the base Dean vortex leads to a $\overline{w}$-drop. The midplane $\overline{T}$-distributions of figure 4.14 show the correlation of secondary flow and heat transport towards the duct core. For case RC900 the $\overline{T}$-increase is comparatively steady, whereas for RC180 and especially for RC60 the $\overline{T}$-increase is continuously growing along the section. Moreover, for cases RC60 and RC180 the initial compression of the temperature boundary layer, which is caused by the upstream influence of the strong radial pressure gradient leads to an only marginal change of the $\overline{T}$-profile with respect to the straight section profile until the first considered position, which is located at 1/6 of the curved section length.

4.3.2 Turbulent Boundary Layer Development

Subsequently the turbulent boundary layer development is discussed comprising an analysis of different scaling transformations and the effect of the varying secondary flow structure along the straight and curved HARCD sections.

The TBL profiles for the adiabatic and the straight heated section are shown in figure 4.15. For normalisation the viscous length scale l_ν^+ and friction velocity u_τ evaluated at the lower heatable wall are utilised. In contrast to the water HARCD investigation, the heating and the associated viscosity increase towards the wall lead to a downward shift of the u^+-profile in the log-region. Thus, the integration constant of the analytical law of the wall reduces from 5.2 to

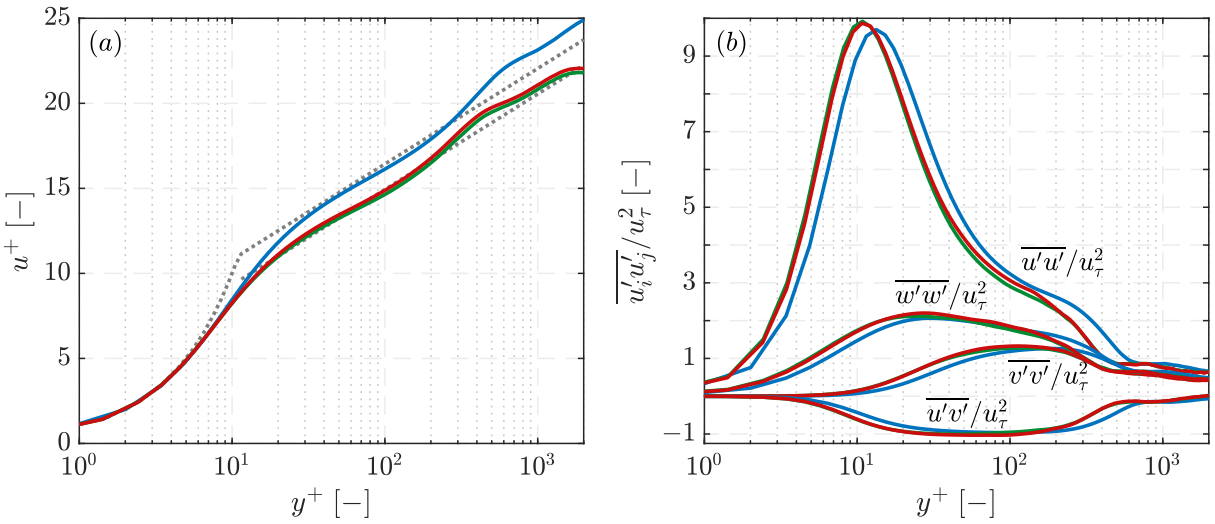

Figure 4.15: Normalised profiles of (a) streamwise velocity and (b) Reynolds stresses along the duct midplane at $z = 0$ for the adiabatic section (——), at 25 mm (——) and at 150 mm (——) after the start of the full heating. The analytical law of the wall (·····) is defined as $u^+ = (1/0.41)\ln y^+ + 5.2$ and $u^+ = (1/0.41)\ln y^+ + 3.7$, respectively.

3.7. For all Reynolds stress components a leftward shift to lower y^+-values is observed and a slight increase of the $\overline{u_i'u_j'}$-maxima noticed. The variation in the distributions of the two heated positions is negligible compared to the differences between adiabatic and heated duct.

The common approach to account for variations of mean quantities in compressible wall-bounded turbulent flows is applying the Van Driest scaling transformation following the concept of a universal law of the wall, collapsing compressible TBL profiles onto the incompressible ones. However, employing the Van Driest transformation for the entire wall TBL is only applicable for adiabatic walls with $\overline{\rho}/\overline{\rho}_w \approx 1$ in the vicinity of the wall (Pirozzoli and Bernardini, 2011; Modesti and Pirozzoli, 2016). Hence, for our case we employ the semi-local scaling transformations proposed by Brun et al. (2008) with subscript $(\cdot)_{BR}$ and by Trettel and Larsson (2016) with subscript $(\cdot)_{TL}$, independently discovered by Patel et al. (2015). The latter achieved the best results in Modesti and Pirozzoli (2016), which gives a good accuracy assessment of various compressibility transformations, and the former is chosen as it additionally considers mean viscosity variations for the Reynolds stress transformation. For a detailed discussion of the influence of mean density and viscosity gradients on turbulence and scaling behaviour we refer to Patel et al. (2015) and Patel et al. (2016). In contrast to the superscript $(\cdot)^+$ for quantities normalised with l_ν^+ and u_τ evaluated at the wall, we employ the superscript $(\cdot)^*$ for quantities with semi-local scaling within this section. The coordinates for Brun- and Trettel-Larsson-transformation read

$$y^*_{BR} = \int_0^{y^+} \left(\frac{\mu_w}{\overline{\mu}}\right) \mathrm{d}y^+ \qquad \text{and} \qquad y^*_{TL} = \frac{\overline{\rho}\sqrt{\tau_w/\overline{\rho}}}{\overline{\mu}} \cdot \Delta y, \tag{4.5}$$

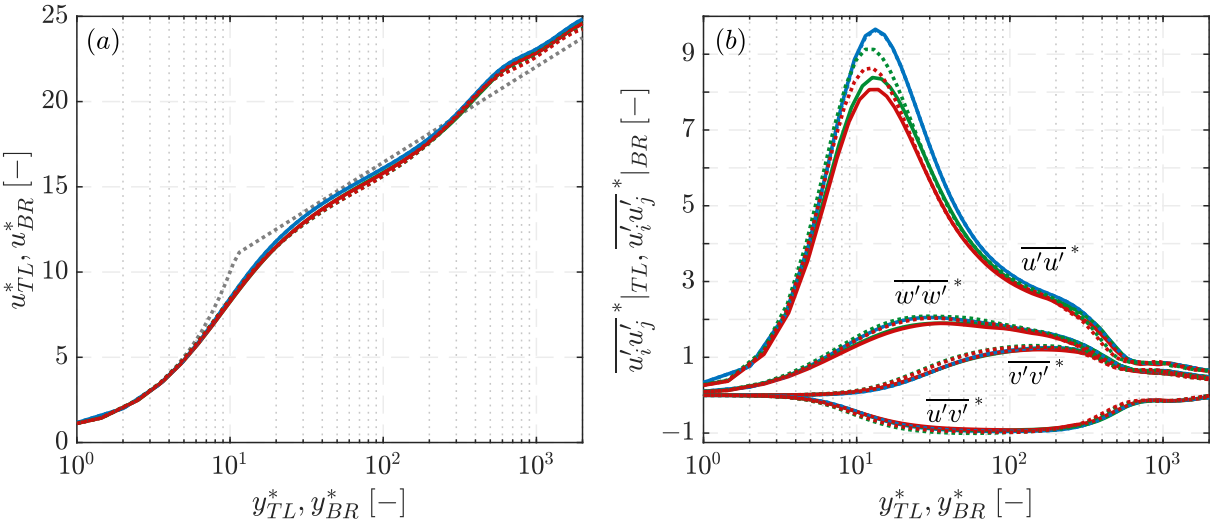

Figure 4.16: Normalised profiles of (a) streamwise velocity and (b) Reynolds stresses along the duct midplane at $z = 0$ with semi-local (solid lines) TL- and (dotted lines) BR-transformations applied for the adiabatic section (——), at 25 mm (——) and at 150 mm (——) after the start of the full heating. The analytical law of the wall (·····) is defined as $u^+ = (1/0.41)\ln y^+ + 5.2$.

with Δy here being the distance from the wall. The velocity is transformed as

$$
\begin{aligned}
u^*_{BR} &= \int_0^{u^+} \left[\left(\frac{y^+}{y^*_{BR}} \right) \sqrt{\frac{\overline{\rho}}{\rho_w}} \left(\frac{\mu_w}{\overline{\mu}} \right) \right] \mathrm{d}u^+, \\
u^*_{TL} &= \int_0^{u^+} \sqrt{\frac{\overline{\rho}}{\rho_w}} \cdot \left[1 + \left(\frac{1}{2} \frac{1}{\overline{\rho}} \frac{\mathrm{d}\overline{\rho}}{\mathrm{d}y} - \frac{1}{\overline{\mu}} \frac{\mathrm{d}\overline{\mu}}{\mathrm{d}y} \right) \Delta y \right] \mathrm{d}u^+,
\end{aligned}
\tag{4.6}
$$

and the Reynolds stresses as

$$
\overline{u'_i u'_j}^*_{TL} = \left(\frac{\overline{u'_i u'_j}}{u^2_\tau} \right) \cdot \left(\frac{\overline{\rho}}{\rho_w} \right) \qquad \text{and} \qquad \overline{u'_i u'_j}^*_{BR} = \left(\frac{\overline{u'_i u'_j}}{u^2_\tau} \right) \cdot \left(\frac{\overline{\rho}}{\rho_w} \right) \cdot \left(\frac{y^+}{y^*_{BR}} \right)^2 \cdot \left(\frac{\mu_w}{\overline{\mu}} \right)^2 . \tag{4.7}
$$

Trettel and Larsson (2016) employ the Morkovin-scaling for turbulent stresses taking the ratio of local density and its wall value into account. This scaling assumes the fluctuations of thermodynamic quantities to be small (Morkovin's hypothesis), i.e. turbulence dynamics are governed by mean property variations, but not by thermodynamic fluctuations (Coleman et al., 1995). For our case RC60, the maximum values are $\sqrt{p'^2}/\overline{p} = 0.001$, $\sqrt{\rho'^2}/\overline{\rho} = 0.055$, $\sqrt{T'^2}/\overline{T} = 0.054$ and the turbulent Mach number reaches a maximum value of $Ma_t = 0.057$ fulfilling the assumptions of Morkovin's hypothesis.

Figure 4.16 depicts the same distributions as figure 4.15 with the semi-local BR- and TL-transformations applied for coordinates, velocity and Reynolds stresses. We observe that the scaled velocity profiles for both transformations collapse well with the unheated distribution, and all profiles are in good agreement with the analytical law of the wall. The TL-transformation

gives a marginally better result than the BR-transformation. For the Reynolds stresses, the TL-scaling leads to a rightward shift of the profiles such that the positions of the streamwise turbulence maxima coincide. However, the maximum levels do not match and the distributions consequently do not collapse. A similar observation has been reported by Patel et al. (2015). Applying the BR-transformation, the rightward shift is smaller and the streamwise turbulence maxima locations do not coincide, but as the maximum levels are predicted higher an overall better collapse of the $\overline{u'u'}^*$- and $\overline{w'w'}^*$-distributions is obtained. The reason for the better coincidence is the consideration of mean viscosity gradients additional to mean density gradients in the Reynolds stress transformation.

Figures 4.17 and 4.18 depict TBL profiles at several positions along the curved sections for the three configurations along the duct midplane and at the off-centre location $2z/L_z = 0.75$ with the TL-transformation applied for all distributions. Note that the streamwise slice positioning is such, that they are taken at the same relative streamwise distance measured with respect to the duct centre. Additionally, the analytical law of the wall and the Reynolds stress distribution of the adiabatic periodic section are included for reference and for comparison, respectively. The two spanwise slice positions experience a substantially different secondary flow field influence. In the midplane the two interacting Dean vortices create a strong upwards oriented flow away from the heated wall and at $2z/L_z = 0.75$ the single Dean vortex of the respective duct half creates a weaker downwards and inwards oriented flow deflecting the cold fluid from the duct core towards the centre line, see also figures 4.8, 4.9 and 4.10 of the previous section for reference.

Overall, the secondary flow impact is clearly visible: the stronger the Dean vortices the higher the deviations of the TBL profiles from the straight heated HARCD reference case only affected by the weaker turbulence-induced secondary flow. On the one hand this can be seen in the midplane slices comparing the different curvature cases with each other and on the other hand comparing the midplane with the off-centre slice for the individual case. For case RC60 with the strongest Dean vortices, the velocity profiles follow the analytical solution only in the viscous sublayer, see figure 4.17 (a). At position 15°, the Dean vortices already cause a significant upward shift of the profile directly in the buffer layer, whereas at 45° the profile follows the law of the wall until $y^*_{TL} \approx 10^2$ in the logarithmic region before an upward shift occurs. In the end section, a slight upward shift is visible in the logarithmic region followed by a significant velocity increase from $y^*_{TL} \approx 400$ onwards. The reason for the different behaviour at 45° compared to the two other positions is the pair of small counter-rotating ICW Dean vortices forming in the duct centre immediately above the heated wall somewhere between 30° and 45°, which become weaker and vanish towards the end of the curved section, see figure 4.8. When this pair is weak or non-existing, the Dean vortex influence reaches closer to the heated wall. At the off-centre location for RC60, see figure 4.18 (a), the u^*_{TL}-distributions for 45° and the end section resemble each other and follow a downwards shifted logarithmic distribution parallel to the analytical law of the wall. This downward shift is expected and due to the shift of the slice position towards the lateral sidewall, see Kaller et al. (2018) for a further discussion. At position 15°, however, no logarithmic behaviour is obtained over the whole range of the TBL due to the disturbing effect of the yet developing Dean vortex system. Like the velocity, also the Reynolds stress distributions are highly affected by the secondary flow motions, see figures 4.17 (b) and 4.18 (b). In the midplane, we observe for all components a reduction in their respective strength

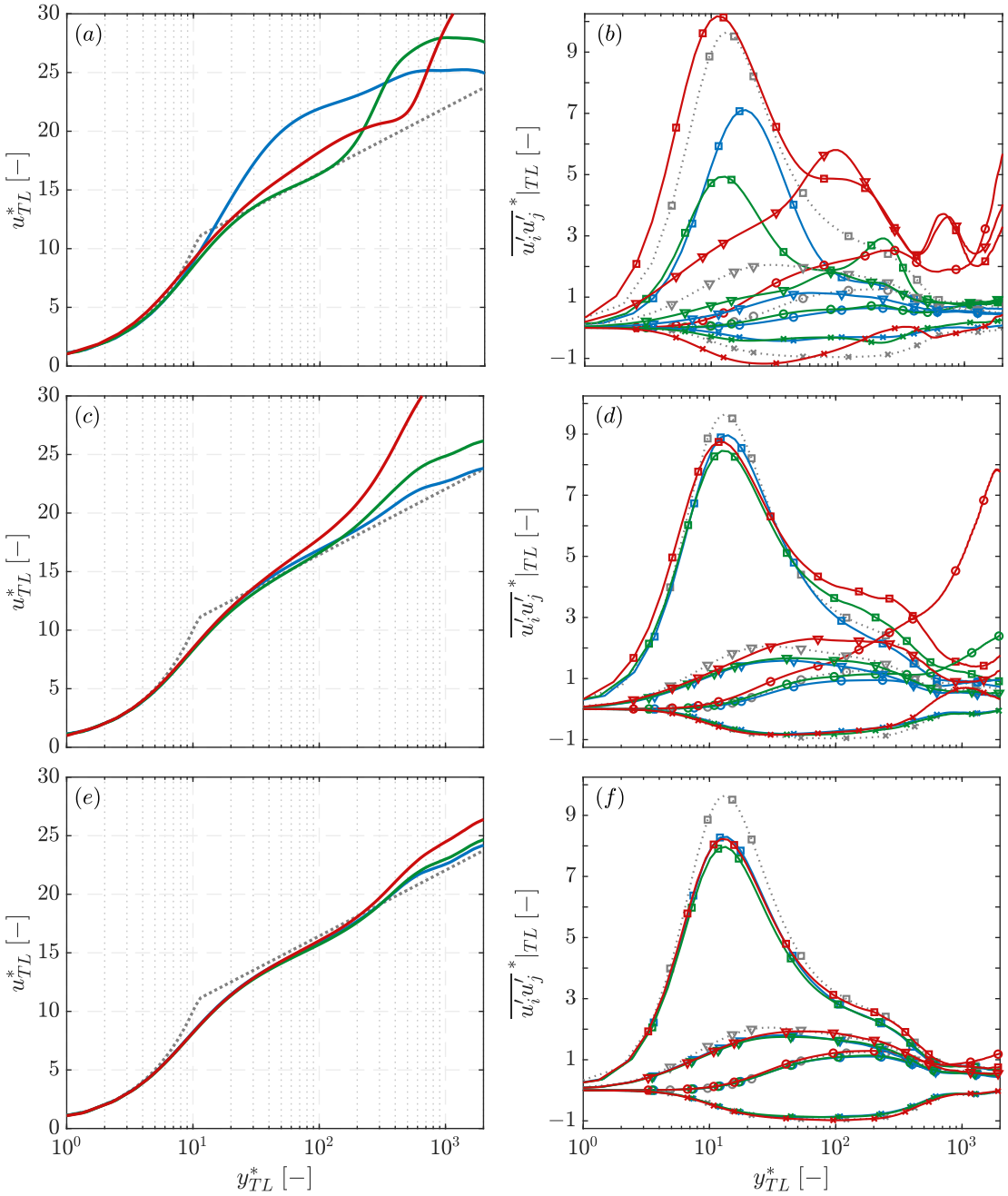

Figure 4.17: Normalised profiles of (a, c, e) streamwise velocity and (b, d, f) Reynolds stresses along the duct midplane at $z = 0$ with semi-local TL-transformation applied for the curved section of cases (a, b) RC60, (c, d) RC180 and (e, f) RC900. The line (——) denotes the position 15° of RC60 and correspondingly 5° for RC180 and 1.5° for RC900, (——) 45° of RC60 and correspondingly 15° for RC180 and 4.5° for RC900, and (——) the respective end sections at 87.5°, 29.17° and 8.75°. The line (·····) defines the analytical law of the wall in the velocity plots and the adiabatic result in the Reynolds stress plots. The markers denote (□) $\overline{u'u'}$-, (○) $\overline{v'v'}$-, (▽) $\overline{w'w'}$- and (×) $\overline{u'v'}$-components.

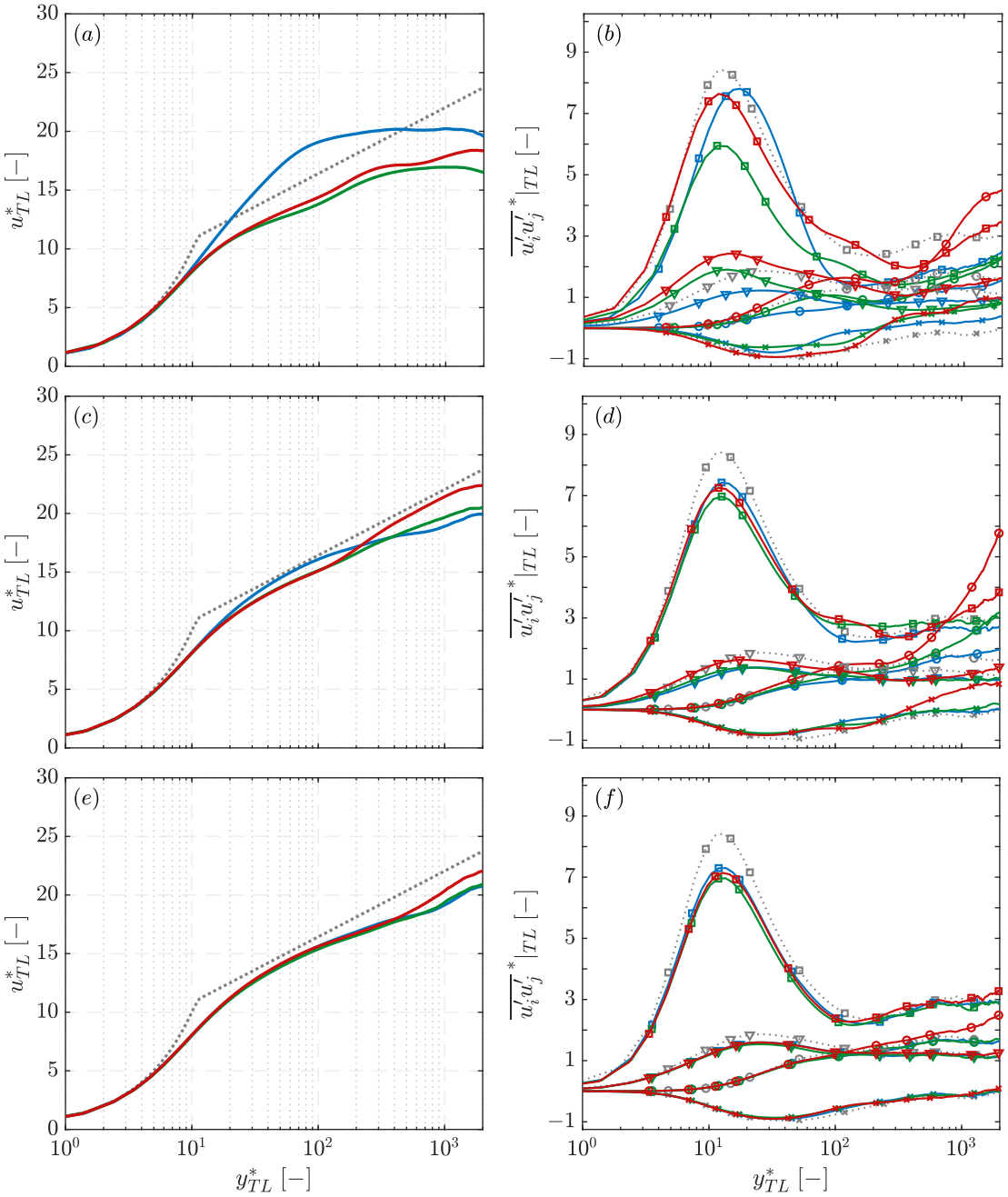

Figure 4.18: Normalised profiles of (a, c, e) streamwise velocity and (b, d, f) Reynolds stresses along $2z/L_z = 0.75$ with semi-local TL-transformation applied for the curved section of cases (a, b) RC60, (c, d) RC180 and (e, f) RC900. The line (——) denotes the position 15° of RC60 and correspondingly 5° for RC180 and 1.5° for RC900, (——) 45° of RC60 and correspondingly 15° for RC180 and 4.5° for RC900, and (——) the respective end sections at 87.5°, 29.17° and 8.75°. The line (·····) defines the analytical law of the wall in the velocity plots and the adiabatic result in the Reynolds stress plots. The markers denote (□) $\overline{u'u'}$-, (○) $\overline{v'v'}$-, (▽) $\overline{w'w'}$- and (×) $\overline{u'v'}$-components.

at the positions 15° and 45° compared to the unheated HARCD profiles. However, in the end section with the Dean vortex system fully developed and the strongest secondary flow field, an increase of all turbulent stress components is visible. Furthermore, the distributions of $\overline{u'u'}$, $\overline{v'v'}$ and $\overline{w'w'}$ experience multiple peaks and $\overline{u'v'}$ an upward dent in the region of $y^*_{TL} \approx 300$. These modulations are caused by the complex Dean vortex system consisting of the base Dean vortex, the vanishing ICW Dean vortex and the split base Dean vortex. Specifically the developing split base Dean vortex close to the inner radius wall, which is accompanied by a considerable dent in the upwards oriented $\overline{v}$-velocity, as shown in figure 4.13 (k) of the previous section, exhibits a significant impact on the Reynolds stress distributions. For the off-centre slices, the weaker local secondary flow strength also leads to smaller deviations with respect to the unheated reference profiles. As expected, the presence of a strong cross-sectional flow hinders the applicability of transformation laws to collapse the TBL distributions.

For the medium curvature case RC180, the overall secondary flow strength reaches approximately half the value of RC60. Consequently, a reduced influence on the TBL profiles is to be expected and observed. The velocity profile in figure 4.17 (c) for the first streamwise position at 5° follows well the analytical law of the wall. In the middle of the curved section at position 15°, u^*_{TL} follows a logarithmic profile only until $y^*_{TL} \approx 150$ and then experiences an upward shift due to the increasing strength of the Dean vortex interaction zone in the midplane. In the end section, the u^*_{TL}-profile matches the law of the wall just in the viscous sublayer and shows a similar uplift at the end of the buffer layer as previously seen in the RC60 results. For the off-centre location in figure 4.18 (c), a similar progression of the distributions is observed as for case RC60, but the downward shift and the deviations are significantly reduced as the Dean vortex structure is indeed similar, although the vortices are weaker. Likewise the Reynolds stress profiles are affected less by the weaker secondary flow and the highest deviations with respect to the unheated straight HARCD are present in the end section, where the Dean vortices are strongest and exhibit an uplifting effect. In contrast to RC60, no multiple peak structure is observed for $\overline{u'u'}$ and $\overline{w'w'}$ as neither the ICW Dean vortex nor the split base Dean vortex is forming in the vicinity of the inner radius wall. Thus, the $\overline{v}$-profile shows a steadily increasing strength towards the duct core, see figure 4.13 (h), effecting the predominant rise of $\overline{v'v'}$ towards the end of the shown section. For the case RC900 with the lowest curvature and the weakest Dean vortices, the trend continues and only minor deviations of both the velocity and turbulent stress profiles are noticeable. The most prominent deviation is the drop of the $\overline{u'u'}$-peak compared to the unheated straight HARCD. However, this drop has already been observed for the straight duct and is not attributed to the Dean vortex influence, see figure 4.16. Hence, we conclude that for case RC900 with only weak Dean vortex influence and an overall weak cross-sectional secondary flow field the TL-transformation can be successfully employed to collapse the TBL distributions.

For collapsing the temperature profile, Kader (1981) proposed a relation similar to the law of the wall with

$$\Delta T^+ = \begin{cases} Pr\, y^+ & \text{in the viscous sublayer for } y^+ \lessapprox 5 \\ 2.12 \ln(y^+) + \beta(Pr) & \text{in the logarithmic region for } y^+ \gtrapprox 30 \end{cases}. \tag{4.8}$$

The term $\beta(Pr)$ is defined as $\beta(Pr) = (3.85\, Pr^{(1/3)} - 1/3)^2 + 2.12 \ln(Pr)$ and ΔT^+ is the

normalised temperature difference with respect to T_w. For the molecular Prandtl number we use its value evaluated directly at the wall. Note, the so-called Kader's law is derived based on the assumption of a channel flow without secondary flow influence, a constant Pr and a constant $Pr_t = 0.85$. All three assumptions are violated by our investigated configurations limiting the comparability. In analogy to the velocity profile, a friction temperature is introduced for normalisation of the temperature profile as $T_\tau = q_w/(\rho_w c_{p_w} u_\tau)$, based on the local friction velocity u_τ and wall heat flux q_w. Guo et al. (2018) proposed a relation analogous to the TL-transformation for the temperature profile, which reads

$$\Delta T^*_{TL} = \int_0^{\Delta T^+} \sqrt{\frac{\overline{\rho c_p^2}}{\rho_w c_{p_w}^2}} \cdot \left[1 + \left(\frac{1}{2}\frac{1}{\overline{\rho c_p^2}}\frac{\mathrm{d}\overline{\rho c_p^2}}{\mathrm{d}y} - \frac{1}{\overline{\mu}}\frac{\mathrm{d}\overline{\mu}}{\mathrm{d}y}\right)\Delta y\right] \mathrm{d}(\Delta T^+). \tag{4.9}$$

In figure 4.19, the normalised midplane and off-centre temperature profiles are depicted for the straight and curved sections. Both the temperature distributions with normalisation by T_τ and with the TL-transformation applied are included as well as the empirical Kader's law for comparison. In figure 4.19 (a) the development of the temperature profile along the straight heated section shows the expected distribution for a thermal entrance problem with evolving temperature boundary layer. We observe that the profiles normalised with the friction temperature follow Kader's law in the viscous sublayer, but run parallel to it in the logarithmic region experiencing a nearly constant downward shift. Applying the TL-transformation leads to an upward shift, such that all profiles coincide with Kader's law. This match in semi-local coordinates proves that the temperature profile shift is a viscosity effect and not a turbulence-induced secondary flow effect. With growing distance of the considered slice positions from the onset of the heating, i.e. with increasing growth of the temperature boundary layer, the individual profiles follow the logarithmic profile longer and level off at the bulk temperature at higher y^+- and y^*_{TL}- values, respectively.

For the following discussion of the curved section results, we focus solely on the TL-transformed profiles. Overall, we observe for the temperature profiles a similar behaviour as for the velocity profiles previously: both are highly affected by the strong secondary flow presence. In figure 4.19 (b), the midplane distributions for case RC60 with the strongest Dean vortices are presented. The temperature profiles at all streamwise positions follow Kader's law only in the viscous sublayer. At the first position of 15°, the Dean vortices intensify the upward transport of hot fluid towards the duct core leading to a significant uplifting of the temperature profile. In contrast, for the end section a downward shift of the ΔT^*_{TL}-profile is present. At this position, the candle flame shaped structure of the $\overline{T}$-contour has developed, see figure 4.8 (n), i.e. the Dean vortices reach a strength, where they transport enough cold fluid from the lateral sidewalls into the midplane to effect a drop of the local temperature. At the midway position of 45°, the influence of the pair of small ICW Dean vortices is similar as for the velocity profiles, see figures 4.8 (i) and 4.17 (a). The presence of the counter-rotating vortices above the heated wall centre leads to a reduced overestimation with respect to Kader's law until $y^*_{TL} \approx 100$, where the base Dean vortex pair mixing causes a significant ΔT^*_{TL}-uplift. For the midplane profile of case RC180 in figure 4.19 (c), we observe a reasonably well collapse of the ΔT^*_{TL}-profiles. At all positions ΔT^*_{TL} follows Kader's law in the sublayer and deviates from it in the logarithmic region. The

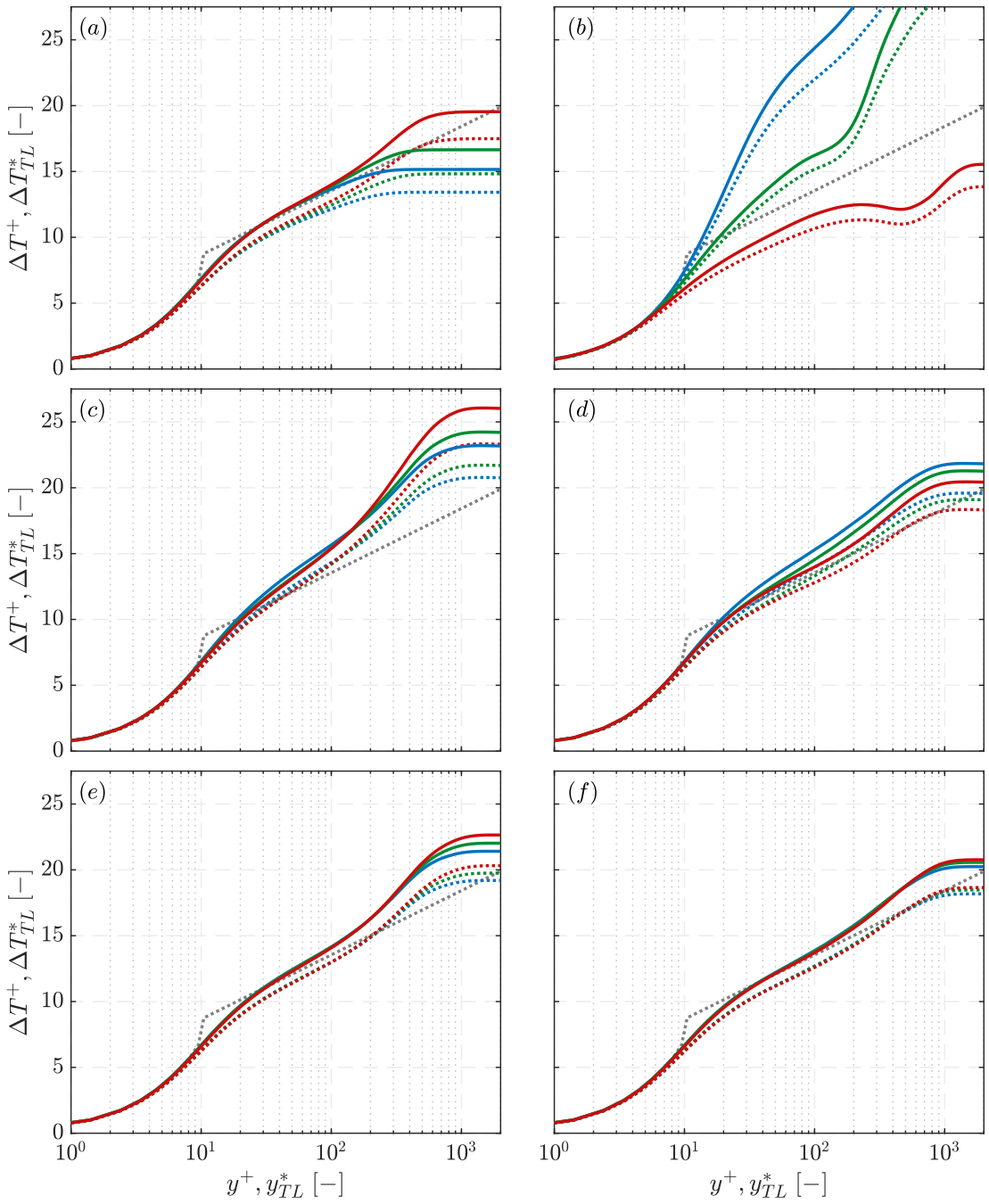

Figure 4.19: Normalised temperature profiles (dotted lines) and with semi-local TL-transformation applied (solid lines) for the (a) straight section at positions of 25 mm (——), 50 mm (——), 150 mm (——) and for the curved section of (b) case RC60 at positions of 15° (——), 45° (——), 87.5° (——) along the midplane at $z = 0$, of (c, d) case RC180 correspondingly at positions of 5°, 15°, 29.17° for $z = 0$ (left) and $2z/L_z = 0.75$ (right) and of (e, f) case RC900 correspondingly at positions of 1.5°, 4.5°, 8.75° for $z = 0$ (left) and $2z/L_z = 0.75$ (right). The analytical profile following Kader (1981) is represented by (·····), see equation 4.8.

weaker Dean vortices and accordingly weaker upward transport of hot fluid produces for this case logarithmic ΔT^*_{TL}-distributions, although at a steeper angle than predicted by Kader's law. At the off-centre position for case RC180 no collapse of the temperature profiles is achieved using the TL-transformation. With streamwise distance and growing Dean vortex strength, i.e. with increased bulging of the $\overline{T}$-contour, see the right column of figure 4.9, the local $\overline{T}$-reduction causes the ΔT^*_{TL}-profiles to approach Kader's law distribution. For RC900 with the weakest secondary flow, the normalised temperature distributions collapse both in the midplane and at the off-centre location. As for case RC180, the ΔT^*_{TL}-distribution follows a logarithmic law, although at a slightly steeper angle as proposed by Kader's law, due to the secondary flow induced upward transport of hot fluid away from the heated wall. Compared to RC180 the steepness is reduced due to the weaker cross-flow. At the off-centre-location the slope is further reduced, such that the ΔT^*_{TL}-profiles almost follow Kader's law. Overall, we come to a similar conclusion as for the velocity TBL profiles: employing the TL-transformation achieves a reasonably well collapse of the TBL profiles only for cases affected by sufficiently weak cross-sectional secondary flow influence.

4.3.3 Streamwise Vorticity Field

Within this subsection the influence of heating and streamwise curvature on the cross-sectional secondary flow field is investigated by analysing the mean streamwise vorticity equation. Analogous to section 3.5.2 of the previous water HARCD analysis in chapter 3, a special focus is set on the development in the duct corner regions. The main differences are the increasing viscosity towards the heated wall and especially the additional formation of Prandtl's flow of the first kind interacting with the turbulence-induced secondary flow. After an initial cross-sectional $\overline{\omega}_x$ overview, the discussion in the first part is centred on the heating effect on $\overline{\omega}_x$ as well as its source and sink terms in the corner region including a short comparison with the water HARCD results. Then, in the second part the influence of curvature-induced secondary flow on the $\overline{\omega}_x$-distribution and the terms of its balance equation is analysed.

For the definition of the individual terms of the mean streamwise vorticity equation the reader is referred to equation 3.3 in section 3.5.2. In contrast to the straight heated water HARCD investigation, the vortex stretching and tilting terms $T_{\overline{\omega}_x,stretch/tilt}$ now differ from zero due to the curvature-induced secondary flow development and the local homogeneity assumption is dropped, i.e. streamwise gradients $\partial(\cdot)/\partial x \neq 0$. The normalisation of streamwise vorticity and the single terms $T_{\overline{\omega}_x,(\cdot)}$ is performed in outer scales, i.e. $\overline{\omega}^o_x = \overline{\omega}_x/(u_b/d_h)$ and $T^o_{\overline{\omega}_x,(\cdot)} = T_{\overline{\omega}_x,(\cdot)}/(u_b/d_h)^2$ to allow for an identical procedure and comparability throughout the complete duct cross-section, i.e. for regions influenced by wall-heating and for essentially unaffected regions close to the outer radius wall. Note, as pointed out in section 3.5.2 and by Pirozzoli et al. (2018), only the core vorticity scales in outer units (u_b/d_h), whereas the corner vorticity scales in mixed units (u_b/l^+_ν).

Figure 4.20 depicts the mean streamwise vorticity distribution for the straight and the curved sections of the three configurations over the complete cross-section. The overall differences between heated and adiabatic as well as the low curvature case RC900 are marginal compared to the medium and high curvature cases RC180 and RC60, respectively. For the latter two a significant structural modification and strength increase of $\overline{\omega}_x$ can be observed along the curved

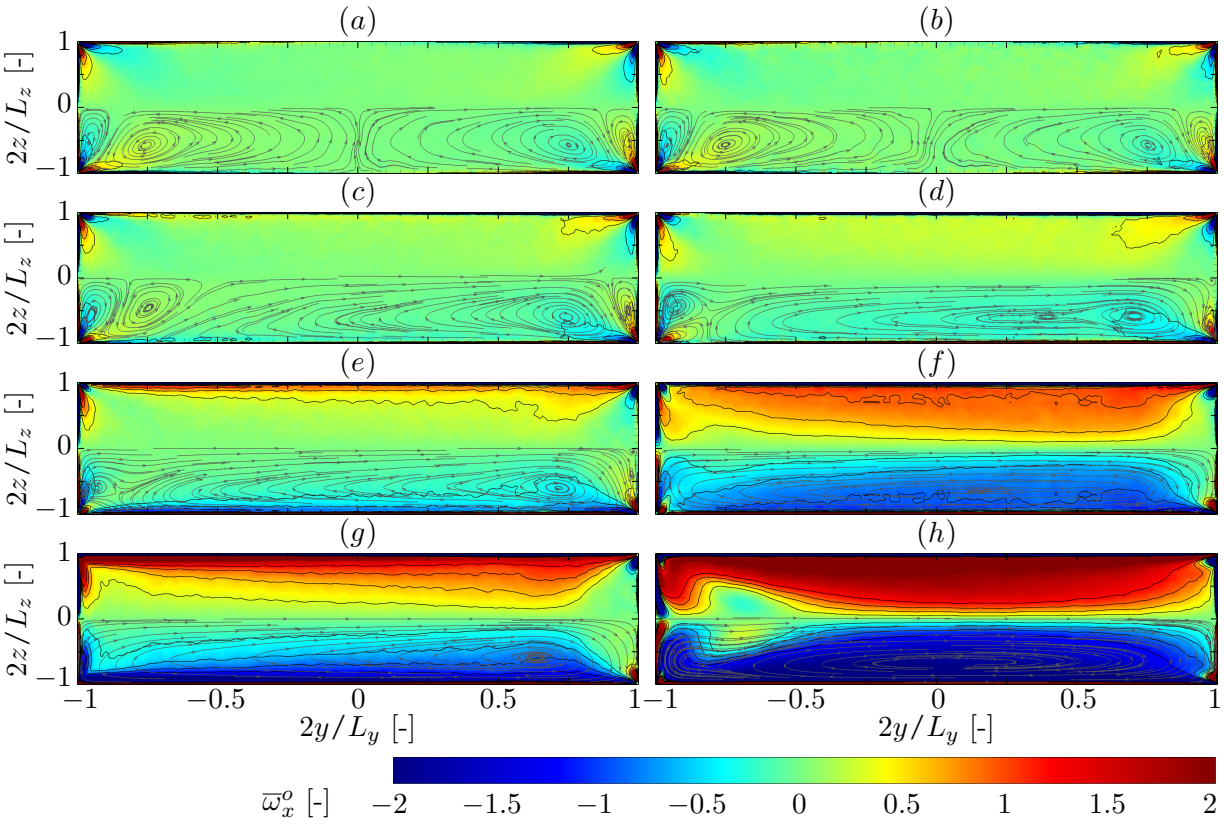

Figure 4.20: Normalised distributions of the mean streamwise vorticity in the HARCD cross-section with $\overline{\omega}_x^o = \overline{\omega}_x/(u_b/d_h)$: (a) adiabatic section and (b) heated straight section at a position of 150 mm, (c, d) case RC900 at 1.5° (left) and 8.75° (right), (e, f) case RC180 at 5° (left) and 29.17° (right) and (g, h) case RC60 at 15° (left) and 87.5° (right). Isolines are drawn from −1.2 to 1.2 in steps of 0.3 and streamlines added for secondary flow visualisation.

section due to the strong Prandtl's flow of the first kind superimposing and superseding the turbulence-induced secondary flow field. For RC900, however, the two types of Prandtl's flow are of comparable strength and consequently interact with each other without one displacing the other.

Initially the heating influence is analysed in the duct corners of the straight segment analogous to section 3.5.2. Due to the inverse behaviour of the fluid viscosity with rising temperature, the inverse trends are expected for air instead of water as working fluid. Despite the relatively short distance of 150 mm, over which the asymmetric heating is applied, it is observed that the corner vorticity becomes weaker both in the primary vorticity patches around the corner bisecting line as well as along the lateral sidewall, compare figures 4.21 (a) and (b) as well as figures 4.22 (a) and (e). Likewise the corner vorticity penetrates less deep into the duct corners and the vorticity layers along the walls broaden. These observations are in qualitative agreement with Pirozzoli et al. (2018) as the wall heating leads to a local decrease of Re_τ in our case. For the core vorticity an asymmetric behaviour can be seen: the core vorticity associated with the small lower wall vortex increases, whereas the core vorticity associated with the large sidewall vortex

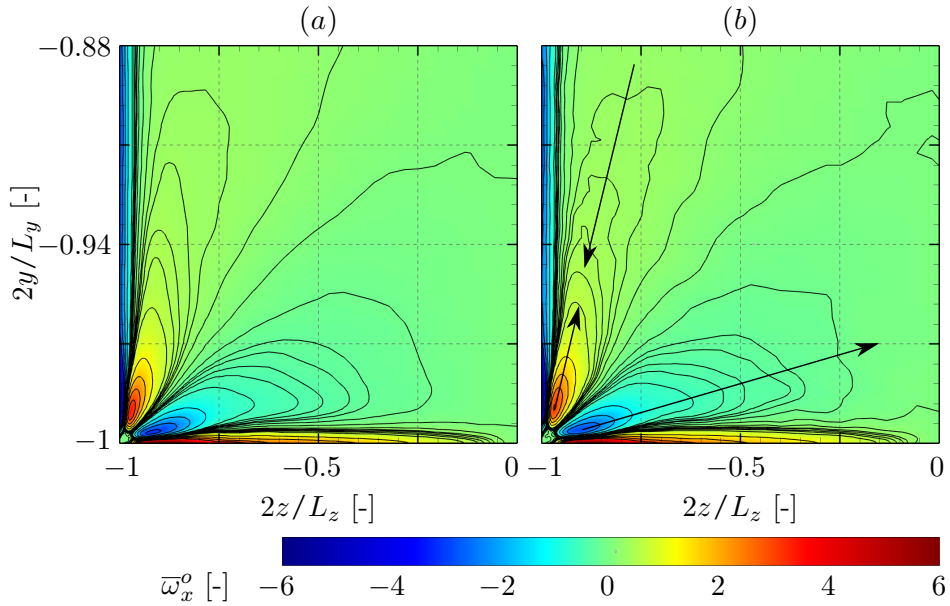

Figure 4.21: Normalised distributions of the mean streamwise vorticity in the lower left HARCD corner with $\overline{\omega}_x^o = \overline{\omega}_x/(u_b/d_h)$: (a) adiabatic section and (b) heated straight section at a position of 150 mm. Isolines are drawn from −3 to 3 in steps of 0.6 and additionally for ±0.15, ±0.25, ±0.3, ±0.375 and ±0.45. The arrows in (b) indicate the heating-induced shift of the isolines. Results are based on combined statistics for RC60, RC180 and RC900.

decreases slightly, compare figures 4.21 (a) and (b). The heating-induced vorticity modulation is indicated using arrows and the result smoothed by combining the statistics for all three cases RC60, RC180 and RC900. The observation of the asymmetric vorticity change is in accordance with the asymmetric secondary flow velocity modulation shown in figure 4.6 of the previous section 4.3.1.

The corner distributions of the individual terms of equation system 3.3, i.e. of the convective term $T^o_{\overline{\omega}_x,conv}$ in figure 4.23, the sum of viscous terms $T^o_{\overline{\omega}_x,visc,sum}$ in figure 4.24 and the sum of turbulence terms $T^o_{\overline{\omega}_x,turb,sum}$ in figure 4.26 all possess a similar structure as discussed in section 3.5.2. Likewise the turbulence and viscosity terms are again the dominating ones compared to the convective term. Nevertheless, differences for $T^o_{\overline{\omega}_x,visc,sum}$ and $T^o_{\overline{\omega}_x,turb,sum}$ compared to the water HARCD set-up are noticed. For the viscous term distributions the narrow inverse-sign layer between the primary $T^o_{\overline{\omega}_x,visc,sum}$-zone and the sidewalls is more pronounced, which is probably due to an improved local mesh resolution facilitated by the lower Re_b and Re_τ of the air HARCD configuration. The deviation of the duct corner extensions below the primary zones with respect to the results by Pirozzoli et al. (2018) are identical as before. Thus, the extension region is orientated in parallel to the sidewalls and not in parallel to the corner bisecting line. A further difference encompasses the viscosity gradient terms $T^o_{\overline{\omega}_x,visc,2}$ and $T^o_{\overline{\omega}_x,visc,3}$. In contrast to the water HARCD, these regions now have a positive sign reinforcing the $T^o_{\overline{\omega}_x,visc,1}$-maximum, see figure 4.25. For the turbulence term distributions two minor disparities are observable with respect to the INCA results: on the one hand the primary regions are slightly tilted and on the

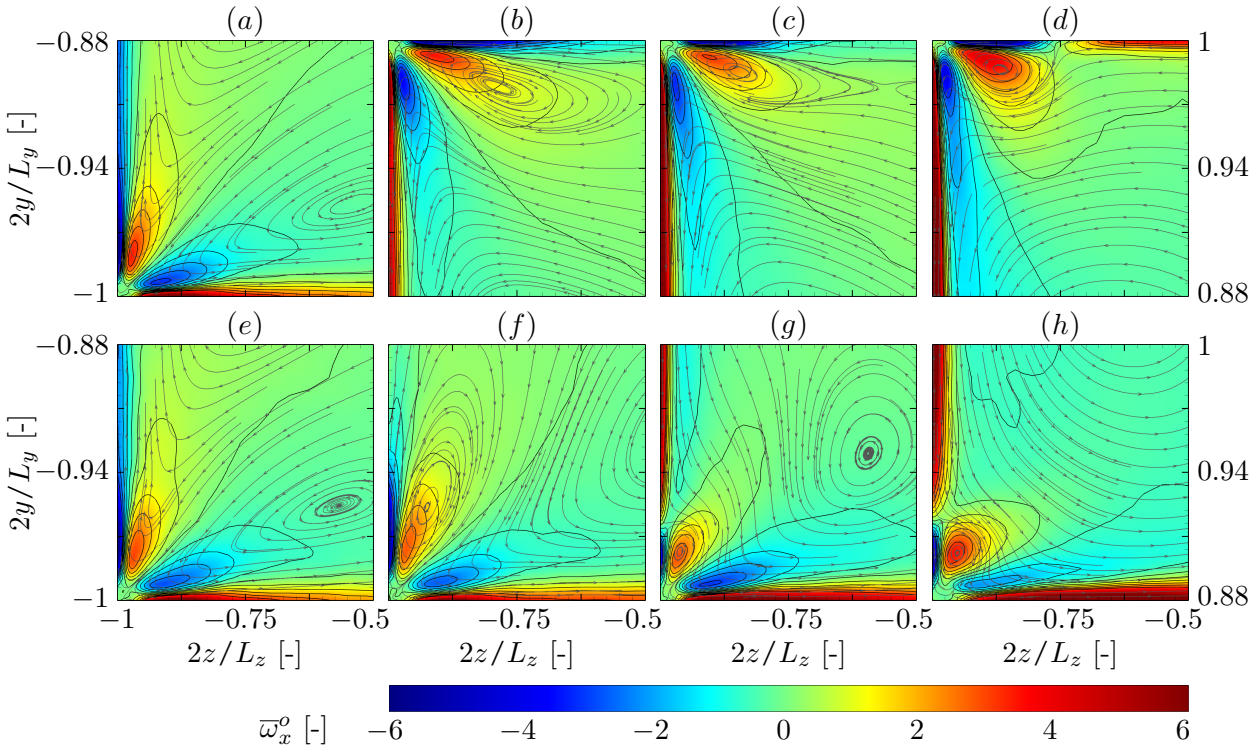

Figure 4.22: Mean streamwise vorticity distributions in the lower and upper left corners with $\overline{\omega}_x^o = \overline{\omega}_x/(u_b/d_h)$: lower corner of the (a) adiabatic section and (e) straight heated section at 150 mm, (b, f) upper/lower corner of case RC900 at 8.75°, (c, g) upper/lower corner of case RC180 at 5° and (d, h) upper/lower corner of case RC180 at 29.17°. Isolines are drawn from −3 to 3 in steps of 0.6 and streamlines visualise the secondary flow.

other hand the inverse-sign layers forming along the sidewalls below the primary regions towards the duct centre are not present. Besides the different configuration, boundary conditions and grid resolution this deviation is partly attributed to the use of a different ALDM turbulence model, see also section 4.2.

When heating is applied, we observe for the individual terms of the $\overline{\omega}_x$-equation $T^o_{\overline{\omega}_x,(\cdot)}$ the inverse behaviour as for the water HARCD, similarly as for the $\overline{\omega}_x$-distribution. Both the convective and the turbulence term distributions decrease noticeably in strength and penetrate less deep into the duct corner due to the heating-induced viscosity increase and local Re_τ decrease, respectively, compare figures 4.23 (a, e) and 4.26 (a, e). Likewise $T^o_{\overline{\omega}_x,visc,sum}$ penetrates deeper into the duct corner in the adiabatic case. However, the strength modulation is different at the lower and lateral wall due to the asymmetrically applied heating. The $T^o_{\overline{\omega}_x,visc,sum}$-minimum region along the lateral sidewall is weakened noticeably, whereas the level of the $T^o_{\overline{\omega}_x,visc,sum}$-maximum along the lower wall drops only slightly. The peak values for the straight duct $\overline{\omega}_x$-production and -destruction terms $T^o_{\overline{\omega}_x,turb,sum}$ and $T^o_{\overline{\omega}_x,visc,sum}$ are listed in table 4.6 and the associated heating-induced change in table 4.7.

For the water HARCD investigation the asymmetric modulation of turbulence and viscosity terms in the duct corner has coincided with the observed asymmetric heating-induced change of

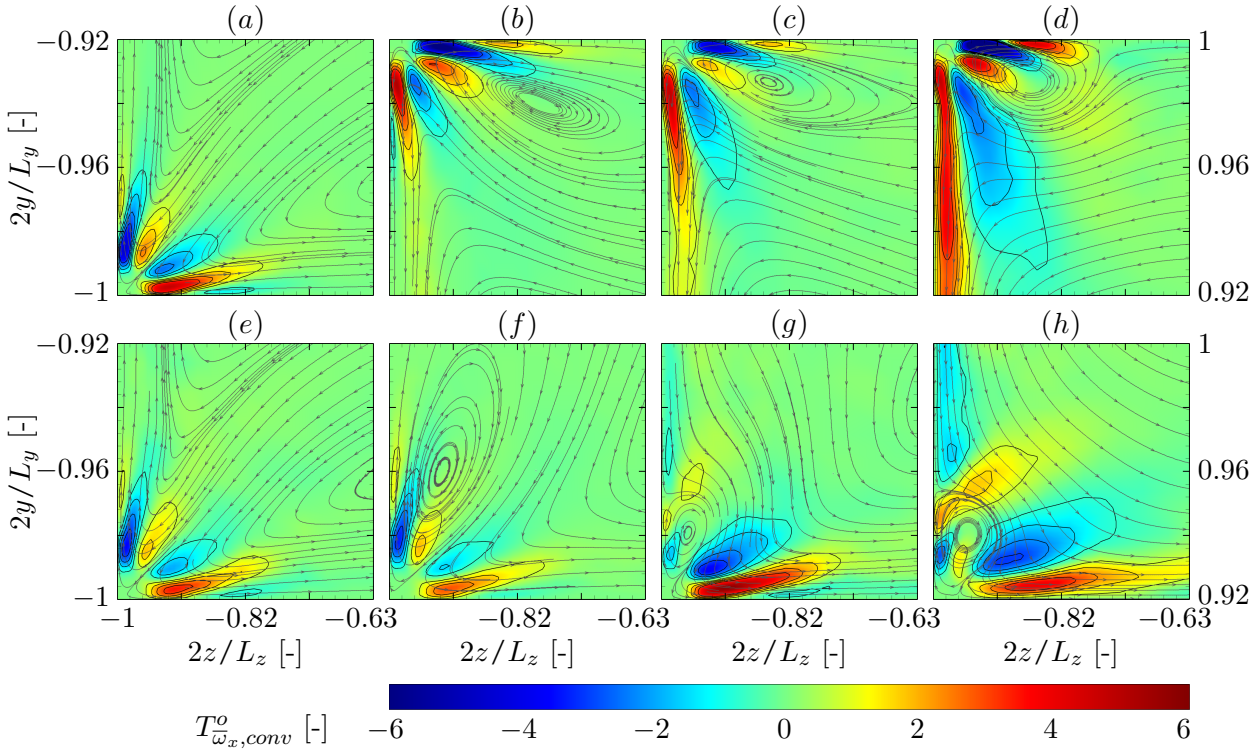

Figure 4.23: Convective term distribution of the $\overline{\omega}_x$-equation 3.3 in the lower and upper left corners with $T^o_{\overline{\omega}_x,conv} = T_{\overline{\omega}_x,conv}/(u_b/d_h)^2$: lower corner of the (a) adiabatic section and (e) straight heated section at 150 mm, (b, f) upper/lower corner of case RC900 at 8.75°, (c, g) upper/lower corner of case RC180 at 5° and (d, h) upper/lower corner of case RC180 at 29.17°. Isolines are drawn from −3 to 3 in steps of 0.75 and streamlines visualise the secondary flow.

wall/domain	$T^*_{\overline{\omega}_x,turb,sum}$ [−]	$T^o_{\overline{\omega}_x,turb,sum}$ [−]	$T^*_{\overline{\omega}_x,visc,sum}$ [−]	$T^o_{\overline{\omega}_x,visc,sum}$ [−]
lower/adiabatic	−2.323	−8.737	3.142	11.813
lower/heated	−2.248	−7.475	3.439	11.416
lateral/adiabatic	2.342	8.801	−3.160	−11.882
lateral/heated	2.444	8.119	−3.121	−10.361

Table 4.6: Peak values of $T_{\overline{\omega}_x,turb,sum}$ and $T_{\overline{\omega}_x,visc,sum}$ in the lower left corner for the straight adiabatic and heated duct at 150 mm, $(\cdot)^*$ denotes normalisation by $(u_b/l^*_\nu)^2$ and $(\cdot)^o$ by $(u_b/d_h)^2$. Results are based on combined statistics for RC60, RC180 and RC900.

wall	$\Delta T^*_{\overline{\omega}_x,turb,sum}$[%]	$\Delta T^o_{\overline{\omega}_x,turb,sum}$[%]	$\Delta T^*_{\overline{\omega}_x,visc,sum}$[%]	$\Delta T^o_{\overline{\omega}_x,visc,sum}$[%]
lower	3.228	14.444	9.459	−3.366
lateral	4.352	−7.748	1.225	12.798

Table 4.7: Heating-induced change of $T_{\overline{\omega}_x,turb,sum}$ and $T_{\overline{\omega}_x,visc,sum}$ peaks in the lower left corner at 150 mm, $(\cdot)^*$ denotes normalisation by $(u_b/l^*_\nu)^2$ and $(\cdot)^o$ by $(u_b/d_h)^2$, see also table 4.6. Results are based on combined statistics for RC60, RC180 and RC900.

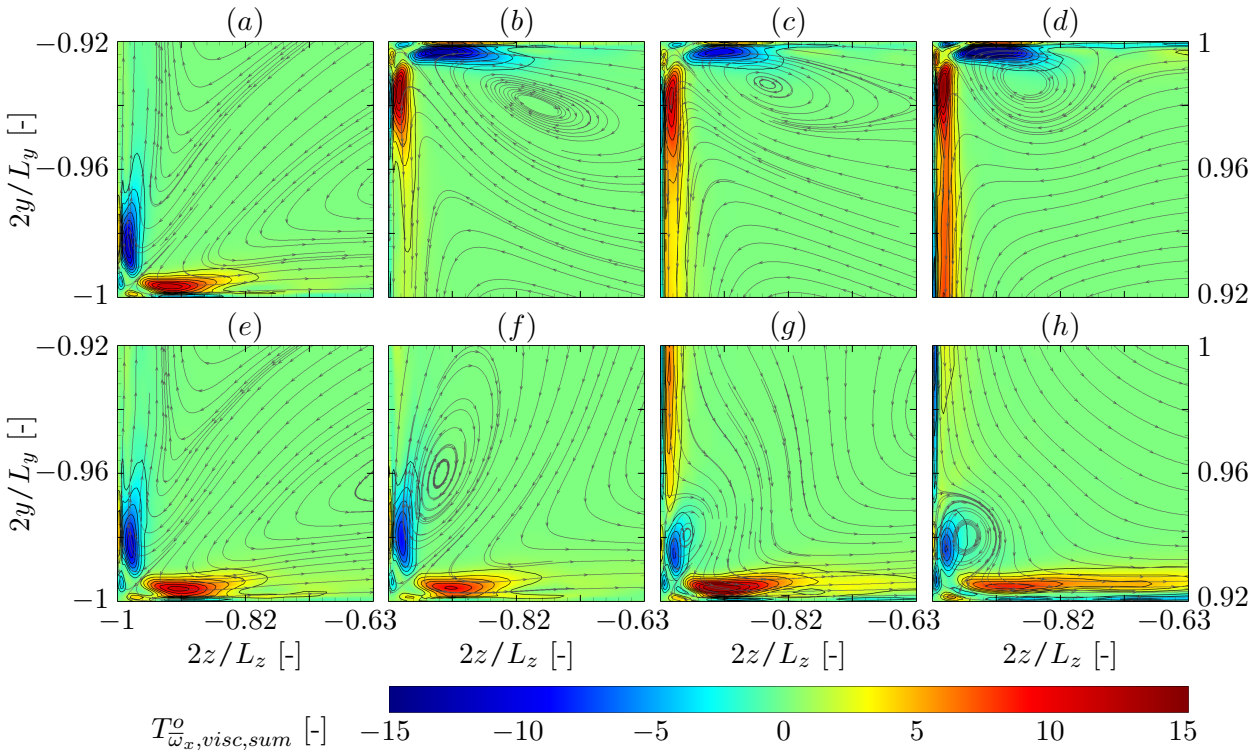

Figure 4.24: Sum of viscous terms distributions of the $\overline{\omega}_x$-equation 3.3 in the lower and upper left corners with $T^o_{\overline{\omega}_x,visc,sum} = T_{\overline{\omega}_x,visc,sum}/(u_b/d_h)^2$: lower corner of the (a) adiabatic section and (e) straight heated section at 150 mm, (b, f) upper/lower corner of RC900 at 8.75°, (c, g) upper/lower corner of RC180 at 5° and (d, h) upper/lower corner of case RC180 at 29.17°. Isolines are drawn from −12 to 12 in steps of 1.5 and streamlines visualise the secondary flow.

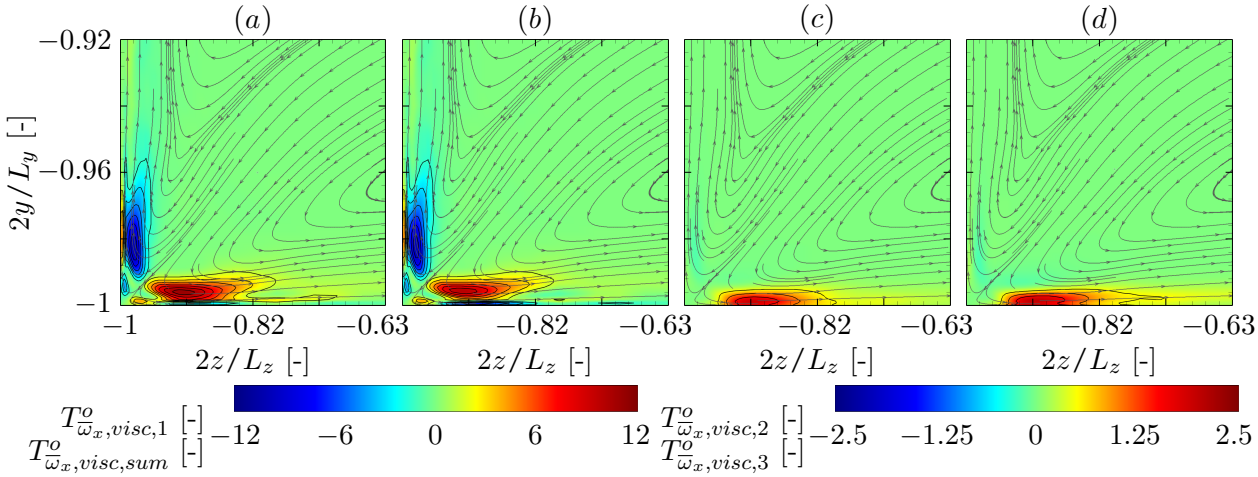

Figure 4.25: Viscous terms distributions of the $\overline{\omega}_x$-equation 3.3 in the lower left corner at 150 mm with $T^o_{\overline{\omega}_x,visc,(\cdot)} = T_{\overline{\omega}_x,visc,(\cdot)}/(u_b/d_h)^2$: (a) $T^o_{\overline{\omega}_x,visc,sum}$, (b) $T^o_{\overline{\omega}_x,visc,1}$, (c) $T^o_{\overline{\omega}_x,visc,2}$ and (d) $T^o_{\overline{\omega}_x,visc,3}$. Isolines are drawn from (a, b) −10.5 to 10.5 in steps of 1.5 and (c, d) −1.5 to 1.5 in steps of 0.5, and streamlines visualise the secondary flow.

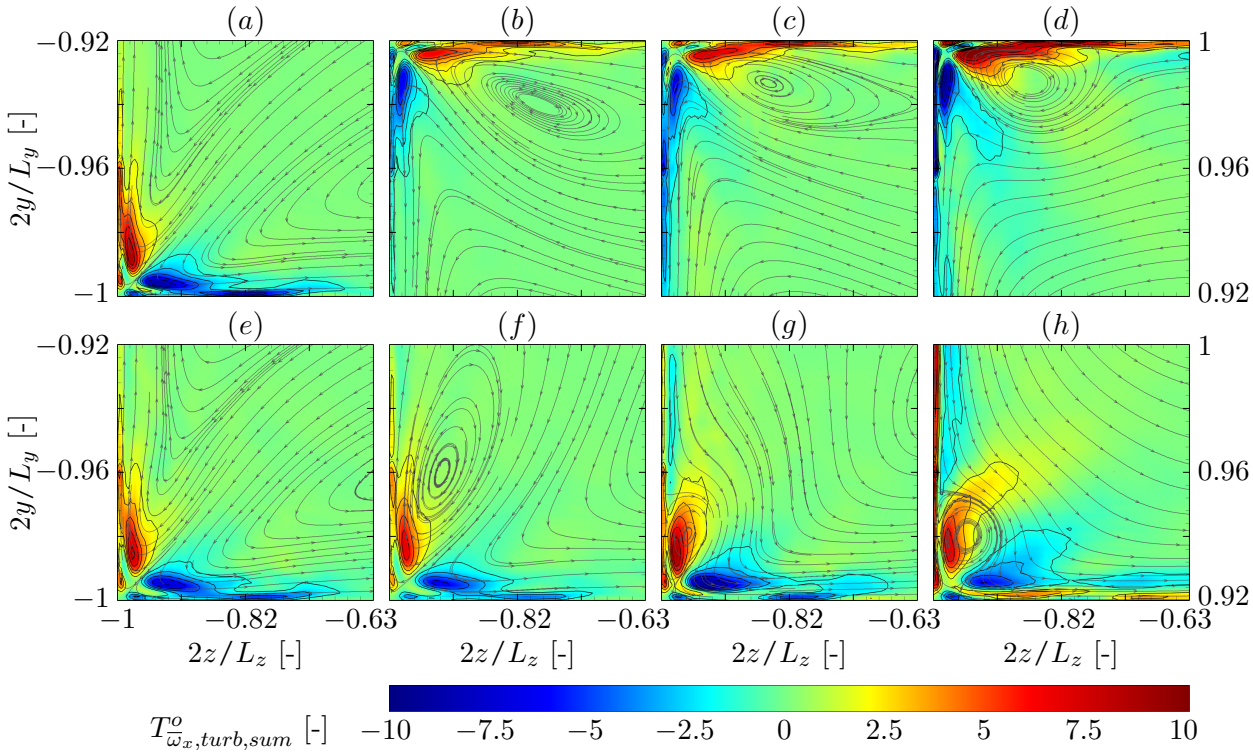

Figure 4.26: Sum of turbulence terms distributions of the $\overline{\omega}_x$-equation 3.3 in the lower and upper left corners with $T^o_{\overline{\omega}_x,turb,sum} = T_{\overline{\omega}_x,turb,sum}/(u_b/d_h)^2$: lower corner of the (a) adiabatic section and (e) straight heated section at 150 mm, (b, f) upper/lower corner of RC900 at 8.75°, (c, g) upper/lower corner of case RC180 at 5° and (d, h) upper/lower corner of RC180 at 29.17°. Isolines are drawn from −7.5 to 7.5 in steps of 1.5 and streamlines visualise the secondary flow.

the secondary flow velocity. Likewise for the air HARCD configuration an asymmetric behaviour is present with the small vortex strength increasing noticeably, whereas that of the large lateral wall vortex decreases slightly, see the discussion in the previous section 4.3.1. As listed in table 4.7, in the small vortex influence region close to the lower wall, the turbulence peak value gets weakened by ≈ 14.4%, whereas the viscous term peak value drops only by 3.4% due to the viscosity gradient terms $T^o_{\overline{\omega}_x,visc,2}$ and $T^o_{\overline{\omega}_x,visc,3}$. In contrast, at the lateral sidewall the turbulence peak drops by 7.7% and the viscous term by 12.8%. Hence, the viscous terms at the lower wall become relatively stronger compared to the turbulence terms when heating is applied and inversely at the lateral sidewall. The duct corner vorticity peaks in the wall-adjacent layer drop accordingly stronger at the lower wall with a reduction of ≈ 14.6% compared to that at the lateral wall with ≈ 11.5%. Conversely, the weaker vorticity peaks along the corner bisecting line are reduced by 8.5% for the small vortex region and by 9.9% for the large vortex region. It has to be noted, however, that the two counter-rotating corner vortices are strongly correlated (Vinuesa et al., 2014), leading to both vortices being significantly affected by the asymmetric heating. For completeness, the convective term peaks at the sidewalls drop by ≈ 24.2% at the lower wall and by ≈ 19.2% at the lateral wall. Unlike in section 3.5.2, the viscosity-induced asymmetric behaviour of the corner vorticity and the terms of the vorticity equation is not able

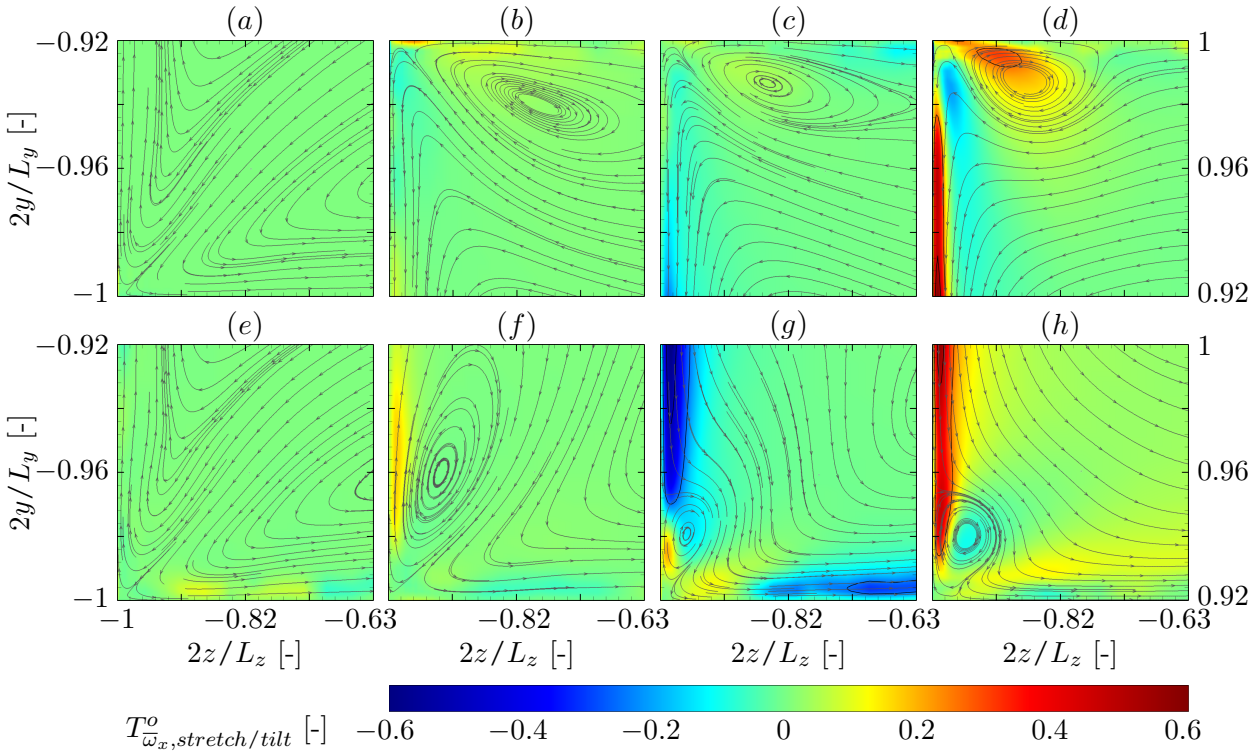

Figure 4.27: Vortex stretching and tilting term distributions of the $\overline{\omega}_x$-equation 3.3 in the lower and upper left corners with $T^o_{\overline{\omega}_x,stretch/tilt} = T_{\overline{\omega}_x,stretch/tilt}/(u_b/d_h)^2$: lower corner of the (a) adiabatic section and (e) straight heated section at 150 mm, (b, f) upper/lower corner of RC900 at 8.75°, (c, g) upper/lower corner of RC180 at 5° and (d, h) at 29.17°. Isolines are drawn from −0.5 to 0.5 in steps of 0.25 and streamlines visualise the secondary flow.

to explain the modulation of the core vorticity. An indication for this different heating-induced vorticity behaviour of water and air HARCD is given by the scaling analysis of Pirozzoli et al. (2018). They showed using several symmetric square duct cases, that with increasing ratio of Re_b/Re_τ the corner vorticity exhibits an increasingly smaller impact on the total circulation of the turbulence-induced secondary flow as the former scales in mixed units of (u_b/l_ν^+) and the latter in outer units (u_b/d_h). For our configurations this ratio for the adiabatic sections is comparable with $(Re_b/Re_\tau)_{water\ duct} = 22.82$ and $(Re_b/Re_\tau)_{air\ duct} = 20.23$. However, when heating is applied the ratio drops to $(Re_b/Re_\tau)_{water\ duct} = 15.17$ for the water HARCD and increases to $(Re_b/Re_\tau)_{air\ duct} = 28.69$ for the air HARCD. Consequently, for the water HARCD configuration the relative influence of the corner vorticity on the overall secondary flow field increases, whereas it decreases for the air HARCD configuration. Note, the ratio (Re_b/Re_τ) is here estimated using Re_τ in the heatable wall centre.

In the remainder of this subsection the modulation of the streamwise vorticity equation terms in the presence of the additional curvature-induced secondary flow is analysed. As the developing Dean vortex system is only symmetric with respect to the y-axis, the secondary flow impact on the $\overline{\omega}_x$ field at both the heated inner and the adiabatic outer radius walls is discussed separately. Note that the evolution of $\overline{\omega}_x$ and its balance equation terms at the inner radius wall is the

result of a superposition of secondary flow and viscosity effects, whereas at the outer radius wall changes can be attributed solely to the additional curvature-induced secondary flow. The following changes are observed in the corner regions

- for the $\overline{\omega}_x$ field in figure 4.22: The streamwise vorticity is strongly associated with the change of the cross-sectional secondary flow structure. In the end section of case RC900, the secondary flow field consists of a relatively weak base Dean vortex accompanied at the outer radius side by a turbulence-induced vortex adjacent to the upper wall and at the inner radius side by a pair of turbulence-induced vortices constricted to the heated wall vicinity. The constriction and breakup process of the turbulence-induced vortices is associated with a weakening and shortening of the minimum $\overline{\omega}_x$-layers along the sidewalls and an intensification of the maximum $\overline{\omega}_x$-layers. In the vorticity patches left and right of the corner bisecting line a weakening is noticeable at the heated inner radius wall and a strengthening at the outer radius wall. Similar tendencies are observed for case RC180, which intensify along the curved section such that in the end section only two turbulence-induced vortex regions remain alongside the dominating Dean vortex in each duct half. One of these is located in the outer radius wall corner adjacent to the short upper sidewall and the other at the inner radius wall corner adjacent to the lateral sidewall. In the vorticity field the minimum regions along the sidewalls get replaced by stronger maximum regions associated with the developing base Dean vortex, whereas the previous maximum regions get strengthened, i.e. in each duct half the base Dean vortex absorbs the two turbulence-induced vortices of equal spin and represses the two others of opposite spin. As a consequence, the vorticity regions around the corner bisecting line are modified asymmetrically with one expanding and the other shrinking at the inner radius side and remaining of constant size at the outer radius side, respectively. The vorticity strength and the size of the turbulence-induced vortex is significantly smaller at the inner radius side, which is partly attributed to viscosity effects and partly to the Dean vortex asymmetry.

- for the $T^o_{\overline{\omega}_x,conv}$ field in figure 4.23: The convective term distribution in the end section of RC900 is structurally similar to the straight duct results. At the heated wall a further weakening is noticeable, which is attributed to the steady viscosity increase along the duct, whereas at the outer radius wall a slight increase of the $T^o_{\overline{\omega}_x,conv}$-levels is visible, which is attributed to the Dean vortex presence. The stronger secondary flow strength for case RC180 leads to more pronounced changes. At the outer radius wall a decoupling of the $T^o_{\overline{\omega}_x,conv}$ peak regions occurs. The three patches associated with the remaining turbulence-induced vortex at the upper side shrink in size and intensify in strength. One of the remaining three peak regions closest to the lateral wall vanishes and the other two are stretched towards the duct centre. Likewise, at the inner radius side the Dean vortex motion causes a stretching of the $T^o_{\overline{\omega}_x,conv}$ zones towards the duct centre. Partly due to the additional viscosity increase the overall levels are lower at the heated wall.

- for the $T^o_{\overline{\omega}_x,visc,sum}$ field in figure 4.24: The distributions of the sum of viscous terms in the end section of case RC900, see figures 4.24 (b, f), possess a similar structure as the straight duct result. The weak Dean vortex leads to a marginal stretching of the maximum region at the outer radius wall and a marginal compression of the minimum region at the

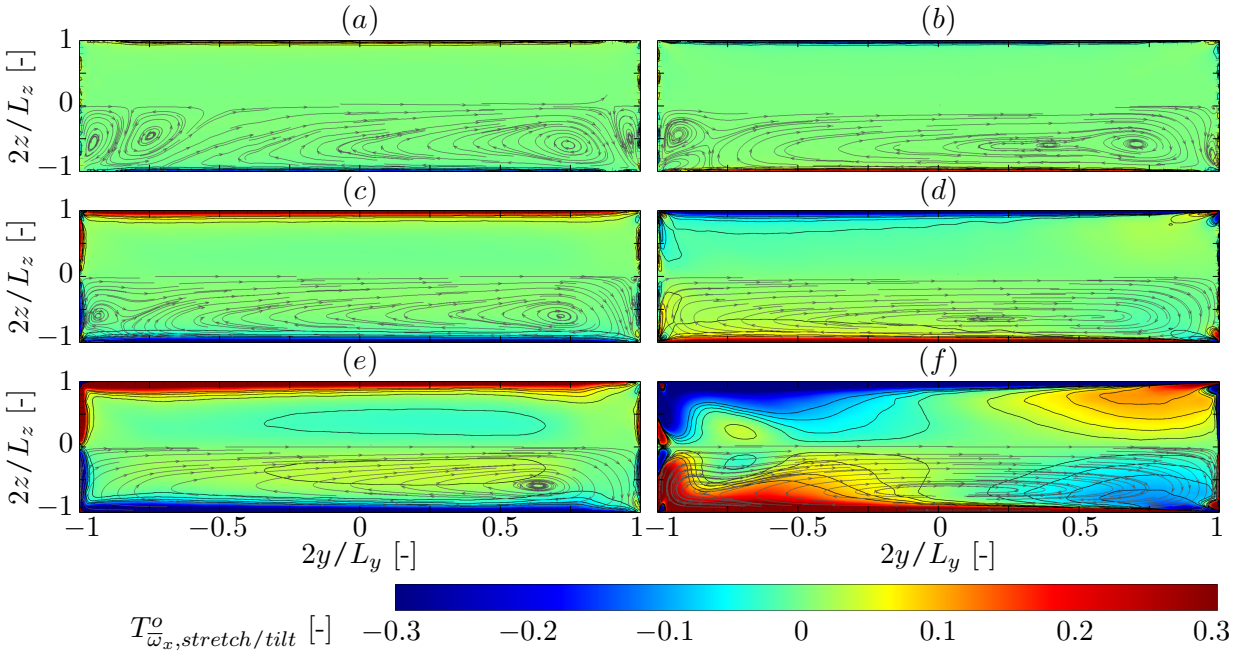

Figure 4.28: Vortex stretching and tilting term distributions in the HARCD cross-section with $T^o_{\overline{\omega}_x,stretch/tilt} = T_{\overline{\omega}_x,stretch/tilt}/(u_b/d_h)^2$: (a, b) RC900 at 1.5° (left) and 8.75° (right), (c, d) RC180 at 5° (left) and 29.17° (right) and (e, f) RC60 at 15° (left) and 87.5° (right). Isolines are drawn from −0.1 to 0.1 in steps of 0.025 and streamlines visualise the secondary flow.

inner radius wall. Despite the viscosity increase, $T^o_{\overline{\omega}_x,visc,sum}$ is significantly reduced at the heated wall compared to the adiabatic upper wall. The stretching of the positive-signed peak regions becomes more pronounced with the stronger Dean vortex of case RC180. Likewise, the negative-signed peak regions are now visibly constricted to the regions of the remaining turbulence-induced vortices. As before, the viscous terms are significantly weaker at the inner radius side, whereas at the adiabatic upper side the evolution, i.e. the constriction and intensification of the small top vortex leads to a significant local growth of the streamwise vorticity gradient and the associated viscous term $T^o_{\overline{\omega}_x,visc,sum}$.

- for the $T^o_{\overline{\omega}_x,turb,sum}$ field in figure 4.26: The sum of turbulence terms shows a rather similar behaviour as the sum of viscous terms. Focusing on case RC180, we observe at the outer radius wall an initial decrease of both peaks in figure 4.26 (c), and a significant intensification along the curved duct section until the end section in figure 4.26 (d). Conversely, at the inner radius side in figure 4.26 (g) an initial rise of the $T^o_{\overline{\omega}_x,turb,sum}$ peaks is noticeable caused by the Dean vortex motions, which increases turbulence intensity gradients in the vicinity of the walls. However, towards the end section the peak levels drop due to the continuous heating. The $T^o_{\overline{\omega}_x,turb,sum}$ corner peak values behave asymmetrically at both the outer and inner radius side, the positive-signed peak region residing within the respective influence area of the turbulence-induced vortex being noticeably stronger than the neighbouring $T^o_{\overline{\omega}_x,turb,sum}$-minimum. Moreover, due to the increasing Dean vortex strength a slight rightwards stretching of the peak regions towards the duct midplane is

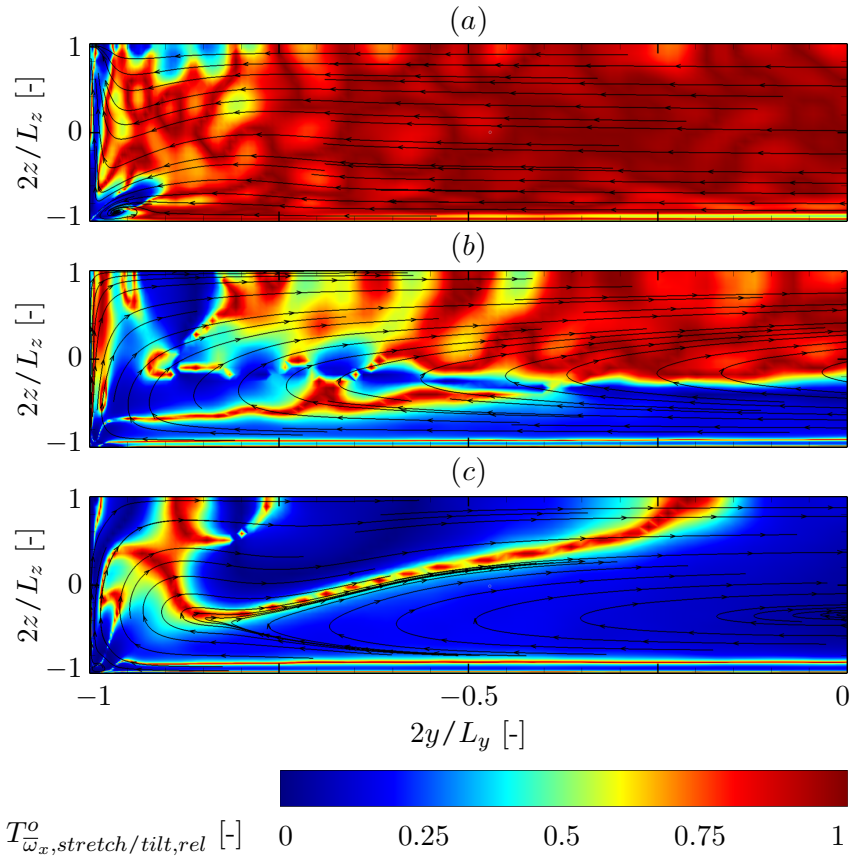

Figure 4.29: Distribution of the relative contribution of the vortex stretching and tilting terms, $T^o_{\overline{\omega}_x,stretch/tilt,rel} = |T^o_{\overline{\omega}_x,stretch/tilt}|/(|T^o_{\overline{\omega}_x,stretch/tilt}| + |T^o_{\overline{\omega}_x,turb,sum}|)$ in the lower left HARCD quarter for RC60: (a) straight duct end section, (b) at 15° and (c) at 87.5°. Streamlines are added for flow visualisation.

visible and a narrow layer of positive $T^o_{\overline{\omega}_x,turb,sum}$ is emerging along the lateral sidewall followed by a weaker negative-signed layer.

- for the $T^o_{\overline{\omega}_x,stretch/tilt}$ field in figure 4.27: Overall the vortex stretching and tilting terms associated with Prandtl's flow of the first kind are relatively weak, especially in the corner region, and the peak values are restricted to a narrow layer along the lateral sidewalls. Consequently, the streamwise vorticity dynamics in the duct corner are mainly determined by a balance of viscous and turbulence and, to a lesser extent, convective terms. Along the lateral sidewalls towards the duct centre, the vorticity dynamics are then determined by a balance of viscous, turbulence and curvature terms, with the former dominating and the $T^o_{\overline{\omega}_x,stretch/tilt}$ influence depending on the streamwise position along the curved section and the curvature radius. After a certain streamwise distance along the curved section a sign change of $T^o_{\overline{\omega}_x,stretch/tilt}$ occurs, compare the left and right columns of figure 4.28, i.e. inlet and outlet of the curved sections for the three configurations. The sign change starts to emerge at similar streamwise distances of $\approx 2/3$ of the curved section length, i.e.

$\overline{u'v'}_{(\cdot)}$	Q1		Q2		Q3		Q4	
	O1	O4	O2	O3	O6	O7	O5	O8
u'	$\oplus$		$\ominus$		$\ominus$		$\oplus$	
v'	$\oplus$		$\oplus$		$\ominus$		$\ominus$	
T'	$\oplus$	$\ominus$	$\oplus$	$\ominus$	$\oplus$	$\ominus$	$\oplus$	$\ominus$

Table 4.8: Quadrant and octant definition for the Reynolds stress quadrant analysis exemplary for the stress component $\overline{u'v'}$ at the lower heatable wall. Positive fluctuations are denoted by $\oplus$ and negative ones by $\ominus$. At the upper wall the v'-signs are inverted accordingly.

from $\approx 60°$(RC60), $\approx 20°$(RC180) and $\approx 6°$(RC900) onwards. Figure 4.28 highlights the significantly increasing $T^o_{\overline{\omega}_x,stretch/tilt}$ levels and the associated influence growth of vortex stretching and tilting terms on streamwise vorticity dynamics within the whole HARCD cross-section, especially for the higher curvature cases.

In figure 4.29, the relative contribution of $T^o_{\overline{\omega}_x,stretch/tilt}$ to the sum of secondary flow source terms of $T^o_{\overline{\omega}_x,stretch/tilt}$ for Prandtl's flow of the first kind and $T^o_{\overline{\omega}_x,turb,sum}$ for Prandtl's flow of the second kind is shown exemplary for case RC60 in the lower left duct quarter. Neglecting the convective term, high values of $T^o_{\overline{\omega}_x,stretch/tilt,rel}$ signify the local vorticity dynamics being mainly controlled by a balance of $T^o_{\overline{\omega}_x,stretch/tilt}$ and viscous terms. When the pressure difference between outer and inner radius side effects a downwards oriented secondary flow and the Dean vortices start to emerge, $T^o_{\overline{\omega}_x,stretch/tilt,rel}$ is dominating in the majority of the cross-section except for the duct corners and lower wall. Along the curved section with the Dean vortices having fully established, their strong mixing motion leads to a distortion of the cross-sectional turbulence field and in consequence to rising Reynolds stress gradients and increasing levels of $T^o_{\overline{\omega}_x,turb,sum}$. Hence, the relative contribution $T^o_{\overline{\omega}_x,stretch/tilt,rel}$ becomes weaker. In the curved duct end section $T^o_{\overline{\omega}_x,stretch/tilt}$ remains only dominant in a narrow layer along the lateral wall, the base Dean vortex streamline turning point close to the heatable wall and along the streamwise $\overline{u}$-bulge. For the corresponding streamwise velocity field see figure 4.12 (d).

4.3.4 Turbulent Sweeping and Ejection Motions

The Reynolds quadrant and octant analysis methods are employed to decompose the Reynolds shear stress term $\overline{u'v'}$ analogous to section 3.5.3. The goals are to analyse (I) the viscosity-induced modulation of the $\overline{u'v'}$-contributions and the accompanying effects on turbulence-induced secondary flow as well as (II) their modulation by the additional presence of the Dean vortex system and its evolution along the heated curved HARCD section. In (III) the joint probability density function (JPDF) distributions are utilised to support the first two parts and gain a deeper insight. A special focus is set on near-wall turbulent sweep and ejection motions as the latter is the dominant turbulent mechanism for the turbulence-induced secondary flow generation (Huser and Biringen, 1993).

The definition of the $\overline{u'v'}$-quadrants and -octants is given in table 4.8. A positive v'-value points away from the respective wall, i.e. at the upper wall with the wall-normal being orientated in negative y-direction the v'-sign is inverted. Note, the results presented for the curved

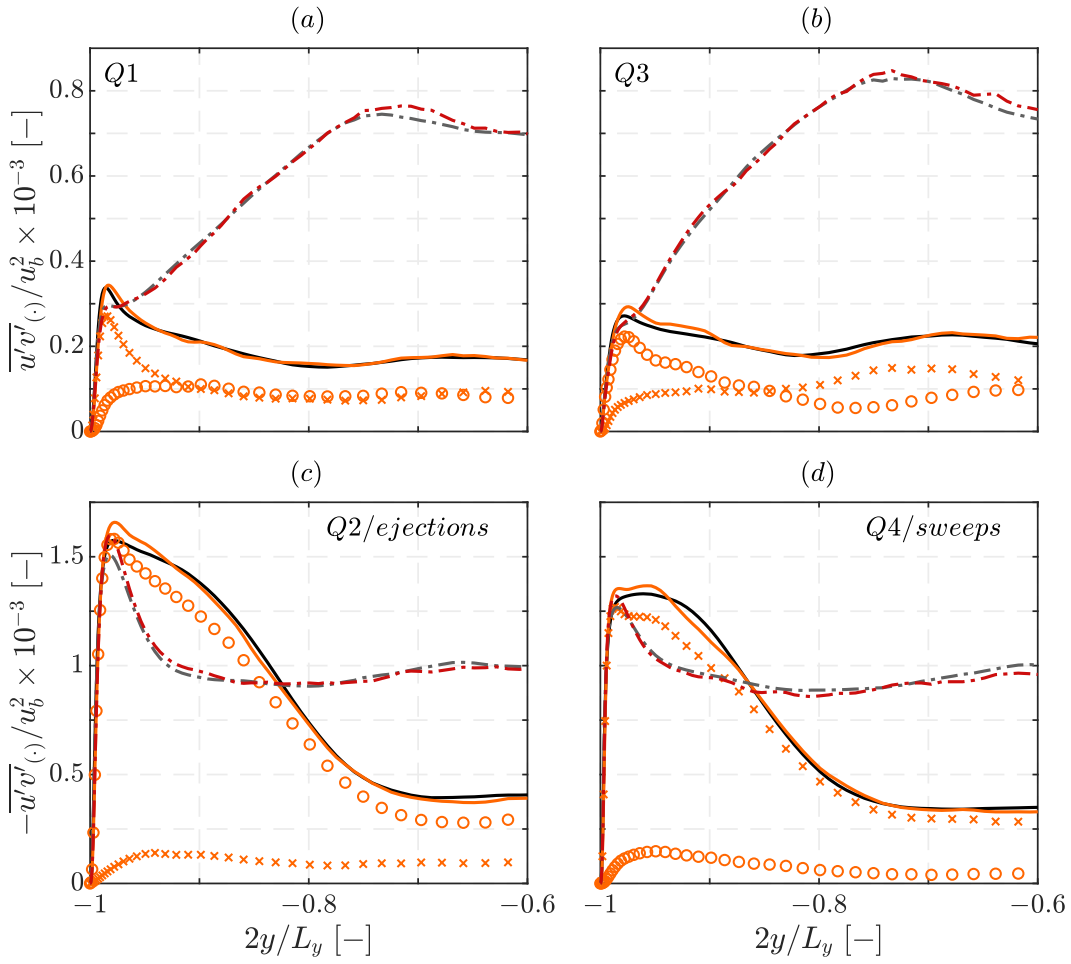

Figure 4.30: Quadrant and octant analysis of Reynolds shear stress $\overline{u'v'}$ along the centre line $z = 0$ and at $2z/L_z = 0.75$ for the adiabatic (black/grey) and the heated duct at 150 mm (orange/red): (*a*) quadrant Q1 and octants O1 (○)/O4 (×), (*b*) quadrant Q3 and octants O6 (○)/O7 (×), (*c*) quadrant Q2 and octants O2 (○)/O3 (×) and (*d*) quadrant Q4 and octants O5 (○)/O8 (×). Solid lines represent quadrants at $z = 0$, dash-dotted lines quadrants at $2z/L_z = 0.75$ and symbols octants at $z = 0$. See table 4.8 for the definition of the quadrants and octants.

sections are based on a shorter temporal averaging period of 10.1 FTT with respect to the heated section length of the respective configuration, because as prerequisite for the quadrant analysis a sufficiently converged mean flow field is required for the concurrent evaluation of fluctuations. Combining the periodic and heated straight HARCD statistics for all three curvature configurations allows for an evaluation of the heating-induced $\overline{u'v'}$-modulation based on ≈ 30 FTT.

(I) heating-induced $\overline{u'v'}$-modulation

Figure 4.30 depicts the quadrant and octant analysis at the lower heatable wall. In the centre, the dominant contribution to $\overline{u'v'}$ comes from the turbulent ejection and sweeping motions (quadrants Q2 and Q4), where especially in the near-wall region $\overline{u'v'}_{Q2}$ reaches higher values

than $\overline{u'v'}_{Q4}$. The heating-induced near-wall viscosity rise exhibits the highest impact on the Q2- and Q3-distributions (for both $u' < 0$), whereas smaller changes are noticeable for Q4 and especially Q1. The $\overline{u'v'}_{Q3}$-peak increases by 7.89%, the $\overline{u'v'}_{Q2}$-peak by 5.27% and the $\overline{u'v'}_{Q4}$-peak by 2.77%. The Q1- and Q3-peaks are marginally shifted rightwards. The quadrant Q4 forms a dented near-wall profile with two local extrema, which is absent in the unheated section, whereas a single peak is observed for Q2. The results are qualitatively in good agreement with the previous ones for the water HARCD presented in section 3.5.3, for which the inverse behaviour has been observed due to an opposite viscosity gradient towards the heated wall. The observable changes, however, are less pronounced in the air HARCD as the heated wall is significantly shorter and additionally the flow velocity higher. The individual quadrant contributions in the heated duct section are further subdivided into octants depending on the local temperature and associated viscosity fluctuation. The turbulent ejection and sweep contributions are markedly dominated over the whole range by octants O2 ($T' > 0$) and O8 ($T' < 0$), respectively, while Q1 and Q3 are dominated by octants O4 ($T' < 0$) and O6 ($T' > 0$) only in the near-wall region. As an area of hot fluid has formed in the heated wall vicinity, this result meets the theoretical expectation for the gradient-type motions: ejection events are mainly associated with the upward shift of hot fluid and sweep events with a downward shift of comparatively cooler fluid. For the countergradient-type motions Q1 and Q3, the near-wall result of dominating O4 and O6 agrees qualitatively with the heated TBL octant analysis by Park et al. (2012). Moving towards the lateral sidewall, the contributions $\overline{u'v'}_{(\cdot)}$ of all quadrants decrease marginally in the near-wall region of the lower wall, whereas they increase significantly along the y-axis towards the duct centre, with the strongest rise present for Q3. Moreover, the peak-regions of turbulent ejections and sweeps become narrower. The influence of increased temperature and viscosity at the off-centre location for Q1 and Q2 is similar as observed in the duct centre. The quadrant contribution Q4 shows a comparable increase as Q2 and no effect is visible for Q3.

Based on the viscosity-induced asymmetric change of turbulent ejections from the walls, the previously observed asymmetric modulation of the turbulence-induced vortex system in the straight duct section can be analysed, see section 4.3.1. Figure 4.31 depicts the near-wall distribution of ejection events along both the lower heatable and the lateral sidewall. Especially the lateral sidewall statistics of straight HARCDs expect a very slow convergence rate, see e.g. Vinuesa et al. (2014). Hence, for convergence improvement the streamwise averaging for this analysis is performed over an increased distance of $\Delta x = 30$ mm instead of the standard $\Delta x = 5$ mm used throughout the current chapter 4. The turbulence-induced secondary flow in rectangular geometries develops as a consequence of the turbulent ejections varying significantly from duct corner to centre. In the respective sidewall centre, the strong shear enhances turbulent ejections, whereas the weak shear in the corner inhibits them (Salinas-Vásquez and Métais, 2002). Applying an asymmetric heating distorts this distributions as shown in figure 4.31 by the $\overline{u'v'}_{Q2}$- and $\overline{u'w'}_{Q2}$-profiles. The distributions denoted by solid lines are taken along a wall-parallel at a fixed wall-distance of $2y/L_y = -0.978$ and $2z/L_z = -0.925$, respectively. There, the respective wall centre $\overline{u'v'}_{Q2}$-peak is located. Towards the corner as well as with heating applied, the ejection peaks may shift and be located at a different wall distance. Hence, the dotted lines are included, which represent the respective peak values reached at a certain position along the sidewall. Noticeable deviations between these two distributions occur only in the vicinity of

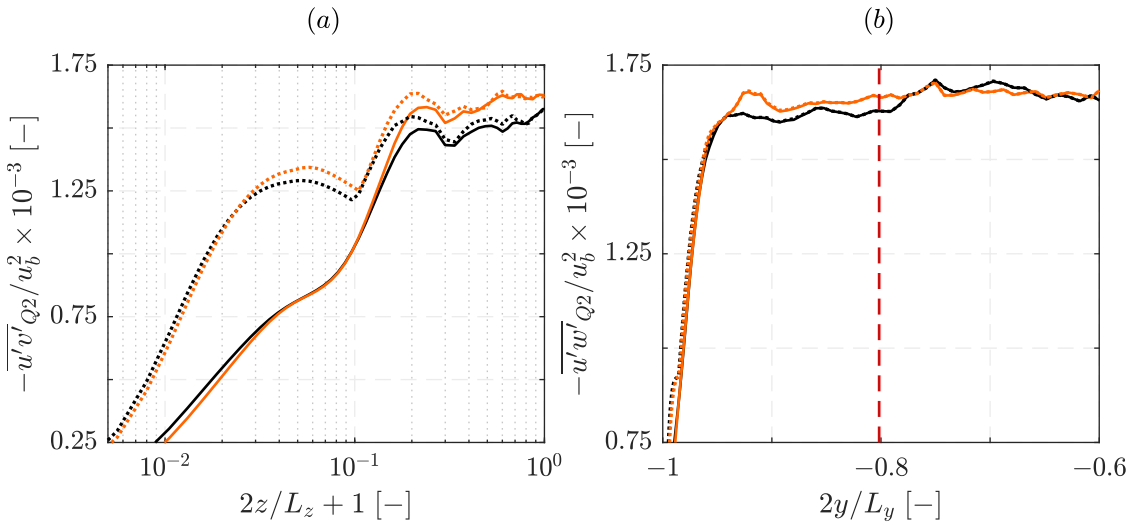

Figure 4.31: Near-wall turbulent ejection events measured by $\overline{u'v'}_{Q2}$ and $\overline{u'w'}_{Q2}$ for the adiabatic (——)/(·····) and the heated duct (——)/(·····) at 140 mm along the (a) lower heatable wall and (b) lateral sidewall. Solid lines represent the profile taken along the wall-parallel at (a) $2y/L_y = -0.978$ and at (b) $2z/L_z = -0.925$, respectively. Dotted lines represent the local peak values reached at the specific location along the sidewall. The line (- - - -) represents a temperature increase of $\Delta\overline{T} = 10$ K with rising levels leftwards and dropping levels rightwards.

the duct corner. Here, exemplarily the detected $\overline{u'v'}_{Q2}$-peak is located further away from the heatable wall in the interaction zone of heated and lateral wall TBLs and the counter-rotating vortex pair. Consequently, this $\overline{u'v'}_{Q2}$-peak does not correspond to a turbulent ejection event from the heatable wall. Hence, the remainder of the discussion focuses on the solid lines. The heating-induced rise of $\overline{u'v'}_{Q2}$-levels in the lower wall centre increases the overall difference between centre and corner ejections, and thus delivers an explanation for the previously observed increase of the turbulence-induced secondary flow in the small vortex region, see figure 4.31 (a). Zooming into the immediate duct corner region, however, reveals higher $\overline{u'v'}_{Q2}$-levels in the adiabatic section compared to the heated section, which is in accordance with the observed corner vorticity reduction of the previous section 4.3.3. Due to the hot fluid upward transport also the adiabatic lateral sidewall TBLs are affected by the heating, although restricted to the lowest part closest to the heated wall. For orientation the $\Delta\overline{T} = 10$ K-line (- - - -) is added in figure 4.31 (b), indicating that only below $2y/L_y \approx -0.8$ a relevant heating influence on turbulence statistics is expected. Accordingly, the $\overline{u'w'}_{Q2}$-levels reached in the lateral wall centre are similar for the adiabatic and the heated section. Between $2y/Ly \approx -0.95$ and $2y/Ly \approx -0.8$ the viscosity increase is accompanied by an $\overline{u'w'}_{Q2}$-increase, evening out the difference of turbulent ejection strength between lateral wall centre and corner region. Thus, an explanation is given for the weakening of the lateral sidewall vortex discussed in section 4.3.1. Similar as for the heated wall in figure 4.31 (a), for the immediate corner region of the lateral wall the $\overline{u'w'}_{Q2}$-levels of the adiabatic duct are slightly higher than for the heated duct (not explicitly shown).

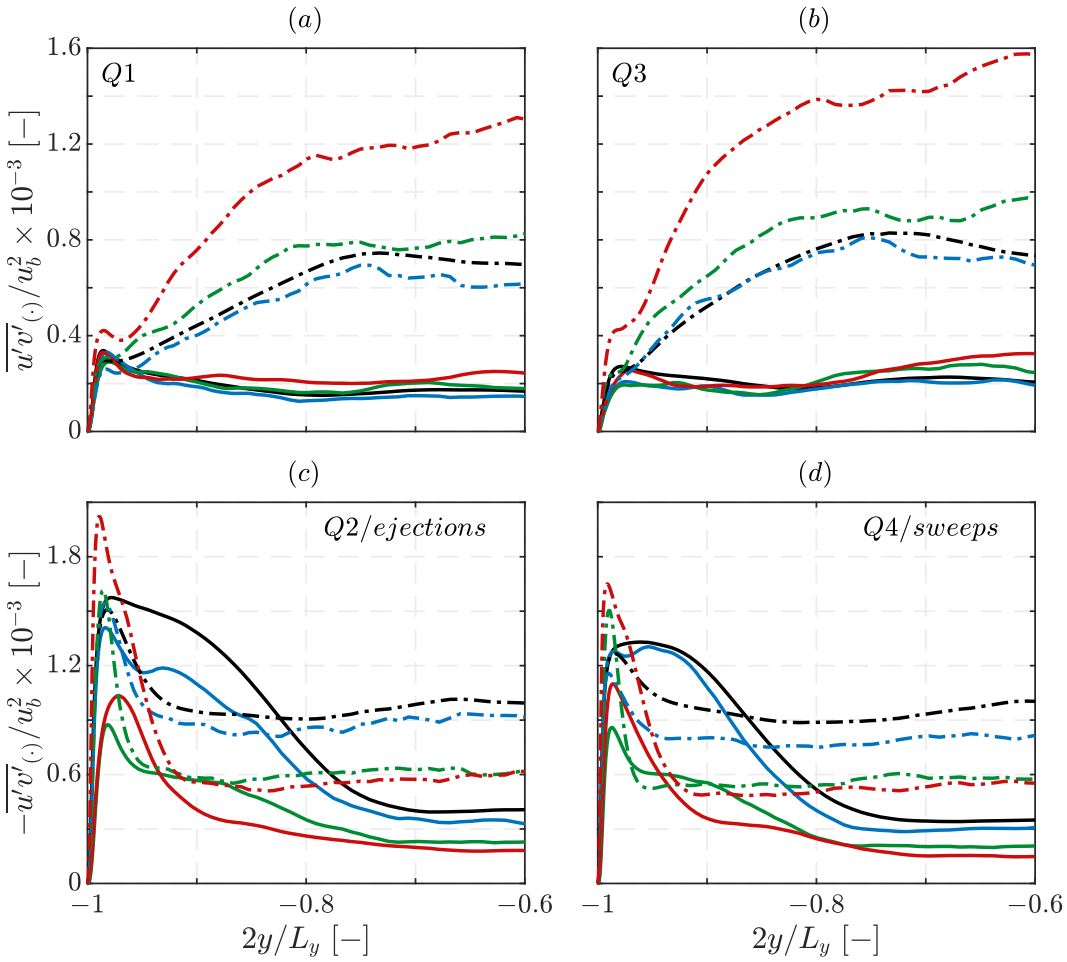

Figure 4.32: Quadrant analysis of the Reynolds stress component $\overline{u'v'}$ for case RC60 along the centre line $z = 0$ (solid lines) and at $2z/L_z = 0.75$ (dash-dotted lines) in the lower heatable wall vicinity for the adiabatic duct (——) as well as the heated duct in the straight part end section (——), in the curved part at 15° (——) and at 30° (——): (*a*) quadrant Q1, (*b*) quadrant Q3, (*c*) quadrant Q2 and (*d*) quadrant Q4. See table 4.8 for the quadrant definition.

(II) curvature-induced $\overline{u'v'}$-modulation

The modification of the turbulence structure in presence of the additionally forming curvature-induced secondary flow is depicted in figure 4.32 for the lower heatable wall and in figure 4.33 for the upper wall with a focus on the curved section beginning of case RC60. Note, for the former an interaction of heating and secondary flow effect is present and for the latter only the secondary flow effect. The cross-sectional secondary flow field structure at the three analysed streamwise positions can be taken from figure 4.8 of section 4.3.1 and is as follows: (I)/(——) at the end of the straight heated section the pressure difference between outer and inner radius wall leads to a downwards oriented secondary flow superimposing the existing turbulence-induced one, (II)/(——) in the curved section at 15° the Dean vortex cores have developed, yet the vortex system is still developing and relatively weak, and (III)/(——) at 30° the Dean vortex

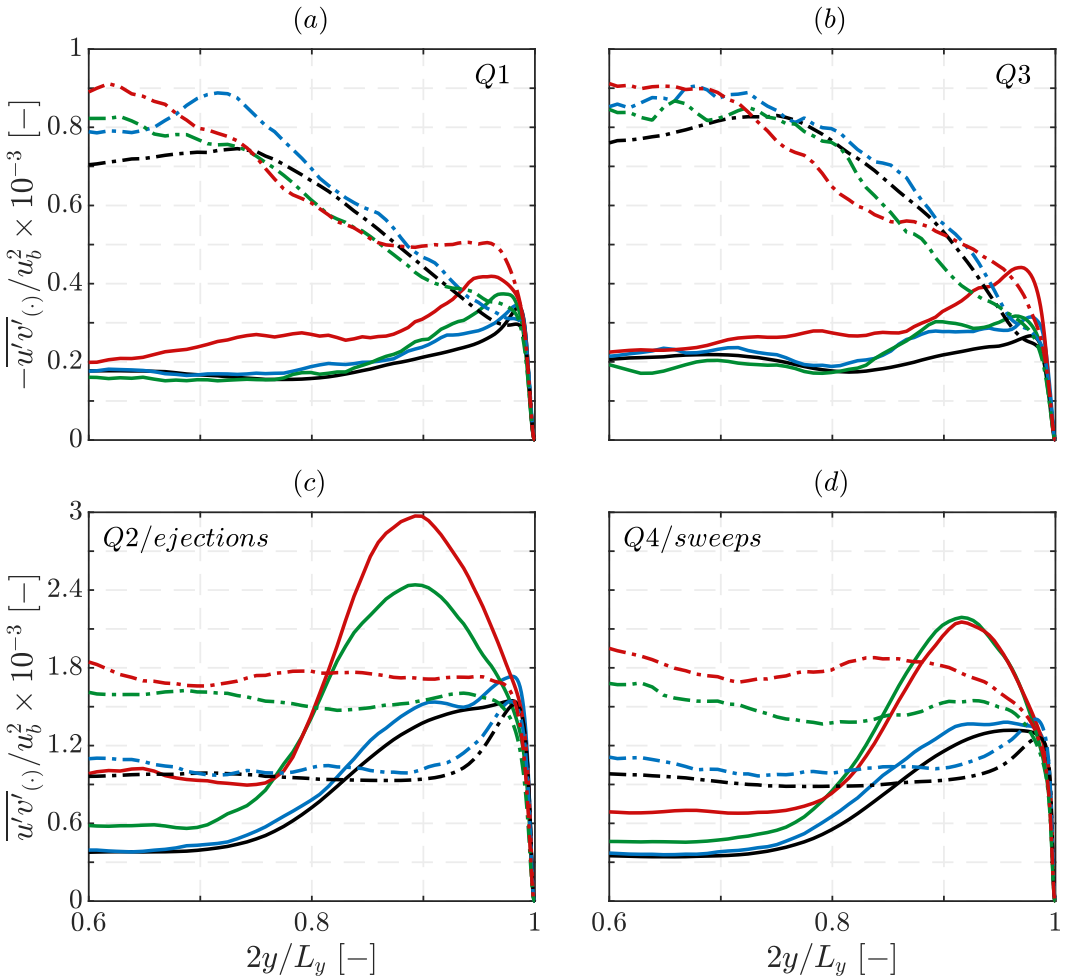

Figure 4.33: Quadrant analysis of the Reynolds shear stress component $\overline{u'v'}$ for case RC60 along the centre line $z = 0$ (solid lines) and at $2z/L_z = 0.75$ (dash-dotted lines) in the upper wall vicinity for the adiabatic duct (——) as well as the heated duct in the straight part end section (——), in the curved part at 15° (——) and at 30° (——): (a) quadrant Q1, (b) quadrant Q3, (c) quadrant Q2 and (d) quadrant Q4. See table 4.8 for the quadrant definition.

system is structurally fully developed and already has a significant strength. At the inner radius side, i.e. in figure 4.32, the following Dean vortex effects on the $\overline{u'v'}$-contributions are visible:

- Q1/figure 4.32 (a): In the centre profiles only marginal changes are noticeable, whereas towards the lateral wall the downwards oriented secondary flow leads initially to a slight drop and the subsequent Dean vortex system to an overall noticeable increase of $\overline{u'v'}_{Q1}$.
- Q3/figure 4.32 (b): In the centre initially a drop is visible with the near-wall $\overline{u'v'}_{Q3}$-profile falling below the adiabatic duct profile and rising again along the curved section. For the off-centre profiles a continuous increase of the $\overline{u'v'}_{Q3}$-contribution is observable over the complete range studied.

- Q2/figure 4.32 (c): The turbulent ejection contribution becomes first lower in the centre and slightly higher at the off-centre position until the Dean vortex system has established. Then, the increasing Dean vortex mixing leads to a rise of $\overline{u'v'}_{Q2}$, especially towards the lateral wall.

- Q4/figure 4.32 (d): The modulation of the sweep contribution $\overline{u'v'}_{Q4}$ is similar to $\overline{u'v'}_{Q2}$, i.e. after an initial drop in the centre the increasing Dean vortex strength causes an $\overline{u'v'}_{Q4}$-increase and higher values are obtained at the off-centre location.

At the outer radius side, i.e. in figure 4.33, the following Dean vortex effects on the $\overline{u'v'}$-contributions are visible:

- Q1/figure 4.33 (a): A noticeable increase in the $\overline{u'v'}_{Q1}$ levels in the centre near-wall region is present, whereas at the off-centre location the modulation is less pronounced than at the lower wall.

- Q3/figure 4.33 (b): The changes in the $\overline{u'v'}_{Q3}$-profile are similar to those in the $\overline{u'v'}_{Q1}$-profile, i.e. an increase is noticeable especially in the centre and no major impact is visible at the off-centre location.

- Q2/figure 4.33 (c): The weak downwards oriented flow supports a slight $\overline{u'v'}_{Q2}$-increase in the straight duct end section, which intensifies downstream even though the secondary flow direction reverses when the Dean vortices have fully established. Likewise, a significant increase at the off-centre location is observed, which is situated at the edge of the remaining turbulence-induced upper side vortex, see figure 4.8.

- Q4/figure 4.33 (d): The sweeping motions again show a similar behaviour as the turbulent ejections. At the beginning of the curved section, a marginal increase of $\overline{u'v'}_{Q4}$ levels is present, which is growing downstream with the Dean vortex system evolving. At position 30°, however, a discrepancy is present with the $\overline{u'v'}_{Q2}$ centre profile reaching a maximum, whereas the $\overline{u'v'}_{Q4}$ centre profile drops below the distribution at 15°. This drop is caused by the intensifying upwards oriented secondary flow towards the upper wall, which leads to a drop in both $\overline{u'v'}_{Q2}$ and $\overline{u'v'}_{Q4}$, although $\overline{u'v'}_{Q2}$ levels start to drop at a later streamwise position.

The shapes of the $\overline{u'v'}_{Q2}$ peak regions close to the wall (and likewise those for $\overline{u'v'}_{Q4}$) show the compression and stretching effect caused by the curvature-induced secondary flow. At the lower wall, the initial downwards oriented flow leads to a narrowing of the peak regions, i.e. a compression of the TBL. After the formation of the Dean vortex system, the upwards oriented flow in the centre, and the essentially spanwise oriented flow at the off-centre location, respectively, leads to a broadening of the peak regions, i.e. a stretching of the TBL. This effect is best visible comparing the Q2- and Q4- profiles for 15° and 30°. At the outer radius wall these effects are less pronounced at the depicted streamwise positions.

(III) joint probability density function distributions
Examining the joint probability density function (JPDF) distributions of u' and v' allows for a

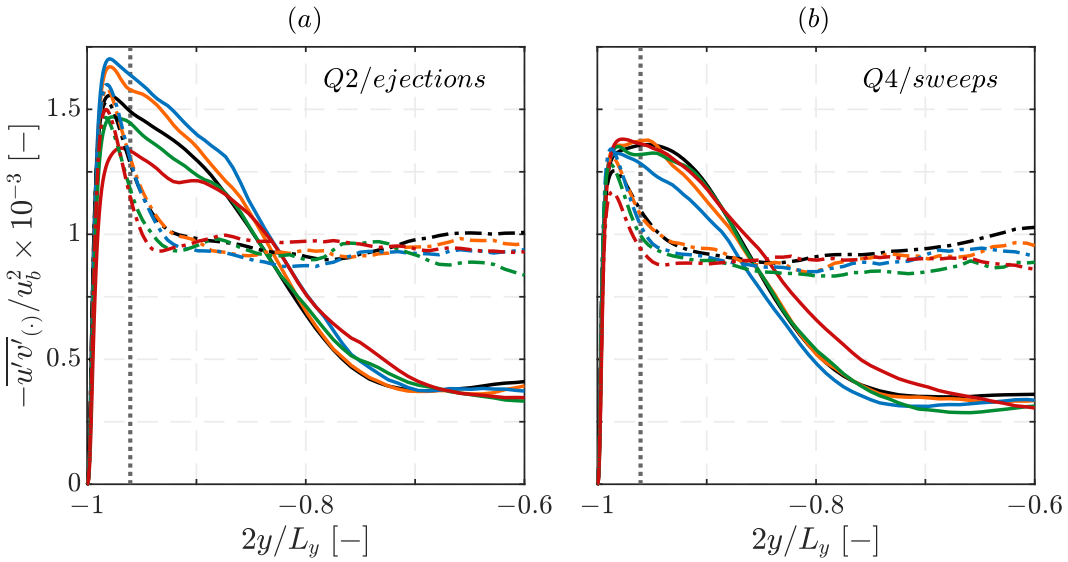

Figure 4.34: Quadrant analysis of the Reynolds stress component $\overline{u'v'}$ for case RC900 along the centre line $z = 0$ (solid lines) and at $2z/L_z = 2/3$ (dash-dotted lines) in the lower heatable wall vicinity for the adiabatic duct (——) as well as for the heated duct at 150 mm (——) and for the curved section at 0.75° (——), 4.5° (——) and 8.75° (——): (a) quadrant Q2 and (b) quadrant Q4. (·····) denotes the JPDF evaluation location for figures 4.35 and 4.36.

deeper insight into the turbulence structure and its change due to heating and curvature effects. The Reynolds shear stress at a specific cross-sectional location $\overline{u'v'}(y, z)$ can be defined as

$$\overline{u'v'} = \int_{-\infty}^{\infty} u'v' P(u', v')\, du'dv', \tag{4.10}$$

with $P(u', v')$ being the JPDF (Wallace, 2016). The focus of the upcoming analysis is set on the near-wall region of the lowest curvature case RC900 to specifically highlight the $\overline{u'v'}$-modulation of turbulent ejection and sweeping motions for the case of comparably strong Prandtl's flow of the first and second kind. The midplane and off-centre distributions along the RC900 configuration for $\overline{u'v'}_{Q2}$ and $\overline{u'v'}_{Q4}$ are depicted in figure 4.34 with the JPDF evaluation location indicated. The profiles behave differently as analysed for case RC60 and changes are more subtle. This deviating behaviour is associated with the different curvature-induced secondary flow field. For the strongest curvature case RC60 the corner vortex system vanishes even before the Dean vortex formation has concluded, whereas for the lowest curvature case RC900 the corner vortex system persists at the inner radius wall until the end section, see the discussion of figures 4.8 and 4.10 in section 4.3.1. For the $\overline{u'v'}_{Q2}$ centre profiles a near-wall heating-induced rise is observed followed by a continuous decrease along the curved section. The off-centre profiles show a similar tendency with a reduced decrease, such that towards the end section the off-centre $\overline{u'v'}_{Q2}$ peak surpasses that in the centre. This trend highlights the continuously growing influence of the Dean vortex on the inner radius wall corner vortex system and their merging process, because pure turbulence-induced secondary flow is characterised and forming due to the turbulent ejection

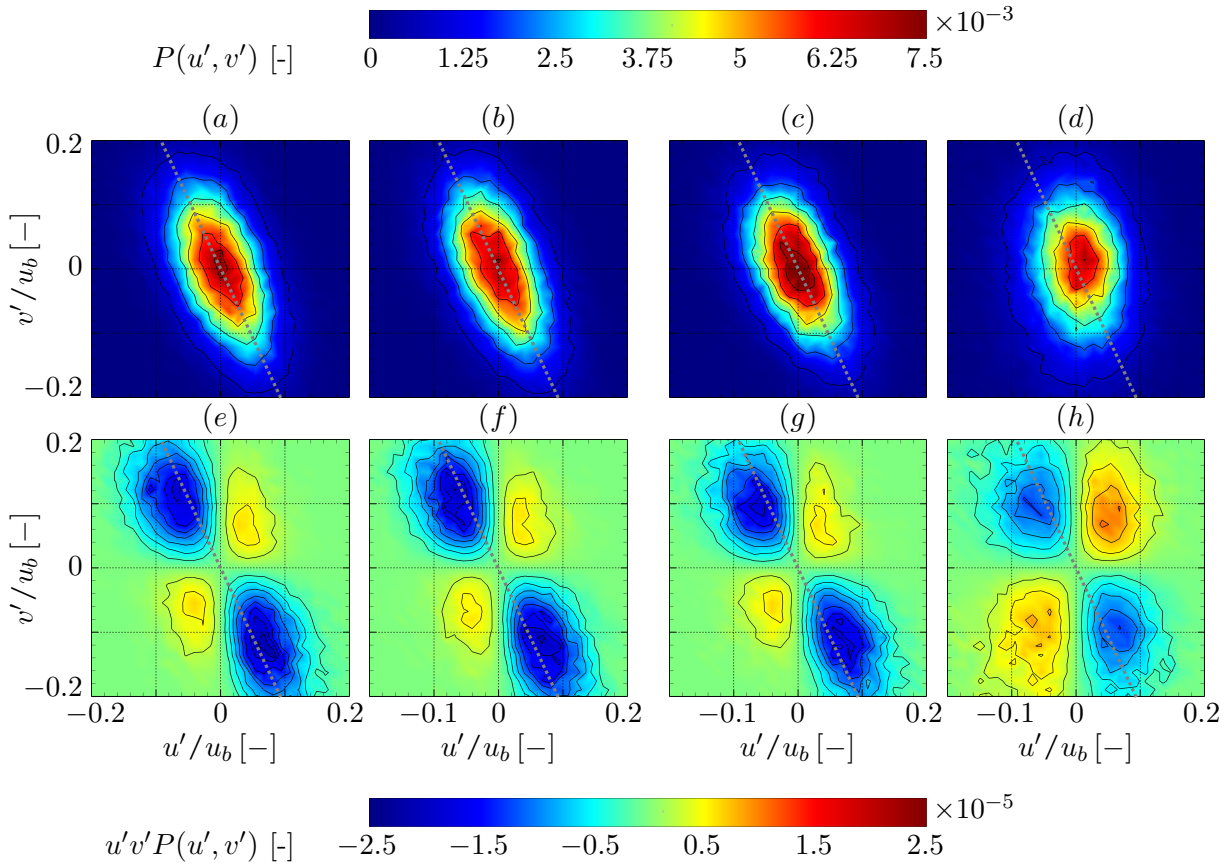

Figure 4.35: Joint probability density function distributions $P(u', v')$ (upper row) and weighted JPDF $u'v'P(u', v')$ (bottom row) for case RC900 at $2y/L_y = -0.9605$: (a, e) adiabatic periodic duct and (b, f) heated section at 150 mm for $2z/L_z = 0$, (c, g) at $2z/L_z = 2/3$ and (d, h) at $2z/L_z = 0.9$. Isolines are drawn from $0.75 \cdot 10^{-3}$ to $7 \cdot 10^{-3}$ in steps of $1.25 \cdot 10^{-3}$ (JPDF) and from $-2.5 \cdot 10^{-5}$ to $2.5 \cdot 10^{-5}$ in steps of $0.25 \cdot 10^{-5}$ (weighted JPDF). The 115°-line (·····) approximates the ellipsis major axis.

imbalance with strong ejections in the wall centre falling off to zero towards the lateral walls. For the turbulent sweeps, i.e. $\overline{u'v'}_{Q4}$, the small heating-induced rise in the centre is followed by an initial near-wall drop in the curved section and rebound towards the outlet. At the off-centre position the inverse behaviour is present, with the $\overline{u'v'}_{Q4}$ peak continuously dropping along the curved section after an initial increase.

The JPDF distributions $P(u', v')$ are evaluated at a lower wall-normal position of $2y/L_y = -0.9605$, corresponding to $y_c^+ = 77.1$ of the adiabatic section and indicated by the grey dotted lines in figure 4.34. The evaluation location has been determined a priori and chosen such that it is situated approximately in the peak region of $\overline{u'v'}_{Q2}$ and $\overline{u'v'}_{Q4}$. The straight HARCD results are depicted in figure 4.35 and the curved section results in figure 4.36. The distributions $P(u', v')$ and $u'v'P(u', v')$ of the adiabatic section in figures 4.35 (a, e) are qualitatively in good accordance with those presented in Wallace and Brodkey (1977) and Mahmoodi-Jezeh and Wang (2020). The $P(u', v')$ profile is approximately elliptical with the major axis forming a path

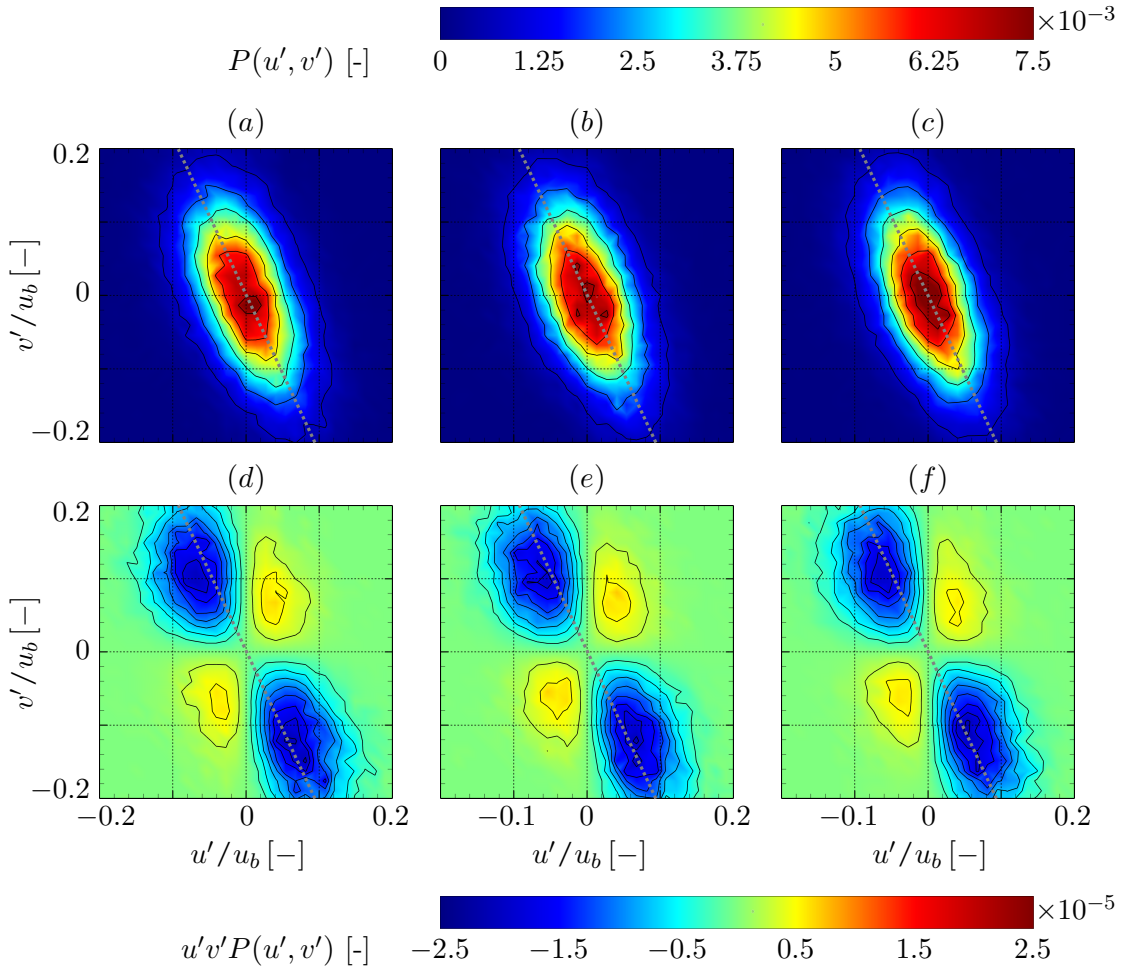

Figure 4.36: Joint probability density function distributions $P(u', v')$ (upper row) and weighted JPDF $u'v'P(u', v')$ (bottom row) for case RC900 at $2y/L_y = -0.9605$ and $2z/L_z = 0$: curved section at (a, d) 0.75°, (b, e) 4.5° and (c, f) 8.75°. Isolines are drawn from $0.75 \cdot 10^{-3}$ to $7 \cdot 10^{-3}$ in steps of $1.25 \cdot 10^{-3}$ (JPDF) and from $-2.5 \cdot 10^{-5}$ to $2.5 \cdot 10^{-5}$ in steps of $0.25 \cdot 10^{-5}$ (weighted JPDF). The 115°-line (·····) approximates the ellipsis major axis.

leading from quadrant Q2 to Q4. The highest probabilities are reached in the centre for relatively small levels of u' and v'. The inclination of the major axis at the considered position is $\approx 115°$, indicated by grey dotted lines, and agrees qualitatively well with the near-wall square duct result of Mahmoodi-Jezeh and Wang (2020). The near-wall HARCD centre weighted JPDF distribution in subfigure (e) highlights the dominant influence of the Q2 and Q4 contributions to the integral $\overline{u'v'}$-value in equation 4.10 compared to Q1 and Q3. When heating is applied, the JPDF-ellipsis in the centre is stretched along its major axis towards quadrant Q2 reducing the central peak, compare figures 4.35 (a, b). Consequently, the probability for higher-value (u', v') pairs increases especially in the second quadrant, signifying a rise of the turbulent ejection strength, which leads to the observed near-wall increase of the $\overline{u'v'}_{Q2}$-peak. Towards the lateral wall the JPDF-ellipsis contracts, i.e. low-value (u', v') pairs become more likely, and the relative Q2- and Q4-contribution

to $\overline{u'v'}$ decreases, see figures 4.35 (c, g). In figures 4.35 (d, h) a noticeable lateral wall influence is present. The $P(u', v')$-distribution changes towards a circle-shaped profile, meaning events in all four quadrants are similarly probable and give a comparable contribution to $\overline{u'v'}$. Note, to gain a complete picture of the turbulence state, especially at the position close to the lateral wall, $\overline{u'w'}$ also has to be analysed due to the interaction of the two sidewall TBLs in the duct corner region. The curvature effect on the distributions of $P(u', v')$ and $u'v'P(u', v')$ is depicted in figure 4.36 for the lower wall centre. The shape of the JPDF-ellipsis remains unchanged with an increase of the probability in the centre, i.e. low-value (u', v') pairs occur more often, giving an explanantion for the observed continuous $\overline{u'v'}_{Q2}$ drop. In the $u'v'P(u', v')$ profiles no significant variation is visible.

4.3.5 Turbulent Heat Transfer

Similar as for the water HARCD in section 3.5.4, we discuss the influence of the secondary flow on the turbulent heat transfer by analysing the development of Nusselt number and turbulent Prandtl number distributions. Besides the varying boundary conditions of the water and air HARCD configurations, the main differences affecting the heat transfer are for the straight section the increase of turbulence-induced secondary flow strength due the inverse viscosity gradient towards the heated wall and the additional development of the stronger Prandtl's flow of the first kind along the curved section.

Figure 4.37 shows the distribution and development of the heat transfer characterised by the Nusselt number along the heated lower wall and figure 4.38 corresponding line plots at several spanwise locations. Note the considerable stretching of the spanwise direction in figure 4.37 to allow for a better view with the ratio of streamwise x- to spanwise z-axis set to 0.1. The distributions are plotted from the beginning of the fully heated part with $T_w = const$, i.e. from $1 \cdot d_h$ after the beginning of the heated section downstream of the temperature ramp. The streamwise heated wall dimensions of the three investigated configurations vary due to the different curvature radii as the set-ups have been defined such, that the streamwise dimensions with respect to the duct centre are identical for cases RC60 and RC180. Case RC900 has been additionally elongated. The results of the straight duct piece follow those of the water HARCD described in section 3.5.4: the corner vortex system causes on the one hand a spanwise heat transfer gradient and on the other hand influences the streamwise heat transfer distribution by an intensified mixing of hot and cold fluid. At $x = 210$ mm the spanwise Nu-variation is with $Nu \approx 54$ in the centre and $Nu \approx 64$ close to the lateral wall corresponding to a spanwise increase of $+18.5\%$ comparable to the $+17.1\%$ for the water HARCD. Likewise, a gradual degradation of the heat transfer is observable in streamwise direction, although the Nusselt number drop is less steep compared to the water HARCD with the Nu-distribution in the centre following a fitted function of $Nu = 7.215 \cdot x^{-0.465} + 39.85$. One reason for the deviating Nu-development is the different behaviour of the turbulence-induced secondary flow strength when heating is applied. In contrast to water as working fluid, for air the viscosity and with it the secondary flow strength increases along the heated duct section, which leads comparatively to a heat transfer enhancement decelerating the streamwise Nusselt number drop.

The dotted lines in figures 4.37 and 4.38 indicate the border between the heated straight and

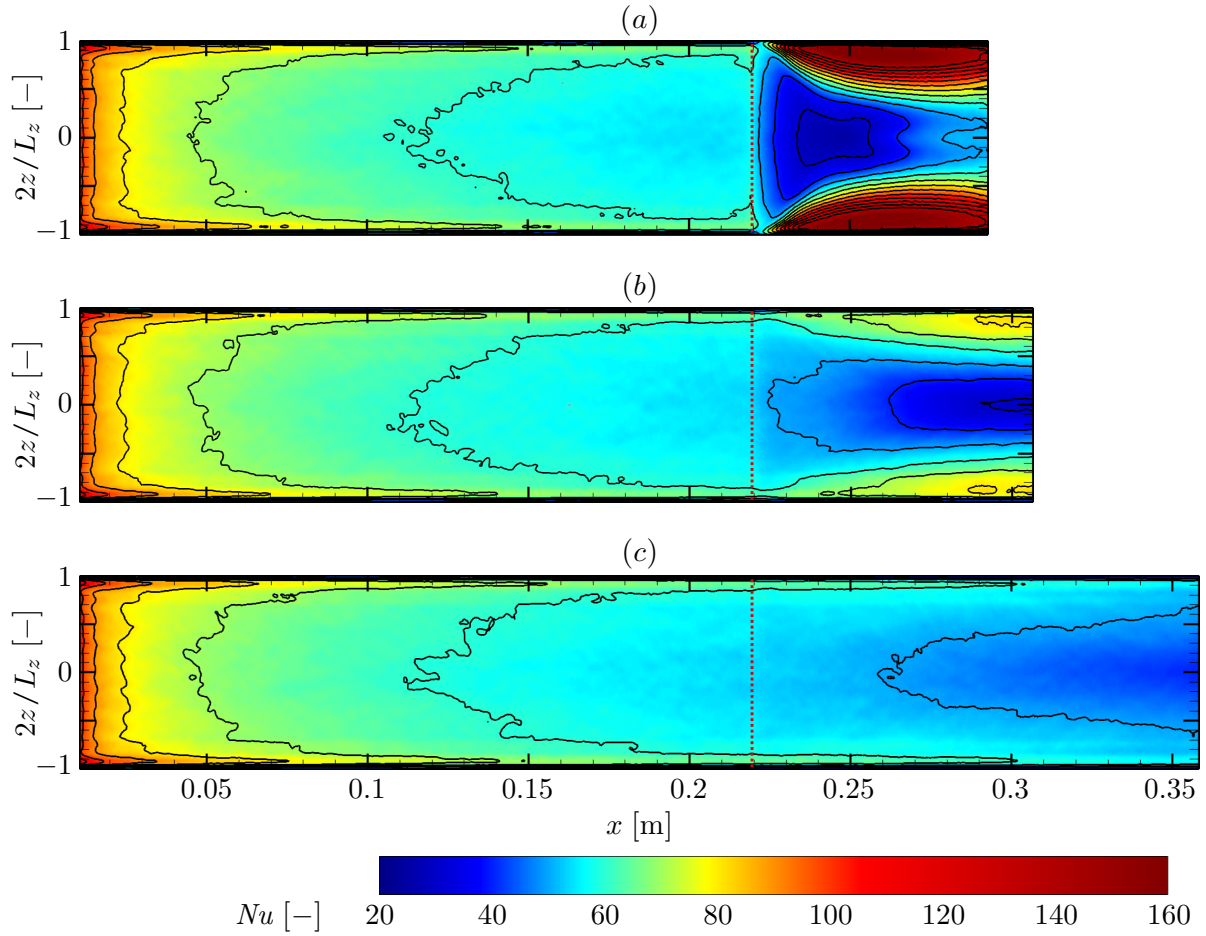

Figure 4.37: Nusselt number distribution along the lower wall of the heated curved duct configuration for the cases (a) RC60, (b) RC180 and (c) RC900. The junction of straight and curved section is indicated by (·····). The contour lines for Nu are drawn from $30 - 140$ in steps of 10. Note, the data is stretched in spanwise direction, such that the axis ratio with respect to the streamwise direction is 0.1.

curved sections. Due to the additional curvature-induced secondary flow, the mixing of hot and cold fluid increases significantly and accordingly the heat transfer into the duct. For case RC60 with the highest secondary flow magnitude the strongest impact on the Nu-distribution is visible, see figures 4.37 (a) and 4.38 (a). For the upcoming discussion we also refer to figure 4.8 of the previous section 4.3.1 for the secondary flow and temperature field. Due to the upstream effect of the pressure variation between outer and inner radius wall and the associated cross-flow, the heat transfer is affected even before entering the curved section. Initially a sharp drop in Nu is present over the whole spanwise width. This decrease is caused by the yet relatively weak secondary flow oriented towards the heated wall, see figures 4.8 $(a - d)$, compressing the incoming temperature boundary layer and consequently decreasing the wall temperature gradient and the associated heat transfer. In figure 4.38 (a), the compression effect is especially well captured

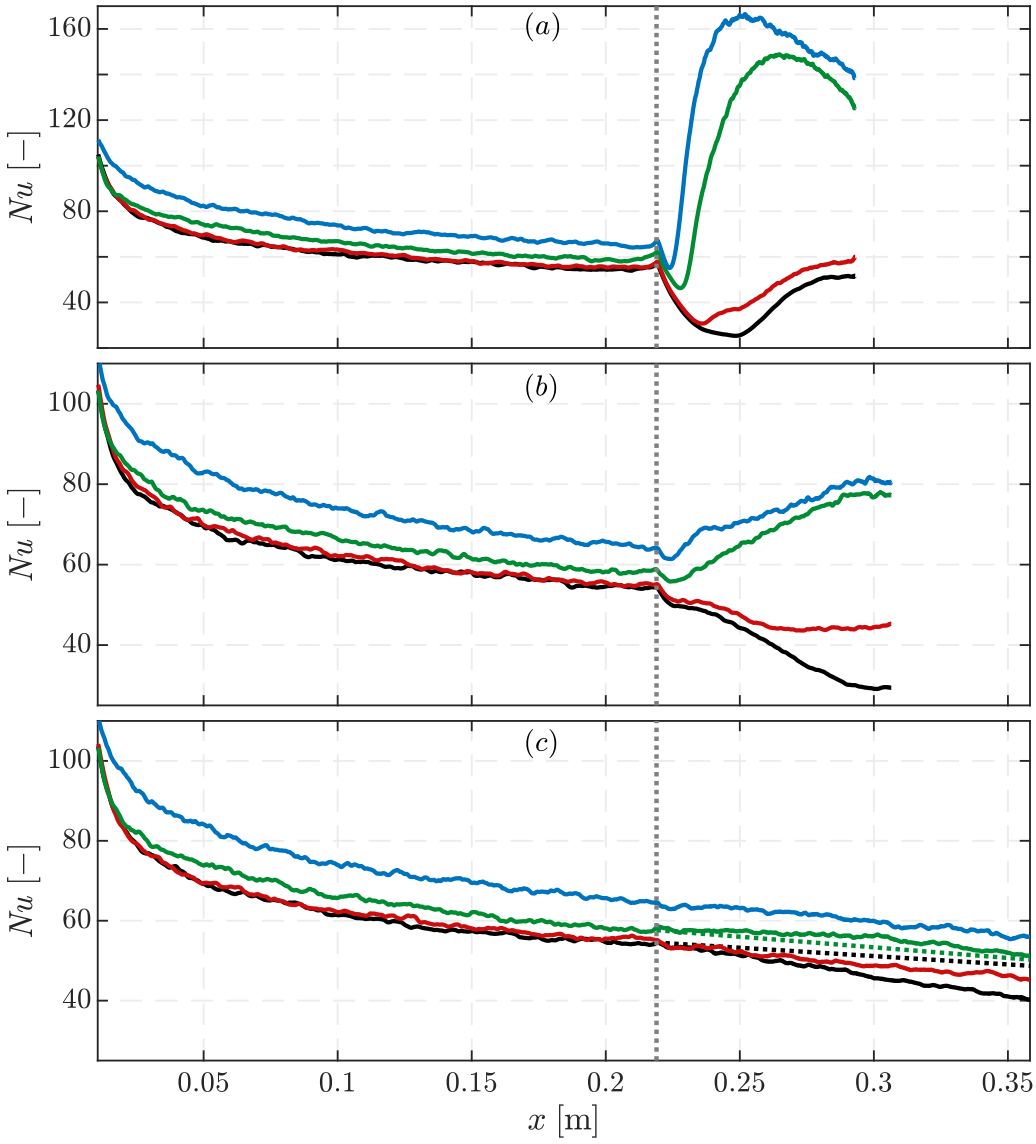

Figure 4.38: Nusselt number development along the lower wall of the heated curved duct configuration for the cases (*a*) RC60, (*b*) RC180 and (*c*) RC900 at spanwise locations of $2z/L_z = 0$ (——), $2z/L_z = 0.33$ (——), $2z/L_z = 0.75$ (——) and $2z/L_z = 0.9$ (——). The junction of straight and curved section is indicated by (·····). The lines (·····) and (·····) are tangential continuations of the respective straight section line to indicate the Dean vortex effect.

and indicated by the local minima of the two distributions at $2z/L_z = 0.75$ and $2z/L_z = 0.9$ entering the curved section. Along the bend the Dean vortex system increases further in strength completely reshaping the incoming temperature boundary layer. By transporting cold fluid along the lateral sidewalls into the duct corner regions, the Dean vortices locally increase the driving temperature difference up to almost the maximum possible value of $T_w - T_b$ from position $\alpha \approx 15°$ onwards. Simultaneously, the hot fluid above the heated wall, i.e. the straight duct temperature boundary layer, is conveyed into the wall centre decreasing the temperature gradient there. As a consequence, a significant spanwise heat transfer gradient is developing. For example at $\alpha = 28.5°$, corresponding to a streamwise distance of $x = 0.2426\,\mathrm{mm}$, the centre Nusselt number is $Nu = 26.27$ compared to $Nu = 166.5$ at $2z/L_z = 0.9$ close to the lateral wall, see figure 4.38 (a). With increasing streamwise distance the region of high Nu expands gradually from the lateral walls towards the centre until the candle flame shaped temperature distribution is forming from $\alpha = 45°$ onwards. This process is associated with transporting the built-up hot fluid above the heated wall centre into the duct core and mixing it with cold fluid. Consequently, the temperature gradient at $z = 0$ is increased and the heat transfer starts to rise again after passing the global minimum. Simultaneously, the temperature boundary layer towards the lateral sidewalls is starting to form anew under the Dean vortex presence, see figures 4.8 (l, n). Thus, the corner region temperature gradient and heat transfer are reduced towards the outlet. In the heated wall centre, the region of low Nu experiences a dent of slightly increased heat transfer, see the contour-line behaviour in figure 4.37 (a). This dent is caused by the small pair of counter-rotating ICW Dean vortices located directly above the heated wall centre in the wake area between the large base Dean vortices. Both vortices transport slightly cooler fluid towards the heated wall increasing the local heat transfer. In contrast to the straight section, no simple functional correlation for the streamwise Nu-development can be found due to the increased flow complexity.

For case RC180, an overall similar behaviour can be observed, although the stream- and spanwise Nusselt number variation is less pronounced due to the weaker secondary flow mixing. The delayed and weaker Dean vortex development leads to a downstream shift of the low and high Nu-regions and a significant reduction of the peak values is obtained compared to case RC60. The maximum spanwise Nu-variation is reached only at the end of the curved section and amounts to $Nu = 29.5$ in the centre and $Nu = 80.6$ close to the lateral wall. The heat transfer deviation can be explained with support of the temperature profiles of figure 4.9 in the previous section 4.3.1. Due to the lower curvature, it requires a longer streamwise distance for the turbulence-induced vortices to be replaced by the Dean vortices and longer to transform the temperature boundary layer to the candle flame like shape. The latter is never fully achieved and the cold fluid from the duct core does not come into more or less direct contact with the heated wall as for case RC60. Both effects cause hot fluid to remain near the heated wall, and thus reduce wall temperature gradients and the associated heat transfer. Consequently, the latter is not affected as substantially as for the highest curvature case.

For case RC900, the secondary flow field is defined by the interaction of the comparably strong corner and Dean vortex systems. In the vicinity of the lower wall, the corner vortex pairs remain until the end section and the merging process of turbulence- and curvature-induced vortices leads to an intensification of the secondary flow strength in the small corner vortex influence area, see

	RC60	RC180	RC900
$Nu_{xz}\,[-]$	67.71	61.66	59.50
$Nu_{xz}\vert_{bend}\,[-]$	75.44	53.92	51.41

Table 4.9: Mean Nusselt numbers averaged over the whole configuration Nu_{xz} and only over the curved section $Nu_{xz}|_{bend}$.

also figure 4.10 in section 4.3.1. As a consequence of the lower wall secondary flow field acting similar as an intensified turbulence-induced vortex system, the temperature boundary layer only changes marginally and its structure remains close to the one of the straight duct flow. The $\overline{T}$-contour lines become more wavy indicating a decrease of $\Delta\overline{T}$ in the wall centre and directly at the lateral walls, and an increase of $\Delta\overline{T}$ in between. The Nu-distribution is only weakly affected by the additional curvature-induced secondary flow. Following the observed changes in $\Delta\overline{T}$, when entering the curved section the centre Nu-decrease becomes steeper, whereas at $2z/L_z = 0.75$ it becomes flatter, which is indicated by the tangential line continuations in figure 4.38 (c). At $2z/L_z = 0.33$ and $2z/L_z = 0.9$ no apparent change in the streamwise Nusselt number gradient is present between straight and curved sections.

The discussed heat transfer differences for the three cases also reflect in the integral average Nusselt numbers Nu_{xz} listed in table 4.9, separated into the value for the whole configuration and only for the curved section $Nu_{xz}|_{bend}$. The conclusions are: the higher the curvature and stronger the mixing by the Dean vortices the higher the achievable heat transfer. Moreover, the Dean vortex strength and heat transfer do not correlate linearly. To reach locally the highest possible heat transfer, i.e. the maximum possible driving temperature difference $\Delta T_{max} = T_w - T_b$, a certain threshold Dean number has to be reached, for which cold fluid is able to get into direct contact with the heated wall. This state is only achieved for case RC60, but not RC180 and RC900.

For the remainder of this section the discussion focuses on the turbulent Prandtl number distributions and the angles φ_M and φ_H. The latter quantities denote the angles between Reynolds stresses and velocity gradients (φ_M) and between the turbulent heat fluxes and temperature gradients (φ_H) in the duct cross-section. The derivation and definitions of Pr_t and angles are given in section 3.5.4. Analogous to the water HARCD investigation the goal is to utilise the well-resolved LES data to point out the errors associated with the Boussinesq hypothesis and the constant turbulent Prandtl number assumption often employed in RANS modelling.

Figure 4.39 depicts the cross-sectional angle distribution at 150 mm after the beginning of the full wall heating, i.e. after T_w remains constant following the initial temperature ramp, and at $\alpha = 45°$ in the middle of the curved section of case RC60. The secondary flow field of the former is defined by the corner vortex system and that of the latter by the significantly stronger Dean vortex system. The results for figure 4.39 (a, b) resemble those obtained for the straight water HARCD, see figure 3.27 in section 3.5.4. Slightly lower levels for φ_M and slightly higher ones for φ_H are observable, but the influence of the corner vortices on the distributions remains identical. The results demonstrate once more, that the Boussinesq hypothesis and the assumption of a constant Pr_t implicitly claiming $\varphi_M = \varphi_H = 0$, i.e. an alignment of turbulent flux and gradient vectors, are invalid for HARCD flows affected by turbulence-induced secondary flow. With

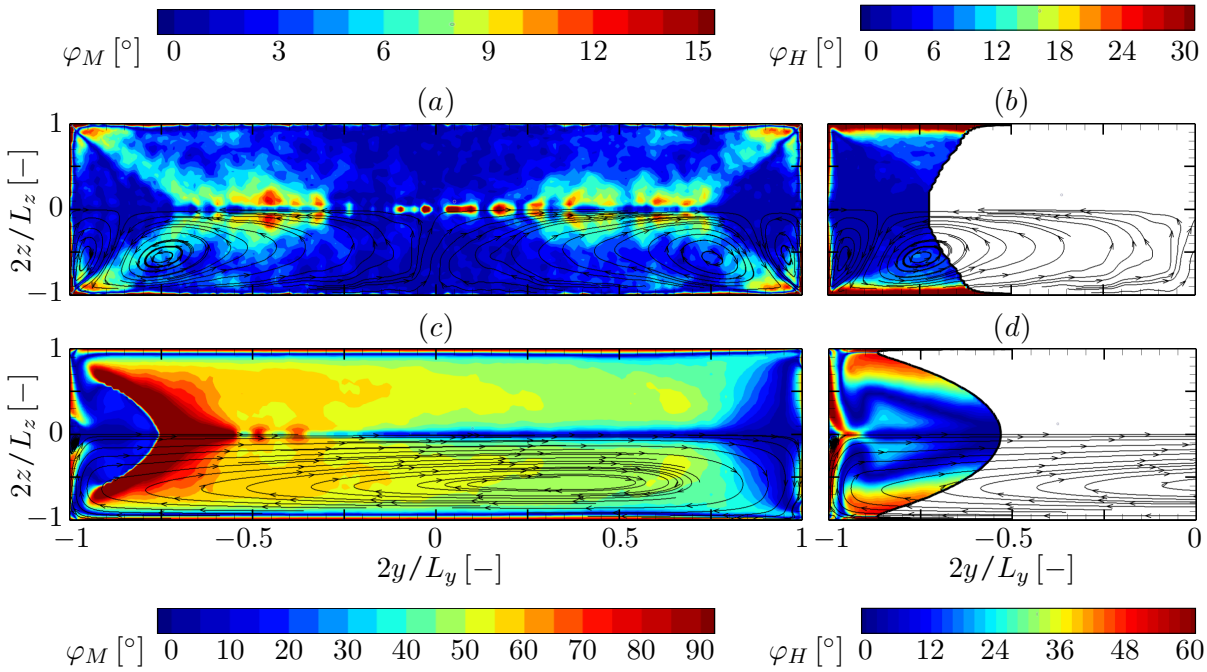

Figure 4.39: Cross-sectional distribution of the angles φ_M and φ_H in the straight section at (a, b) a streamwise location of 150 mm after T_w remains constant, and (c, d) in the middle of the curved section at $\alpha = 45°$ for the case RC60. The angle φ_H is evaluated for $\overline{T} - T_b > 2.5\,\mathrm{K}$. For the angle definitions see equation 3.5 in section 3.5.4.

the stronger curvature-induced secondary flow the errors made by these assumptions increase significantly, see figures 4.39 (c, d) and note the different legend used compared to subfigures (a, b). Especially in the lower duct quarter, where the strong Dean vortices cause noticeable distortions of temperature, velocity and turbulent stress fields, φ_M and φ_H deviate significantly from a presumed vector alignment. A similar observation can be made along the lateral sidewall TBLs due to the induced current towards the inner radius wall.

Figure 4.40 depicts the streamwise development of the cross-sectional Pr_t-distribution. Note that Pr_t is defined as in section 3.5.4, i.e. it is based on a TBL formulation for the heated wall as well as the lateral sidewalls with a least-square optimisation to obtain the $Pr_t(y, z)$-field. In figures 4.40 (a, b), the Pr_t-distributions are only affected by turbulence-induced secondary flow, and thus are comparable to the water HARCD results in figure 3.28. As Pr_t depends on the molecular Prandtl number as well as the wall distance y^+ (Kays, 1994), the results resemble each other, but differences are observable and expectable due to different local flow conditions, especially in Re_τ and Pr. For the water HARCD, the molecular Prandtl number varies between $Pr = 3.0$ at T_b and $Pr = 1.75$ at T_w, whereas for the air HARCD Pr remains approximately constant with $Pr = 0.7082$ at T_b and $Pr = 0.7045$ at T_w. As already observed for the water HARCD, a dome-shaped region of augmented turbulent Prandtl number with $Pr_t \approx 1$

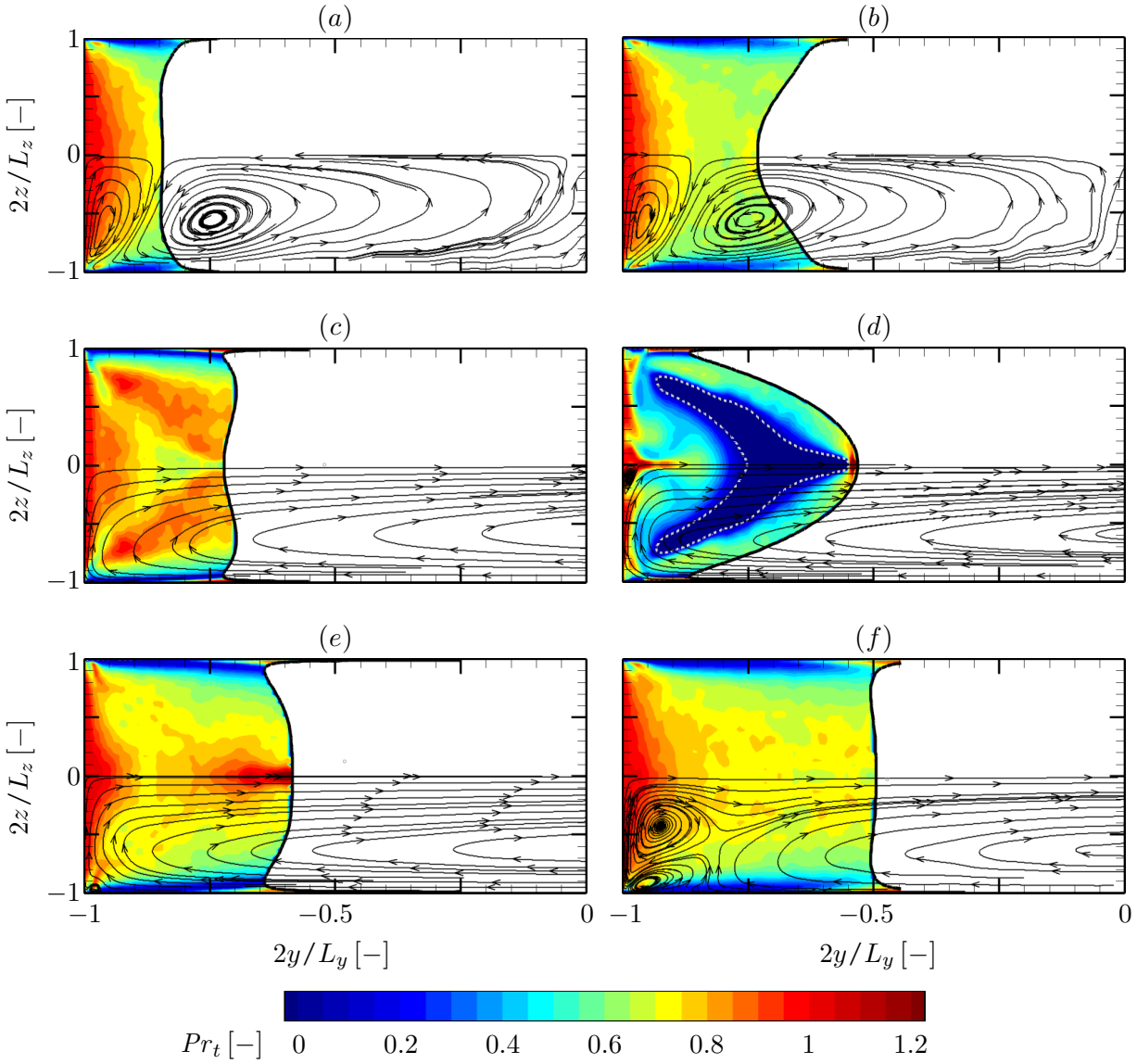

Figure 4.40: Cross-sectional turbulent Prandtl number distributions in the straight section at a streamwise location of (a) 50 mm and (b) 150 mm after T_w remains constant, and in the curved section at (c) $\alpha = 15°$ and (d) $\alpha = 45°$ for case RC60. In (e) the end section distribution of case RC180 at $\alpha = 29.17°$ is depicted and in (f) that of case RC900 at $\alpha = 8.75°$. The isoline $Pr_t = 0$ is marked by (·····) and Pr_t is evaluated for $\overline{T} - T_b > 2.5\,\mathrm{K}$. For the Pr_t definition see section 3.5.4.

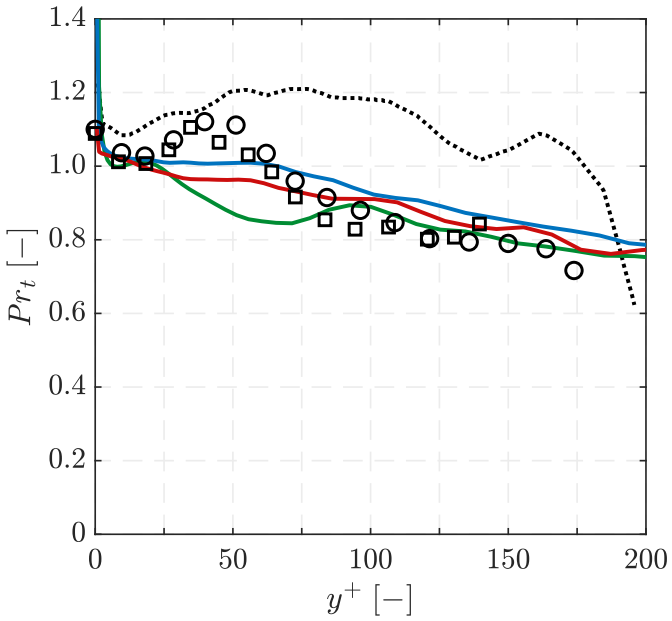

Figure 4.41: Turbulent Prandtl number distributions along $z = 0$ for (——) straight section at 50 mm after T_w remains constant, (——) case RC60 in the curved section at 15° and (——) case RC900 at 8.75°. For comparison LES data by (·····) Schindler et al. (2019) as well as DNS data by (□) Kong et al. (2000) and (○) Kim and Moin (1989) are included.

is forming above the heated wall enclosed by regions of Pr_t approaching zero along the lateral sidewalls due to the adiabatic boundary condition. Likewise, along the duct length the high-Pr_t region is shrinking and slightly moving closer towards the heated wall. In contrast to section 3.5.4, the global maximum located in the interaction zone of the two large corner vortices at $z = 0$ and extending from $2y/L_y \approx -0.75$ towards the duct core has not formed yet due to the shorter streamwise extent of the straight duct section. Hence, it is only indicated by the slight Pr_t-increase in the duct centre at $2y/L_y \approx -0.75$, see figure 4.40 (b). At position $\alpha = 15°$ of case RC60, the secondary flow field is already dominated by the yet relatively weak base Dean vortex pair. The dome-shaped high-Pr_t zone above the heated wall becomes weaker and two additional symmetric high-Pr_t zones are emerging angled from the duct corners towards its centre line. These are caused by the secondary flow motions as indicated by the turning Dean vortex streamlines, see figure 4.40 (c). At a certain position along the curved section of RC60, the base Dean vortices become strong enough to cause a noticeable bulging of the flow profile leading to very high deviations from the states $\varphi_M = 0$ and $\varphi_H = 0$. Consequently, following our definition derived in section 3.5.4, regions of negative Pr_t are obtained, see figures 4.39 (c, d) and figure 4.40 (d). Figures 4.40 (e, f) depict the cases RC180 and RC900, respectively, both experiencing lower secondary flow magnitudes and consequently lower disturbances in the Pr_t-evaluation. In the end section of case RC180, the dome-shaped high-Pr_t zone is weakened by the downward and spanwise Dean vortex flow and intensified by the upward flow along the midplane. In the end section of case RC900, the high-Pr_t region above the heated wall is enhanced by the merging secondary flow structure resembling a strengthened corner vortex system.

The validity of the Pr_t-definition is demonstrated in figure 4.41, comparing our results along the duct centre line against DNS and LES data available in the literature. The DNS data is taken from the heated TBL configuration of Kong et al. (2000) and the heated channel configuration of Kim and Moin (1989), and the LES data from a symmetrically heated square duct of Schindler et al. (2019). Along the midplane our $Pr_t(y, z)$-definition follows essentially a simple TBL-definition for Pr_t in heated wall-normal direction. Note that the comparability is impaired due to different configurations and varying local flow conditions. Nevertheless, the straight section results are in good agreement with DNS data, only missing the Pr_t-increase at $y^+ \approx 30$. Directly at the heated wall centre a value of $Pr_t \approx 1.11$ is reached, which coincides with both of the DNS profiles. The additional presence of Dean vortices especially modifies the Pr_t-levels at the wall, increasing to $Pr_t = 2.92$ for case RC60 at position $\alpha = 15°$ and $Pr_t = 1.55$ for case RC900 at position $\alpha = 8.75°$. Depending on the changing secondary flow field slightly lower Pr_t-values (RC60, $\alpha = 15°$) or slightly higher Pr_t-values (RC900, $\alpha = 8.75°$) are present along the centre line compared to the straight section. With respect to the square duct LES data by Schindler et al. (2019), a noticeable deviation is observed over the whole range, for which the reasons are yet not fully clear. Possible explanations are that in contrast to our simulation constant fluid properties were assumed and the explicit Smagorinski LES model was employed.

The streamwise development of the Pr_t-distributions in figure 4.40 demonstrates, that for configurations affected by secondary flows the Boussinesq isotropic eddy viscosity hypothesis and constant Pr_t assumption are invalid, and that the associated deviation is growing with the secondary flow strength. Likewise, the classical wall-normal Pr_t-distributions in figure 4.41 predict strong variations in the turbulent Prandtl number for even weak secondary flow influence. These variations are between $Pr_t \approx 1.1$ (straight section) and $Pr_t \approx 1.55$ (curved section end plane of case RC900), respectively, at the wall and $Pr_t \approx 0.8$ in the logarithmic region of the TBL. The presented observations motivate the development and application of more accurate turbulence closures for Reynolds stresses and turbulent heat fluxes in RANS modelling.

5 Assessment of RANS Models for Heated HARCD Flows (ANSYS CFX)

The goal of this chapter is to investigate the prediction capabilities of commonly utilised RANS turbulence models available within the industrial flow solver ANSYS CFX for asymmetrically heated straight and curved HARCDs. For this purpose, the LES configurations as presented in the previous chapters, i.e. the straight water HARCD at $Re_b = 110 \cdot 10^3$ of chapter 3 and the curved air HARCD of chapter 4 at $Re_b = 40 \cdot 10^3$, are re-simulated employing various turbulence models and turbulent heat flux closures. The employed turbulence models comprise the Menter's ω-equation based Shear Stress Transport (SST) model, the explicit algebraic BSL EARSM and the BSL Reynolds stress model (BSL RSM) as well as the ε-equation based SSG Reynolds stress model (SSG RSM). The models are utilised with the standard parameter sets as defined in ANSYS Inc. (2020b) and ANSYS Inc. (2020a). Furthermore, the effect of turbulent heat flux modelling is addressed by comparing the common constant turbulent Prandtl number approach, algebraic turbulent heat flux models and models based on solving additional transport equations for $\overline{u_i' h'}$. Within this work, RANS turbulence model parameter optimisation is not investigated. For this, the reader is referred e.g. to Menter et al. (2019) presenting the effects amongst others for a square duct flow configuration in the context of ANSYS CFX.

In sections 5.1 and 5.2 the numerical set-up and accuracy of the RANS simulations is presented and discussed. The following section 5.3 is then subdivided into three parts: (I) the adiabatic water HARCD with a focus on the prediction capabilities of the turbulence-induced corner vortex system, (II) the heated straight water HARCD with a focus on the interaction of turbulence-induced secondary flow and turbulent heat transfer including the effects of turbulent heat flux modelling, and (III) the heated curved air HARCD with a focus on the interaction of Prandtl's flow of the first and second kind as well as turbulent heat transfer. The latter replaces the curved water HARCD analysis of Kaller et al. (2020) while retaining the structure of the original section, but adding the LES database comparison.

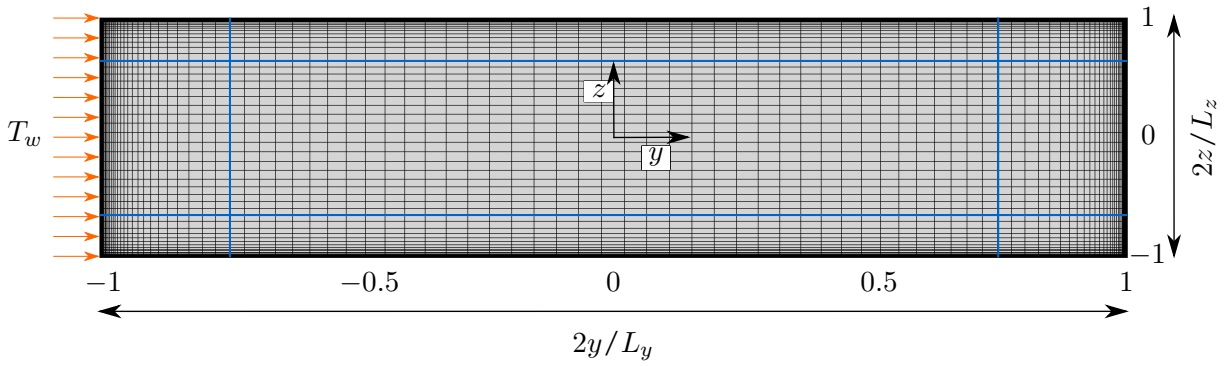

Figure 5.1: Cross-sectional grid and blocking for the RANS simulations.

5.1 Computational Set-up

The numerical RANS set-ups follow those of the LES, see figure 3.2 of section 3.2 for the straight water HARCD configuration and figure 4.1 of section 4.1 for the curved air HARCD configuration. The employed cross-sectional grid is depicted in figure 5.1. The set-up consists of two domains simulated independently. The adiabatic periodic section has a dimension of $50 \times 25.8 \times 6\,\mathrm{mm}^3$, and the heated section consists of a $600 \times 25.8 \times 6\,\mathrm{mm}^3$ straight part followed by a 90° heated bend with a curvature radius of $r_c = 60\,\mathrm{mm}$ and a $50 \times 25.8 \times 6\,\mathrm{mm}^3$ coarsely meshed outlet piece for the water HARCD configuration, and curvature radii of $r_c = 60\,\mathrm{mm}$, $r_c = 180\,\mathrm{mm}$ and $r_c = 900\,\mathrm{mm}$ for the air HARCD configurations, respectively. To determine the required resolution for a wall-resolved RANS simulation, i.e. $y^+ \approx 1$, a grid sensitivity study has been performed for the adiabatic periodic section using the BSL EARSM turbulence model. For the water HARCD the grid is asymmetric with respect to the z-axis to account for the resolution requirements of the temperature boundary layer. Hence, the grid is refined at the lower heated wall. In total $34 \times 115 \times 64 = 250240$ nodes are used for the adiabatic periodic and $512 \times 115 \times 64 = 3768320$ nodes for the heated domain of the water HARCD. For an accuracy assessment of the well-resolved RANS simulations, we refer to the comparison of an adiabatic square duct RANS at a comparable grid resolution as the cooling duct simulation with LES and DNS results in section 5.2. For the air HARCD simulations analogous to the LES set-up a symmetric grid is employed with a comparable number of nodes as for the water HARCD RANS, i.e. due to the lower Reynolds number a better spatial resolution is obtained.

The adiabatic periodic duct serves to generate a fully developed turbulent HARCD inflow profile for the spatially resolved heated domain. The adiabatic simulation is performed with liquid water and ideal gas air, respectively, both treated as an incompressible fluid with fixed properties at $T_b = 333.15\,\mathrm{K}$. All walls are defined as smooth adiabatic walls. In streamwise direction a periodic boundary condition is set with a constant water mass flow of $\dot{m} = 0.8193\,\mathrm{kg/s}$ corresponding to $u_b = 5.3833\,\mathrm{m/s}$ and $Re_b = 110 \cdot 10^3$. For the air HARCD $\dot{m} = 0.0128\,\mathrm{kg/s}$ is defined, which corresponds to $u_b = 78.0419\,\mathrm{m/s}$ and $Re_b = 40 \cdot 10^3$. In table 5.1, the model combinations consisting of the used turbulence model and turbulent heat flux closure are presented for the water HARCD configuration. The same models have been applied for the air HARCD configurations, although with a constant turbulent Prandtl number approach of $Pr_t = 0.9$ for the turbulent

Turbulence model	Turbulence anisotropy	Turbulent heat flux closure	Turbulent Prandtl number
SST EVM	isotropic	Eddy Diffusivity	$Pr_t = 0.9$
BSL EARSM	anisotropic	Eddy Diffusivity	$Pr_t = 0.9$
SSG RSM	anisotropic	Eddy Diffusivity	$Pr_t = 0.9$
		Anisotropic Diffusion	variable Pr_t $C_{ani.\ diff} = 0.244444$ $C_{cross.\ deriv} = 1.0$
BSL RSM	anisotropic	Eddy Diffusivity	$Pr_t = 0.85$
		Eddy Diffusivity	$Pr_t = 0.9$
		Transport Equation	variable Pr_t
		Daly-Harlow model (algebraic)	variable Pr_t
		Younis model (algebraic)	variable Pr_t

Table 5.1: Turbulence closure model combinations used for the water HARCD RANS simulations. Turbulence and heat flux closure model names as specified within ANSYS CFX are used (ANSYS Inc., 2020a). For all models the unaltered standard parameters are employed. Exceptions are the algebraic heat flux closure models, which are not available within the program package, and thus have been added as functional expressions, see section 2.4.

heat flux closure. For each combination of table 5.1 the following procedure is executed: based on an initial solution of $(\overline{u}/\overline{v}/\overline{w}) = (5.3833/0/0)\,\mathrm{m/s}$ and $(\overline{u}/\overline{v}/\overline{w}) = (78.0419/0/0)\,\mathrm{m/s}$, respectively, a physical time step of $\Delta t = 10^{-5}\,\mathrm{s}$ is used for ≈ 20 iterations. Then, a local time scale factor of 50 and a reduced pressure update multiplier changed from the default 0.25 to 0.01 is utilised until a RMS target value of $1 \cdot 10^{-6}$ is surpassed for the momentum and continuity equation residuals.

For the spatially resolved heated duct simulations, the compressible Reynolds-averaged Navier-Stokes as described in section 2.4 are used. Fluid properties are treated as variable and are evaluated based on the IAPWS IF97 formulation for the water HARCD simulations. For the air HARCD configurations the ideal gas equation of state is employed for thermodynamic quantities and Sutherland's law for viscosity and thermal conductivity

$$\frac{\mu}{\mu_0} = \left(\frac{T}{T_0}\right)^{1.5} \cdot \frac{T_0 + S_\mu}{T + S_\mu}, \qquad \frac{k}{k_0} = \left(\frac{T}{T_0}\right)^{1.5} \cdot \frac{T_0 + S_k}{T + S_k}, \tag{5.1}$$

with $T_0 = 273\,\mathrm{K}$, $\mu_0 = 1.716 \cdot 10^{-5}\,\mathrm{N\,s/m^2}$, $k_0 = 0.0241\,\mathrm{W/m\,K}$, $S_\mu = 111\,\mathrm{K}$ and $S_k = 194\,\mathrm{K}$ (White, 2006). All walls are treated as smooth walls with the automatic wall treatment option applied. The lower wall is an isothermal wall with $T_w = 373.15\,\mathrm{K}$ ($T_w = 438.15\,\mathrm{K}$ for the air duct set-up) and the remaining walls are adiabatic. With the bulk flow temperature of $T_b = 333.15\,\mathrm{K}$, this results in a moderate temperature difference of 40 K and 105 K, respectively. As described previously, the wall temperatures for water and air set-up are chosen such that a near-wall viscosity modulation of similar strength and inverse sign is approximatively obtained. At the inlet, the velocity and turbulence profiles extracted from the respective precursor simulation are prescribed. At the outlet a mass flow of $\dot{m} = 0.8193\,\mathrm{kg/s}$ ($\dot{m} = 0.0128\,\mathrm{kg/s}$ for the air

	$N_x \times N_y \times N_z$	$\Delta x^+ \times \Delta y^+_{min} \times \Delta z^+_{min}$	$\frac{\Delta y_{max}}{\Delta y_{min}} \times \frac{\Delta z_{max}}{\Delta z_{min}}$	$\frac{1}{2} Re_{\tau,c}$	$l^+_{\nu,c}$ [µm]
RANS 1	$21 \times 83 \times 83$	$718 \times 1.00 \times 1.00$	52.50	1006	9.9
RANS 2	$64 \times 192 \times 192$	$237 \times 1.01 \times 1.01$	34.01	1009	9.9
INCA LES	$250 \times 136 \times 136$	$65.3 \times 1.06 \times 1.06$	23.41	1089	9.2
DNS	$2048 \times 512 \times 512$	$9.8 \times 0.61 \times 0.62$	10.67	1073	9.3

Table 5.2: Main grid and flow parameters for the RANS-LES-DNS comparison for the square duct simulation at $Re_b = 40 \cdot 10^3$. The index c indicates a wall centre value at $z = 0$. $Re_{\tau,c}$ is halved following the square duct definition by Pirozzoli et al. (2018). The parameters for the INCA LES are repeated from table 3.5 for comparison.

duct set-up) is specified to generate a first solution. Based on this result a second simulation is performed with a prescribed average pressure over the whole outlet of $p_{out} = 101325\,\text{Pa}$ ($p_{out} = 98100\,\text{Pa}$ for the air duct set-up) to obtain a physically valid pressure field within the domain. This approach has proven to allow for an accelerated overall convergence. For each turbulence model combination included within this study, see table 5.1, the following procedure is executed: initially, a physical time step of $\Delta t = 10^{-5}\,\text{s}$ is used for 10 iterations. No specific domain initialisation is set. Then, a local time scale factor of 25 is utilised for further 15 iterations, after which the factor is increased to 50 and the simulation continued until a RMS target value of $1 \cdot 10^{-6}$ is surpassed for the momentum, continuity and total enthalpy equation residuals. Based on this result the outlet boundary condition is modified and p_{out} adjusted as described previously, and the simulation restarted with a local time scale factor of 50 until convergence is reached.

5.2 Assessment of Numerical Accuracy

To assess the numerical accuracy of the RANS HARCD simulations, we additionally simulate the adiabatic square duct case D of Pirozzoli et al. (2018) analogous to the previous LES chapters. The configuration has an edge length of $2h$ with $Re_b = 40 \cdot 10^3$ and $Re_\tau = 1055$.

The RANS grid for this comparison follows the resolution used in our investigation of the water HARCD at $Re_b = 110 \cdot 10^3$, i.e. comparable Δx^+, Δy^+ and Δz^+ are employed. Additionally, a RANS at a finer grid resolution has been performed to show grid convergence. Both simulations are performed using the BSL RSM turbulence model. The grid and simulation parameters for the square duct comparison of DNS, LES(INCA) and RANS results are listed in table 5.2. For further details on the LES data the reader is referred to section 3.3.2.

Figure 5.2 compares the RANS with the LES and the DNS results. The centre friction velocity $u_{\tau,c}$ is used to normalise streamwise velocity and Reynolds stresses, and for the secondary flow components the bulk velocity u_b is employed. The RANS results for the utilised resolution are grid-converged as the comparison with the fine resolution result shows. The streamwise velocity profile has a steeper inclination in the logarithmic region of the boundary layer compared to the DNS, the LES and the analytical law of the wall. Note, for the HARCD at a similar grid resolution the inclination is less steep. In the viscous sublayer the RANS profiles are below the LES and DNS profiles, although the deviation is reduced employing a finer resolution. The secondary flow

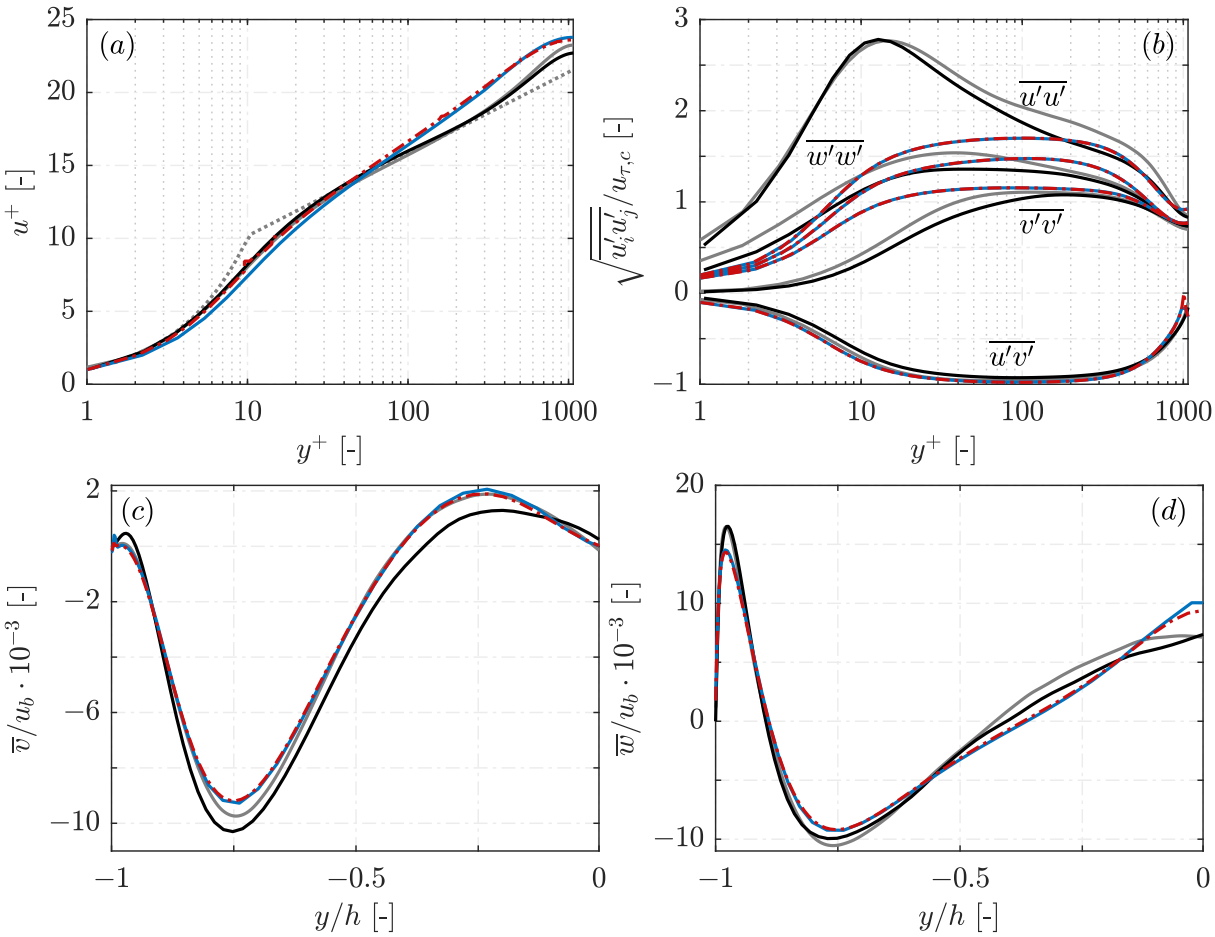

Figure 5.2: Profiles of (a) mean streamwise velocity and (b) Reynolds stresses along the duct midplane at $z = 0$, and (c, d) secondary flow velocities at $z/h = 0.75$ for the LES (——), the DNS (——), the RANS at HARCD-comparable resolution (——) and the RANS at the finest grid resolution (-·-·-) for the adiabatic square duct simulation. In (a) the analytical law of the wall ($u^+ = 1/0.41 \cdot \ln y^+ + 4.55$) is represented by (·····).

strength and location of the vortices is with only slight deviations in good agreement with DNS and LES. For Reynolds stresses, the shear stress term $\overline{u'v'}$ agrees well with DNS results, however, the normal stresses $\overline{u'u'}$, $\overline{v'v'}$ and $\overline{w'w'}$ show noticeable discrepancies with respect to DNS and LES. To rule out any errors various set-up modifications have been performed amongst others employing the BSL EARSM turbulence model as well as significantly extending the domain in streamwise direction and performing a non-periodic resolved RANS with the fluid being treated both incompressible and compressible. However, the observed deviations persist. Moreover, $Re_{\tau,c}$ is underestimated in the RANS, see table 5.2. This is due to a stronger drop of the wall shear stress distribution in the wall centre compared to the DNS and LES (not explicitly shown).

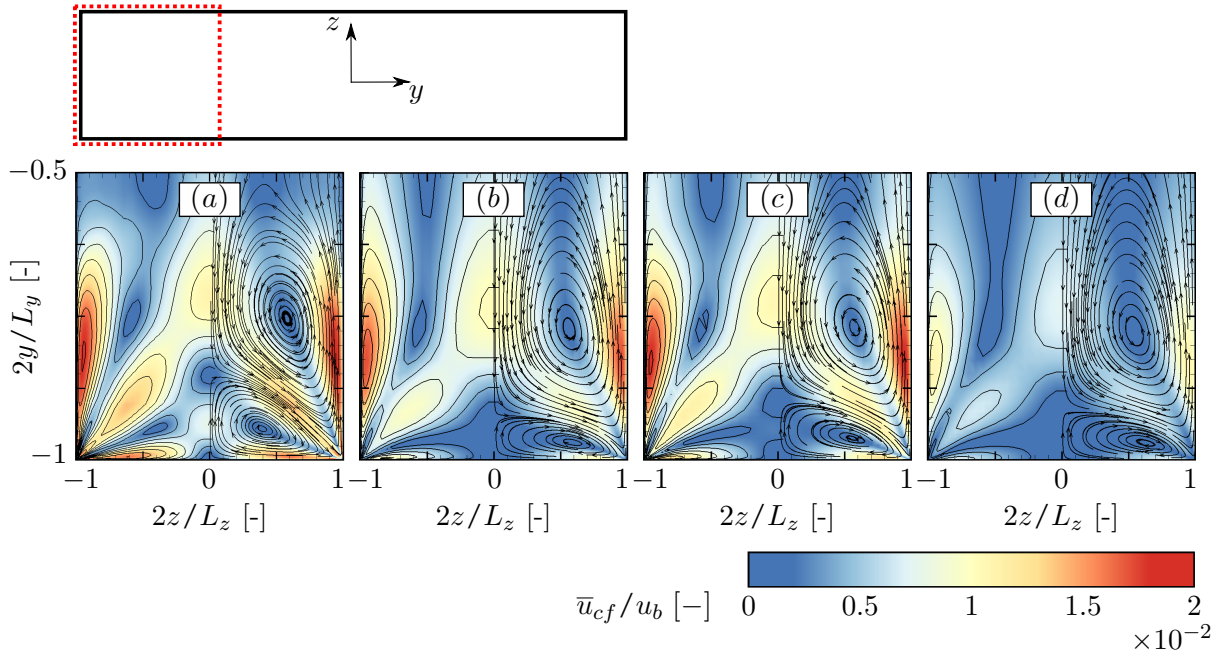

Figure 5.3: Secondary flow in the lower quarter of the adiabatic HARCD for the (a) LES, and the (b) BSL EARSM, (c) BSL RSM and (d) SSG RSM RANS turbulence models. Isolines are drawn from 0 to 2 in steps of 0.2 and $\overline{u}_{cf} = \sqrt{\overline{v}^2 + \overline{w}^2}$.

5.3 Discussion of the Results

In the following subsections, the results of the RANS simulations performed with ANSYS CFX for the different turbulence closure model combinations are presented and compared against the LES. First, results for the straight adiabatic periodic HARCD flow field are analysed with a strong focus on the turbulence-induced secondary flow. Then, we discuss the results for the asymmetrically heated straight HARCD focusing on the cross-section $x = 500$ mm, which is close to the end of the straight section, but not yet affected by the downstream bend. The heated duct investigation is expanded to include different turbulent heat flux closure models. In the last subsection the flow and temperature field of the curved section for the different configurations are presented at selected positions. The first two subsections focus on the water HARCD using the INCA LES reference database of chapter 3, and the third subsection focuses on the air HARCDs using the CATUM LES reference database of chapter 4.

5.3.1 Straight Adiabatic Duct Flow Field

In this section, the adiabatic periodic water HARCD results for different RANS turbulence closure models are compared with the LES. A focus is set on the different representation of turbulence-induced secondary flow strongly affecting the duct flow field.

For the different RANS simulations, figure 5.3 shows the following result: as the SST model (not explicitly shown) is based on an eddy viscosity assumption, it cannot predict turbulence-induced secondary flow. All other turbulence models within this study are able to predict

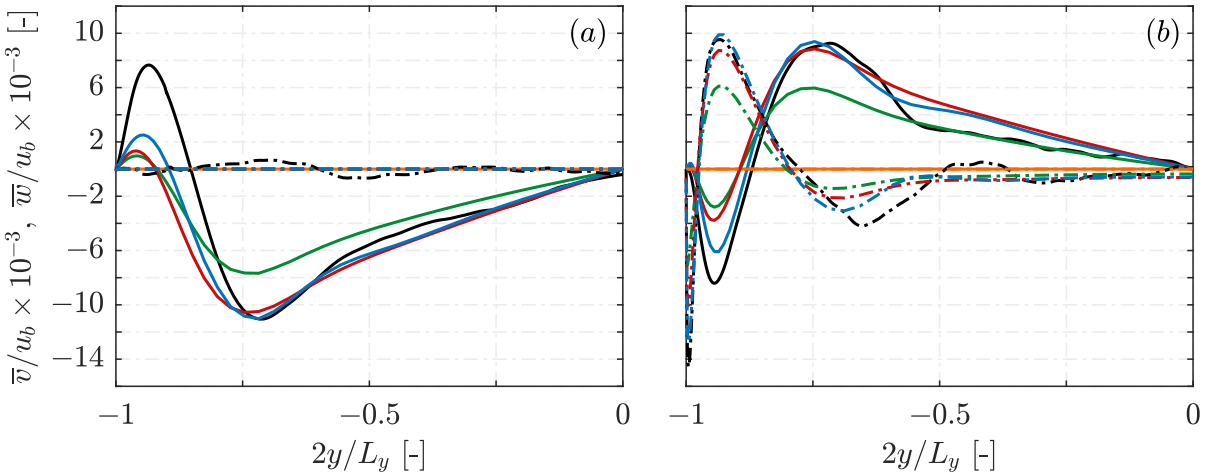

Figure 5.4: Secondary flow velocity distribution along (a) the duct midplane $2z/L_z = 0$ and at (b) $2z/L_z = 0.75$ in the adiabatic HARCD for the LES (——), the SST (——), the BSL EARSM (——), the BSL RSM (——) and the SSG RSM (——). The $\overline{v}$-velocity is represented by solid and the $\overline{w}$-velocity by dash-dotted lines.

turbulence-induced secondary flow, although the vortex strength and location varies. The SSG RSM in figure 5.3 (d) produces the weakest cross-flow velocity, which stems from utilising a simple wall function approach towards the wall instead of resolving the wall boundary layer in the ε-based formulation. Also, the size of the small vortex is underestimated. Better results are obtained with the ω-based BSL EARSM model in figure 5.3 (b). The cross-flow velocity levels are significantly higher than for the SSG RSM, although still slightly lower than for the LES. The overall best RANS results within this study are produced by the BSL RSM in figure 5.3 (c) with an increased size of the small vortices and increased $\overline{u}_{cf}$ levels. However, the small vortex size and strength is still underestimated. In the LES the small vortices extend significantly further towards the duct core, the reason being the higher ratio of small vortex strength to large vortex strength. Consequently, the larger vortex is pushed upwards by the smaller one. We attribute the weaker secondary flow throughout the RANS simulations to differences in the methodology, especially the wall modelling. The mesh resolution can be ruled out, as the RANS results are grid-converged, see the previous section 5.2 for an assessment of the numerical accuracy.

Supporting the already made observations based on the contour plots, figure 5.4 presents the secondary flow components with the duct midplane profiles shown in (a). The $\overline{w}$-component vanishes due to the symmetry with respect to the z-axis. The $\overline{v}$-maximum represents the midplane footprint of the small vortex and the $\overline{v}$-minimum the footprint of the large vortex. We observe that the SSG RSM strongly underestimates the strength of both the small and the large vortex. Moreover, both extremum locations are shifted towards the lower wall in accordance with the already observed vortex shift in figure 5.3. The BSL RSM and the BSL EARSM are both able to correctly predict the large vortex strength, but significantly underestimate the small vortex strength. The $\overline{v}$-maximum is -67.3% weaker for the BSL RSM than in the LES. However, the $\overline{v}$-maximum for the BSL EARSM is yet -46.8% lower than for the BSL RSM. Hence, the

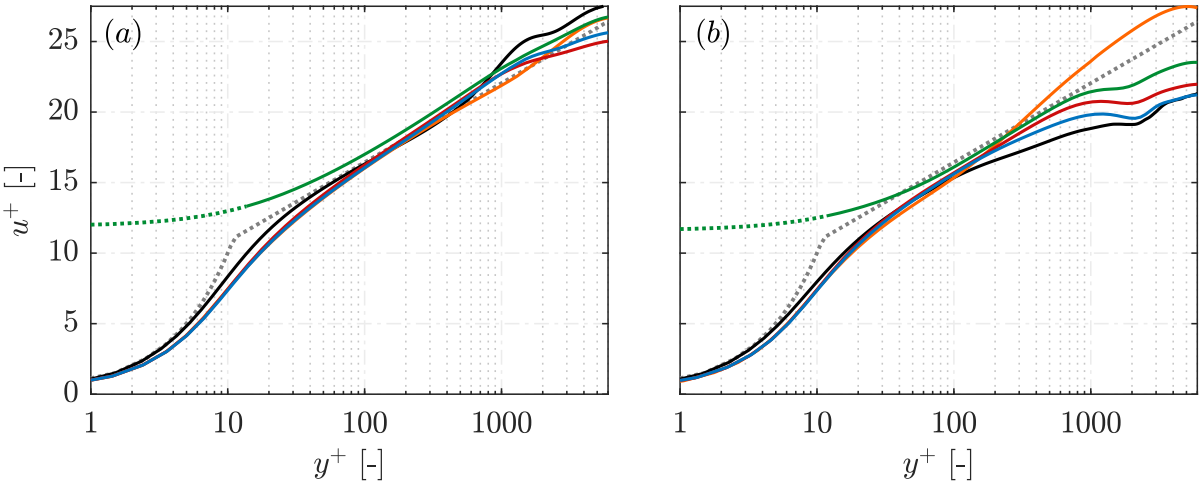

Figure 5.5: Streamwise velocity distribution along (a) the duct midplane $2z/L_z = 0$ and at (b) $2z/L_z = 0.9$ in the adiabatic HARCD for the LES (——), the SST (——), the BSL EARSM (——), the BSL RSM (——) and the SSG RSM (——). The analytical law of the wall ($u^+ = 1/0.41 \cdot \ln y^+ + 5.2$) is represented by (·····).

small vortex strength and size is very sensitive to the chosen turbulence model. Moreover, the extremum locations are shifted towards the lower wall, although stronger for the BSL EARSM. The off-centre cut in figure 5.4 (b) supports the observations made for the duct midplane. The secondary flow strength increases from zero for the SST, over the SSG RSM, the BSL EARSM and the BSL RSM to the LES.

Figure 5.5 shows the dimensionless velocity profiles using the wall centre friction velocity $u_{\tau,c}$ for normalisation. The most prominent result is, that the SSG RSM does not resolve the inner part of the wall boundary layer. Instead the scalable wall function approach is used with a limiter for the y^+-values employed in the logarithmic formulation with $y^+ = max(11.06, y^+)$. Hence, values below $y^+ = 11.06$ are represented as dotted lines in figures 5.5 and 5.6. It has to be mentioned that the used computational grid, which is identical for all RANS models within this study, is actually too fine in the vicinity of the walls for usage with the SSG RSM model due to the specific wall treatment. All other RANS models are ω-based turbulence models and use an identical wall treatment leading to a well-resolved result, see figure 5.5 (a). The velocity in the viscous sublayer and buffer layer of the TBL is slightly underestimated compared to the LES and the analytical solution, and the slope in the logarithmic region is slightly steeper. Although, compared to the square duct case in section 5.2 the slope-discrepancy is less prominent. The highest deviations between the different simulations occur in the outer layer as a consequence of the different secondary flow representation. This is especially visible close to the lateral wall, where the vortices induce a downward kink in the u^+-profile, see figure 5.5 (b). We observe, that the stronger the secondary flow, the earlier and the stronger is this downward kink. The strongest kink forms in the LES and the weakest in the SSG RSM. For the SST model the downward kink is absent as no secondary flow is represented.

Figure 5.6 depicts the normalised Reynolds stress distributions along the duct midplane. We

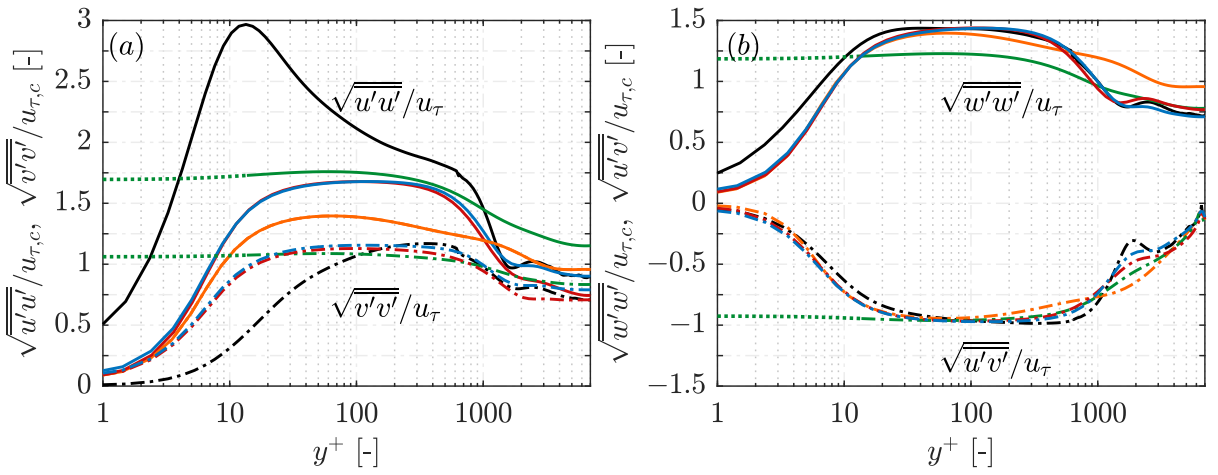

Figure 5.6: Reynolds stress distributions along the duct midplane $2z/L_z = 0$ in the adiabatic HARCD for the LES (——), the SST (——), the BSL EARSM (——), the BSL RSM (——) and the SSG RSM (——). The $\overline{u'u'}$- and $\overline{w'w'}$-terms are represented by solid, and the $\overline{v'v'}$- and $\overline{u'v'}$-terms by dash-dotted lines.

observe that the SSG RSM possesses the highest deviation from the LES profiles. Especially close to the wall the turbulence intensity is overestimated for all components due to not resolving the wall boundary layer as mentioned above. None of the RANS models is able to correctly predict the $\overline{u'u'}$-maximum in the vicinity of the lower wall underestimating the streamwise turbulence intensity significantly. The same observation has been made comparing RANS against DNS square duct results in section 5.2. For the $\overline{v'v'}$- as well as the $\overline{w'w'}$-profiles the BSL RSM and the BSL EARSM agree sufficiently well with the LES in the log-law region and the outer layer of the turbulent boundary layer, whereas the SST model overestimates the turbulence levels. Note that for the SST $\overline{u'u'}$-, $\overline{v'v'}$-profiles and $\overline{w'w'}$-profiles coincide in figure 5.6. As discussed in detail in sections 3.5.3 and 4.3.4, the Reynolds shear stress $\overline{u'v'}$ incorporates turbulent ejection and sweeping motions, the ejections from the wall being the dominant turbulent mechanism generating the secondary flow (Huser and Biringen, 1993). Figure 5.6 (b) shows an overall good agreement of the $\overline{u'v'}$-component for the SST, the BSL EARSM and the BSL RSM with the LES. The highest deviations from the LES are obtained for the SSG RSM, especially in the wall vicinity, and for the SST from $y^+ \approx 100$ onwards. The upward kink at $y+ \approx 2000$ is underestimated for all RANS models depending on the underprediction of the small vortex strength.

Table 5.3 lists the wall shear stresses and friction Reynolds numbers for the adiabatic periodic water HARCD simulations. For the SSG RSM the wall friction and the accompanying pressure loss is reduced for both the long and the short sidewall compared to the ω-based RANS models and the LES. This observation is attributed to the different wall treatment of the ε-based SSG RSM. The wall shear stresses for the BSL EARSM, the BSL RSM and the LES are similar. At the short sidewall $\tau_w|_y$ is slightly overestimated in the RANS, and at the long sidewall the LES value is between that of the BSL EARSM and the BSL RSM. Utilising the SST model $\tau_w|_y$ is significantly underestimated and reduced by -11.5% compared to the LES. We attribute this

	LES	SST	BSL EARSM	BSL RSM	SSG RSM
$\tau_w\|_{y=y_{min}}$ [Pa]	53.19	47.05	54.01	54.76	49.60
$\tau_w\|_{z=z_{min}}$ [Pa]	63.93	65.08	63.09	65.74	58.72
$Re_\tau\|_{y=y_{min}}$ [-]	4778	4493	4814	4847	4613
$Re_\tau\|_{z=z_{min}}$ [-]	5238	5284	5203	5311	5020

Table 5.3: Wall shear stresses and friction Reynolds numbers for the different adiabatic water HARCD simulations. The values represent an averaged value over the whole respective sidewall.

observation to the missing secondary flow influence on the wall shear stress distribution at the lower wall. The long sidewall is less affected by the vortex system and consequently $\tau_w|_z$ has a similar level as the other ω-based RANS models and the LES.

5.3.2 Straight Heated Duct Flow Field

In the following, we discuss the results for the heated water HARCD, concentrating on the location $x = 500$ mm close to the end of the straight section, but sufficiently far away from the curved section such that only the turbulence-induced secondary flow is present. The investigation is mainly focused on the differences in the temperature profiles, turbulent heat fluxes and integral heat transfer. Changes in the duct flow field are also addressed briefly. The results for the RANS closure models for Reynolds stresses and turbulent heat fluxes are compared to the water HARCD LES database of chapter 3.

In figure 5.7 the temperature increase ΔT within the lower duct quarter is depicted. The LES result in figure 5.7 (a) shows the typical bent shape of the temperature profile as a consequence of the mixing of hot and cold fluid by the corner vortices. The upward bent of the ΔT-profile in the centre is caused by the small vortices and those at the lateral adiabatic walls are caused by the respective large vortex. The RANS results show several deviations for the cross-sectional temperature field: the centre upward bent above the heated wall is only visible for the BSL RSM results in figures 5.7 (d, e, f), although it is significantly weaker than in the LES. The reason is the underestimation of the small vortex strength in the RANS. As discussed in the previous section 5.3.1, the small vortices in the LES are substantially stronger and extend further into the duct. The upward bent towards the lateral walls is predicted by all RANS models except for the SST in figure 5.7 (b), lacking the turbulence-induced secondary flow. For the SSG RSM this upward bent is weaker than for the BSL RSM and the BSL EARSM, compare figures 5.7 (g) with 5.7 (c, d). This is due to the underestimation of the large vortex strength in the SSG RSM, whereas for the BSL RSM and BSL EARSM the large vortex strength and location are in good agreement with the LES data. Focusing on how far the topmost 2.5 K-isoline penetrates into the duct core, we observe that the SSG RSM underestimates the overall heat transfer. This result is expected due to the overall underestimation of the secondary flow strength. Likewise, the overall temperature level for the SST is reduced compared to the similar BSL RSM and BSL EARSM, all with $Pr_t = 0.9$, due to the lack of any secondary flow. Relevant differences between the SSG RSM with $Pr_t = 0.9$ and utilising the anisotropic diffusion model are not visible, compare figures

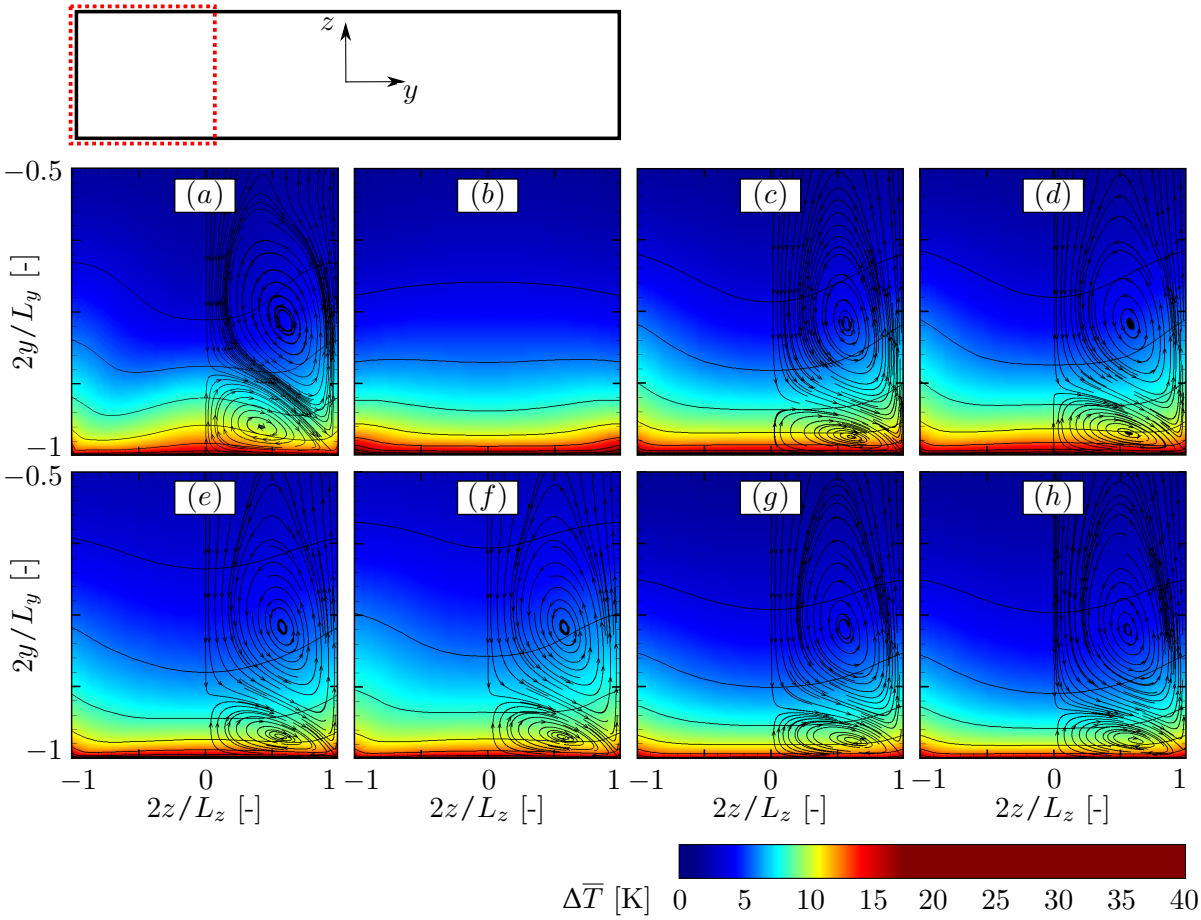

Figure 5.7: Temperature increase $\Delta\overline{T} = \overline{T} - T_b$ in the lower HARCD quarter at $x = 500$ mm for the (a) LES, (b) SST with $Pr_t = 0.9$, (c) BSL EARSM with $Pr_t = 0.9$, (d) BSL RSM with $Pr_t = 0.9$, (e) BSL RSM with the algebraic Younis model, (f) BSL RSM with additional PDEs for $\overline{u_i'h'}$, (g) SSG RSM with $Pr_t = 0.9$ and (h) SSG RSM with the anisotropic diffusion model. Isolines are drawn from 2.5 to 40 in steps of 2.5 K.

5.7 (g) and (h). Employing an anisotropic turbulent heat flux closure in combination with the BSL RSM, we see that the heat transfer into the duct rises from the solution with $Pr_t = 0.9$, over the algebraic Younis-model to the BSL RSM with additional PDEs for $\overline{u_i'h'}$ due to increased turbulent mixing. The result for the less complex Daly-Harlow model (not explicitly shown) lies in between the Younis- and the PDE-result. The deviations between the BSL RSM using $Pr_t = 0.85$ (not explicitly shown) instead of $Pr_t = 0.9$ are relatively small with the heat transfer being slightly lower for the latter.

The temperature line plots of figure 5.8 support the contour plots of figure 5.7. Figure 5.8 (a) depicts the duct midplane, which is dominated by the small vortices in the heated wall vicinity, and figure 5.8 (b) shows the region close to the lateral wall, which is dominated by the large vortex. In the duct midplane $2z/L_z = 0$ we observe for all RANS models noticeable deviations from the LES distribution, which is attributed to the significantly weaker secondary flow in

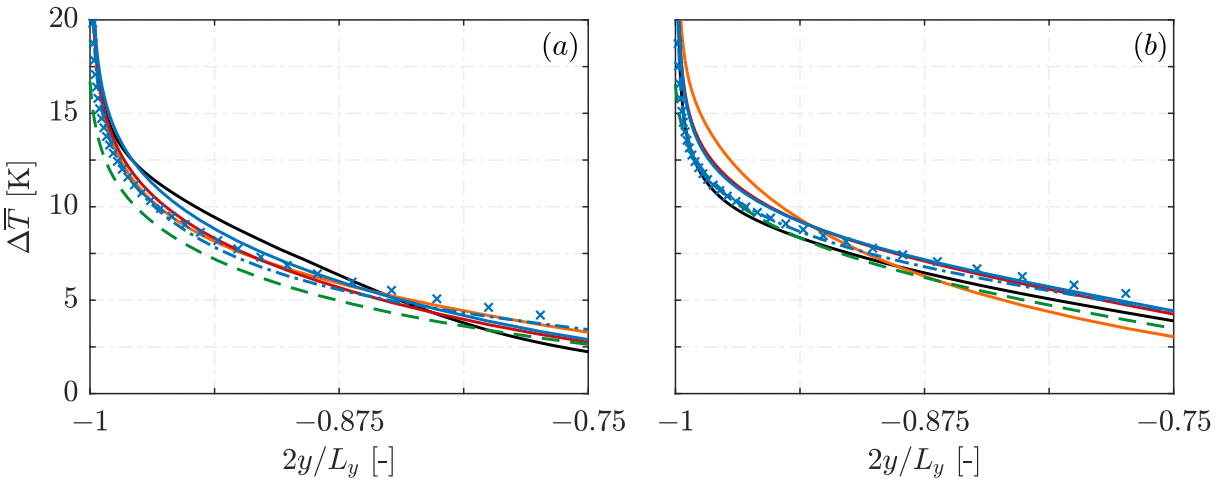

Figure 5.8: Temperature increase $\Delta\overline{T} = \overline{T} - T_b$ at (a) $2z/L_z = 0$ and at (b) $2z/L_z = 0.9$ in the HARCD at $x = 500$ mm for the LES (——), SST with $Pr_t = 0.9$ (——), BSL EARSM with $Pr_t = 0.9$ (——), BSL RSM with $Pr_t = 0.9$ (——), BSL RSM with Younis model (-·-·-), BSL RSM with additional PDEs for $\overline{u_i'h'}$ (×) and SSG RSM with $Pr_t = 0.9$ (——).

this area. Close to the lateral wall, the secondary flow strengths of LES and BSL RSM have a similar level, see section 5.3.1. Consequently, also the ΔT-profiles are in better agreement for the BSL RSM and BSL EARSM. The SST and the SSG RSM models exhibit significant deviations from the LES due to the lack and underestimation of secondary flow, respectively. The slope of the temperature profile towards the lower wall is improved significantly in comparison to the similar BSL RSM and BSL EARSM with $Pr_t = 0.9$ by employing the algebraic Younis model or the BSL RSM with additional PDEs. Overall, for the investigated location the best results are achieved using the BSL RSM in combination with the Younis model. Further away from the heated wall, the temperature increase is slightly overestimated, although less than with the BSL RSM/PDE-combination.

Figure 5.9 depicts the temperature boundary layer using dimensionless temperature profiles at the same spanwise locations as figure 5.8. Analogously to the velocity TBL profiles, the temperature is normalised by the friction temperature $T^+ = \Delta\overline{T}/T_\tau$. For the definition of the friction temperature as well as the empirical function of Kader (1981) the reader is referred to equation 4.8 in section 4.3.2. As value for Pr we utilise the wall Prandtl number of $Pr_w = 1.75$. Note that Kader's law is derived and valid for pure channel flows without secondary flow influence assuming a constant Pr and a constant $Pr_t = 0.85$. However, for the present case, secondary flow motion is present, the turbulent Prandtl number is non-constant and varies within the cross-section, and the molecular Prandtl number varies between $Pr_w = 1.75$ and $Pr_b = 3.0$. The LES follows Kader's law in the viscous sublayer, but shows a constant upward shift in the log-law region for figure 5.9 (a) with the profile slope fitting to that proposed by Kader's law. This is due to the mixing motion by the relatively strong small vortices, which are not present in a channel flow, and significantly weaker in the RANS. The vortices transport warm fluid along the heated wall into its centre leading to a local hot spot and the observed upward shift. In

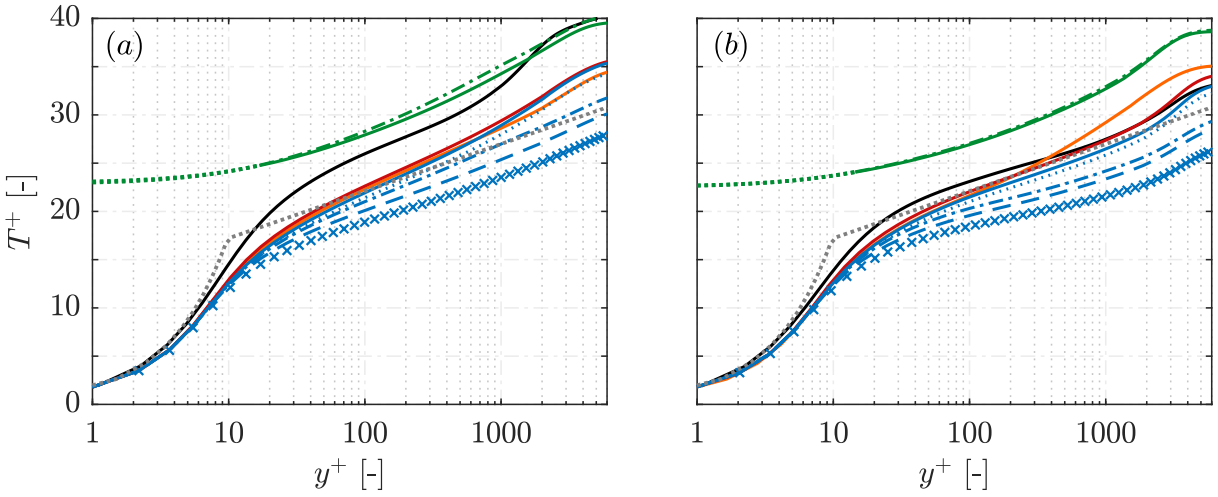

Figure 5.9: Dimensionless temperature profiles along (a) the duct midplane $2z/L_z = 0$ and at (b) $2z/L_z = 0.9$ in the HARCD at $x = 500$ mm for the LES (——), SST with $Pr_t = 0.9$ (——), BSL EARSM with $Pr_t = 0.9$ (——), BSL RSM with $Pr_t = 0.9$ (——), BSL RSM with $Pr_t = 0.85$ (·····), BSL RSM with Daly-Harlow model (- - - -), BSL RSM with Younis model (-·-·-), BSL RSM with additional PDEs for $\overline{u_i' h'}$ (×), SSG RSM with $Pr_t = 0.9$ (——), SSG RSM with the anisotropic diffusion model (-·-·-) and the empirical function of Kader (1981) (·····). Normalisation is performed with the local wall values at the respective spanwise location.

figure 5.9 (b) this upward shift almost vanishes due to a smaller secondary flow influence. As already observed for the momentum boundary layer, the SSG RSM does likewise not resolve the temperature boundary layer using the scalable wall function approach instead. The SST, BSL EARSM and BSL RSM, all with $Pr_t = 0.9$, behave very similar as for the momentum boundary layer, see figure 5.5 (a), as they underestimate T^+ within the viscous sublayer and possess a slightly higher slope in the log-law region. From the BSL RSM with $Pr_t = 0.9$ over $Pr_t = 0.85$ and the algebraic heat flux closure models to the BSL RSM/PDE-combination, we observe an increasing downward shift of the temperature profile from the onset of the logarithmic region. Also, the profile slope is reduced. This downward shift is accompanied by an increased global and local heat flux and consequently a higher T_τ. Hence, the deviation with respect to the LES increases. Comparing the LES and the various BSL RSM results in figure 5.9 (b) supports the notion that the heat flux is overestimated especially for the anisotropic heat flux closure models.

In figure 5.10, the turbulent heat fluxes for the various RANS turbulent heat flux closure models in combination with the BSL RSM are compared to the LES. As the $Pr_t = 0.85$ result is similar to the $Pr_t = 0.9$ result, only the latter is shown. For $Pr_t = 0.9$ the $\overline{u'T'}$-component is approximately zero at $x = 500$ mm due to the vanishing streamwise temperature gradient. The more complex heat flux closure models are able to predict a non-zero $\overline{u'T'}$-distribution. Similarly as the $\overline{u'u'}$-peak close to the heated wall, also the $\overline{u'T'}$-peak can not be reproduced by any RANS model, see the previous sections 5.2 and 5.3.1 for comparison. The more complex algebraic Younis model represents an improvement over the Daly-Harlow model as the $\overline{u'T'}$-deviation with respect

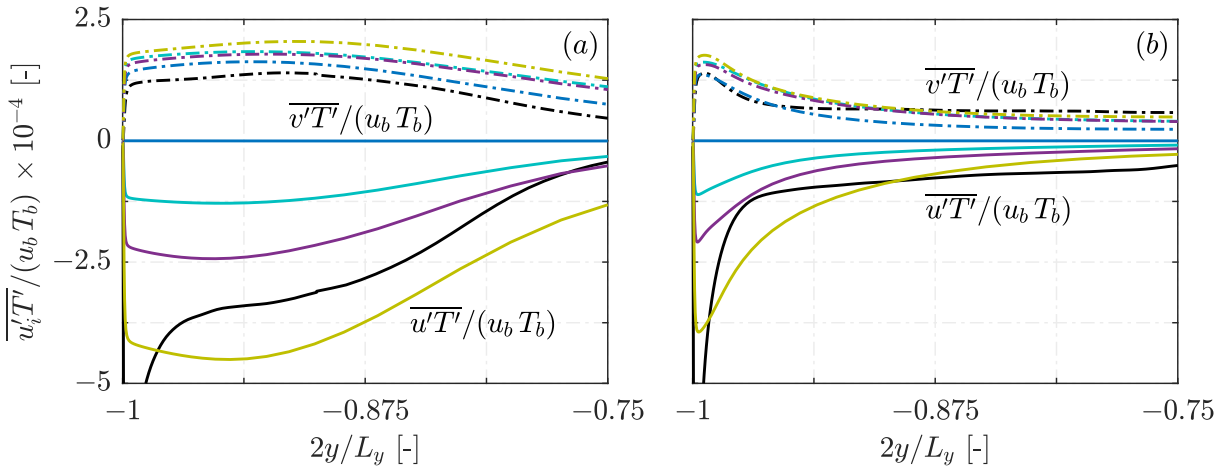

Figure 5.10: Turbulent heat fluxes $\overline{u_i'T'}$ at (a) $2z/L_z = 0$ and at (b) $2z/L_z = 0.9$ in the HARCD at $x = 500$ mm for the LES (——), BSL RSM with $Pr_t = 0.9$ (——), BSL RSM with Daly-Harlow model (——), BSL RSM with Younis model (——) and BSL RSM with additional PDEs for $\overline{u_i'h'}$ (——). $\overline{u'T'}$ is represented by solid and $\overline{v'T'}$ by dash-dotted lines.

	straight duct $0-500$ mm	curved duct	total configuration
LES	3.20		
SST, $Pr_t = 0.9$	3.28	0.58	4.45
BSL EARSM, $Pr_t = 0.9$	3.48	0.60	4.70
SSG RSM, $Pr_t = 0.9$	3.00	0.50	4.05
SSG RSM, anisotropic	2.96	0.49	4.00
BSL RSM, $Pr_t = 0.85$	3.69 (+2.8%)	0.62 (+1.6%)	4.97 (+2.5%)
BSL RSM, $Pr_t = 0.9$	3.59 (+0.0%)	0.61 (+0.0%)	4.85 (+0.0%)
BSL RSM, Daly-Harlow	4.07 (+13.4%)	0.66 (+8.2%)	5.47 (+12.8%)
BSL RSM, Younis	3.90 (+8.6%)	0.64 (+4.9%)	5.25 (+8.2%)
BSL RSM, PDE	4.35 (+21.2%)	0.70 (+14.8%)	5.84 (+20.4%)

Table 5.4: Integral heat fluxes $\dot{Q}$ for the different water HARCD simulations. For the BSL RSM simulations the differences with respect to the case $Pr_t = 0.9$ are included.

to the LES is reduced. Yet, both algebraic models underestimate the streamwise turbulent heat flux. Utilising additional PDEs for the turbulent heat fluxes, $\overline{u'T'}$ is overestimated in the midplane. Close to the lateral wall the conclusions are similar as for the midplane, although the deviations from the LES further away from the heated wall are significantly smaller. The heated wall-normal turbulent heat flux $\overline{v'T'}$ is overestimated by all employed RANS heat flux closure models giving a possible explanation for the higher overall heat transfer into the duct compared to the LES, see table 5.4. The $\overline{w'T'}$-distribution is not explicitly shown as it is zero in the midplane due to the symmetry. Close to the lateral wall it follows a similar trend as $\overline{v'T'}$, although at a lower magnitude.

	$\tau_w\|_{y=y_{min}}$ [Pa]	$\tau_w\|_{z=z_{min}}$ [Pa]	$Re_\tau\|_{y=y_{min}}$ [-]	$Re_\tau\|_{z=z_{min}}$ [-]
LES	45.74 (−14.0%)	64.57 (+1.0%)	7205 (+50.8%)	5264 (+0.5%)
SST, $Pr_t = 0.9$	43.71 (−7.1%)	64.83 (−0.4%)	7043 (+56.8%)	5274 (−0.2%)
BSL EARSM, $Pr_t = 0.9$	49.69 (−8.0%)	62.87 (−0.3%)	7510 (+56.0%)	5194 (−0.2%)
SSG RSM, $Pr_t = 0.9$	47.83 (−3.6%)	58.60 (−0.2%)	7368 (+59.7%)	5015 (−0.1%)
SSG RSM, anisotropic	47.79 (−3.6%)	58.60 (−0.2%)	7365 (+59.6%)	5015 (−0.1%)
BSL RSM, $Pr_t = 0.85$	51.00 (−6.9%)	65.45 (−0.4%)	7608 (+56.9%)	5299 (−0.2%)
BSL RSM, $Pr_t = 0.9$	50.96 (−6.9%)	65.44 (−0.5%)	7605 (+56.9%)	5299 (−0.2%)
BSL RSM, Daly-Harlow	51.06 (−6.8%)	65.43 (−0.5%)	7612 (+57.0%)	5298 (−0.2%)
BSL RSM, Younis	51.03 (−6.8%)	65.43 (−0.5%)	7610 (+57.0%)	5299 (−0.2%)
BSL RSM, PDE	51.13 (−6.6%)	65.42 (−0.5%)	7618 (+57.2%)	5298 (−0.2%)

Table 5.5: Wall shear stresses and friction Reynolds numbers at $x = 500$ mm for the water HARCD simulations, and relative change with respect to the adiabatic case. The values are averaged over the whole respective side wall.

The integral heat fluxes in the left column of table 5.4 support the observations made based on the temperature distributions within the current section: The SSG RSM with $Pr_t = 0.9$ as well as with the usage of the anisotropic diffusion model both underestimate the heat transfer, even though turbulence-induced secondary flow can be represented. This deviation is attributed to the wall treatment of the ε-based model, employing the scalable wall function approach and not resolving the turbulent boundary layer. The SST simulation gives a slightly higher integral heat flux than the LES. This result is unexpected due to the absence of turbulence-induced secondary flow and consequently a weaker mixing of hot and cold fluid. When turbulence-induced secondary flow is present, as in the BSL EARSM result, the mixing and with it the overall heat transfer is augmented with respect to the SST. With the higher secondary flow strength in the BSL RSM result with $Pr_t = 0.9$ the integral heat flux grows further. Modifying $Pr_t = 0.9$ to $Pr_t = 0.85$ further increases the integral heat flux as well as utilising more sophisticated turbulent heat flux closure models, from the Younis over the Daly-Harlow model to the BSL RSM/PDE combination. The latter predicts the strongest heat transfer being over 20% higher than that of the standard BSL RSM with $Pr_t = 0.9$. Hence, compared to the LES a significant overestimation of the turbulent heat flux is observed. Note, however, that modelling $\overline{u_i' h'}$ with additional PDEs is still a beta feature within ANSYS CFX. In table 5.4 the values for the curved section and the total configuration are added for completeness, for a discussion of the curved section results of the water HARCD the reader is referred to Kaller et al. (2020). Analogous to the heat transfer, also the wall shear stresses of the BSL EARSM and BSL RSM model combinations are overestimated in the RANS, see table 5.5. This result meets the expectation as the Reynolds analogy proposes the proportionality $\dot{Q}_w \propto \tau_w$.

The heating and associated viscosity reduction towards the lower wall leads to a weakening of the turbulent fluctuations, reduced wall shear stresses and a reduction of the secondary flow strength along the water HARCD, for a detailed discussion see the result section of chapter

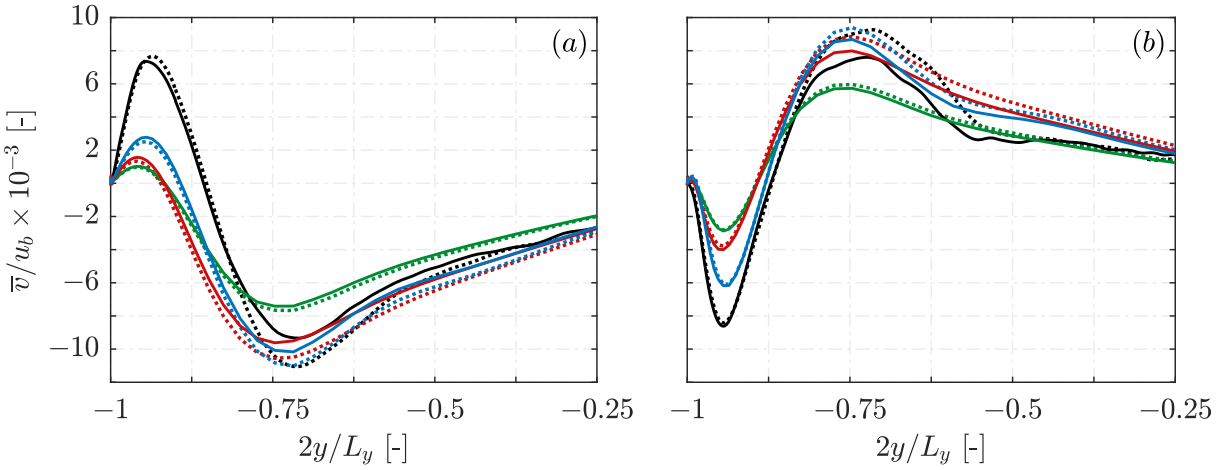

Figure 5.11: Secondary flow distribution at (a) $2z/L_z = 0$ and at (b) $2z/L_z = 0.75$ in the HARCD at $x = 500$ mm for the LES (——), the BSL EARSM with $Pr_t = 0.9$ (——), the BSL RSM with $Pr_t = 0.9$ (——) and the SSG RSM with $Pr_t = 0.9$ (——). The respective adiabatic HARCD results are represented by dotted lines.

3. Figure 5.11 (a) shows the reduction of the secondary flow strength in the midplane using exemplarily the $\overline{v}$-component. For the LES, we observe the expected shift of the small vortex towards the heated wall and a slight reduction of its strength. The $\overline{v}$-minimum of the large vortex is reduced noticeably and its position remains approximately constant. The RANS results show similar tendencies for the large vortex, although the secondary flow strength reduction is weaker. Surprisingly, the small vortex strength increases in the duct midplane. At the off-centre location similar tendencies are visible for the large vortex and the small vortex strength increases slightly for all considered simulations. Comparing the wall shear stresses in table 5.5, we observe a significantly stronger drop in the LES (-14%) as in the ω-based RANS models ($\approx -7\%$), further increasing the deviation from the LES. Likewise the deviation in $Re_\tau|_{y=y_{min}}$ increases further. The lateral wall shear stress is only slightly affected by the heating as an average value over the whole sidewall is considered.

5.3.3 Curved Heated Duct Flow Field

The focus of the current section is the investigation of the secondary flow development in the curved HARCD section, which is characterised by the interaction of turbulence- and curvature-induced secondary flow, and the associated heat transfer for the different RANS models. For this purpose the CATUM LES results for the air HARCD configurations serve as a reference database, see chapter 4 for the set-ups and a detailed result discussion. The turbulent heat flux modelling within this section is based on the constant turbulent Prandtl number assumption with $Pr_t = 0.9$ for all RANS models. For the curved section results of the water HARCD configuration including a variation of the turbulent heat flux modelling the reader is referred to Kaller et al. (2020), although without LES data comparison.

The secondary flow and temperature fields are exemplarily analysed for the highest curvature

case RC60 at the beginning of the curved section at a position of 7.5° and in the middle at 45° in figures 5.12 and 5.14. For the latter a detailed view of the near-wall vortex system is given in figure 5.15. Figure 5.16 then presents the distributions in the end section of the lowest curvature case RC900. For all analysed slices a streamwise averaging of the flow field is performed over ±2.5° with respect to the slice position for RC60 and correspondingly ±0.165° for RC900. For case RC60 the Dean vortices are dominating the secondary flow field, whereas for RC900 curvature- and turbulence-induced secondary flow are of comparable strength. Consequently, for RC900 the specific choice of turbulence model has an overall stronger impact as for RC60.

In figure 5.12 the Dean vortex system is starting to emerge. The overall secondary flow field is similar for all simulations and the vortex core close to the outer radius wall lies approximately at the same y-position except for the SST result, where an upward shift towards the outer radius wall is observable. This shift is due to the absence of turbulence-induced secondary flow in the SST result, having formed upstream of the curved section for the other RANS models. For the SSG RSM, a slight shift of the vortex core towards the duct midplane is noticeable. Furthermore, all RANS models show an underestimation of the secondary flow strength along the lateral sidewalls compared to the LES. The lowest values are obtained for the SSG RSM model, whereas the remaining ω-based RANS models reach similar $\overline{u}_{cf}$ levels. The temperature distribution in the right column of figure 5.12 is mainly a result of the upstream straight duct heat transfer and only slightly affected by the yet developing Dean vortex system. The results follow tendentially those observed for the straight water HARCD in the previous section with the notable exception, that the heat transfer in the air HARCD LES surpasses that of the RANS, see also table 5.6 for a comparison of the integral heat flux values. As depicted in figure 5.13, the deviating heat transfer behaviour of air and water HARCD can be attributed to an underestimation of the wall-normal turbulent heat flux along the straight duct section by the RANS models. The opposite tendency has been observed for the water HARCD in the previous section 5.3.2 with a negative viscosity gradient towards the wall instead of a positive one as for the air HARCD. Furthermore, comparing the LES in figure 5.12 (b) with the RANS results shows that the higher secondary flow strength in the LES, i.e. the enhanced mixing, leads to a deeper penetration of the $\overline{T}$-isolines towards the duct core. The weaker mixing of the ω-based RANS models results in a thickened high-temperature layer close to the heated wall in comparison to the LES, whereas the SSG RSM has a very narrow temperature boundary layer due to a heat transfer underestimation. For the SST model, the absence of turbulence-induced secondary flow upstream of the curved section becomes apparent by the strong downwards bending of the temperature isolines in the vicinity of the lateral sidewalls. For all other models the downwards oriented curvature-induced secondary flow up to position 7.5° has neutralised the upwards bending effect of the corner vortex system in the vicinity of the lateral sidewalls.

The Dean vortex system is fully established in the middle of the curved section at an angular position of 45°, see figures 5.14 and 5.15. The deviation of $\overline{u}_{cf}$ levels between LES and RANS results has further increased, especially visible in the duct midplane and along the sidewall boundary layers. However, until the end section at 87.5° (not shown), the midplane deviation vanishes and a similar Dean vortex strength is reached. The deviation of secondary flow development can be partially attributed to the coarser streamwise resolution of the RANS and partially on the different turbulence models employed. Between the various RANS results also

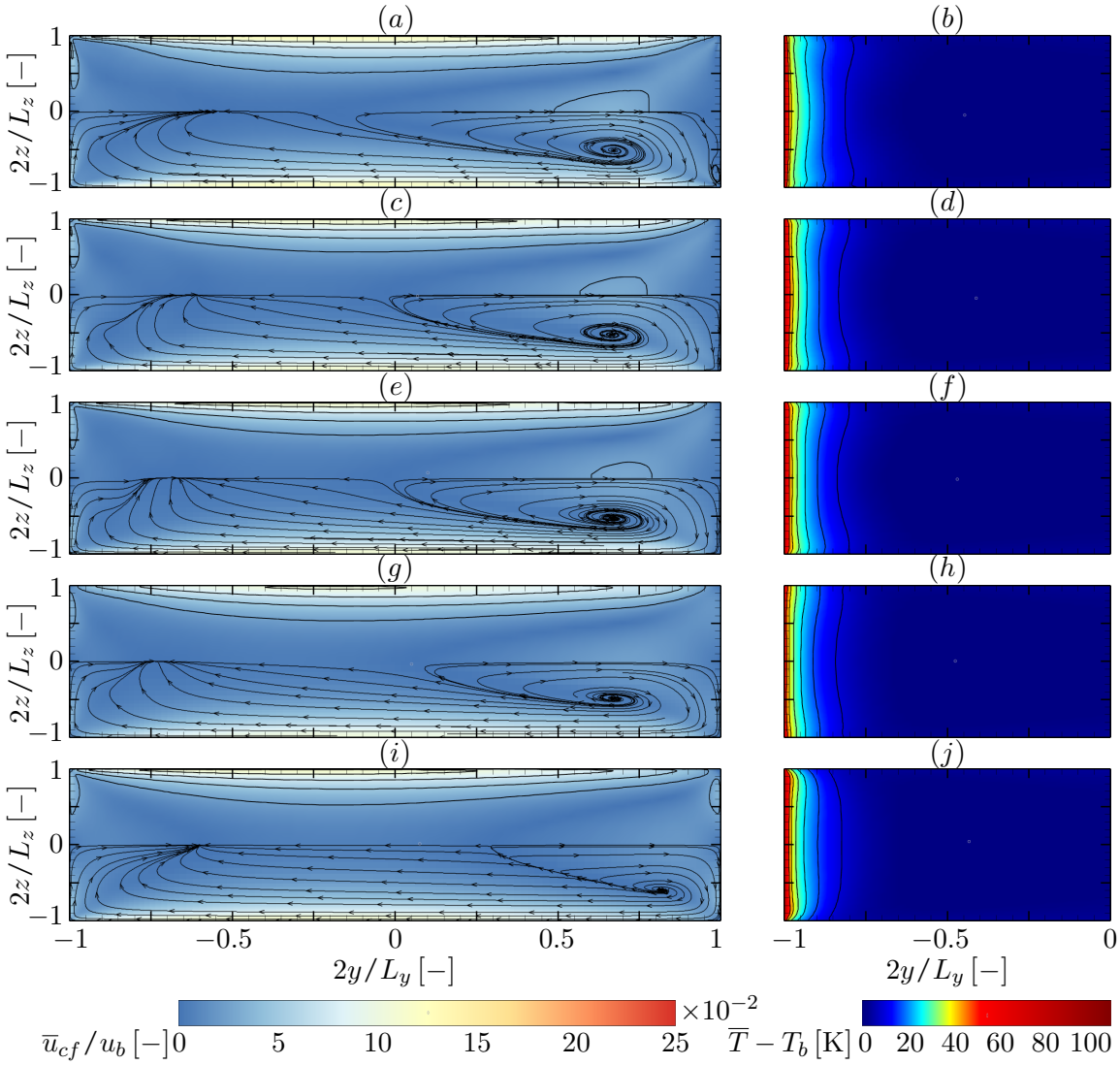

Figure 5.12: Cross-sectional secondary flow field $\overline{u}_{cf} = \sqrt{\overline{v}^2 + \overline{w}^2}$ (left column) and temperature increase $\Delta\overline{T} = \overline{T} - T_b$ (right column) for case RC60 in the curved section at a position of 7.5°: (a, b) CATUM LES results and RANS results for the (c, d) BSL RSM, (e, f) BSL EARSM, (g, h) SSG RSM and (i, j) SST turbulence model. The turbulent Prandtl number is set to $Pr_t = 0.9$. Isolines are drawn from 0 to $25 \cdot 10^{-2}$ in steps of $25 \cdot 10^{-3}$ for $\overline{u}_{cf}$ and from 7.5 K to 45 K in steps of 7.5 K for $\Delta\overline{T}$, and streamlines are added for flow visualisation.

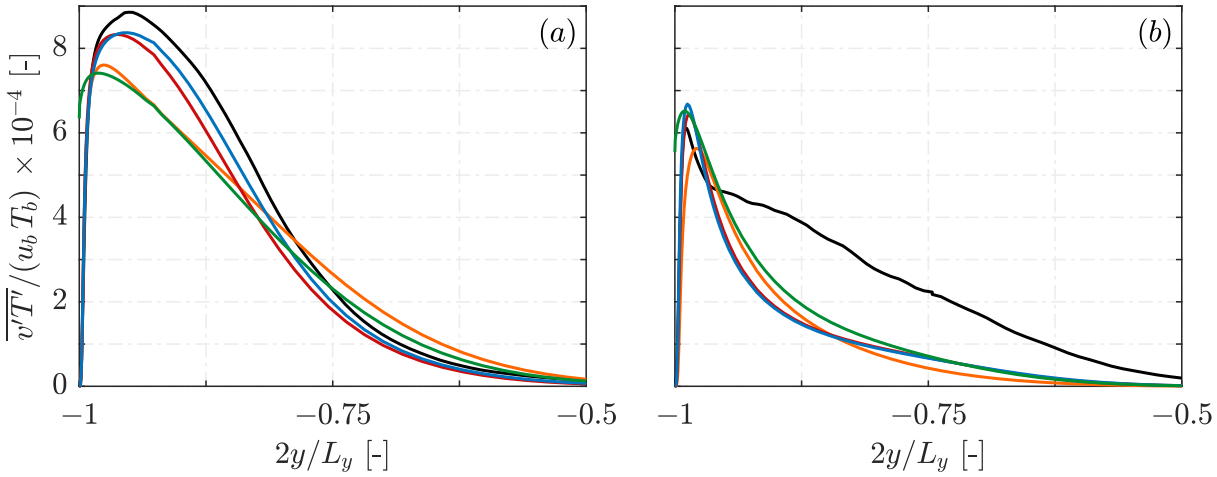

Figure 5.13: Wall-normal turbulent heat flux $\overline{v'T'}$ at (a) $2z/L_z = 0$ and at (b) $2z/L_z = 0.9$ in the straight section of the air HARCD at $x = 150$ mm for the LES (——), SST (——), BSL EARSM (——), BSL RSM (——) and SSG RSM (——). The turbulent Prandtl number for all RANS models is $Pr_t = 0.9$.

differences in the $\overline{u}_{cf}$ distributions are noticeable with higher midplane levels reached by the BSL and SSG RSM, and lower sidewall levels by the SSG RSM compared to the ω-based models. Furthermore, variations of the Dean vortex core position are present, with the SST position coinciding with that of the LES. The BSL RSM and SSG RSM Dean vortex cores are slightly shifted towards the inner radius wall and that of the BSL EARSM further. The small ICW Dean vortex forming above the inner radius wall centre is strongest pronounced in the LES, see the upper row of figure 5.15 for a detailed view. For both the BSL RSM and the SST the ICW Dean vortex is flattened with an increased spanwise extent, whereas for the BSL EARSM its spanwise extent is diminished noticeably. For the SSG RSM, the ICW Dean vortex is absent. Likewise, the small vortices in the inner and outer radius wall corners can not be represented by the SSG RSM. This deficiency is attributed to the usage of the scalable wall function approach as for all ω-based RANS models the corner vortices are present. As the LES results in figures 5.15 (a, f) show, only that vortex of each turbulence-induced corner vortex pair remains, which has an opposite sense of rotation than the respective Dean vortex. Consequently, in figure 5.15 (f), the corner vortex is adjacent to the upper short sidewall, whereas at the lower wall it is adjacent to the lateral sidewall, see figure 5.15 (a). For the ω-based RANS models, the corner vortices are significantly weaker than in the LES and consequently further restricted into the duct corner region. Nevertheless, for the BSL RSM and BSL EARSM the corner vortices remain oriented adjacent to the upper wall at the outer radius wall and to the lateral sidewall at the inner radius wall causing a disturbance of the Dean vortex isolines, see especially figures 5.15 (g, h). The weaker turbulence-induced vortex structures in the RANS compared to the LES is in accordance with the observations described for the straight water HARCD of the previous section 5.3.2. As with utilising the SST model, turbulence-induced secondary flow can not be represented, weaker and smaller corner vortices are forming in the wake regions of the Dean vortices. These are

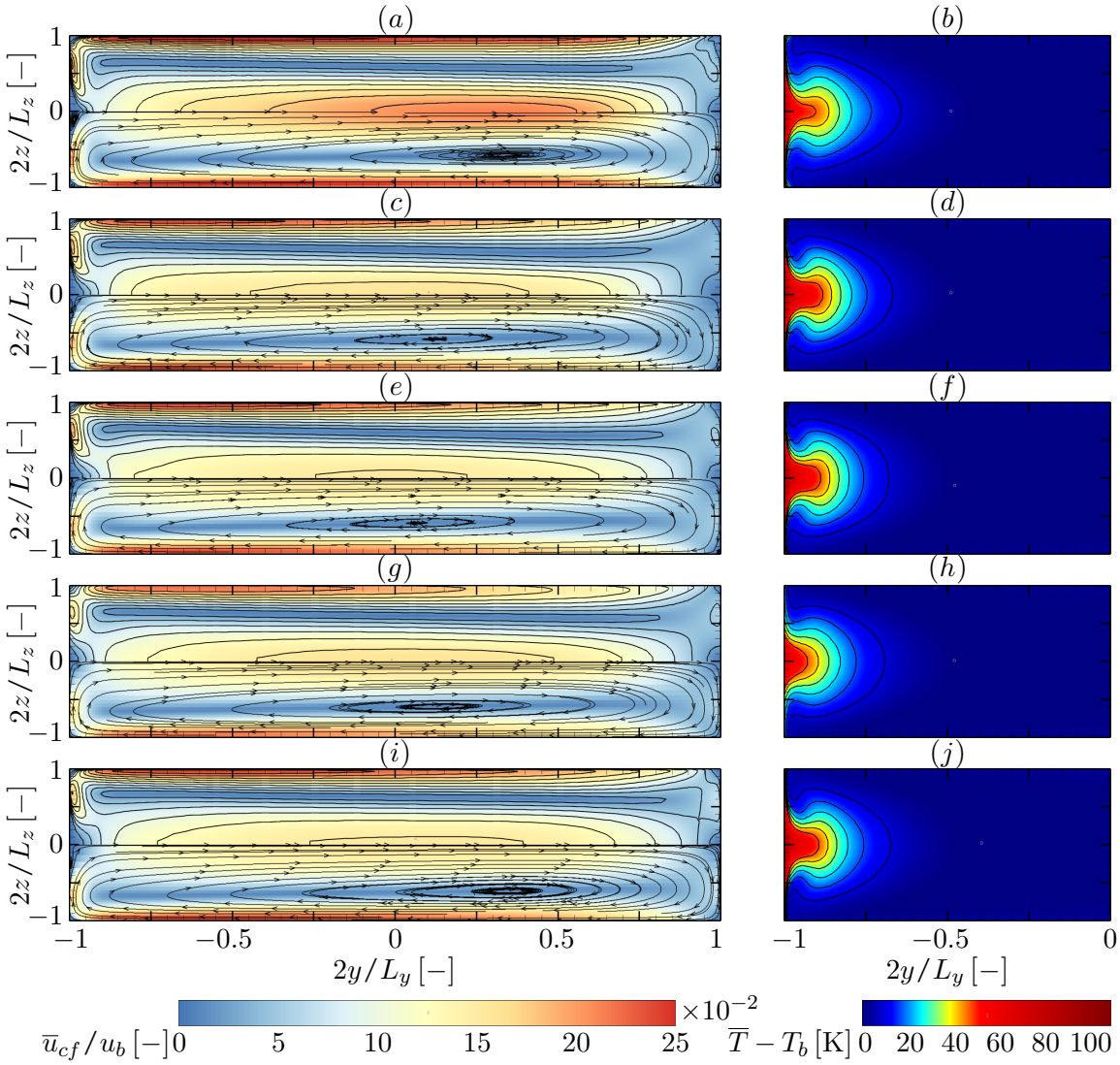

Figure 5.14: Cross-sectional secondary flow field $\overline{u}_{cf} = \sqrt{\overline{v}^2 + \overline{w}^2}$ (left column) and temperature increase $\Delta\overline{T} = \overline{T} - T_b$ (right column) for case RC60 in the curved section at a position of 45°: (a, b) CATUM LES results and RANS results for the (c, d) BSL RSM, (e, f) BSL EARSM, (g, h) SSG RSM and (i, j) SST turbulence model. The turbulent Prandtl number is set to $Pr_t = 0.9$. Isolines are drawn from 0 to $25 \cdot 10^{-2}$ in steps of $25 \cdot 10^{-3}$ for $\overline{u}_{cf}$ and from 7.5 K to 45 K in steps of 7.5 K for $\Delta\overline{T}$, and streamlines are added for flow visualisation.

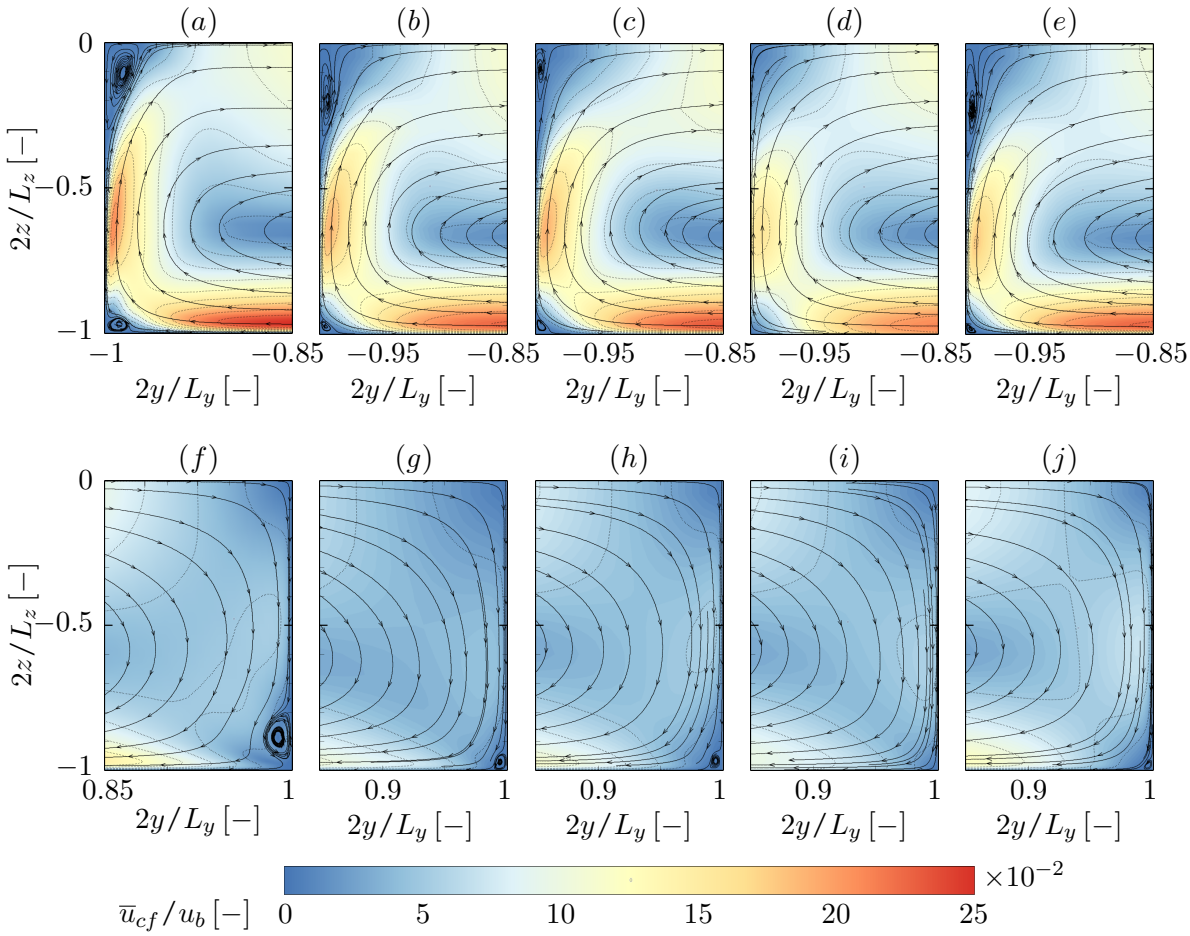

Figure 5.15: Cross-sectional secondary flow field $\overline{u}_{cf} = \sqrt{\overline{v}^2 + \overline{w}^2}$ for case RC60 in the curved section at a position of 45° in the inner radius wall (upper row) and outer radius wall vicinity (lower row): (a, f) CATUM LES results and RANS results for the (b, g) BSL RSM, (c, h) BSL EARSM, (d, i) SSG RSM and (e, j) SST turbulence model. Streamlines (solid lines) are added for visualisation and isolines (dotted lines) are drawn from 0 to $25 \cdot 10^{-2}$ in steps of $25 \cdot 10^{-3}$.

symmetrically located in the duct corners and are unable to disturb the Dean vortex isolines. All temperature distributions at 45° depict the mushroom-shaped profile, see the right column of figure 5.14. For the ω-based RANS models, the thickened high-temperature region discussed for position 7.5° leads further downstream at 45° to an enlarged region of high-temperature fluid above the heated wall centre, whereas in the LES the stronger secondary flow mixing effects a better equalisation of temperature differences. No noticeable difference can be made out between the SST, BSL EARSM and BSL RSM models. For the SSG RSM results, the weaker heat transfer again is associated with a reduced high-temperature region and weaker penetration of the $\overline{T}$-isolines towards the duct core.

In the end section of the lowest curvature case RC900, the interaction of the comparably strong turbulence- and curvature-induced secondary flow determines the HARCD flow field. Hence, the differences between the investigated models are more pronounced than for case RC60 due to

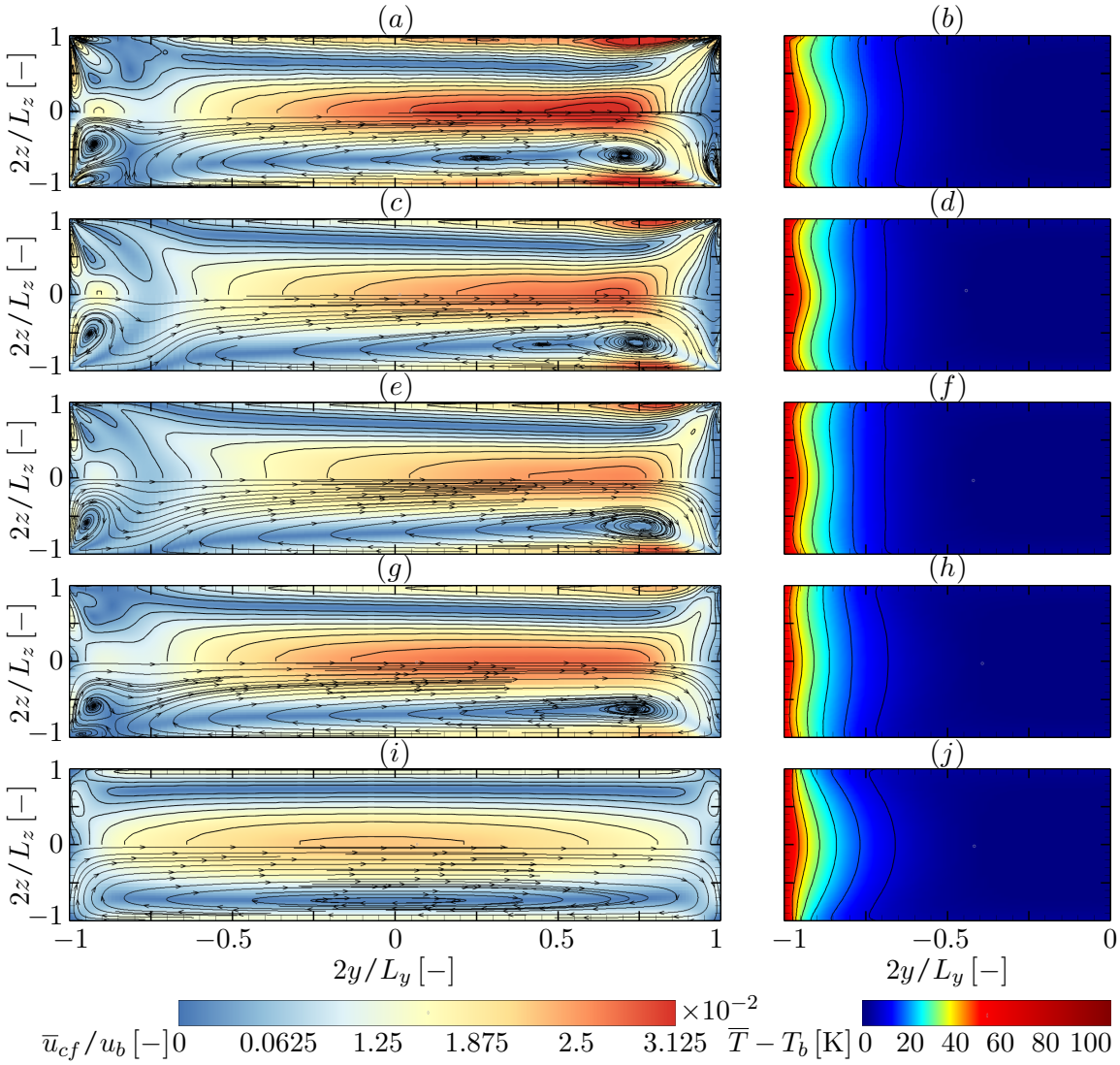

Figure 5.16: Cross-sectional secondary flow field $\overline{u}_{cf} = \sqrt{\overline{v}^2 + \overline{w}^2}$ (left column) and temperature increase $\Delta\overline{T} = \overline{T} - T_b$ (right column) for case RC900 in the curved duct end section at 8.75°: (a, b) CATUM LES results and RANS results for the (c, d) BSL RSM, (e, f) BSL EARSM, (g, h) SSG RSM and (i, j) SST turbulence model. The turbulent Prandtl number is set to $Pr_t = 0.9$. Isolines are drawn from 0 to $3.125 \cdot 10^{-2}$ in steps of $3.125 \cdot 10^{-3}$ for $\overline{u}_{cf}$ and from 7.5 K to 45 K in steps of 7.5 K for $\Delta\overline{T}$, and streamlines are added for flow visualisation.

the varying ability to correctly represent Prandtl's flow of the second kind. The most distinct deviation is observed for the SST model as the secondary flow field only consists of the Dean vortex structure, the corner vortex system being not representable. Also for the remaining RANS models significant deviations with respect to the LES are visible: the turbulence-induced vortex adjacent to the upper wall can not be correctly represented, and at the inner radius wall only the SSG RSM predicts the turbulence-induced vortex adjacent to the lateral sidewall, although noticeably weaker than in the LES. The remaining inner radius wall vortex is represented, but underestimated for both RSM models and the BSL EARSM. As seen before, the $\overline{u}_{cf}$ levels are significantly higher for the LES in the complete cross-section, i.e. both at the outer radius wall with the dominant Dean vortex and at the inner radius wall with the strengthened turbulence-induced vortex pair. The BSL RSM result reaches the highest cross-flow velocity levels for the investigated RANS models. In the temperature distributions the penetration of the $\overline{T}$-isolines towards the core and the thickness of the high-temperature region in the lower wall vicinity again illustrate the stronger mixing and higher heat transfer of the LES compared to the ω-based RANS models as well as the heat transfer underestimation in the SSG RSM results. The variations in the secondary flow field effect variations in the $\overline{T}$-field. For the SST, the sole presence of Dean vortices without the corner vortex system leads to a central upwards bulging of the temperature profile, whereas for the remaining models a corrugated profile is obtained. The magnitude of the $\overline{T}$-isoline waves strongly depends on the strength of the inner radius wall corner vortex pair. Consequently, the wavy structure of the temperature profile is most pronounced in the LES followed by the BSL RSM, and then by the BSL EARSM and the SSG RSM.

Table 5.6 lists the integral pressure loss and heat flux for the various simulations divided into the straight section share and the complete configuration value. Note, the comparability between the configurations is somewhat restricted as the mean streamwise curved section length of RC900 is elongated by 50% compared to RC180 and RC60. Furthermore, the heated surface area of RC60 is set-up-related slightly shorter than that of RC180. The straight section results comprise the complete straight section, i.e. deviations between the configurations are mainly due to the different upstream effect of the curved section causing an additional downward secondary flow in the rear part of the straight section, see section 4.3.1 for a detailed discussion. The integral pressure losses of the RANS simulations agree well with those of the LES with deviations of $\approx \pm 10\%$. Counterintuitively, the SST model without turbulence-induced secondary flow shows the closest coincidence with the LES. For the BSL EARSM, a pressure loss overestimation is present, which further increases for the BSL RSM, whereas for the SSG RSM a noticeable pressure loss underestimation is observed. With exception of the SST model, the $\Delta\overline{p}$ results are in good agreement with the wall shear stress deviations presented in section 5.3.1 for the water HARCD. The integral heat flux is underestimated by all RANS models compared to the LES. The smallest values, i.e. the highest deviation from the LES, are obtained employing the SSG RSM, which is attributed to the specific wall-treatment of the ε-based model. The SST model achieves the lowest heat transfer level of the ω-based models. With increasing turbulence-induced secondary flow strength the heat transfer is expectedly augmented over the BSL EARSM to the BSL RSM. The BSL RSM shows the overall best agreement with the LES, with a heat flux underestimation of only $\approx 4.1\%$ in the straight section. Hence, compared to the previous straight water HARCD configuration, the heat transfer deviation of the BSL RSM with $Pr_t = 0.9$ is reduced from

	$\Delta\overline{p}_{straight}$ [Pa]	$\Delta\overline{p}_{total}$ [Pa]	$\dot{Q}_{straight}$ [W]	$\dot{Q}_{total}$ [W]
RC60				
LES	1778	2804	31.40	43.13
SST	1795 (+ 1.0%)	2858 (+ 1.9%)	27.88 (−11.2%)	39.46 (− 8.5%)
BSL EARSM	1832 (+ 3.0%)	2911 (+ 3.8%)	30.08 (− 4.2%)	42.30 (− 1.9%)
SSG RSM	1630 (− 8.3%)	2570 (− 8.4%)	27.38 (−12.8%)	37.89 (−12.2%)
BSL RSM	1902 (+ 7.0%)	3024 (+ 7.9%)	30.47 (− 3.0%)	42.70 (− 1.0%)
RC180				
LES	1755	2609	31.37	41.48
SST	1739 (− 0.9%)	2536 (− 2.8%)	27.71 (−11.7%)	37.59 (− 9.4%)
BSL EARSM	1799 (+ 2.5%)	2625 (+ 0.6%)	29.92 (− 4.6%)	40.06 (− 3.4%)
SSG RSM	1597 (− 9.0%)	2321 (−11.0%)	27.27 (−13.1%)	36.48 (−12.1%)
BSL RSM	1869 (+ 6.5%)	2723 (+ 4.4%)	30.30 (− 3.4%)	40.62 (− 2.1%)
RC900				
LES	1746	2901	31.37	47.20
SST	1729 (− 1.0%)	2893 (− 0.3%)	27.49 (−12.4%)	41.61 (−11.8%)
BSL EARSM	1775 (+ 1.7%)	2955 (+ 1.9%)	29.68 (− 5.4%)	44.76 (− 5.2%)
SSG RSM	1578 (− 9.6%)	2620 (− 9.7%)	27.04 (−13.8%)	41.28 (−12.5%)
BSL RSM	1844 (+ 5.6%)	3069 (+ 5.8%)	30.07 (− 4.1%)	45.40 (− 3.8%)

Table 5.6: Pressure loss $\Delta\overline{p}$ and integral heat fluxes $\dot{Q}$ for the different air HARCD simulations. The included differences are based on the LES as reference. For all RANS models Pr_t is set constant to 0.9.

$\approx +12.2\%$ to $\approx -4.1\%$. As previously discussed, the inverse trend of underestimating the air HARCD heat transfer by the various RANS results instead of overestimating it, can be attributed to the inverse behaviour of the turbulent heat flux distributions, see figure 5.13. With increasing influence of curvature-induced compared to turbulence-induced secondary flow, the heat flux deviations between RANS and LES decrease as the secondary flow mixing of hot and cold fluid becomes more similar. Exemplary for case RC60, the heat flux deviation between BSL RSM and LES for the complete configuration reduces to merely $\approx 1\%$, whereas for the medium curvature case RC180 the same value is $\approx 2.1\%$ and for the lowest curvature case RC900 $\approx 3.8\%$.

6 Concluding Remarks

The conclusion summarises the results of this thesis, consisting of three parts based on the main chapters, and presents possible directions for future research in an outlook section.

6.1 Summary

We have performed well-resolved LES and RANS of straight and curved high aspect ratio cooling duct configurations with asymmetric wall heating at a moderate temperature difference. The first straight HARCD set-up using liquid water at a bulk Reynolds number of $Re_b = 110 \cdot 10^3$ and $T_w - T_b = 40\,\mathrm{K}$ was derived in close cooperation with Rochlitz et al. (2015) providing experimental PIV and PTV comparison data. The second HARCD set-up using air at $Re_b = 40 \cdot 10^3$ and $T_w - T_b = 105\,\mathrm{K}$ is based upon the first one with a shortened straight section and an additional curved end section of varying curvature radius. The main focus has been put on the investigation of the interaction of turbulence-induced secondary flow and turbulent heat transfer as well as on the interaction with additional curvature-induced secondary flow. The LES results may serve as a high-quality database for the development and improvement of RANS turbulence models and wall-modelled LES for duct flows at higher Reynolds number. Analogous to the thesis itself, the summary is split based on the three main chapters into the discussion of (I) straight water HARCD LES results, (II) curved air HARCD results and (III) prediction capabilities of RANS simulations for the investigated configurations.

The straight water HARCD LES results have been presented in chapter 3. The comparison of LES and experimental PIV/PTV results has shown an overall good agreement of velocity and turbulence profiles. In a 2^{nd} measurement campaign with a modified set-up, revised partly based on findings of the LES, the congruence was further improved. The high quality of the well-resolved LES database is further substantiated by a comparison against DNS data for an unheated square duct case at comparable resolution as the HARCD simulation. Based on the numerical results, we analysed the turbulence-induced secondary flow and its impact on flow evolution and especially on the developing temperature boundary layer. Due to the high aspect ratio the system of counter-rotating vortex pairs forming symmetrically in each duct quadrant is made up of a small vortex adjacent to the short wall (at the lower side heated) and a large vortex adjacent to the lateral wall. The corner vortex system is relatively weak with a maximum cross-flow velocity of $\approx 2\%$ of the bulk flow velocity. Nevertheless, a noticeable effect on cross-sectional streamwise velocity and temperature distributions has been visible. The temperature rise is accompanied by a viscosity reduction towards the heated wall, which may drop by up to $\approx 38\%$ directly at the wall. Despite the overall relatively moderate viscosity modulation restricted to the heated wall vicinity, a significant continuous secondary flow weakening along the duct has been reported.

Further heating-induced changes between adiabatic and heated duct flow field were analysed.

A significant increase of Re_τ by up to 50.4% in the heated wall centre and correspondingly decrease of the viscous length scale l_ν^+ by up to −39.1% was noted. Accordingly, the TBL profiles of the heated section showed a constant upward shift of the normalised velocity profile u^+ in the log-law region as well as a decrease of all Reynolds stress components compared to the adiabatic section due to the stabilising effect of reduced viscosity on the boundary layer. Employing the Reynolds quadrant analysis, the decomposition of the $\overline{u'v'}$-term in the vicinity of the heated wall revealed that turbulent sweeps and ejections are becoming weaker in size and intensity when heating is applied. Investigating turbulence anisotropy, a profile qualitatively similar to that of a turbulent channel or boundary layer flow has been obtained in the duct midplane, and a temperature-induced anisotropy reduction has been observed in the vicinity of the heated wall. We found this decrease to be stronger towards the duct corner than in the midplane. Both the reduced turbulent ejections and turbulence anisotropy effect a weaker source of streamwise vorticity production and lead in consequence to a weakening of Prandtl's flow of the second kind.

The secondary flow modulation has been further investigated discussing the heating-induced changes of mean streamwise vorticity and the terms of its balance equation. Analogous to the square duct cases of Pirozzoli et al. (2018), the vorticity dynamics in the HARCD corner region are dominated by a balance of turbulence and viscous terms, the former acting as source and the latter as sink term. When heating is applied, the corner vortex pair weakens and accordingly the vorticity decreases asymmetrically with the large vortex being weakened more significantly than the small one. All $\overline{\omega}_x$ balance equation terms intensify and their peak regions are shifted towards the duct corner. It has been shown that the asymmetric modulation of corner turbulence and viscous terms in the influence regions of large and the small vortex are in accordance with the asymmetric change of vortex strength.

Utilising autocorrelation functions allowed for analysing the turbulent length scales, showing on the one hand the sufficient streamwise extent of the periodic adiabatic duct section and on the other hand the heating-induced shortening of turbulent scales. It has been noted that longitudinal length scales of streamwise velocity drop by up to −10.2% adjacent to the heated wall and spanwise length scales of streamwise velocity by up to −31% in the duct corner region. Furthermore, we observed that the length scale shortening is not a mere function of local viscosity drop, but depends on the probing location due to the heating-induced secondary flow modulation.

The heat transfer into the cooling duct is significantly influenced by the turbulence-induced secondary flow as has been shown discussing the stream- and spanwise distributions of Nusselt as well as cross-sectional distributions of turbulent Prandtl numbers. For the latter the assumption of a constant Pr_t was demonstrated to be invalid for turbulent heat transfer in an asymmetrically heated duct especially due to the cross-flow influence. The streamwise Nusselt number profiles demonstrated the continuous degradation of heat transfer typically encountered for a thermal entrance problem with a developing thermal boundary layer. Due to the secondary flow mixing the heat transfer drop is decelerated such that the heat flux follows a function of $Nu \approx -220\, x^{-0.1} + c$ in the presented HARCD case. The corner vortex system also causes a spanwise heat transfer gradient causing the spanwise varying constant c. Midway along the duct with an established temperature boundary layer, Nu in the centre is ≈ 15% lower than in the corner region.

The curved air HARCD LES results have been presented in chapter 4. The straight section results are similar as for the water HARCD with an inverse behaviour observed for the secondary

flow modulation when heating is applied. A secondary flow intensification of the small vortex and a slight weakening of the larger vortex has been noted caused by the viscosity rise towards the heated wall. Due to the shorter straight section, the effects have been less pronounced as for the water HARCD. Along the following curved section Prandtl's flow of the first kind is additionally developing. The secondary flow field structure depends heavily on the respective curvature radius r_c of the three cases RC60 with $r_c = 60\,\mathrm{mm}$, RC180 with $r_c = 180\,\mathrm{mm}$ and RC900 with $r_c = 900\,\mathrm{mm}$. For the highest curvature case RC60, we noted the pressure difference between outer and inner radius wall to cause a significant downwards oriented flow upstream of the actual curved section, displacing the corner vortex system. The Dean vortex system rapidly evolves along the curved section and dominates the secondary flow field with $\overline{u}_{cf}$ reaching up to 26.1% of u_b, i.e. it is over an order of magnitude stronger than the turbulence-induced secondary flow. Furthermore, it has been observed that the ICW Dean vortices emerge at the inner radius wall centre as secondary flow instability and vanish again towards the outlet. Prandtl's flow of the second kind is reduced to four minor vortices restricted to the ultimate corner regions. The RC180 secondary flow field resembles that of RC60, although the noticeably weaker Dean vortices require a longer distance to supersede the turbulence-induced secondary flow. For case RC900, turbulence- and curvature-induced secondary flows are of comparable strength with $\overline{u}_{cf}$ reaching up to 3.8% of u_b. Hence, the corner vortex system is not replaced by the Dean vortex system, but both systems are steadily merging. We have described the significant influence of the $\overline{u}_{cf}$-field on streamwise velocity and temperature fields. Especially for case RC60, a strong distortion of the mean flow has been shown. Likewise, the temperature boundary layer is distorted markedly by the curvature-induced secondary flow. For case RC60 with the strongest mixing, the temperature distribution has been noted to change its form to a candle flame structure with cold fluid reaching up to the heated wall. For the weaker Dean vortex cases a strong bulging and augmented corrugation of the temperature profiles has been observed.

For the TBL profiles of the straight heated section an inverse behaviour has been described as for the water HARCD with a decrease of Re_τ by $\approx 30\%$, a constant downward shift of the u^+-profile and an increase of all Reynolds stress components. The application of semi-local scaling transformations revealed that the formulation by Trettel and Larsson (2016) and Patel et al. (2015), respectively, results in the overall best collapse for velocity, turbulence and temperature profiles. Furthermore, it has been shown that the applicability of transformation laws is limited to situations of weak cross-flow influence, achieving the best results for the straight section with only weak turbulence-induced secondary flow present, and the curved section of case RC900. As expected, for the medium and high curvature cases deviations are rising and no collapse of the profiles is achieved.

The mean streamwise vorticity and the terms of its balance equation have been analysed to further investigate the secondary flow structure. For the straight section corner region, we have expectedly observed the inverse behaviour as for the water HARCD with all terms weakening when heating is applied and penetrating less deep into the duct corner. In contrast to the water HARCD, the asymmetric variation of corner turbulence and viscous terms has been found not to be in accordance with the asymmetric vortex modulation, the small vortex getting noticeably stronger and the large vortex slightly weaker. However, this deviation has been shown to agree with the scaling arguments of Pirozzoli et al. (2018), predicting a separation of corner and

core vorticity for a high enough ratio of Re_b/Re_τ. Due to the inverse effect of heating on the viscosity, this ratio drops locally for the water HARCD and rises for the air HARCD. With the additional presence of Prandtl's flow of the first kind the vorticity dynamics change drastically, being dominated by a balance of turbulence, viscous and curvature terms. For cases RC180 and RC900, we have observed that from the original corner vortex pairs those four vortices with equal spin as the emerging Dean vortices get absorbed and only those with opposite spin remain. The latter are restricted towards the HARCD corner areas asymmetrically attached to short and lateral sidewall, respectively, and are intensifying along the curved section. It has been shown that this strengthening process of the remaining turbulence-induced vortices is accompanied by a strengthening of the turbulence and viscous terms of the vorticity balance equation, which is more pronounced at the outer than at the heated inner radius wall.

Employing Reynolds quadrant and octant analysis methods, the latter including temperature fluctuations, the heating- and curvature-induced modulations of the Reynolds shear stress term $\overline{u'v'}$-contributions have been investigated. As expected and in contrast to the water HARCD, a heating-induced strengthening of turbulent ejections ($\overline{u'v'}_{Q2}$) and sweeps ($\overline{u'v'}_{Q4}$) has been noted. The octant analysis has further revealed that turbulent ejections are mainly associated with positive values of T' and sweeps with negative ones. Evaluating near-wall turbulent ejection distributions along the lower heatable and adiabatic lateral sidewalls has produced an explanation for the asymmetric secondary flow modulation as well as the differing behaviour of corner and core vorticity, with the driving mechanism for turbulence-induced secondary flow being the variation between core and corner turbulent ejection strength. It has been shown that along the lower wall, the heated duct $\overline{u'v'}_{Q2}$-profiles surpass those for the adiabatic duct except for in the ultimate corner region. Expectedly, the small vortex becomes stronger in the centre and the corner vorticity weaker. Along the lateral wall, turbulent ejections intensify in the lower 10% affected by the heating except for a slight drop in the ultimate corner region, and remain unchanged with respect to the adiabatic duct for the remainder. Thus, the ejection intensity variation decreases between corner and core as well as the ultimate corner region, explaining the large vortex weakening and the corner vorticity reduction. The development of Prandtl's flow of the first kind causes a noticeable variation in the $\overline{u'v'}$-contributions depending on the local cross-flow intensity. For the midplane profiles of case RC60 a $\overline{u'v'}_{Q2}$- and $\overline{u'v'}_{Q4}$-weakening at the inner and a strengthening at the outer radius wall has been noted, whereas for the off-centre profiles a near-wall peak (inner radius wall) and general increase (outer radius wall) has been observed. A further investigation for case RC900 based on the JPDF distribution of (u', v') has revealed that the heating-induced rise of $\overline{u'v'}_{Q2}$ is due to a stretching of the central JPDF-ellipsis towards higher value pairs of (u', v'), whereas the curvature-induced drop is accompanied by a contraction towards lower value pairs of (u', v'). Moreover, by the JPDF-distribution changing from an elliptical to a circular shape it has been demonstrated that in the duct centre $\overline{u'v'}$ is dominated by ejection and sweeping events and towards the lateral wall all quadrants give a comparable $\overline{u'v'}$-contribution.

The turbulent heat transfer analysis using Nusselt and turbulent Prandtl number distributions has highlighted the significant impact of secondary flow presence. The cross-sectional distribution of Pr_t in the straight section of the air HARCD has supported the water HARCD conclusion that the assumption of a constant Pr_t is invalid for an asymmetrically heated cooling duct

configuration. With the additional presence of curvature-induced secondary flow, deviations increase noticeably depending on the respective Dean vortex strength. Midplane near-wall Pr_t-profiles, exhibiting a good agreement with available DNS data, have revealed that even a weak secondary flow influence leads to strong local variations in the turbulent Prandtl number, e.g. the midplane profiles of Pr_t vary from $\approx 1.1 - 0.8$ for the straight and from $\approx 1.55 - 0.8$ for the curved section of case RC900. The straight section Nusselt number distribution has shown a similar progression as for the water HARCD, depicting a continuous degradation of the heat transfer with $Nu \approx 7.2\, x^{-0.465} + c$. With curvature-induced secondary flow developing, the stream- and spanwise heat transfer gradients increase significantly. Exemplary for case RC60, the spanwise variation may reach up to $Nu = 26.3$ in the centre and $Nu = 166.5$ close to the lateral wall, where the strong Dean vortex mixing causes cold fluid to reach the heated wall. Overall, we have observed that the additional secondary flow mixing leads to an intensification of the heat transfer along the curved section with the integral heat flux of case RC60 surpassing that of case RC900 by 50%. Case RC180 has achieved an increase of only 5% as the Dean vortex mixing is too weak for cold fluid to come into direct contact with the heated wall and the temperature boundary layer thus acts as an insulation.

In chapter 5, the results for well-resolved RANS simulations have been presented for the asymmetrically heated straight water HARCD configuration and the curved air HARCD configurations. The set-ups have been recreated based on the LES set-ups for the simulation with the flow solver ANSYS CFX. We have included the SST and BSL EARSM turbulence models as well as the BSL and SSG Reynolds stress models in this analysis with their standard parameters as defined within ANSYS CFX. The turbulent heat flux modelling has been varied from employing the standard constant turbulent Prandtl number approach over algebraic models to introducing additional transport equations for the single components of the turbulent heat flux vector $\overline{u_i' h'}$. The LES-RANS comparison has been subdivided into three parts based on the three HARCD sections: (I) the periodic adiabatic feed line has served to analyse the prediction capabilities of turbulence-induced secondary flow, (II) the straight heated section to investigate the interaction of turbulence-induced secondary flow and turbulent heat transfer and (III) the heated curved section with varying curvature radius to discuss the interaction of curvature- and turbulence-induced secondary flow and turbulent heat transfer.

The comparison of the adiabatic section corner vortex system has shown that the overall best agreement with the water HARCD LES data is achieved by employing the BSL RSM model followed by the BSL EARSM model. The larger vortices oriented along the lateral sidewalls are well represented both in position and strength, whereas the intensity and extension of the smaller ones oriented along the short sidewalls are noticeably underestimated. Employing the SST model, secondary flow is absent due to the isotropic turbulence assumption. In the SSG RSM, the secondary flow is overall significantly underestimated as the TBL is not resolved using the scalable wall function approach instead. All RANS models have shown deficiencies predicting the near-wall Reynolds stress distributions. Even for the BSL RSM especially the streamwise $\overline{u'u'}$-peak is significantly underestimated compared to the HARCD LES as well as the square duct DNS by Pirozzoli et al. (2018). The wall shear stress comparison at the short sidewall has revealed a slight overprediction for the BSL RSM and BSL EARSM, and a slight underprediction for the SSG RSM and SST model.

Along the straight heated water HARCD, considerable deviations in the temperature profile for all RANS models compared to the LES have been noticed, which are due to the underestimation of the corner vortices above the heatable wall. The two small corner vortices transport warmed-up fluid above the heated wall towards the duct midplane and then upwards creating a hot spot region. The associated $\overline{T}$-isoline upwards bulging in the centre is most prominent in the LES and significantly less pronounced in the RANS, where the BSL RSM again has shown the overall best agreement with LES data. The lowest integral heat transfer has been predicted by the SSG RSM, which is attributed to the wall function approach of the ε-based model. For the ω-based models, the combination SST/$Pr_t = 0.9$ without secondary flow influence has surprisingly predicted a similar heat flux as the LES. Consequently, for the combinations BSL EARSM/$Pr_t = 0.9$ and BSL RSM/$Pr_t = 0.9$ an increasing overestimation is present depending on the small vortex secondary flow strength. Employing various turbulent heat flux closure models in combination with the BSL RSM has shown that the near-wall temperature profile can be improved by using the algebraic Younis model or additional PDEs for $\overline{u_i'h'}$ instead of using the default $Pr_t = 0.9$. However, for the more complex heat flux closure models a further integral heat transfer overestimation has been noted. This deviation has been attributed to an overestimation of the heated wall-normal turbulent heat flux component $\overline{v'h'}$ with respect to the LES, which is present for all investigated BSL RSM simulations. The overestimation is lowest for the combination BSL RSM/$Pr_t = 0.9$ and increases further when more complex heat flux closure models are utilised. Hence, the highest integral heat flux deviation has been observed for the BSL RSM employing additional PDEs followed by algebraic closure models. Similar as the heat flux, also the wall shear stress at the heated wall is overestimated and the deviation with respect to the LES is higher than for the adiabatic duct. As expected, the specific choice of turbulent heat flux closure has shown an only minor impact on the wall shear stress.

For the straight inlet section of the curved air HARCD configurations with rising viscosity towards the heated wall, the observed behaviour and deviations of the straight water HARCD have been reproduced and the expected inverse heating effect on flow statistics and turbulence-induced secondary flow has been obtained. The secondary flow fields for the various configurations have shown, that all RANS models tend to underestimate $\overline{u}_{cf}$ in the straight as well as in the curved sections. The most prominent deviations occur for case RC900 as turbulence-induced secondary flow is of comparable strength as the curvature-induced one. Likewise, noticeable $\overline{u}_{cf}$ differences are present in between the various RANS models, with the BSL RSM coming closest to the LES results. These secondary flow deviations effect variations in the temperature field. In contrast to the water HARCD, an overall underestimation of the integral heat flux is present, which has been attributed to an underestimation of the heated wall-normal turbulent heat flux component $\overline{v'h'}$. The lowest deviations with respect to the LES have been achieved by the combination BSL RSM/$Pr_t = 0.9$ as more complex turbulent heat flux models have not been applied for the curved HARCD simulations.

6.2 Outlook

For future numerical investigations of realistic liquid-propellant rocket engine cooling duct configurations for industrial as well as academic applications, three abilities are crucial. The

abilities to

- efficiently and accurately perform the simulations for complex geometries,
- cover real gas effects for cryogenic coolants, especially of liquid hydrogen and methane, including rapid substantial changes of thermodynamic quantities,
- and account for wall roughness effects as additive manufacturing technologies become more and more important and printed ducts generally exhibit a higher wall roughness than milled ones.

Based on the well-resolved LES results and the comparison with RANS presented within this work, it can be decided for which HARCD configuration or parts of it a high accuracy LES is required and for which the RANS prediction capabilities are sufficient to capture the interaction of secondary flows and heat transfer. Furthermore, the LES databases may serve to adjust RANS turbulence model parameters and turbulent heat flux closure models for HARCD simulations, similar as shown e.g. in Menter et al. (2019) for an adiabatic square duct flow.

When a higher accuracy is required, a well-resolved LES has to be conducted. The LES has to be able to accurately predict the interaction of secondary flows, heat transfer and real gas effects. The ability to cover real gas thermodynamics is available and validated both in INCA and CATUM, by either employing real gas equations of state or via a tabulated thermodynamics approach, cf. Matheis (2017) and Doehring et al. (2021). Accurately representing real gas flows generally requires a smaller time step size and depending on the specific thermodynamic effects an increased spatial resolution, e.g. to capture the pseudo-boiling line in transcritical flows. Consequently, computational costs increase. The high Reynolds numbers of realistic cooling duct flows, which are an order of magnitude higher than in the present thesis, effect a further rise of the numerical effort. A method to alleviate computational costs of LES is wall-modelled LES (WMLES).

In WMLES the innermost $10-20\%$ of the TBL are not resolved, but the turbulence field is modelled. Thus a coarser spatial resolution and larger time step size can be employed leading to a significant reduction of computational costs. One of the major challenges of WMLES is to correctly predict the corner vortex system as well as the interaction of turbulence- and curvature-induced secondary flow as the regions of highest vorticity source and sink terms are located within the under-resolved modelled part of the flow field. The well-resolved LES databases generated within this thesis may support the development of efficient and accurate WMLES. Promising methods would be the enrichment of the WMLES by secondary flow modes extracted from a proper orthogonal decomposition or applying machine learning based WMLES as recently presented by Lozano-Durán and Bae (2020), with our LES databases as training sets. Subsequently, an extension of the WMLES wall model for example by a statistical roughness model can be assessed to include roughness effects on flow field and heat transfer.

Bibliography

Adams, N.A., Hickel, S., Franz, S., 2004. Implicit subgrid-scale modeling by adaptive deconvolution. Journal of Compututational Physics 200, 412–431. doi:10.1016/j.jcp.2004.04.010.

Ahn, J., Choi, H., Lee, J.S., 2005. Large eddy simulation of flow and heat transfer in a channel roughened by square or semicircle ribs. Journal of Turbomachinery 127, 263–269. doi:10.1115/1.1811098.

ANSYS Inc., 2020a. ANSYS CFX-solver modeling guide. Release 2020 R1.

ANSYS Inc., 2020b. ANSYS CFX-solver theory guide. Release 2020 R1.

Baines, W.D., Brundrett, E., 1964. The production and diffusion of vorticity in duct flow. Journal of Fluid Mechanics 19, 375–394. doi:10.1017/S0022112064000799.

Banerjee, S., Krahl, R., Durst, F., Zenger, C., 2007. Presentation of anisotropy properties of turbulence, invariants versus eigenvalue approaches. Journal of Turbulence 8, 1–27. doi:10.1080/14685240701506896.

Bhunia, A., Chen, C.L., 2009. Flow characteristics in a curved rectangular channel with variable cross-sectional area. Journal of Fluids Engineering 131, 091102. doi:10.1115/1.3176970.

Breuer, M., Rodi, W., 1994. Large-eddy simulation of turbulent flow through a straight square duct and a 180° bend, in: Voke, P., Kleiser, L., Chollet, J. (Eds.), Direct and Large-Eddy Simulation I. Springer. volume 26 of *Fluid Mechanics and Its Applications*, pp. 273–285. doi:10.1007/978-94-011-1000-6_24.

Brun, C., Petrovan Boiarciuc, M., Haberkorn, M., Comte, P., 2008. Large eddy simulation of compressible channel flow. Theoretical and Computational Fluid Dynamics 22, 189–212. doi:10.1007/s00162-007-0073-y.

Brundrett, E., Burroughs, P.R., 1967. The temperature inner-law and heat transfer for turbulent air flow in a vertical square duct. International Journal of Heat and Mass Transfer 10, 1133–1142. doi:10.1016/0017-9310(67)90079-8.

Budich, B., 2018. Shock phenomena in cavitating flow and its application to ship propellers. Ph.D. thesis. Technical University of Munich.

Budich, B., Schmidt, S.J., Adams, N.A., 2018. Numerical simulation and analysis of condensation shocks in cavitating flow. Journal of Fluid Mechanics 838, 759–813. doi:10.1017/jfm.2017.882.

Chandratilleke, T.T., Nadim, N., Narayanaswamy, R., 2012. Vortex structure-based analysis of laminar flow behaviour and thermal characteristics in curved ducts. International Journal of Thermal Sciences 59, 75–86. doi:10.1016/j.ijthermalsci.2012.04.014.

Chandratilleke, T.T., Nursubyakto, A., 2003. Numerical prediction of secondary flow and convective heat transfer in externally heated curved rectangular ducts. International Journal of Thermal Sciences 42, 187–198. doi:10.1016/S1290-0729(02)00018-2.

Choi, H., Moin, P., 2012. Grid-point requirements for large eddy simulation: Chapman's estimates revisited. Physics of Fluids 24, 011702. doi:10.1063/1.3676783.

Choi, H.S., Park, T.S., 2013. The influence of streamwise vortices on turbulent heat transfer in rectangular ducts with various aspect ratios. International Journal of Heat and Fluid Flow 40, 1–14. doi:10.1016/j.ijheatfluidflow.2012.12.003.

Choi, K.S., Lumley, J.L., 2001. The return to isotropy of homogeneous turbulence. Journal of Fluid Mechanics 436, 59–84. doi:10.1017/S002211200100386X.

Coleman, G., Kim, J., Moser, R., 1995. A numerical study of turbulent supersonic isothermal-wall channel flow. Journal of Fluid Mechanics 305, 159–183. doi:10.1017/S0022112095004587.

Daly, B.J., Harlow, F.H., 1970. Transport equations in turbulence. Physics of Fluids 13, 2634–2649. doi:10.1063/1.1692845.

Dean, W., 1927. Note on the motion of fluid in a curved pipe. The London, Edinburgh, and Dublin Philosophical Magazine and Journal of Science 4, 208–223. doi:10.1080/14786440708564324.

Dean, W., 1928. The streamline motion of fluid in a curved pipe. The London, Edinburgh, and Dublin Philosophical Magazine and Journal of Science 5, 673–695. doi:10.1080/14786440408564513.

Demuren, A.O., Rodi, W., 1984. Calculation of turbulence-driven secondary motion in non-circular ducts. Journal of Fluid Mechanics 140, 189–222. doi:10.1017/S0022112084000574.

Doehring, A., Kaller, T., Schmidt, S.J., Adams, N.A., 2021. Large-eddy simulation of turbulent channel flow at transcritical states. Journal of Heat and Fluid Flow 89, 108781. doi:10.1016/j.ijheatfluidflow.2021.108781.

Ducros, F., Ferrand, V., Nicoud, F., Weber, C., Darracq, D., Gacherieu, C., Poinsot, T., 1999. Large-eddy simulation of the shock/turbulence interaction. Journal of Computational Physics 152, 517–549. doi:10.1006/jcph.1999.6238.

Egerer, C., 2016. Large-eddy simulation of turbulent cavitating flows. Ph.D. thesis. Technical University of Munich.

Egerer, C.P., Schmidt, S.J., Hickel, S., Adams, N.A., 2016. Efficient implicit LES method for the simulation of turbulent cavitating flows. Journal of Computational Physics 316, 453–469. doi:10.1016/j.jcp.2016.04.021.

Emory, M., Iaccarino, G., 2014. Visualizing turbulence anisotropy in the spatial domain with componentality contours, in: Annual Research Briefs, Center for Turbulence Research, Stanford University, pp. 123–138.

Fan, Y., Li, W., Pirozzoli, S., 2020. Energy-based decomposition of friction drag in turbulent square-duct flows. International Journal of Heat and Fluid Flow 86, 108731. doi:10.1016/j.ijheatfluidflow.2020.108731.

Fang, X., Yang, Z., Wang, B.C., Tachie, M.F., Bergstrom, D.J., 2017. Large-eddy simulation of turbulent flow and structures in a square duct roughened with perpendicular and V-shaped ribs. Physics of Fluids 29, 065110. doi:10.1063/1.4985715.

Fellouah, H., Castelain, C., Ould El Moctar, A., Peerhossaini, H., 2006. A criterion for detection of the onset of Dean instability in Newtonian fluids. European Journal of Mechanics, B/Fluids 25, 505–531. doi:10.1016/j.euromechflu.2005.11.002.

Garnier, E., Adams, N.A., Sagaut, P., 2009. Large Eddy Simulation for Compressible Flows. Springer Netherlands. doi:10.1007/978-90-481-2819-8.

Gavrilakis, S., 1992. Numerical simulation of low-Reynolds-number turbulent flow through a straight square duct. Journal of Fluid Mechanics 244, 101–129. doi:10.1017/S0022112092002982.

Gessner, F.B., Jones, J.B., 1965. On some aspects of fully-developed turbulent flow in rectangular channels. Journal of Fluid Mechanics 23, 689–713. doi:10.1017/S0022112065001635.

Ghosal, S., 1996. An analysis of numerical errors in large-eddy simulations of turbulence. Journal of Computational Physics 125, 187–206. doi:10.1006/jcph.1996.0088.

Gottlieb, S., Shu, C., 1998. Total variation diminishing Runge-Kutta schemes. Mathematics of Computation 67, 73–85. doi:10.1090/S0025-5718-98-00913-2.

Grilli, M., Schmid, P.J., Hickel, S., Adams, N.A., 2012. Analysis of unsteady behaviour in shockwave turbulent boundary layer interaction. Journal of Fluid Mechanics 700, 16–28. doi:10.1017/jfm.2012.37.

Guala, M., Hommema, S.E., Adrian, R.J., 2006. Large-scale and very-large-scale motions in turbulent pipe flow. Journal of Fluid Mechanics 554, 521–542. doi:10.1017/S0022112006008871.

Günther, O., Kaller, T., Doehring, A., 2020. Heat transfer in nozzle cooling channels [PowerPoint presentation], in: Final Colloquium of the Collaborative Research Center TRR40, 16.-17. Nov. 2020, Technical University of Munich, Garching, Germany.

Guo, J., Yang, X.I.A., Ihme, M., 2018. Thermal structures and heat transfer in wall-bounded flows at transcritical conditions, in: Annual Research Briefs, Center for Turbulence Research, Stanford University, pp. 273–284.

Haynes, H.M. (Ed.), 2016. CRC Handbook of Chemistry and Physics. 97 ed., CRC Press.

Hébrard, J., Métais, O., Salinas-Vásquez, M., 2004. Large-eddy simulation of turbulent duct flow: heating and curvature effects. International Journal of Heat and Fluid Flow 25, 569–580. doi:10.1016/j.ijheatfluidflow.2004.03.002.

Hébrard, J., Salinas-Vásquez, M., Métais, O., 2005. Spatial development of turbulent flow within a heated duct. Journal of Turbulence 6, N8. doi:10.1080/14685240500103184.

Hickel, S., Adams, N.A., 2007. On implicit subgrid-scale modeling in wall-bounded flows. Physics of Fluids 19, 105106. doi:10.1063/1.2773765.

Hickel, S., Adams, N.A., 2008. Implicit LES applied to zero-pressure-gradient and adverse-pressure-gradient boundary-layer turbulence. International Journal of Heat and Fluid Flow 29, 626–639. doi:10.1016/j.ijheatfluidflow.2008.03.008.

Hickel, S., Adams, N.A., Domaradzki, J.A., 2006. An adaptive local deconvolution method for implicit LES. Journal of Computational Physics 213, 413–436. doi:10.1016/j.jcp.2005.08.017.

Hickel, S., Adams, N.A., Mansour, N.N., 2007. Implicit subgrid-scale modeling for large-eddy simulation of passive-scalar mixing. Physics of Fluids 19, 095102. doi:10.1063/1.2770522.

Hickel, S., Egerer, C.P., Larsson, J., 2014. Subgrid-scale modeling for implicit large eddy simulation of compressible flows and shock-turbulence interaction. Physics of Fluids 26. doi:10.1063/1.4898641.

Hirota, M., Fujita, H., Yokosawa, H., 1994. Experimental study on convective heat transfer for turbulent flow in a square duct with a ribbed rough wall (characteristics of mean temperature field). Journal of Heat Transfer 116, 332–340. doi:10.1115/1.2911405.

Hirota, M., Fujita, H., Yokosawa, H., Nakai, H., Itoh, H., 1997. Turbulent heat transfer in a square duct. International Journal of Heat and Fluid Flow 18, 170–180. doi:10.1016/S0142-727X(96)00151-8.

Hoagland, L.C., 1960. Fully developed turbulent flow in straight rectangular ducts – secondary flow, its cause and effect on the primary flow. Ph.D. thesis. Department of Mechanical Engineering, Massachusetts Institute of Technology.

Hötte, F., Günther, O., von Sethe, C., Haupt, M., Scholz, P., Rohdenburg, M., 2021. Lifetime experiments of regeneratively cooled rocket combustion chambers and PIV measurements in a high aspect ratio cooling duct, in: Adams, N.A., Schröder, W., Radespiel, R., Haidn, O.J., Sattelmayer, T., Stemmer, C., Weigand, B. (Eds.), Future Space-Transport-System Components under High Thermal and Mechanical Loads: Results from the DFG Collaborative Research Center TRR40. Springer. volume 146 of *Notes on Numerical Fluid Mechanics and Multidisciplinary Design*, pp. 279–293. doi:10.1007/978-3-030-53847-7_18.

Humphrey, J.A.C., Whitelaw, J.H., Yee, G., 1981. Turbulent flow in a square duct with strong curvature. Journal of Fluid Mechanics 103, 443–463. doi:10.1017/S0022112081001419.

Huser, A., Biringen, S., 1993. Direct numerical simulation of turbulent flow in a square duct. Journal of Fluid Mechanics 257, 65–95. doi:10.1017/S002211209300299X.

IAPWS, 2008. Release on the IAPWS Formulation 2008 for the Viscosity of Ordinary Water Substance. Available from http://www.iapws.org.

IAPWS, 2011. Release on the IAPWS Formulation 2011 for the Thermal Conductivity of Ordinary Water Substance. Available from http://www.iapws.org.

Joung, Y., Choi, S.U., Choi, J.I., 2007. Direct numerical simulation of turbulent flow in a square duct: Analysis of secondary flows. Journal of Engineering Mechanics 133, 213–221. doi:10.1061/(ASCE)0733-9399(2007)133:2(213).

Kader, B., 1981. Temperature and concentration profiles in fully turbulent boundary layers. International Journal of Heat and Mass Transfer 24, 1541–1544. doi:10.1016/0017-9310(81)90220-9.

Kaller, T., Hickel, S., Adams, N.A., 2018. LES of an asymmetrically heated high aspect ratio duct at high reynolds number at different wall temperatures, in: 2018 Joint Thermophysics and Heat Transfer Conference, Atlanta, USA. doi:10.2514/6.2018-4287.

Kaller, T., Hickel, S., Adams, N.A., 2020. Prediction capability of RANS turbulence models for asymmetrically heated high-aspect-ratio duct flows, in: AIAA Scitech 2020 Forum, Orlando, USA. doi:10.2514/6.2020-0354.

Kaller, T., Pasquariello, V., Hickel, S., Adams, N.A., 2017. Large-eddy simulation of the high-Reynolds-number flow through a high-aspect-ratio cooling duct, in: Proceedings of the 10th International Symposium on Turbulence and Shear Flow Phenomena (TSFP-10), Chicago, USA.

Kaller, T., Pasquariello, V., Hickel, S., Adams, N.A., 2019. Turbulent flow through a high aspect ratio cooling duct with asymmetric wall heating. Journal of Fluid Mechanics 860, 258–299. doi:10.1017/jfm.2018.836.

Kang, S., Iaccarino, G., 2010. Computation of turbulent Prandtl number for mixed convection around a heated cylinder, in: Annual Research Briefs, Center for Turbulence Research, Stanford University, pp. 295–304.

Kays, W.M., 1994. Turbulent Prandtl number - where are we? Journal of Heat Transfer 116, 284–295. doi:10.1115/1.2911398.

Kim, H.T., Kline, S.J., Reynolds, W.C., 1971. The production of turbulence near a smooth wall in a turbulent boundary layer. Journal of Fluid Mechanics 50, 133–160. doi:10.1017/S0022112071002490.

Kim, J., Moin, P., 1989. Transport of passive scalars in a turbulent channel flow, in: André, J.C., Cousteix, J., Durst, F., Launder, B.E., Schmidt, F.W., Whitelaw, J.H. (Eds.), Turbulent Shear Flows 6, Springer Berlin Heidelberg. pp. 85–96. doi:10.1007/978-3-642-73948-4_9.

Kim, S.Y., Kim, C.S., Cho, H.K., 2021. Local flow structure and turbulence quantities inside a heated rectangular riser in turbulent forced and mixed convection heat transfers. Experimental Thermal and Fluid Science 122, 110297. doi:10.1016/j.expthermflusci.2020.110297.

Kline, S.J., Reynolds, W.C., Schraub, F.A., Runstadler, P.W., 1967. The structure of turbulent boundary layers. Journal of Fluid Mechanics 30, 741–773. doi:10.1017/S0022112067001740.

Ko, T.H., Wu, C.P., 2009. A numerical study on entropy generation induced by turbulent forced convection in curved rectangular ducts with various aspect ratios. International Communications in Heat and Mass Transfer 36, 25–31. doi:10.1016/j.icheatmasstransfer.2008.08.016.

Kobayashi, H., 2005. The subgrid-scale models based on coherent structures for rotating homogeneous turbulence and turbulent channel flow. Physics of Fluids 17, 045104. doi:10.1063/1.1874212.

Kong, H., Choi, H., Lee, J.S., 2000. Direct numerical simulation of turbulent thermal boundary layers. Physics of Fluids 12, 2555–2568. doi:10.1063/1.1287912.

Kravchenko, A., Moin, P., 1997. On the effect of numerical errors in large eddy simulations of turbulent flows. Journal of Computational Physics 131, 310–322. doi:10.1006/jcph.1996.5597.

Lammers, P., Jovanović, J., Frohnapfel, B., Delgado, A., 2012. Erlangen pipe flow: the concept and DNS results for microflow control of near-wall turbulence. Microfluidics and Nanofluidics 13, 429–440. doi:10.1007/s10404-012-0972-0.

Launder, B.E., Ying, W.M., 1972. Secondary flows in ducts of square cross-section. Journal of Fluid Mechanics 54, 289–295. doi:10.1017/S0022112072000680.

Launder, B.E., Ying, W.M., 1973. Prediction of flow and heat transfer in ducts of square cross-section. Proceedings of the Institution of Mechanical Engineers 187, 455–461. doi:10.1243/PIME_PROC_1973_187_131_02.

Lee, J., Jung, S.Y., Sung, H.J., Zaki, T.A., 2013. Effect of wall heating on turbulent boundary layers with temperature-dependent viscosity. Journal of Fluid Mechanics 726, 196–225. doi:doi:10.1017/jfm.2013.211.

Lemmon, E.W., Jacobsen, R.T., 2004. Viscosity and thermal conductivity equations for nitrogen, oxygen, argon, and air. International Journal of Thermophysics 25, 21–69. doi:10.1023/B:IJOT.0000022327.04529.f3.

Leonard, A., 1975. Energy cascade in large-eddy simulations of turbulent fluid flows, in: Frenkiel, F., Munn, R. (Eds.), Turbulent Diffusion in Environmental Pollution. Elsevier. volume 18 of *Advances in Geophysics*, pp. 237 – 248. doi:10.1016/S0065-2687(08)60464-1.

Lesieur, M., Métais, O., Comte, P., 2005. Large-Eddy Simulations of Turbulence. Cambridge University Press. doi:10.1017/CBO9780511755507.

Li, Y., Wang, X., Yuan, S., Tan, S.K., 2016. Flow development in curved rectangular ducts with continuously varying curvature. Experimental Thermal and Fluid Science 75, 1–15. doi:10.1016/j.expthermflusci.2016.01.012.

Li, Y., Wang, X., Zhou, B., Yuan, S., Tan, S.K., 2017. Dean instability and secondary flow structure in curved rectangular ducts. International Journal of Heat and Fluid Flow 68, 189–202. doi:10.1016/j.ijheatfluidflow.2017.10.011.

Ligrani, P., 2013. Heat transfer augmentation technologies for internal cooling of turbine components of gas turbine engines. International Journal of Rotating Machinery 2013, 275653. doi:10.1155/2013/275653.

Lozano-Durán, A., Bae, H.J., 2020. Self-critical machine-learning wall-modeled LES for external aerodynamics, in: Annual Research Briefs, Center for Turbulence Research, Stanford University, pp. 197–210.

Lozano-Durán, A., Jiménez, J., 2014. Effect of the computational domain on direct simulations of turbulent channels up to $Re_\tau = 4200$. Physics of Fluids 26, 011702. doi:10.1063/1.4862918.

Lumley, J.L., 1979. Computational modeling of turbulent flows. Advances in Applied Mechanics 18, 123–176. doi:10.1016/S0065-2156(08)70266-7.

Madabhushi, R.K., Vanka, S.P., 1991. Large eddy simulation of turbulence-driven secondary flow in a square duct. Physics of Fluids A: Fluid Dynamics 3, 2734–2745. doi:10.1063/1.858163.

Mahmoodi-Jezeh, S.V., Wang, B.C., 2020. Direct numerical simulation of turbulent flow through a ribbed square duct. Journal of Fluid Mechanics 900, A18. doi:10.1017/jfm.2020.452.

Mani, M., Babcock, D., Winkler, C., Spalart, P., 2013. Predictions of a supersonic turbulent flow in a square duct, in: 51st AIAA Aerospace Sciences Meeting, Dallas, USA. doi:10.2514/6.2013-860.

Marin, O., Vinuesa, R., Obabko, A.V., Schlatter, P., 2016. Characterization of the secondary flow in hexagonal ducts. Physics of Fluids 28, 125101. doi:10.1063/1.4968844.

Matheis, J., 2017. Numerical simulation of fuel injection and turbulent mixing under high-pressure conditions. Ph.D. thesis. Technical University of Munich.

Matin, R., Hellström, L.H., Hernández-García, A., Mathiesen, J., Smits, A.J., 2018. Coherent structures in turbulent square duct flow. International Journal of Heat and Fluid Flow 74, 144–153. doi:10.1016/j.ijheatfluidflow.2018.08.007.

Melling, A., Whitelaw, J.H., 1976. Turbulent flow in a rectangular duct. Journal of Fluid Mechanics 78, 289–315. doi:10.1017/S0022112076002450.

Menter, F., Lechner, R., Matyusheno, A., 2019. Best practice: generalized k-ω two-equation turbulence model in ANSYS CFD (GEKO). Technical Report. ANSYS, Inc.

Meyer, M.L., 1997. The effect of cooling passage aspect ratio on curvature heat transfer enhancement. Technical Report. NASA Lewis Research Center. TM-107426.

Modesti, D., Pirozzoli, S., 2016. Reynolds and Mach number effects in compressible turbulent channel flow. International Journal of Heat and Fluid Flow 59, 33–49. doi:10.1016/j.ijheatfluidflow.2016.01.007.

Modesti, D., Pirozzoli, S., Grasso, F., 2019. Direct numerical simulation of developed compressible flow in square ducts. International Journal of Heat and Fluid Flow 76, 130–140. doi:10.1016/j.ijheatfluidflow.2019.02.002.

Monin, A.S., Yaglom, A.M., Lumley, J.L., 2007. Statistical Fluid Mechanics, Volume II: Mechanics of Turbulence. Dover Publications.

Monty, J.P., 2005. Developments in smooth wall turbulent duct flows. Ph.D. thesis. The University of Melbourne.

Monty, J.P., Stewart, J.A., Williams, R.C., Chong, M.S., 2007. Large-scale features in turbulent pipe and channel flows. Journal of Fluid Mechanics 589, 147–156. doi:10.1017/S002211200700777X.

Münch, C., Métais, O., 2006. Large eddy simulations of the turbulent flow in curved ducts: influence of the curvature radius, in: Lamballais, E., Friedrich, R., Geurts, B., Métais, O. (Eds.), Direct and Large-Eddy Simulation VI. Springer, pp. 209–216. doi:10.1007/978-1-4020-5152-2_24.

Münch, C., Métais, O., 2007. Large eddy simulations in curved square ducts: variation of the curvature radius. Journal of Turbulence 8, 1–18. doi:10.1080/14685240601142859.

Nikuradse, J., 1930. Untersuchungen über turbulente Strömungen in nicht kreisförmigen Rohren. Ingenieur-Archiv 1, 306–332. doi:10.1007/BF02079937.

O'Neill, P.L., Nicolaides, D., Honnery, D., Soria, J., 2004. Autocorrelation functions and the determination of integral length with reference to experimental and numerical data, in: Behnia, M., Lin, W., McBain, G.D. (Eds.), Proceedings of the Fifteenth Australasian Fluid Mechanics Conference, The University of Sydney.

Orlandi, P., 1990. Vortex dipole rebound from a wall. Physics of Fluids A: Fluid Dynamics 2, 1429–1436. doi:10.1063/1.857591.

Orlandi, P., Modesti, D., Pirozzoli, S., 2018. DNS of turbulent flows in ducts with complex shape. Flow, Turbulence and Combustion 100, 1063–1079. doi:10.1007/s10494-018-9911-9.

Pallares, J., Davidson, L., 2002. Large-eddy simulations of turbulent heat transfer in stationary and rotating square ducts. Physics of Fluids 14, 2804–2816. doi:10.1063/1.1489684.

Park, G.I., Wallace, J.M., Wu, X., Moin, P., 2012. Boundary layer turbulence in transitional and developed states. Physics of Fluids 24, 035105. doi:10.1063/1.3693146.

Pasquariello, V., Grilli, M., Hickel, S., Adams, N.A., 2014. Large-eddy simulation of passive shock-wave/boundary-layer interaction control. International Journal of Heat and Fluid Flow 49, 116–127. doi:10.1016/j.ijheatfluidflow.2014.04.005.

Pasquariello, V., Hickel, S., Adams, N.A., 2017. Unsteady effects of strong shock-wave/boundary-layer interaction at high Reynolds number. Journal of Fluid Mechanics 823, 617–657. doi:10.1017/jfm.2017.308.

Patel, A., Boersma, B.J., Pecnik, R., 2016. The influence of near-wall density and viscosity gradients on turbulence in channel flows. Journal of Fluid Mechanics 809, 793–820. doi:10.1017/jfm.2016.689.

Patel, A., Peeters, J.W.R., Boersma, B.J., Pecnik, R., 2015. Semi-local scaling and turbulence modulation in variable property turbulent channel flows. Physics of Fluids 27, 095101. doi:10.1063/1.4929813.

Pinelli, A., Uhlmann, M., Sekimoto, A., Kawahara, G., 2010. Reynolds number dependence of mean flow structure in square duct turbulence. Journal of Fluid Mechanics 644, 107–122. doi:10.1017/S0022112009992242.

Pirozzoli, S., Bernardini, M., 2011. Turbulence in supersonic boundary layers at moderate Reynolds number. Journal of Fluid Mechanics 688, 120–168. doi:10.1017/jfm.2011.368.

Pirozzoli, S., Grasso, F., Gatski, T.B., 2004. Direct numerical simulation and analysis of a spatially evolving supersonic turbulent boundary layer at $M = 2.25$. Physics of Fluids 16, 530–545. doi:10.1063/1.1637604.

Pirozzoli, S., Modesti, D., Orlandi, P., Grasso, F., 2018. Turbulence and secondary motions in square duct flow. Journal of Fluid Mechanics 840, 631–655. doi:10.1017/jfm.2018.66.

Pizzarelli, M., Nasuti, F., Onofri, M., 2011. Analysis of curved-cooling-channel flow and heat transfer in rocket engines. Journal of Propulsion and Power 27, 1045–1053. doi:10.2514/1.B34163.

Pope, S.B., 2000. Turbulent Flows. Cambridge University Press. doi:10.1017/CBO9780511840531.

Prandtl, L., 1926. Über die ausgebildete Turbulenz, in: Proceedings of the International Congress for Applied Mechanics, Zurich, Switzerland, pp. 62–74.

Prandtl, L., 1927. On developed turbulence. N.A.C.A. TM 435.

Qin, Z., Pletcher, R.H., 2006. Large eddy simulation of turbulent heat transfer in a rotating square duct. International Journal of Heat and Fluid Flow 27, 371–390. doi:10.1016/j.ijheatfluidflow.2006.01.003.

Quaatz, J.F., Giglmaier, M., Hickel, S., Adams, N.A., 2014. Large-eddy simulation of a pseudo-shock system in a Laval nozzle. International Journal of Heat and Fluid Flow 49, 108–115. doi:10.1016/j.ijheatfluidflow.2014.05.006.

Remmler, S., 2016. Gravity-wave breaking and turbulence in the atmosphere. Ph.D. thesis. Technical University of Munich.

Remmler, S., Hickel, S., 2012. Direct and large eddy simulation of stratified turbulence. International Journal of Heat and Fluid Flow 35, 13–24. doi:10.1016/j.ijheatfluidflow.2012.03.009.

Remmler, S., Hickel, S., 2014. Spectral eddy viscosity of stratified turbulence. Journal of Fluid Mechanics 755, R6. doi:10.1017/jfm.2014.423.

Remmler, S., Hickel, S., Fruman, M.D., Achatz, U., 2015. Validation of large-eddy simulation methods for gravity wave breaking. Journal of the Atmospheric Sciences 72, 3537–3562. doi:10.1175/JAS-D-14-0321.1.

Rochhausen, S., 2017. Modellierung des turbulenten Wärmeflusses in Turbomaschinenströmungen. Ph.D. thesis. Ruhr-Universität Bochum.

Rochlitz, H., Scholz, P., 2015. Application of particle image velocimetry and laser induced fluorescence in a cooling duct flow, in: 31st AIAA Aerodynamic Measurement Technology and Ground Testing Conference, Dallas (USA). doi:10.2514/6.2015-2868.

Rochlitz, H., Scholz, P., 2018. Application of laser-induced fluorescence technique in a duct flow with one heated wall. Experiments in Fluids 59, 1–20. doi:10.1007/s00348-018-2508-1.

Rochlitz, H., Scholz, P., Fuchs, T., 2015. The flow field in a high aspect ratio cooling duct with and without one heated wall. Experiments in Fluids 56, 1–13. doi:10.1007/s00348-015-2071-y.

Salinas-Vásquez, M., Métais, O., 2002. Large-eddy simulation of the turbulent flow through a heated square duct. Journal of Fluid Mechanics 453, 201–238. doi:10.1017/S0022112001006887.

Salinas-Vásquez, M., Vicente Rodríguez, W., Issa, R., 2005. Effects of ridged walls on the heat transfer in a heated square duct. International Journal of Heat and Mass Transfer 48, 2050–2063. doi:10.1016/j.ijheatmasstransfer.2004.10.036.

Sameen, A., Govindarajan, R., 2007. The effect of wall heating on instability of channel flow. Journal of Fluid Mechanics 577, 417–442. doi:10.1017/S0022112007004636.

Schindler, A., Younis, B.A., Weigand, B., 2019. Large-eddy simulations of turbulent flow through a heated square duct. International Journal of Thermal Sciences 135, 302–318. doi:10.1016/j.ijthermalsci.2018.09.018.

Schmidt, S.J., 2015. A low Mach number consistent compressible approach for simulation of cavitating flows. Ph.D. thesis. Technical University of Munich.

Sekimoto, A., Kawahara, G., Sekiyama, K., Uhlmann, M., Pinelli, A., 2011. Turbulence- and buoyancy-driven secondary flows in a horizontal square duct heated from below. Physics of Fluids 23, 075103. doi:10.1063/1.3593462.

Shah, R.K., London, A.L., 1978. Laminar Flow Forced Convection in Ducts. Academic Press, New York, NY.

Simonsen, A.J., Krogstad, P.Å., 2005. Turbulent stress invariant analysis: Clarification of existing terminology. Physics of Fluids 17, 1–4. doi:10.1063/1.2009008.

Speziale, C.G., 1982. On turbulent secondary flows in pipes of noncircular cross-section. International Journal of Engineering Science 20, 863–872. doi:10.1016/0020-7225(82)90008-8.

Su, M.D., Friedrich, R., 1994. Numerical simulation of fully developed flow in a curved duct of rectangular cross-section. International Journal of Heat and Mass Transfer 37, 1257–1268. doi:10.1016/0017-9310(94)90210-0.

Tracy, H.J., 1963. Turbulent flow in a three-dimensional channel. Ph.D. thesis. Georgia Institute of Technology.

Trettel, A., Larsson, J., 2016. Mean velocity scaling for compressible wall turbulence with heat transfer. Physics of Fluids 28, 026102. doi:10.1063/1.4942022.

Trummler, T., Schmidt, S.J., Adams, N.A., 2020. Investigation of condensation shocks and re-entrant jet dynamics in a cavitating nozzle flow by Large-Eddy Simulation. International Journal of Multiphase Flow 125. doi:10.1016/j.ijmultiphaseflow.2020.103215.

Turnow, J., Kornev, N., Zhdanov, V., Hassel, E., 2012. Flow structures and heat transfer on dimples in a staggered arrangement. International Journal of Heat and Fluid Flow 35, 168–175. doi:10.1016/j.ijheatfluidflow.2012.01.002.

Vidal, A., Vinuesa, R., Schlatter, P., Nagib, H., 2017a. Impact of corner geometry on the secondary flow in turbulent ducts, in: Proceedings of the 10th International Symposium on Turbulence and Shear Flow Phenomena (TSFP-10), Chicago, USA.

Vidal, A., Vinuesa, R., Schlatter, P., Nagib, H., 2017b. Influence of corner geometry on the secondary flow in turbulent square ducts. International Journal of Heat and Fluid Flow 67, 69–78. doi:10.1016/j.ijheatfluidflow.2017.07.009.

Vinuesa, R., Noorani, A., Lozano-Duran, A., El Khoury, G., Schlatter, P., Fischer, P.F., Nagib, N.M., 2014. Aspect ratio effects in turbulent duct flows studied through direct numerical simulation. Journal of Turbulence 15, 677–706. doi:10.1080/14685248.2014.925623.

Vreman, A., Geurts, B., Kuerten, H., 1995. A priori tests of large eddy simulation of compressible plane mixing layer. Journal of Engineering Mathematics 29, 299–327. doi:10.1007/BF00042759.

Wagner, W., Pruß, A., 2002. The IAPWS formulation 1995 for the thermodynamic properties of ordinary water substance for general and scientific use. Journal of Physical and Chemical Reference Data 31, 387–535. doi:10.1063/1.1461829.

Wallace, J.M., 2016. Quadrant analysis in turbulence research: history and evolution. Annual Review of Fluid Mechanics 48, 131–158. doi:10.1146/annurev-fluid-122414-034550.

Wallace, J.M., Brodkey, R.S., 1977. Reynolds stress and joint probability density distributions in the $u - v$ plane of a turbulent channel flow. Physics of Fluids 20, 351–355. doi:10.1063/1.861897.

Wallace, J.M., Eckelmann, H., Brodkey, R.S., 1972. The wall region in turbulent shear flow. Journal of Fluid Mechanics 54, 39–48. doi:10.1017/S0022112072000515.

Wardana, I.N.G., Ueda, T., Mizomoto, M., 1992. Structure of turbulent two-dimensional channel flow with strongly heated wall. Experiments in Fluids 13, 17–25. doi:10.1007/BF00208070.

Wardana, I.N.G., Ueda, T., Mizomoto, M., 1994. Effect of strong wall heating on turbulence statistics of a channel flow. Experiments in Fluids 18, 87–94. doi:10.1007/BF00209364.

White, F.M., 2006. Viscous Fluid Flow. 3*rd* ed., McGraw-Hill.

Wilcox, D.C., 2006. Turbulence Modeling for CFD. 3*rd* ed., DCW Industries Inc.

Willmarth, W.W., Lu, S.S., 1972. Structure of the Reynolds stress near the wall. Journal of Fluid Mechanics 55, 65–92. doi:10.1017/S002211207200165X.

Yang, H., Chen, T., Zhu, Z., 2009. Numerical study of forced turbulent heat convection in a straight square duct. International Journal of Heat and Mass Transfer 52, 3128–3136. doi:10.1016/j.ijheatmasstransfer.2009.01.029.

Younis, B.A., Speziale, C.G., Clark, T.T., 2005. A rational model for the turbulent scalar fluxes. Proceedings of the Royal Society A: Mathematical, Physical and Engineering Sciences 461, 575–594. doi:10.1098/rspa.2004.1380.

Zhang, H., Xavier Trias, F., Gorobets, A., Tan, Y., Oliva, A., 2015. Direct numerical simulation of a fully developed turbulent square duct flow up to $Re_\tau = 1200$. International Journal of Heat and Fluid Flow 54, 258–267. doi:10.1016/j.ijheatfluidflow.2015.06.003.

Zheng, D., Wang, X., Yuan, Q., 2019. The flow and heat transfer characteristics in a rectangular channel with convergent and divergent slit ribs. International Journal of Heat and Mass Transfer 141, 464–475. doi:10.1016/j.ijheatmasstransfer.2019.06.060.

Zhu, Z., Yang, H., Chen, T., 2010. Numerical study of turbulent heat and fluid flow in a straight square duct at higher Reynolds numbers. International Journal of Heat and Mass Transfer 53, 356–364. doi:10.1016/j.ijheatmasstransfer.2009.09.021.

Zonta, F., Marchioli, C., Soldati, A., 2012. Modulation of turbulence in forced convection by temperature-dependent viscosity. Journal of Fluid Mechanics 697, 150–174. doi:10.1017/jfm.2012.67.